UNIVERSITY OF SOUTHAMPTON
FACULTY OF ENGINEERING, SCIENCE AND MATHEMATICS
SCHOOL OF CHEMISTRY

Oxygen Reduction at Microelectrodes: Application to the Dissolved Oxygen Sensor for *in situ* Oceanographic Measurements.

by

Maciej Sosna

Thesis for the degree of Doctor of Philosophy

September 2006

UNIVERSITY OF SOUTHAMPTON

ABSTRACT

FACULTY OF ENGINEERING, SCIENCE AND MATHEMATICS
SCHOOL OF CHEMISTRY

Doctor of Philosophy

OXYGEN REDUCTION AT MICROELECTRODES: APPLICATION TO DISSOLVED OXYGEN SENSOR FOR IN SITU OCEANOGRAPHIC MEASUREMENTS

by Maciej Sosna

This work describes the development of an accurate and reliable electrochemical dissolved oxygen sensor for oceanographic measurements. The amperometric response of the sensor gives direct information on the concentration of dissolved oxygen, which is reduced at a microdisc cathode to peroxide species and water. A number of parameters including electrode material, potential waveform, the apparent number of electrons (n_{app}) as well as temperature, salinity and flow effects, are investigated with the aim to gain more insight into the fundamentals of oxygen electroreduction and to optimise the sensor performance.

Parameters for platinum microcathodes electrochemical cleaning are reported, which yield very stable amperometric response under continuous operation, with a maximum standard deviation of the limiting current under 1.5%. An automated calibration method developed to accurately characterise the electrodes is described. Excellent linearity is obtained for electrodes tested and in each case n_{app} is extracted. As an alternative to calibration, an analytical treatment which accounts for temperature and salinity effects is given to calculate the dissolved oxygen concentration directly from the limiting current. A complete error treatment is presented for both calibration and analytical approach.

A prototype oceanographic dissolved oxygen sensor which includes flow control arrangement is described. Its performance in field trials carried out during the RRS Discovery transatlantic cruise D279 is presented. The results of eight deep sea deployments are compared with the dissolved oxygen - depth profiles obtained by on-board Winkler titration of the samples bottled at discrete depths.

Two approaches alternative to the limiting current measurements are also reported, with the aim to perform the measurements directly in the water column on a moving probe: the vibration of the microelectrode (in the bulk solution and in the vicinity of an insulating surface) to create controlled forced convection and transient measurements with the potential step durations down to 1 ms. The latter is shown to be capable of quantitative determination of oxygen, while showing high immunity to the external flow.

Acknowledgments

First of all, I would like to express my gratitude to my supervisor Dr. Guy Denuault for his guidance and the time devoted to the project. His ideas, help and long discussions advanced not only my research but also my appreciation of electrochemical science. I thank Prof. Derek Pletcher for his constructive criticism and guidance. My special thanks go to the team at the Oceanography Centre: Dr. Ralf Prien, Robin Pascal and Dr. Matt Mowlem for their ideas and instrumentation expertise. Without them, the oceanographic sensor would never see the day light (or rather dark cold abyss for most of the time).

I would also like to thank Toru, Kirsty, Dave, Timmy, Rob, Veronica and all past and present members of Guy's and Phil's groups for making this PhD experience so enjoyable. Particularly big cheers! goes to Alex and Sergio for endless discussions on science, life, fine beverages, women… you name it, and simply for being around.

Last but not least, my thanks go to all my family, and in particular to Tomek and Wiesia for all their support.

Pracę tą dedykuję
moim rodzicom.

Table of contents

List of Symbols

Symbol	Description	usual unit
A	(a) area	cm^2
	(b) amplitude of sinusoidal voltage	V
a	microdisc electrode radius	μm
a_j	activity of species j	-
C	conductivity	S
C_{dl}	double layer capacitance	F
c_j	molar concentration of species j	mol dm^{-3}
c_{mj}	molal concentration (molality) of species j	mol kg^{-1}
c_{sat}	oxygen concentration in oxygen saturated solution	mol dm^{-3}
c_w	molar concentration of water	mol dm^{-3}
c^∞	molar concentration in the bulk solution	mol dm^{-3}
D_j	diffusion coefficient of species j	cm^2 s^{-1}
D_w	oxygen diffusion coefficient in water	cm^2 s^{-1}
$E_{1/2}$	half-wave potential	V
$E_{1/4}$, $E_{3/4}$	quartile potentials	V
E_a	activation energy in Arrhenius type relationships	J mol^{-1}
E_{cl}	cleaning potential	V
E_{mix}	mixed potential for a potentiometric sensor	V
E_{ref}	reference electrode potential	V
E_v	activation energy of viscous flow	J mol^{-1}
F	the Faraday constant, 96385	C mol^{-1}
f	resonant frequency of a piezoelectric	Hz
ΔG^*	free energy of activation of diffusing particle	J mol^{-1}
H	Henry's coefficient	mol dm^{-3} Pa^{-1}
h	(a) Planck constant, 6.626×10^{-34}	J s
	(b) half-width of a rectangular flow channel	cm

Symbol	Description	usual unit
i	current	A
i_{lim}	limiting current	A
i_{ss}	steady state current	A
K_{SV}	Stern-Volmer quenching constant	$dm^3\ mol^{-1}$
k	rate constant of the reaction	$mol\ dm^{-3}\ s^{-1}$
M_j	formula weight of species j	$g\ mol^{-1}$
m_j	mass transfer coefficient of species j	$cm\ s^{-1}$
N_0	Avogadro's number, 6.02×10^{23}	mol^{-1}
n	number of electrons transferred in redox reaction	-
n_{app}	apparent number of electrons transferred in oxygen reduction reaction	-
p	pressure	Pa
p_B	barometric pressure	Pa
p_j	partial pressure of gas j	Pa
p_w	water vapour pressure	Pa
Q_a	anodic charge density	$C\ cm^{-2}$
R	gas constant, 8.314	$J\ mol^{-1}\ K^{-1}$
R_T	conductivity ratio (defined in equation 7.1)	-
R_u	uncompensated solution resistance	Ω
S	salinity	-
S^0	solubility of oxygen in water	$\mu M\ O\ kPa^{-1}$
S_A	absolute salinity	-
t	time	s
t_x	time needed to achieve x percent of the steady state response	s
T	absolute temperature	K
T_C	temperature	°C
T_S	scaled temperature defined in equation (1.30)	-

Symbol	Description	usual unit
V_{ex}	volume exchanged to increment oxygen concentration in calibration procedure	ml
V_f	volume flow rate	ml s^{-1}
V_m	molar volume	dm^3 mol^{-1}
V_{tot}	volume of experimental cell	cm^3
V_w	molar volume of water	dm^3 mol^{-1}
v	(a) liquid velocity in channel flow	cm s^{-1}
	(b) scan rate	mV s^{-1}
v_0	maximal liquid velocity in the centre of the flow channel	cm s^{-1}
$\overline{v}$	average liquid velocity in channel flow	cm s^{-1}
x_j	molar fraction of species j	-
y	distance from the wall of a flow channel	cm
z	distance travelled by flowing solution	cm
α	component of free energy of activation of diffusing solute due to cation	J mol^{-1}
$\Delta\alpha$	coefficient defined by $\alpha-\gamma$	J mol^{-1}
β	component of free energy of activation of diffusing solute due to anion	J mol^{-1}
$\Delta\beta$	coefficient defined by $\beta-\gamma$	J mol^{-1}
γ	component of free energy of activation of diffusing solute due to water	J mol^{-1}
δ_0	diffusion layer thickness	cm
δ_{bulk}	distance from the electrode surface where the bulk concentration is reached	cm
ε	coefficient in equation (1.28)	-
η	dynamic viscosity	Pa s
θ	total relative surface coverage	-
κ	the Boltzmann constant, 1.381×10^{-23}	J K^{-1}

Symbol	Description	usual unit
κ_0	coefficient in equation (1.28)	-
λ	coefficient in equation (1.28)	-
ρ	density	g cm^{-3}
τ	(a) potential step duration	s
	(b) dimensionless time (= $4Dt/a^2$)	-
τ_0	unquenched excited state lifetime	s
τ_c	double layer charging time	s
τ_q	quenched excited state lifetime	s
ϕ	coefficient in equation (1.27)	-

Common abbreviations

Abbreviation	Meaning
AUV	autonomous underwater vehicle
BDD	boron-doped diamond
CTD	conductivity, temperature, depth probe
DO	dissolved oxygen
EQCM	electrochemical quartz crystal microbalance
EQCN	electrochemical quartz crystal nanobalance
ESEM	environmental scanning electron microscope
HMDE	hanging mercury drop electrode
NHE	normal hydrogen electrode
ORR	oxygen reduction reaction
PTFE	polytetrafluoroethylene (Teflon)
PVC	polyvinyl chloride
RDE	rotating disc electrode
RE	reference electrode
RF	roughness factor
ROV	remotely operated vehicle
RRDE	rotating ring-disc electrode
SCE	saturated calomel electrode
SD	standard deviation
SEM	scanning electron microscopy
SMSE	saturated mercurous sulphate electrode
WE	working electrode

1 Introduction

1.1 Dissolved oxygen measurements

The concentration of dissolved oxygen (DO) is a vital parameter in industry, physiology and environmental sciences. Therefore quantitative determination of DO is desired as it can provide key information on the controlled or studied system. This is continuously a driving force for extensive research towards development of new DO sensors.

Continuous *in situ* monitoring of oxygen levels is needed in many technological and biotechnological processes, where DO concentrations have to be precisely controlled. Some examples of industrial processes in which monitoring and controlling DO concentration are crucial are listed below:

- food industry – where air or dissolved oxygen can damage foodstuffs (beverages, oils, fats, dairy products, fruit juices) by affecting their shelf-life, organoleptic properties or nutritional values,
- aquacultures and fish farms – where certain levels of oxygenation are required to sustain life and growth of the product,
- water quality monitoring, municipal and sewage water treatment – where oxygen is consumed by microorganisms to break down organic pollutants,
- pharmaceutical industry – where DO concentration has to be optimised during synthesis and storage,
- power plants cooling installations – where oxygen levels have to be kept down to ppb in order to prevent the system corrosion,
- metallurgy – where oxygen is often a key parameter in corrosion processes.

The DO concentration monitoring in tissues and physiological fluids is also of paramount importance. Monitoring the oxygen availability at the cellular level provides vital information on the tissues or organs functions and condition. *In vivo* DO measurements are needed to study e.g. heart diseases and brain injuries [1-3],

tumours development and angiogenesis [4, 5] or muscles work and dysfunction [6, 7]. Blood oxygen level can give valuable data when investigating the overall metabolism rate, cardiovascular and respiratory systems.

DO measurements are also of great significance in environmental sciences. One of the central fields of interest is monitoring DO in natural waters, both inland fresh waters and the open ocean. Oxygen can serve as a tracer for processes ranging in time scale from diurnal to those taking centuries and longer. It can provide vital information on local and global scale changes.

On short time scales DO can be closely correlated with biological activity. Rising DO concentrations can serve as a direct measure of the biological production of photosynthesising organisms. On the other hand, a net decrease in DO gives information on the respiration processes of the aquatic fauna and flora. Introduction of pollutants into a water system will also dramatically decrease the DO concentration (sometimes resulting even in completely anoxic conditions) due to high oxygen consumption in metabolic processes of bacteria and other life forms.

DO in surface waters is in constant equilibrium with air. Its concentration is a result of air-water oxygen dynamic exchange, biological life and mixing rates with deeper water masses. Particularly in the case of seawater, high spatial resolution vertical profiles of shallow waters and continuous DO monitoring at fixed depths can contribute to a quantitative description of air-sea fluxes. Since DO has a complex origin, often the measurements have to be supported by determination of other tracers (e.g. biologically inert gases) to assess simultaneously occurring biological and physical phenomena.

While surface equilibria are established on a time scale of weeks, significantly more time is required for the vertical mixing in deeper regions. Again, DO concentration can serve as an indicator of water masses movement and mixing. Vertical profiles from the surface to full ocean depth depict transitions between zones of different types of biological activity and show the efficiency of vertical mixing. Furthermore, more rapid changes of oxygenation level can reveal the geographical origin of water masses.

Measurements of DO concentration distribution in deep ocean waters and sediments allow insight into seabed-water interaction. Sediment-water oxygen fluxes mirror the rates of remineralisation of organic matter, dissolution or precipitation of minerals such as carbonates or metal oxides, and microbial activity. Combined with monitoring of other vital chemical species, DO measurements can help to create a wider picture of biogeochemical cycles operating constantly in the very complex ocean-sediments system.

Finally, DO levels in the world ocean are believed to be linked very strongly with the evolution of the global climate. Climate models predict the outgassing of oxygen from the oceans due to reduced water circulation as the global warming proceeds [8]. This effect is caused primarily by increased density stratification in high latitudes of both hemispheres, resulting in lowered rates of convectional mixing and subduction of bottom waters [9]. Still, experimental data to support the climate modelling is very scarce. There is a renewed need for monitoring of DO and other parameters at multiple locations worldwide. Since the problem concerns changes taking place over decades and centuries, long term measurements are essential.

1.2 Microelectrodes in analysis

Microelectrodes have long been recognised as a powerful tool in analytical chemistry [10]. Except the obvious advantage of small size, allowing sampling of small volumes and analysis in remote locations, far more important are other features intrinsic to microelectrodes. In this section a brief review of microelectrodes and their properties is presented. If not stated otherwise, microelectrodes with disc geometry (microdisc electrodes) are assumed, when describing or illustrating some of the characteristic features of microelectrodes.

Since microdisc electrodes were used in the entire experimental part of the presented work, only the expressions for predicting the current response of electrodes of this geometry are given. Current-concentration relationships for other geometries are available in the literature [11-13].

1.2.1 Definition

Microelectrodes are defined as electrodes characterised by at least one critical dimension small enough, that their properties are a function of its size [12]. Recently, a more precise definition has been given describing microelectrode as any electrode with a characteristic dimension which is, under the given experimental conditions, comparable to or smaller than the diffusion layer thickness [14]. The dimension defining the microelectrode properties can be radius for disc, sphere, hemisphere, cylinder or width for other geometries, e.g. microband or microring. In practice, on typical experimental timescales microdisc or microband less than 50 μm in diameter or width, respectively, can be considered a microelectrode.

1.2.2 Properties

Several important properties are observed as a direct result of the very small electroactive area of microelectrodes. These properties constitute the advantages of microelectrode techniques over traditional 'large' electrodes. A brief description of some microelectrode features is given below. For detailed information the reader is referred to extensive literature dealing with microelectrodes [10, 12, 14, 15]

Mass transport

In order to describe the mass transport around the microelectrode, a simple model is assumed. In this model the solution contains only species O which can be reduced in one electron reaction to species R:

$$O + e^- \rightarrow R \qquad (1.1)$$

Following the step from a potential where no reaction occurs to a potential where the reaction proceeds under mass transport limitation, a faradaic current begins to flow. While this current can be described using the Cottrell equation [16] for a large

electrode with planar diffusion, the current at a microdisc cannot be approximated in a similar way. When the electrode size is comparable to the diffusion layer size the radial component of the diffusion has to be taken into account. A far more accurate current-time model for microdisc electrodes was analytically derived by Aoki and Osteryoung [17, 18]. This model predicts two limiting cases depending on the value of the dimensionless time τ defined as

$$\tau = \frac{4Dt}{a^2} \tag{1.2}$$

where D is the diffusion coefficient of electroactive species, t is time and a is the microdisc radius. For small values of τ ($\tau \prec 1$) the current is given by

$$i = 4nFDc^{\infty}a\left(\frac{\pi}{4} + \left(\frac{\pi}{4\tau}\right)^{1/2} + 0.094\tau^{1/2}\right) \tag{1.3}$$

and for $\tau > 1$

$$i = 4nFDc^{\infty}a\left(1 + 0.71835\tau^{-1/2} + 0.05626\tau^{-3/2} - 0.00646\tau^{-5/2}\right) \tag{1.4}$$

with n denoting the number of electrons transferred in the reaction, F the Faraday constant and c^{∞} the bulk concentration of species O. The curves obtained with equations (1.3) and (1.4) overlap where $0.82 < \tau < 1.44$. It is assumed that the electron transfer is fast enough and it does not affect the rate of the process. Moreover, the mass transport due to convection and migration is ignored. Under these conditions the current is controlled solely by the diffusion of O from the bulk to the surface, where it is instantly reduced to R, so the concentration of O at the electrode surface is zero.

Depending on the timescale of an experiment, the radial diffusion to the electrode edges becomes comparable, and eventually greater than the planar diffusion. In other words, at extremely short times microelectrode behaves like a large electrode with the flux of species perpendicular to the surface i.e. current in

equation (1.3) tends to be proportional to $t^{-1/2}$. As t increases the contribution of radial diffusion increases, leading to the development of a hemispherical diffusion layer. As a consequence, the rate of depletion of species at the electrode surface is balanced by the efficient diffusion, which results in the steady state current observed at microelectrodes (t dependent terms in equation (1.4) tend to zero). For microdisc with radius a the steady state current i_{ss} is then given by equation (1.5):

$$i_{ss} = 4nFDc^{\infty}a \tag{1.5}$$

Double layer charging

Any change in potential is accompanied by charging of the double layer. The charging time τ_c is a function of the solution uncompensated resistance, R_u and the double layer capacitance, C_{dl} (1.6).

$$\tau_c = R_u \times C_{dl} \tag{1.6}$$

The latter is directly proportional to the electrode surface, therefore at microelectrodes the charging time can be significantly reduced. Since the charging time limits the availability of the faradaic information (no faradaic data for $t<3\tau_c$), the use of microelectrodes enables the investigation of short lived species and very fast electron transfer.

IR drop

The currents measured with microelectrodes are very small: the steady state current is approximately 0.2 nA / μm radius / mM (for n=1). Thus, the distortion of potential due to ohmic drop is also significantly reduced. This allows the measurements in solutions without supporting electrolyte and in poorly conducting media. Moreover, a two-electrode experimental arrangement is possible, where the reference electrode serves also as a counter electrode.

1.2.3 Current-concentration relationships for microdisc electrode

From the point of view of analytical applications of microelectrodes the most important expression is the one describing the steady state current (i_{ss}) at the microdisc, which was presented earlier (1.5), e.g. [11]. For this equation to be valid the electrode reaction has to be solely diffusion controlled, i.e. no convection or migration is present in the system. The steady state current has the same value irrespective of the way it was achieved, i.e. potential step or sweep, and is time independent. Nevertheless, in practice the steady state measurements have to be limited in duration to less than one minute due the contribution of current originating from natural convection.

Current-time relationships describing times preceding the steady state were derived by Oldham [19] and digitally simulated in works of Kakihana *et al.* [20] and Heinze [21]. A very neat and precise analytical solution was later obtained by Aoki and Osteryoung [17, 18], who expressed the current at a microdisc in form of two functions for different ranges of dimensionless time (see above, section 1.2.2). The predicted curves overlap in the region of $0.82<\tau<1.44$ within 0.5% error. Experimental study [22] using microdiscs constructed from glassy carbon electrodes proved the validity of their equations for $0.006 \leq \tau \leq 19.0$. Outside this domain the current is accurately predicted by Cottrell equation and steady state expression (at short and long times, respectively). Later, using both analytical and digital simulation techniques Shoup and Szabo [23] presented a single equation predicting the chronoamperometric current with accuracy of 0.6% over full time domain. The details of the abovementioned models are shown later in the Appendix (section 9.4.1) where the analysis of oxygen reduction transients is presented. Recently another model was proposed by Mahon and Oldham [24, 25]. Similarly to Aoki and Osteryoung's model the formula is given in the form of a bipartite expression for times shorter and longer than $1.281\ a^2/D$, where the solution for intermediate times was calculated using Cope-Tallman method [26].

1.3 The methods of dissolved oxygen determination

In this section a selection of dissolved oxygen determination methods is presented. A range of methods of analysis of oxygen in gaseous phase, after extraction from liquids of interest, are omitted here and can be found in [27] and source references cited therein. The emphasis is put on electrochemical detection and sensors used in marine applications. Oceanographic oxygen sensors for vertical profiling, sediments measurements and others are reviewed.

1.3.1 Chemical methods

1.3.1.1 Winkler method

The Winkler titration [28] is the oldest and still the most accurate method of determination of dissolved oxygen concentration. In general, manganese (II) salt is added to the sample followed by alkalisation of the solution. Manganese (II) hydroxide precipitates (1.7) and quantitatively reduces molecular oxygen (1.8). Subsequently, an acidified iodide solution is added and iodine is liberated after iodide oxidation by Mn(III) species (1.9), (1.10). The iodine is later titrated with thiosulphate as in any other iodometric method (1.11).

$$Mn^{2+} + 2OH^- \rightarrow Mn(OH)_2 \downarrow \quad (1.7)$$

$$2Mn(OH)_2 + \tfrac{1}{2}O_2 + H_2O \rightarrow 2Mn(OH)_3 \quad (1.8)$$

$$2Mn(OH)_3 + 6H^+ + 3I^- \rightarrow 2Mn^{2+} + I_3^- + 6H_2O \quad (1.9)$$

$$I_3^- \rightarrow I_2 + I^- \quad (1.10)$$

$$I_2 + 2S_2O_3^{2-} \rightarrow 2I^- + S_4O_6^{2-} \quad (1.11)$$

While the principle remains unchanged, various modifications were introduced to minimise the errors caused by interfering oxidants/reductants that can be present in the sample [27]. In addition, instrumental methods of determination of the end point of titration (spectrophotometric, potentiometric, amperometric) can be used to improve detection limits, precision and accuracy.

The laboriousness and use of chemical reagents practically exclude the method from *in situ* analysis. Nevertheless, the majority of oceanographic investigations involving oxygen level measurements still rely on automated Winkler titration, which is carried out on-board on samples collected in purpose built containers (e.g. Niskin bottles – see 7.2).

1.3.1.2 Colorimetric and other methods

The colorimetric methods are based on the oxidation of a reduced form of a dye by molecular oxygen. The oxidation is accompanied by a colour change which allows quantitative oxygen determination by absorption spectroscopy. Examples of such determination can be found in [27, 29] and references therein. While the determination is fast and accurate, it requires samples that are clean and free of interfering agents, which could absorb light at the wavelengths used for the detection of the indicator molecule.

Other chemical methods (like Winkler analysis) involve initial reduction of oxygen followed by titration of the oxidised reagent species. The possible reductants are e.g. Ce(III), Cu(I) or NO_2^-, followed by titrants appropriate to the reactions products. Approaches other than Winkler can be used in special cases where the iodometric titration is not possible, but they do not bring appreciable improvements when dealing with seawater samples or solutions of similar composition.

1.3.2 Optical sensors

Optical sensors have recently received much attention as oxygen probes, in particular those based on luminescence quenching. They possess numerous advantageous features making them the most common alternative to electrochemical devices. The method principles [30] rely on the use of molecules able to absorb light and form excited states. Following the formation of the excited state, emission of absorbed energy in the form of luminescence occurs. Each luminophore is characterised by a specific luminescence time (excited state lifetime), i.e. the time needed for the total radiative decay of luminescence. If a suitable acceptor (e.g. oxygen) is present, some of the energy can be transferred in a non-radiative way. In our case the indicator molecule relaxation can also be achieved by energy transfer to oxygen molecule, which advances to a singlet state. The non-radiative transfer reduces the luminescence time, and the effect is commonly referred to as luminescence quenching. The relation between luminescence parameters and the quencher concentration, [Q] is given by the Stern-Volmer expression (1.12):

$$\frac{\tau_0}{\tau_q} = 1 + K_{SV}[Q] \tag{1.12}$$

where τ_0 and τ_q are unquenched and quenched excited state lifetimes, respectively, and K_{SV} is the Stern-Volmer quenching constant. Since the measured signal follows an exponential decay, an increase in oxygen concentration lowers the magnitude of the signal. This is why luminescence quenching method offers a unique feature of higher sensitivity at low oxygen concentrations.

Most of the sensors of this type contain transition metal (Ru, Pd, Pt, Os) complexes as indicating molecules, encapsulated in silicone matrix. Such design results in complete immunity to stirring effects as the measured response depends only on the diffusion of oxygen within the matrix. It has to be stressed that the matrix homogeneity, and in consequence the dye distribution is crucial for the system to follow the Stern-Volmer behaviour. Also, the matrix has to be impenetrable for the solution in order to prevent the luminophore molecules leakage.

With regard to the use of optrodes in oceanographic research, the initial studies [31] show very good pressure behaviour: <1% signal variation, not correlated with pressure, in range 0 - 275 atm. Thus, the optical probes seem to be very promising alternative to electrochemical sensing. The sensors can be easily miniaturised and the cost of construction lowered by the use of optical fibres and integrated light sources for excitation. Several types of oxygen optrodes are already commercially available from Ocean Optics Inc., Oxford Optronix and Aanderaa Instruments. The latter has been recently deployed [32] from profiling floats in the Labrador Sea, where the sensor was operated simultaneously with the Seabird electrochemical Clark-type device. A critical comparison between the Ocean Optics sensor and an electrochemical probe was also recently published [33].

1.3.3 Electrochemical sensors

1.3.3.1 Potentiometric sensors

While potentiometric oxygen analysis in gaseous phase (high temperature) using pure or yttrium doped zirconia is well established, very little work is available on the potentiometric oxygen sensing in solution. The principles of the method are simple and rely on measuring the potential between electrodes which react with oxygen in a reversible manner. However in practice, finding a suitable electrode for potentiometric oxygen analysis in solution proved to be very difficult. The most promising attempts were made by Meyerhoff and co-workers [34-38].

According to the authors, with bare platinum electrodes a stable potential, ascribed to the reversible surface reaction (1.13) can be achieved.

$$Pt+O_2 \rightleftarrows Pt(I)\text{-}O_2^- \qquad (1.13)$$

Although without a constant cathodic polarisation the Nernstian response cannot be maintained for more than two days [34] due to irreversible platinum oxidation. Attempts were made to improve potentiometric sensor lifetimes by modification of

the electrode surface with cobalt(II) tetraethylene pentamine doped PVC films [34, 35], metallic copper [34, 36] or by using cobalt electrodes [37, 38]. For cobalt complex modified electrodes a potential (E_{mix}) termed by the authors as mixed potential was observed:

$$E_{mix} = E_{ref} + \frac{RT}{nF}\left(\ln \frac{[Pt]p_{O2}}{Pt(I)\text{-}O_2^-} + \ln p_{O2} \right) \tag{1.14}$$

where E_{ref} is the reference electrode potential and p_{O2} is the oxygen partial pressure. The first logarithmic term represents the potential due to platinum oxidation and the second originates from reversible one electron oxidation of cobalt complex centre (assuming 1:1 stoichiometry). At open circuit this sensor lifetime did not exceed one week, with response changing from super-Nernstian (both redox sites contributing to overall potential) to values much smaller than 59 mV per unity of log p_{O2} (both platinum electrode surface and the cobalt complex are irreversibly oxidised). Better stability (up to one month) was achieved with copper film electrodes where the observed potential was the equilibrium potential of two simultaneous processes: copper oxidation and oxygen reduction. With cobalt electrodes a similar mechanism occurs, but this sensor also suffers form significant potential drift (from 2.1 mV h^{-1} to 0.25 mV h^{-1} depending on the electrode preconditioning time, 24 to 96 h, respectively [37]).

The stability of the electrode potential remains the main problem of the potentiometric sensors performance. Moreover, the measured potential is very sensitive to stirring, pH and ionic strength, which forces the sensor design to include internal electrolyte and oxygen permeable membrane. This inevitably increases the sensor response time. At present the amperometric detection offers much higher reliability and potentiometric oxygen sensors for solution measurements are not commercially available.

1.3.3.2 Clark type sensors

Among amperometric oxygen sensors the Clark type devices are today the most widely used. The original idea of Clark [39] led to the development of numerous sensors over the years and the theory for such devices is well established. Detailed reviews, along with extensive material on Clark probes performance and theory of operation can be found in several books [27, 40, 41].

In principle, a Clark oxygen probe consists of a metallic sensing cathode covered with an oxygen permeable membrane. The electrode and the membrane are separated by a thin layer of internal electrolyte. These elements are common to all Clark type devices. The variations include different reference and counter electrodes and general construction, both dependent on the sensor application. Very often a two electrode system is used. A schematic representation of a Clark type sensor is shown in Figure 1.1.

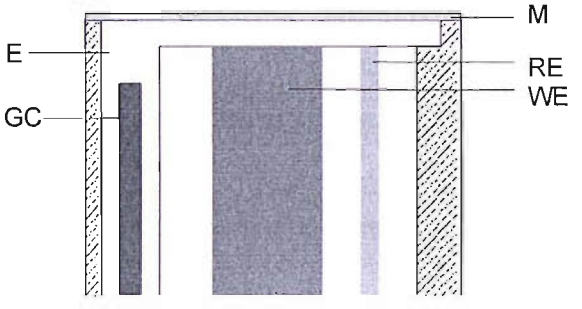

Figure 1.1 A schematic representation of the Clark type sensor head: M – oxygen permeable membrane, E – internal electrolyte, RE – reference electrode, WE – working electrode, GC – guard cathode (optional). For clarity, the sensor elements are not to scale.

The membrane has several important functions. Its selective permeability protects the cathode from any fouling agents and results in enhanced selectivity of the probe towards oxygen. It also guarantees very reproducible mass transport conditions: the recorded current depends only on the diffusion of oxygen within the membrane and subsequently in a layer of internal electrolyte of constant thickness.

Therefore, the response is much less sensitive to external flow. Moreover, the structure dependent solubility and diffusivity of oxygen in the membrane and the thickness of the membrane are factors that contribute strongly to sensor sensitivity and response time. Optimal parameters have to be found in order to obtain good operational characteristics and robustness at the same time. The most commonly used membranes are made of hydrophobic polymers, e.g. polyethylene, Mylar, silicone rubber, halogenated hydrocarbons: polytetrafluoroethylene (PTFE), polyvinyl chloride (PVC), with thickness down to fractions of a micrometer [27].

The internal electrolyte has to provide sufficient conductivity between the electrodes and be appropriate for the anodic reaction. For example, concentrated chloride salt solutions are used when using Ag/AgCl anode, while alkaline electrolytes are employed for metal/metal oxide type anodes. Nevertheless, electrolytes in all pH range can be used as long as they do not affect electrode reactions and do not interfere with the membrane. The losses of electrolyte due to diffusion through the membrane can be minimised by incorporating a sufficiently large internal electrolyte reservoir in the sensor body. The internal electrolyte pH can also show variations, which may pose a problem. When operated continuously and/or for extended periods of time the concentration of hydroxide generated on the cathode will build up increasing the pH of the internal electrolyte. This in turn causes a shift of the oxygen reduction wave and consequently can alter the magnitudes of the recorded reduction currents. The effect will be more pronounced for larger cathodes and limits the sensor lifetime.

It has to be stressed, that internal electrolytes always contain some dissolved oxygen which contributes to the overall response. This problem can be overcome by polarising the cathode for sufficiently long times before taking the measurements. The necessary time will depend directly on the internal electrolyte volume to cathode surface ratio. A modification to Clark type sensor was introduced for large amounts of internal electrolyte [42]: the sensor contains an additional electrode – a so called guard cathode. The guard cathode is usually a high surface platinum electrode used to deplete the internal electrolyte from oxygen by means of oxygen reduction. It is also possible to remove the electrolyte layer between the electrode and the membrane. E.g. Mitsubayashi et al. [43] reported the fabrication of a sensor for

transcutaneous oxygen monitoring where both working and reference electrodes are spin coated directly onto the membrane. In this case the observed currents are controlled solely by the diffusion of oxygen within the membrane.

At present, commercially available electrochemical oxygen sensors are almost exclusively Clark type devices. They are available with various cathode materials and sizes ranging from standard macroelectrodes to microelectrodes incorporated in needle type sensor bodies. The latter are characterised by sub-second response times, despite employing a membrane [44]. The advances in microfabrication techniques led to the development of miniaturised Clark type sensors. Devices fabricated using thin film technology on silicon chips were constructed and successfully tested [45, 46]. Fabrication of a microsensor employing an array of 1024 individually addressed Clark cells for two dimensional concentration mapping was also reported [47].

One common drawback of membrane covered probes is their sensitivity to pressure. The membrane permeability is strongly affected as the membrane pores contract when external pressure increases. This causes very significant signal losses when measurements are performed at larger depths (up to 50% at pressure corresponding to the depth of 5000 m [48]). The membranes are also sensitive to mechanical factors and biofouling.

1.3.3.3 Sensors employing unshielded solid electrodes

Removal of the membrane has several important consequences. The response time is improved as oxygen does not have to diffuse through the membrane. Moreover, the sensor response dependence on temperature and pressure results only from changes in the value of oxygen diffusion coefficient, whereas Clark type devices need also corrections for the membrane permeability, which changes with temperature and pressure. On the other hand, the absence of the internal electrolyte makes the electrode more susceptible to fouling, as it is in direct contact with the analysed solution. The fouling problem is particularly important in environmental analysis, where composition of the medium is not known and can be variable. As a result, the use of a bare electrode forces the introduction of surface reconditioning

procedures. Also, the composition of the analysed solution (along with temperature and pressure) has to be known in order to accurately calculate the value of the oxygen diffusion coefficient. Another issue concerns the sensitivity of the response to external flow and convective mass transport.

A constant activity of the electrode surface towards oxygen reduction can be achieved through periodic electrochemical cleaning, i.e. by polarising the electrode to force surface reactions that renew the surface. With platinum electrodes, the cleaning procedure can be as simple as cycling the potential between oxide formation and hydrogen evolution or stepping the potential to the oxide formation region. These approaches were investigated by Pletcher and Sotiropoulos [49] for a microelectrode sensor and the results showed stable response over periods of 12 h and longer. Preidel *et al.* [50] held glassy carbon electrodes at potentials of 0 V vs. Ag/AgCl between measuring steps at -1 V vs. Ag/AgCl and report stable response for over 60 h in saline solutions. Conditioning potential steps are also used to maintain the activity of mercury coated gold microelectrodes for voltammetry in seawater as reported by Brendel and Luther [51]. An innovative approach was presented by Rychen [52], where a gold microdisc array was used as a working cathode. The gold electrodes are cleaned by highly oxidising hydroxyl radicals, which are periodically generated on the boron-doped diamond (BDD) auxiliary electrode. The BDD electrode occupies the surface between the recesses containing gold microdiscs at their bottom. As a result the distance from each microdisc to the BDD electrode is of order of the depth of the recess, i.e. micrometers. This also allows calibrating the microdiscs by *in situ* oxygen generation on the BDD electrode.

Convection effects can be minimised by decreasing the electrode size, thus microelectrodes are common choice when developing new sensors. However even the response of micrometer size electrodes is affected at high flow rates (e.g. a conductivity-temperature-depth probe, CTD, falls at ~1 m s^{-1}). Higher immunity to convection can be achieved by placing the electrode in a recess. Morita and Shimizu [53] reported a sensor with an array of platinised carbon fibres as working cathode. Each carbon fibre (diameter 4 – 7 μm) was at the bottom of a recess. The authors report much lower sensitivity to flow comparing to an inlaid microdisc: at a flow rate of 50 cm s^{-1} the limiting current values were 1.42× and 1.25× that of the limiting

current in stagnant solution for recess depths of 100 and 200 μm, respectively. They remained constant under higher flow rates. Due to planar diffusion in the recess, increasing its depth also increased the response time: t_{90} ranged from 4 s for 80 μm to 64 s for 370 μm deep recesses. Sensors based on the microhole cathode were later tested on a CTD profiler [54]. Recessed electrodes were also employed by other research groups. Braun *et al.* [55] used recessed microelectrodes to investigate tumour and normal tissue oxygenation and Rychen [52] reported reduced flow dependence of recessed gold microdiscs array used to monitor oxygen in sewage water environment.

1.3.4 Electrochemical DO sensors for measurements in natural waters – review

In this section, DO sensors developed and used for *in situ* measurements in natural waters are reviewed and compared. The measurements considered are mainly those targeted in this research: CTD vertical profiles, water – sediment profiles (*in situ* and in extracted cores) and other deep sea measurements. Selected research notes on sensor development and deployment in fresh waters are also included.

The vast majority of oxygen measurements in natural waters are performed with Clark type sensors. For shallow waters applications where the response time and the device physical dimensions are not crucial, the commercial Clark probes from YSI or Seabird Electronics are used. The performance of the former was independently evaluated [56] both in lab and field conditions with reference to precision Winkler titrations. Needle type Clark sensors are used to obtain high spatial resolution profiles, e.g. at sediment – water interface. Electrodes of this type were first constructed by Baumgärtl and Lübbers [57] in 1973. Since then they were further miniaturised and developed, e.g. internal silver guard cathode was introduced [42]. They are commercially available from Unisense, Denmark with tip diameters down to 2 μm, and attempts are made to use them on CTDs, microprofilers and in benthic chambers in marine research.

Significantly less work has been published on the application of unshielded electrodes in natural waters. Luther and co-workers in a series of papers [51, 58-61] presented development and field deployments results of a sensor operating in

voltammetric mode. The sensor utilises an amalgamated gold microelectrode and is used to simultaneously detect dissolved oxygen, Fe, Mn and total S(-II). Voltammetric mode and multiple species detection are in many respects beneficial, but also result in increased response time. The duration of a complete measurement including linear scan voltammetry (v=200 mV s^{-1}), square wave voltammetry and electrode conditioning steps is around 3 min. Moreover, the sensitivity to flow remains a problem. Bare metallic electrodes were used also in amperometric mode by Atkinson *et al.* [62] for vertical CTD profiling. Profiles in shallow waters were obtained with a gold thick film multicathode probe. However, the sensor was sensitive to flow and the cathode lifetime in seawater was limited to only few days. Another approach included the use of microhole array sensor [54, 63] reported earlier by Morita and Shimizu [53]. The cathode consisted of an array of platinised carbon fibres, each of them lying at the bottom of ~50 μm deep recesses, which made the response much less sensitive to flow. The sensor presented a good response time (t_{99}=2 s), especially in comparison with membrane covered probes [64]. However at the same time it suffered from long turn-on time and drift. These were presumably caused by the potentiostatic operation of the sensor.

Recent applications of electrochemical tools for dissolved oxygen sensing in natural waters are listed in Table 1.1. Reviews on benthic biogeochemistry measurements technologies [65] and *in situ* electrochemical tools for aquatic systems [66] are available and can provide some more data on dissolved oxygen and other sensors. A review of the majority of presently used oxygen sensors (not only electrochemical) as well as some promising new oxygen sensing methodologies (membrane inlet mass spectrometry, gas tension devices) can also be found in a recent paper by Daly *et al.* [67]. It has to be stressed, that while all electrochemical sensors are used *in situ*, all are recalibrated using Winkler titrations in the samples taken at the location of deployment.

Table 1.1 Applications of dissolved oxygen electrochemical sensors in natural waters.

Measurement environment	Sensor description	Reference
Coastal sediments, cores (depth 4-44 m)	Amperometric, Clark type needle sensor	[57, 68]
Shallow estuary sediments, cores	Amperometric, Clark type needle sensor	[57, 69]
Microbial mat from hypersaline pond, cores	Amperometric, Clark type needle sensor	[57, 70]
Acidic microbial mat, cores	Amperometric, Clark type, Au coated Pt microelectrode	[71]
Shallow sediments, cores	Amperometric, Clark type, Au coated Pt microelectrode	[72]
Shallow sediments, cores	Amperometric, Clark type, Au coated Pt microelectrode	[73]
Vertical profile (free fall CTD, depth 0-15 m)	Amperometric, unshielded Au multicathode	[62]
Deep sea sediments, *in situ*	Amperometric, Clark type, Au coated Pt microelectrode	[74]
Vertical profiles from CTD (0-5000 m)	Amperometric, microhole array of platinised carbon fibre microelectrodes	[53, 54, 63]
Shallow sediments, *in situ*	Amperometric, Clark type, Au coated Pt microelectrode	[75]
Microalgae photosynthetic activity, *ex situ*	Amperometric, Clark type,1 mm diameter Pt cathode integrated with optical fibres	[76]
Vertical profiles (depth 0-10 m), fresh water	Amperometric, Clark type, Au coated Pt microelectrode	[77]
Sediments, cores	Amperometric, Clark type, Au coated Pt microelectrode	[78]
Surface waters, air – sea gas fluxes	Amperometric, Clark type, YSI + gas tension device	[79]
Salt marsh sediments, cores	Voltammetric, Hg coated Au microelectrodes	[51]
Sediments, cores	Voltammetric, Hg coated Au microelectrodes	[61]
Shallow sediments, *in situ* from ROV	Voltammetric, Hg coated Au microelectrodes	[60]
Deep sea hydrothermal vents	Voltammetric, Hg coated Au microelectrodes	[59]
Long term shallow sea waters (depth 0-40 m) oxygen monitoring	Amperometric, Clark type, YSI	[80]
Long term oxygen monitoring (depth 50 m)	Amperometric, Clark type, YSI	[81]
Sediments, *in situ* microbenthic chamber	Voltammetric, Hg coated Au microelectrodes	[82]

1.4 Oxygen reduction reaction (ORR)

The principle of operation of every amperometric oxygen sensor is the oxygen reduction reaction (ORR) taking place at the sensing cathode. The ORR is a subject of extensive literature in the fields of fuel cells, corrosion, batteries and sensors. Several reviews and books on oxygen electrochemistry and ORR in particular are available [27, 83-87]. In this section some fundamental aspects of the ORR are discussed in the context of the oxygen sensor application, i.e. measurements in natural waters using microelectrodes. The emphasis is put on oxygen reduction in neutral, chloride containing solutions on platinum and gold cathodes.

1.4.1 Mechanism

It is well known that ORR is not a straight forward reaction. In general, we can distinguish two main pathways in the overall reaction mechanism: a direct reduction of oxygen to water (four-electron pathway) and a two-electron reduction to hydrogen peroxide. The peroxide intermediate can be reduced further to water or undergo catalytic disproportionation to form oxygen and water. The contribution of each pathway depends upon several factors: reaction environment (including pH), electrode material and mass transport conditions. Thus, the apparent number of electrons transferred during ORR (n_{app}) can vary between 2 and 4. Numerous reaction mechanisms were suggested by various researchers and they are summarised in reference [83]. One of the most widely accepted mechanistic models is that proposed by Wroblowa *et al.* [88], (1.15).

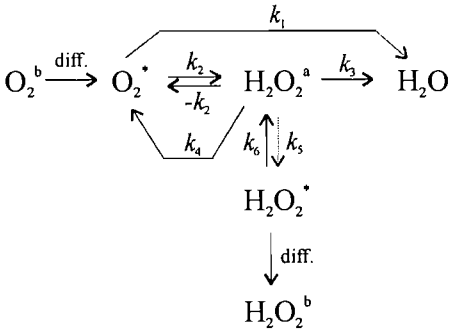

(1.15)

Superscripts a, b and * denote here species adsorbed, in the bulk solution and in the vicinity of the electrode, respectively and 'diff' stands for the diffusion of species in solution. According to this reaction scheme, oxygen can be reduced directly to water (1) or via two-electron pathway to form adsorbed hydrogen peroxide (2). The peroxide can be reduced in the next two-electron step to water (3) or decompose via paths (3) and (4). Moreover, pathways (1) and (2) or, (1) and (2) followed by (3), can occur in parallel. These steps are mainly defined by the electrode material (electrocatalyst). The ratio of parallel pathways will also be influenced by the reaction environment as the intermediate peroxide species (H_2O_2, H_2O^-) can be further oxidised/reduced in a chemical step as well as in the step involving charge transfer through the electrode interface. The solution composition (presence of adsorbing species, e.g. anions) can also affect the adsorption equilibria of oxygen and reaction intermediates, and these changes will be reflected in the overall reaction mechanism and kinetics. Finally, the mass transport conditions will determine how fast the oxygen is supplied to the electrode and how fast the intermediate peroxide is removed. More complex reaction schemes have also been proposed. For instance, the mechanism proposed by Bagotskii *et al.* [89] includes an additional step: adsorption of molecular oxygen ($O_2^* \rightleftarrows O_2^a$).

In summary, the apparent number of electrons (n_{app}) transferred in the ORR can vary between 2 and 4 reflecting the contribution of each reaction path to the overall oxygen reduction process. It is mainly determined by the electrocatalyst, but other factors like local chemical environment or mass transport conditions can significantly influence it.

1.4.2 ORR on various electrode materials

The electrode material determines to a large extent the pathway of the ORR. For the four-electron pathway to dominate the electrode surface has to efficiently catalyse the cleavage of the oxygen-oxygen bond. On the basis of the catalytic properties towards ORR the electrode materials can be divided into two main groups: these promoting four-electron oxygen reduction to water and the others promoting two-electron (series) pathway. The first group includes noble metals like Pt, Pd, Ag, Cu, Ni, Fe, Sn, Pb [90] and some transition metal complexes with macrocycles, where e.g. Fe or Ni are chelated by four nitrogen atoms [83]. The two-electron pathway is favoured on gold [91], graphite [92], carbons [87], oxide covered metals (Co, Ni) [93] and some metaloporphyrins [87]. Similarly to gold, also on mercury electrodes the ORR proceeds via two two-electron reduction steps. Since the hydrogen evolution overpotential is very high on Hg, two well defined waves of equal magnitude are observed on the voltammogram: the first due to reduction of O_2 to H_2O_2 and the second corresponding to further reduction of H_2O_2 to H_2O [85]. In the remainder of this section, ORR on polycrystalline platinum and gold will be discussed in more detail as these are the electrode materials used in all the experimental work.

ORR on polycrystalline Pt

In general, on platinum, which is considered to be one of the best electrocatalyst for oxygen reduction, the predominant reaction pathway is the four-electron reduction. Nevertheless, the reaction is complex as it involves heterogeneous transfers of four electrons and reactions with four solvated protons from the aqueous phase. Most studies on the ORR products where carried out using a rotating ring-disc electrode (RRDE), where the amount of intermediate peroxide formed on the disc is detected at the ring. Other methodologies included the use of an array of microband electrodes [94] and a dual-disc microelectrode [95]. Yet none of these approaches can give an estimation of all rate constants involved, as the

distinction between path (1) and the path consisting of steps (2) and (3) in sequence is very difficult solely on the basis of intermediate peroxide detection. The experimental data is also supported by *ab initio* calculations of activation energies of reactions comprising the ORR. Anderson and Albu [96, 97] proposed the following lowest energy pathway for the reduction of adsorbed oxygen to adsorbed water:

$$\text{Pt-}O_2 + H^+(aq) + e^- \rightarrow \text{Pt-OOH} \tag{1.16}$$

$$\text{Pt-OOH} + H^+(aq) + e^- \rightarrow \text{Pt-(OHOH)} \tag{1.17}$$

$$\text{Pt-(OHOH)} + H^+(aq) + e^- \rightarrow \text{Pt-OH} + H_2O \tag{1.18}$$

$$\text{Pt-OH} + H^+(aq) + e^- \rightarrow \text{Pt-}OH_2 \tag{1.19}$$

The first electron transfer is the most commonly accepted as the rate determining step. However, other mechanisms and rate-determining steps seem to be possible. They are beyond the scope of this introduction and will not be described further. The reader is referred to a review by Gnanamuthu and Petrocelli [98] were a number of proposed mechanisms are described.

ORR on polycrystalline gold

On gold electrodes oxygen reduction proceeds only via the series mechanism with hydrogen peroxide as the reaction intermediate [91]. Unlike platinum, gold is not a good hydrogen peroxide decomposition catalyst. In alkaline solutions quantitative reduction of O_2 to H_2O_2 is observed, followed by partial peroxide reduction to water. The rate of the second step appears to be potential independent, which suggests it is determined by a chemical step involving the adsorbed peroxide species, e.g. according to the mechanism proposed in reference [99]:

$$H_2O_2 \rightarrow 2OH^{\bullet} \tag{1.20}$$

or

$$H_2O_2 \rightarrow H_2O + O^{\bullet} \quad (1.21)$$

$$O^{\bullet} + H_2O + e^- \rightleftharpoons OH^{\bullet} + OH^- \quad (1.22)$$

which is followed by a fast reaction including charge transfer:

$$OH^{\bullet} + e^- \rightleftharpoons OH^- \quad (1.23)$$

On the oxygen reduction voltammogram the first wave corresponding to the reduction to peroxide has a well defined current plateau. The second wave is usually quite poorly defined, falling smoothly into the hydrogen formation region both in alkaline [91, 100] and neutral electrolytes [100, 101]. Two waves with well defined diffusion limited plateaux for oxygen reduction to hydrogen peroxide and to water were observed in 2.5 mM KCl unbuffered solutions in a microelectrode study by Pletcher and Sotiropoulos [102]. The authors proposed that the shape of the voltammogram is due to increased irreversibility of the reduction processes resulting from rapid mass transport at the microelectrode.

1.4.3 ORR dependence on the reaction environment

Regarding the scope of this work, the development of an oxygen sensor for seawater applications, two major factors and their implications with respect to the ORR will be considered: pH 7-8 and the presence of chloride ions in the analyte. Their influence on the ORR pathway and consequently on the position and magnitude of the voltammetric response has to be assessed in order to accurately predict the current – concentration relationship.

pH and ORR

ORR in acidic and alkaline solution is very widely described in the literature due to its importance in the fuel cells research. Fewer data is available on oxygen reduction in neutral pH and especially in unbuffered neutral solutions. Reports

concerning the ORR in neutral solutions can be found for Ni [103], Fe [104, 105], Cu [106], Pt [102, 107, 108], Ag [102, 109] and Au [100, 102] electrodes. A very general study for various common metals can also be found in work of Kozawa *et al.* [101] and Delahay [90].

In the case of oxygen reduction on gold the pH of the electrolyte influences neither the half-wave potential of the first reduction wave nor the value of its limiting current. However, it affects the second voltammetric wave corresponding to the reduction of intermediate peroxide species to water [100]. A decrease of the pH value narrows the potential window between the onset of the wave and the onset of hydrogen evolution. A relatively well defined second wave is observed in alkaline solutions, but no distinguishable plateau can be found in pH 7 phosphate buffer electrolytes [100]. A better shaped plateau is obtained with the aforementioned gold microelectrode [102] (see section 1.4.2).

Similarly to the first current plateau on gold, the magnitude of the diffusion limited current due to four-electron reduction on Pt is not affected by the pH of the medium. But as the reaction involves protonation steps, it is pH dependent and the position of the wave will differ for different pH values. Moreover, in neutral solutions, due to the local build-up of reaction products (OH^-), variations in the wave shape, namely the values of $E_{1/4}$-$E_{3/4}$ will be altered depending on the buffer capacity of the solution [102].

Cl^- influence on the ORR

Chloride anions adsorb on the platinum electrode surface in the whole potential window: from hydrogen evolution to the potentials where Cl^- is oxidised. The electrode coverage is a function of Cl^- concentration and the electrode potential, as shown with a tracer technique utilising ^{36}Cl by Horanyi *et al.* [110]. Although the process is reversible, the mobility of adsorbed Cl^- is low and rinsing of the electrode does not remove Cl^- from the surface completely [111]. As the ORR mechanism includes adsorbed species, it can be anticipated that the presence of adsorbing anions will influence the reaction. Indeed, several authors observed changes, which could be directly correlated to the chloride anion effect. Kaska *et al.* [107] investigated

oxygen reduction on platinum in borate buffered solutions containing ClO_4^- and Cl^- anions. The RRDE study showed two major effects of chloride on the ORR. Firstly, the half-wave potential, $E_{1/2}$, of oxygen reduction in solutions of pH 8-10 shifts to more cathodic potentials as the chloride concentration increases. Secondly, the reduction currents are lower, and the production of H_2O_2 is enhanced comparing to the solutions containing only ClO_4^-. The values of the apparent number of electrons transferred (n_{app}) found in the study were 3.2-3.4 per oxygen molecule in 0.5 M $NaClO_4$ and 2.7-3.3 in 0.5 M NaCl. While the absolute values of n_{app} should be treated with care due to uncertainty in D_{O2} and oxygen solubility, the decrease due to the presence of chloride is evident. Moreover, the presented kinetic analysis showed that reaction constants k_1 and k_2 (see reaction (1.15)) decreased in chloride solutions. k_1 decreased to larger extent in agreement with the proposed promotion of two two-electron series reaction pathway with the intermediate H_2O_2. Similar results in terms of increased H_2O_2 production were obtained on Ni [103], where 30.8% of oxygen is reduced to H_2O_2 in KCl solutions comparing to 8.8% in K_2SO_4 solutions, and on Pt [112] in acidic solutions, 14.2% in 0.5 M H_2SO_4, 30.5% in 1 M H_2SO_4 + 3.3 mM KCl and 36.9% in 1 M HCl. Pletcher and Sotiropoulos also report shifts to more cathodic potentials in chloride medium compared to NaOH solutions [108].

The findings are interpreted in terms of differences in configuration of adsorbed intermediates of the ORR in the presence of Cl^-. The models for oxygen adsorption are shown in Figure 1.2 together with the resulting subsequent pathways for oxygen reduction. As chloride or other adsorbing solution species adsorb on the Pt surface, less sites are available for oxygen. The 'end-on' (Pauling) configuration, where oxygen is adsorbed via only one atom becomes more probable than the 'bridge' configuration where oxygen occupies two Pt sites with each oxygen atom interacting with one platinum atom.

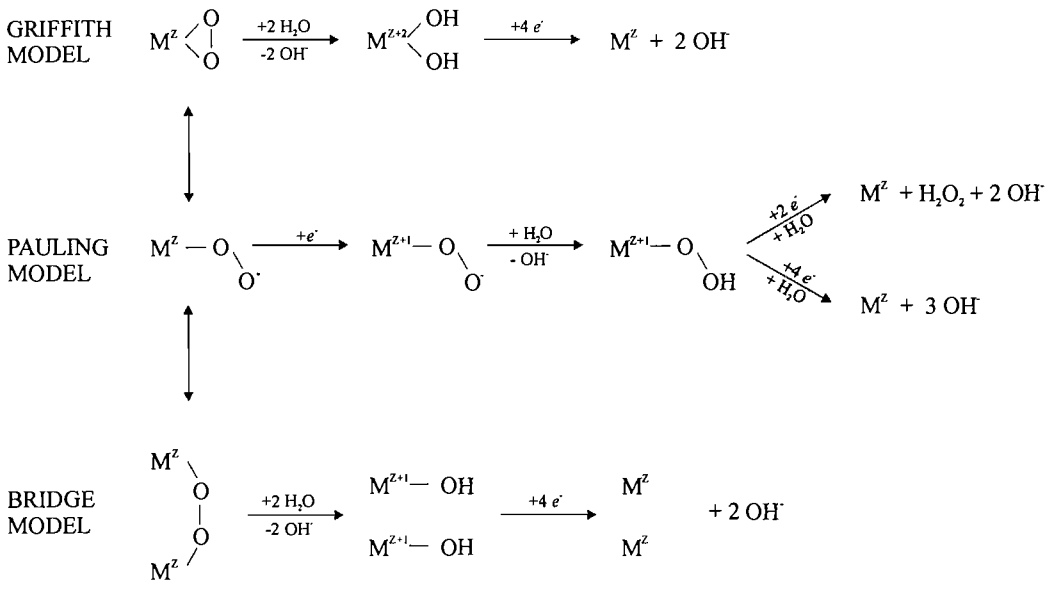

Figure 1.2 Griffith [113], Pauling [114] and bridge [115] models for oxygen adsorption and the pathways of oxygen reduction in neutral solution. M denotes a single site on the electrode surface and Z its oxidation state.

It can be seen that the 'end-on' configuration will promote the two-electron reduction without the cleavage of the O-O bond yielding peroxide as the main product. Similar results were also obtained on Pt(111) single crystal electrodes, where oxygen reduction was inhibited by submonolayer Ag deposits [116] and on halide covered silver electrodes, where the four-electron reduction changed to two two-electron reduction steps in presence of adsorbed halides [109]. The decrease in magnitude of mass transport limited currents is much smaller on Pt than for example on Ag. The reason being a possibility of Griffith type along with bridge type adsorption of oxygen on Pt as postulated by Fisher and Heitbaum [117]. The competition for adsorption sites between oxygen and other adsorbates is also responsible for the increase in the oxygen reduction overpotential and in consequence the shift of the voltammetric wave to more cathodic values.

On gold electrodes where oxygen is reduced only to hydrogen peroxide, the adsorbed anions effect will concern mainly the position of the voltammetric wave, but not its magnitude. No explicit data was found on ORR on polycrystalline gold

electrodes in presence of chloride. Some information can though be obtained from studies involving other halides. Adzic and Wang [118] reported strong inhibition of ORR on Au(100) (the most active single crystal surface towards the ORR) by adsorbed bromide. The oxygen reduction wave shifts ~300 mV in the cathodic direction, to potentials negative enough for the bromide layer coverage to fall down to zero. One can suspect that chloride ions, which also strongly adsorb on gold, will cause qualitatively similar effects.

All the considerations above assume excess of supporting electrolyte. With media of very low ionic strength, small additions of electrolytes (including chloride salts) will cause an adverse effect to the one described above. Added electrolyte will eliminate the uncompensated *IR* drop and the oxygen reduction overpotential will decrease. Such effects were experimentally observed on platinum microelectrodes, where the wave shifted towards more anodic potentials as the concentration of NaCl increased from 0 to 2.5 mM [102]. These observations are in agreement with the predicted microelectrode behaviour in media with very small supporting electrolyte to electroactive species concentration ratios [119].

1.4.4 ORR under enhanced mass transport conditions

Enhanced mass transport conditions have some important consequences for the ORR pathway and final products of the reaction. Platinum rotating disc electrode (RDE) and microelectrode studies [108] revealed that increasing the mass transfer coefficient (higher rotation rates for RDE and smaller microelectrodes radii) results in the decrease of the n_{app}. This proves not only that the series pathway of the ORR takes place, but also that its contribution to the overall mechanism is increasing under high mass transport regimes. Similar trend was also reported by Chen and Kucernak [120], who investigated the ORR on single submicrometer-sized Pt particles. The results suggest that the ratio of two-electron to four-electron reduction products (H_2O_2 to H_2O) increases with the mass transfer coefficient. The most convincing explanation is that significant amount of the intermediate peroxide

species are present in desorbed form and diffuse away before they can be further reduced. In addition, the voltammetric waves tend to shift to more negative potential indicating the increased irreversibility of oxygen reduction. This was observed not only on Pt but also on Au and Ag microelectrodes [102]. Rapid transport of oxygen reduction products (OH^-) away from the electrode also minimises any localised pH changes which could influence the reaction.

1.4.5 Temperature and pressure effects on ORR

Very little information is available on the influence of temperature on ORR in aqueous solutions in low temperature region (up to 50 °C). Most investigations were reported by Sepa and co-workers [121-124] and concerned the estimation of the apparent enthalpies of activation of the ORR on the basis of Tafel plots analysis. Their findings led to the conclusion that the mechanism of the ORR on Pt does not change with temperature and has the same rate determining step in both low current density region (where the surface coverage, by oxygen species and reaction intermediates, θ, is high) and high current density region (low coverage, $\theta<0.05$, approximately). The differences in Tafel slopes in these regions were interpreted in terms of altering adsorption conditions: from Langmuir adsorption at low coverage to Temkin adsorption conditions at higher coverage. The Tafel slopes were found to be temperature independent on Au and to follow a conventional dependence of 2.3 $RT/\beta F$, with the symmetry factor $\beta=1/2$ on Pt. Qualitatively similar temperature dependence was found by Zinola *et al.* [125] on Pt single crystal electrodes. These temperature effects concern only kinetically controlled currents. Thus, they should be insignificant for the amperometric response of the sensor operating in the diffusion controlled region. The effect of temperature on the oxygen diffusion coefficient is far more important and will directly influence the measured currents.

Pressure affects the ORR in three ways: changes in the limiting current, voltammetric wave position and wave shape. The magnitude of the current will be affected by the changes of the species diffusivity. Since the diffusion coefficient is inversely proportional to the medium viscosity, increased pressure will lower the

value of the diffusion coefficient. More detailed description of oxygen diffusivity can be found in section 1.5.2. The changes of the wave position and shape will reflect the changes in the kinetics of the reaction. Golas *et al.* [126] investigated the influence of pressure on the microelectrode voltammetric response. The authors employed cylindrical microelectrodes for their study of both, reversible system (reduction of $Fe(CN)_6^{3-}$) and irreversible system of oxygen reduction. In the range of 1 to 8000 bars, kinetically determined oxygen reduction voltammograms shifted to more positive potentials. This would suggest that the volume of reactant is larger than the volume of the intermediate in the rate determining step and the increasing pressure drives the reaction forward. These observations are in agreement with all the mechanistic models. The observed shift in the wave position did not seem to exceed 150 mV between ambient pressure and 8000 bar. The deepest oceans locations where the CTD probe is usually deployed are approximately 7 km, which corresponds to a pressure of *circa* 700 bars. Taking this into consideration, the maximal potential shift will not be larger than 15 mV. Provided the measuring potential of the sensor lies well in the plateau region of the oxygen reduction wave, the influence of pressure on the wave position can be neglected.

1.4.6 Summary

It is generally accepted that the first electron transfer is the rate-determining step of the ORR, and the overall reaction rate results from the combined effects of electron transfer rates, diffusion and adsorption of oxygen. There is no clear agreement on the detailed reaction mechanism or pH dependence [84, 127]. Moreover, no information is available concerning the temperature effects on the apparent number of electrons transferred in the ORR, especially in particular case of ORR on microelectrodes.

1.5 Dissolved oxygen physical chemistry

1.5.1 Oxygen solubility

In order to accurately predict the oxygen concentration in seawater or any other medium of interest the oxygen solubility has to be known. Equations that allow calculation of DO concentrations become a necessity when chemical determination is impossible (e.g. due to very small volume of sample). It is particularly important when attempting a sensor calibration, which is a crucial test during any sensing device development.

Oxygen solubility in water was a subject of numerous studies over the years [128-135]. Benson *et al.* [132] used an empirical approach and reported a set of solubility data, which was the most precise and in use for almost two decades. At present, more accurate (maximum deviation of Henry's coefficient reported as 0.039%) solubility data from Rettich *et al.* [135]. The solubility constants were obtained by thermodynamically rigorous methods on the basis of experimental study between 274.15 and 328.14 K and are considered to be the most reliable and are recommended for reference.

The solubility of any gas in liquid is governed by Henry's law which states that the concentration of gas in the liquid is directly proportional to the gas partial pressure in the gas phase, which is in equilibrium with the liquid (i.e. the gas phase is saturated with the liquid vapour):

$$c = H \cdot p_i \tag{1.24}$$

where c is the gas concentration in liquid, H the Henry's coefficient (dependent on temperature and liquid phase composition) and p_i is the partial pressure of the gas. For oxygen – water system the equation can be rewritten in terms of the barometric pressure, p_B and water vapour pressure, p_W:

$$c = S^0 \cdot (p_B - p_w) \tag{1.25}$$

S^0 stands here for the solubility of oxygen in pure water. The data presented in [135] were numerically fitted by Rasmussen and Rasmussen [136] yielding polynomial equations to calculate S^0 and p_w as a function of temperature, T_C (in °C):

$$S^0 = 9.0701 - 2.4864 \cdot 10^{-1} T_C + 5.3749 \cdot 10^{-3} T_C^2 - 7.1835 \cdot 10^{-5} T_C^3 + 4.4871 \cdot 10^{-7} T_C^4 \tag{1.26}$$

$$p_w = 0.546 + 6.16 \cdot 10^{-2} T_C + 6.60 \cdot 10^{-5} T_C^2 + 6.65 \cdot 10^{-5} T_C^3 \tag{1.27}$$

where S^0 is in μM DO atoms kPa^{-1} and p_w in kPa.

Having the DO concentration at given temperature and pressure, it is possible to determine the DO concentration in an aqueous solution of inorganic compound by means of a model developed by Tromans [137]. It is based on the experimental solubility data for 21 solutes reported earlier and assumes that the temperature dependent solubility function remains unchanged for water and the aqueous solution of interest. According to this model a coefficient ϕ gives the ratio of molal concentrations in pure water and a given solute solution (1.28):

$$c_{mO2(I)} = \phi \cdot c_{mO2(w)} \tag{1.28}$$

where $c_{mO2(I)}$ is the molal concentration of oxygen in electrolyte solution and $c_{mO2(w)}$ is the molal concentration of oxygen in pure water. ϕ is a constant (<1) characteristic for a given solute and is given by the equation (1.29):

$$\phi = \left(\frac{1}{1 + \kappa_0 (c_{mI})^{\varepsilon}} \right)^{\lambda} \tag{1.29}$$

Here c_{mI} is the molal concentration of the solute I and κ_0, λ, ε are temperature independent coefficients specific for the solute and are tabulated [137]. For instance,

for NaCl, which is subsequently used to model seawater, the coefficients are as follows:

$\kappa_0 = 0.075502,$

$\varepsilon = 1.009502,$

$\lambda = 4.223927.$

DO concentrations predicted with the above equations and coefficients are in excellent agreement with earlier experimental data [138] up to 475 K. Deviations appear at higher temperatures and in the range 273 – 300 K at high NaCl concentrations (above 2.5 mol kg^{-1}). Equations (1.26) - (1.29) are later used to predict DO concentrations at given temperature and pressure in experimental solutions and compared with the values determined by Winkler titration.

In the case of real seawater, where the available parameters are temperature and salinity (S) the solubility data can be found in the work of Carpenter [130] ($0.5 \geq T_C \geq 36°C$; $5.2 \geq Cl \geq 20°/_{oo}$, Cl denotes here chlorinity) and Murray and Riley [139] ($0.7 \geq T_C \geq 35°C$; $0 \geq S \geq 40°/_{oo}$). Even more precise data was later presented by Benson and Krause [140] ($0.2 \geq T_C \geq 45°C$; $0 \geq S \geq 50°/_{oo}$). The oxygen concentration c_0^* in seawater, which is in equilibrium with water vapour saturated atmosphere at standard pressure, is commonly described with the Setchenov equation:

$$\ln c_0^* = A + BS \tag{1.30}$$

where A and B are experimentally found coefficients in the form of polynomial temperature functions. The experimental data in [139, 140] were fitted with the equations of the above form. The fits agreed well with experimental data except the extremes of temperature and salinity ranges, where the deviations were significantly higher. Recently Garcia and Gordon [141] presented improved equations for calculating DO concentration in seawater based on experimental solubility data from

[130, 139, 140]. Their formula includes additional salinity terms and uses a scaled temperature T_S:

$$T_S = \ln\frac{298.15 - T_C}{273.15 + T_C} \tag{1.31}$$

The complete equation has the following form and the coefficients are listed in Table 1.2. The error of the fit was estimated by the authors to be 1 nmol kg^{-1} in the temperature range from freezing to 40 °C and for salinities $0 \geq S \geq 42° / \infty$.

$$\ln c_0^* = A_0 + A_1 T_S + A_2 T_S^2 + A_3 T_S^3 + A_4 T_S^4 + A_5 T_S^5 + S(B_0 + B_1 T_S + B_2 T_S^2 + B_3 T_S^3) + C_0 S^2 \tag{1.32}$$

Table 1.2 Values of the coefficients used in equation (1.32). Taken from Garcia and Gordon [141].

Coefficient	Value / μmol kg^{-1}	Coefficient	Value / μmol kg^{-1}
A_0	5.80818	B_0	-7.01211×10^{-3}
A_1	3.20684	B_1	-7.25958×10^{-3}
A_2	4.11890	B_2	-7.93334×10^{-3}
A_3	4.93845	B_3	-5.54491×10^{-3}
A_4	1.01567	C_0	-1.32412×10^{-7}
A_5	1.41575		

1.5.2 Oxygen diffusivity

The oxygen diffusion coefficient (D_{O2}) is necessary to calculate oxygen concentrations from the response of any amperometric sensor. The values found in the literature for oxygen diffusion coefficient in water, D_w differ significantly and

average to ~2.20×10^{-5} cm^2 s^{-1} at 25 °C. A selection of literature values is presented in Table 1.3 together with the various methods used for D_w determination.

Table 1.3 Comparison of literature values of oxygen diffusion coefficient in water.

Value / 10^{-5} cm^2 s^{-1}	Temperature / °C	Method of determination	Reference
1.96	25.3	Taylor dispersion with optical absorbance detection at 200 nm	[142]
2.41	25	diaphragm cell	[143]
2.00	22	transient interferometry	[144]
2.20	25	laminar dispersion in capillary	[145]
2.11	22	polarography	[146]
3.40	25	diaphragm cell technique	[147]
2.07	25	hydrodynamic chronocoulometry	[148]
2.22	25	hydrodynamic chronocoulometry	[149]
2.60	25	measurement of the rate of collapse of small bubbles	[150]

Several reports are also available on oxygen diffusivity in aqueous inorganic electrolyte solutions. Hung and Dinius [147] determined oxygen diffusion coefficients in NaCl, Na_2SO_4 and Na_3PO_4 solutions ($0 < c_{NaCl} < 2$ M, $0 < c_{Na2SO4} < 0.9$ M, $0 < c_{Na3PO4} < 0.05$ M) and Ho *et al.* [146] in solutions of NaCl, KCl, Na_2SO_4 and $MgSO_4$ (in ranges up to 4, 3, 1.5 and 2 M, respectively). Both research groups used membrane covered polarographic probes and observed a decrease of D_{O2} with increasing salt concentration. Similar trends were observed in KCl, LiCl and $MgCl_2$ by Ikeuchi *et al.* [151], who employed oxygen reduction on hanging mercury drop electrode (HMDE) to determine D_{O2}. Jovancicevic *et al.* [152] used chronoamperometry at microelectrodes to obtain D_{O2} in borate solutions and also found it to decrease with increasing ionic strength. Inconsistent with these reports is the work of van Stroe and Janssen [153]. Their data obtained with Pt RDE using the transient pulse technique in concentration range $0.085 < c_{NaCl} < 0.85$ M showed no dependence of D_{O2} on NaCl concentration.

A very comprehensive study was presented by Akita [154] who investigated oxygen transport properties in aqueous solutions of combinations of as many as 18

species of cations and 13 species of anions. On the basis of the experimental data (obtained by use of membrane covered oxygen sensor and Winkler determination of DO concentration) and Eyring theory of rate processes [155] the author developed a model to predict oxygen diffusivity in a solution of any combination of examined solutes. According to this model D_{O2} can be expressed as follows

$$D_{O2} = \left(\frac{\kappa}{h}\right)\left(\frac{V_m}{N_0}\right)^{2/3} T \exp\left(-\frac{\Delta G^*}{RT}\right) \tag{1.33}$$

where

$$V_m = \left(\Sigma c_i + c_w\right)^{-1} \tag{1.34}$$

and

$$c_w = \frac{\rho - \sum_i M_i c_i}{0.01802} \tag{1.35}$$

The symbols here signify: κ - Boltzmann's constant, h – Planck's constant, V_m – molar volume of the solution, N_0 – Avogadro's number, ΔG^* – free energy of activation of diffusing particle, c_i – molar concentration of species i, c_w – molar concentration of water, ρ - density of the solution, M_i – formula weight of species i. The free energy of activation can be expressed as a sum of partial quantities for all solution components. For a single salt solution, the equation (1.33) can be rewritten as:

$$D_{O2} = \left(\frac{\kappa}{h}\right)\left(\frac{V_m}{N_0}\right)^{2/3} T \exp\left(-\frac{\alpha x_+ + \beta x_- + \gamma x_w}{RT}\right) \tag{1.36}$$

and further rearranged to

$$D_{O2} = \left(\frac{\kappa}{h}\right)\left(\frac{V_m}{N_0}\right)^{2/3} T \exp\left(-\frac{\Delta\alpha x_+ + \Delta\beta x_- + \gamma}{RT}\right) \tag{1.37}$$

where $\Delta\alpha, \Delta\beta$ are values defined by $\alpha-\gamma$ and $\beta-\gamma$, respectively. α, β, γ are temperature independent (in the examined range of temperatures 10 – 60 °C) components of free energy of activation of diffusing solute in aqueous solution, due to cation (α), anion (β) and water (γ). The molar fractions of cation, anion and water are denoted by x_+, x_- and x_w, respectively. Whereas $\Delta\alpha$ and $\Delta\beta$ were determined and tabulated [154], γ can be extracted from the measurement of the diffusion coefficient of oxygen in pure water (D_w) when (1.37) simplifies to (1.38):

$$D_w = \left(\frac{\kappa}{h}\right)\left(\frac{V_w}{N_0}\right)^{2/3} T \exp\left(-\frac{\gamma}{RT}\right) \tag{1.38}$$

Thus, the diffusion coefficient as a function of salt concentration can be calculated provided the D_w and the solution density are known. In this work all the data were processed using $D_w = 2.11\times10^{-5}$ cm^2 s^{-1} at 22 °C, from Ho *et al.* [146], and yielded γ=13835 J mol^{-1}. The predicted values for NaCl solutions agree very well with the experimental data published by other researchers [146]. A graphical representation of D_{O2} as a function of NaCl concentration and absolute temperature is shown in Figure 1.3, which covers the full range of natural waters salinity and the temperature range typical for oceanographic measurements.

The temperature dependence of the diffusion coefficient has an Arrhenius form ($\ln D_{O2} \propto 1/T$) in all the above equations. This is complimentary to the temperature dependence of solution viscosity, η as proposed by Eyring (1.39), [155] and the Walden rule stating that the $D\eta$ product has a constant value.

$$\left[\frac{\partial \ln \eta}{\partial(1/T)}\right]_p = \frac{E_v}{R} \tag{1.39}$$

E_v denotes here the activation energy of viscous flow. In the overall expression for D_{O2} the viscosity is accounted for by the exponential term and the molar volume.

Both are functions of the solute concentration, which determines the value of the solution viscosity.

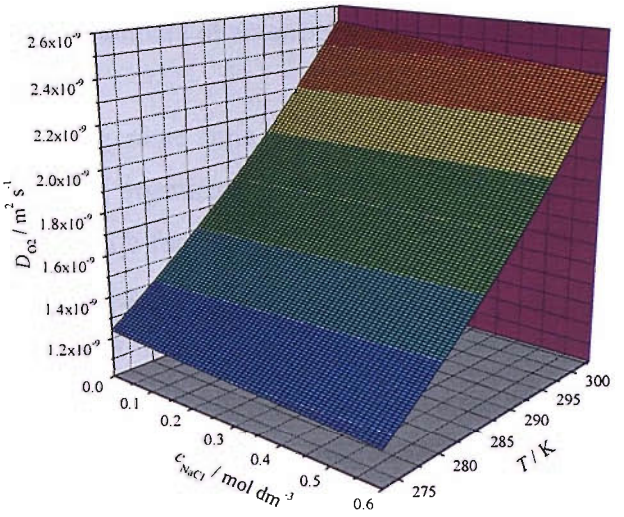

Figure 1.3 Oxygen diffusion coefficient as a function of temperature and NaCl concentration as calculated from equation (1.37).

1.5.3 Oxygen in the oceans

Sources and sinks

There are three main sources of oxygen in the ocean waters:

a) Dissolution of oxygen from air, which is in constant equilibrium with surface waters. The net exchange of oxygen depends on air and water temperatures, water salinity (as governed by solubility laws) and the effectiveness of convective oxygen transport between the surface and deeper water.

b) Dissolution of oxygen contained in bubbles, which are forced into the bulk water by waves. Unlike the case of diffusive fluxes, this oxygen source can

lead to oversaturation of surface waters [156]. The greater the degree of shallow waters turbulence the more efficient the oxygenation process.

c) Production of oxygen by photosynthesising organisms. The net increase in the biologically originated DO occurs in diurnal cycles as it is conditional to the availability of sunlight. For the same reason, oxygen production decreases with depth as the amount of autotrophic organisms able to survive decreases.

Similarly, at the same time DO is consumed in biological and physical processes. Heterotrophic organisms use it continuously for respiration purposes, while photosynthesising life forms metabolise DO when the sunlight is not available (night, eutrophicated waters). Throughout the bulk and in oceanic sediments the microbial life uses oxygen in the remineralisation processes of organic matter. Also anthropogenic sources may result in DO consumption as the organics introduced into ocean water are broken down. Finally, the ocean-atmosphere oxygen equilibrium will force the ocean to outgas whenever the highly oxygenated cold water masses reach the higher temperature surface.

Distribution

Vertical distribution of oxygen is a result of combination of all the processes listed above and the circulation and mixing of large water masses. From the surface, where the water is oversaturated with oxygen, the DO concentration decreases as the depth increases, primarily due to the biological activity of the oceanic fauna and flora. More oxygen is consumed in respiration processes and less is generated by phytoplankton. At some point, called the compensation depth, these two processes balance each other and the net oxygen production is zero. Below this level, no phytoplankton growth is possible [157] and the DO concentration continues to decrease due to the uptake by animals and oxidation of organic debris by microorganisms. After reaching the minimum (at depths of 500-1000 m, depending on location) the oxygen level rises again as dense highly oxygenated waters sinking in polar regions are introduced. The bottom waters show only very slight decrease in DO concentration, despite the oxygen uptake in the sediments. This is due to the

much higher efficiency of convective water mixing in comparison with diffusive fluxes into the sediments (the sediments are characterised by a diffusive layer thickness of *circa* 1 mm [75]). The vertical DO profiles vary depending on geographical location, although they always show the abovementioned features (Figure 1.4). The variability is a result of the amount of biological life and large scale water circulation and temperature. The temporal changes (at given geographical location) of the vertical profiles are very small over hours or days. The short term variations can be observed mainly in shallow waters due to the biological life day-night cycles.

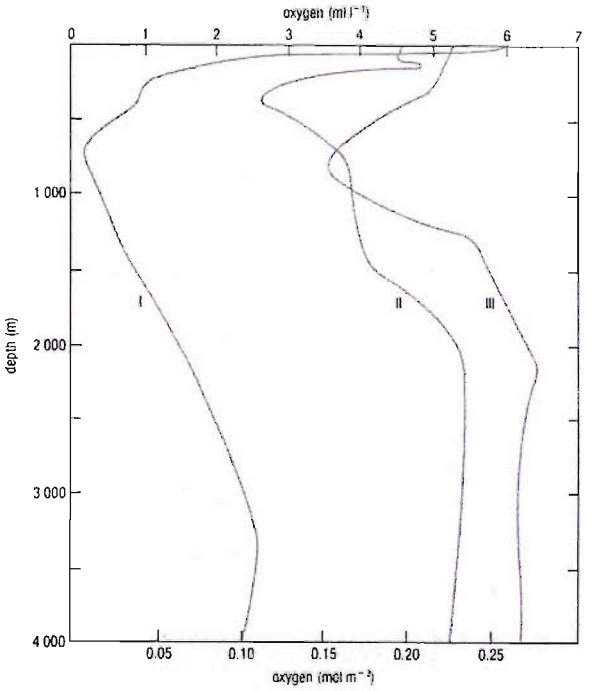

Figure 1.4 The vertical distribution of dissolved oxygen: I – South of California, II – eastern part of South Atlantic, III – Gulf Stream. Reproduced from reference [157].

1.6 Research aims

The aim of this work is to develop a fast and reliable amperometric microelectrode DO sensor. The sensor is primarily intended for the use in oceanographic research. The targeted applications are:

a) to obtain vertical profiles of DO concentration from the surface to full oceanic depth while the sensor is mounted on a CTD profiler,
b) to continuously monitor DO concentration at a fixed location with the sensor placed on a buoy or mooring,
c) to obtain vertical DO concentration profiles of variable range on submersible floats,
d) other DO concentration profiling, e.g. on remotely operated vehicles (ROVs), autonomous underwater vehicles (AUV), sediments – water vertical profiling, etc.

All of the above are long term applications with the sensor operation times ranging from hours to months. Therefore a durable sensor with a very stable response is needed. Moreover, due to the character of oceanic measurements the ideal sensor should be robust and require very low or no maintenance. Successful performance is also a subject to the ability to withstand very harsh environmental conditions. The sensor has to cope with high salinity, high pressures at large depths (up to 7000 m) and variable temperatures ranging from *circa* 25 °C close to the surface to 0 °C in deep waters and arctic regions. Moreover, in between CTD dips the sensor is on deck and has to withstand even more extreme temperatures (-20 to +35 °C). Since any form of mechanical or chemical conditioning of the electrode is not possible, a stable and reliable response should be maintained exclusively by a suitable potential program.

Important aspects of DO concentration measurements in oceanography are spatial and temporal resolutions in the case of moving and stationary probes, respectively. Thus, a desirable feature of the developed sensor would be its short response time. Most of the commercially available oceanographic DO sensors have a response time in range of 30 to 60 s, with a single device from Unisense claiming

sub-second response [67]. However, due to its fragile construction and the presence of a membrane it is not suitable for some applications. For vertical DO profiling in conjunction with a CTD probe, a sub-second (ideally of order of 0.1 s) response time is sought. With the CTD probe moving at an average speed of *circa* 1 m s^{-1} the water column could be sampled every 1 m or even every 10 cm in ideal case.

While the main scope of this study is to develop a sensor for oceanographic measurements, its possible application in estuaries, freshwater and processed waters would be very advantageous.

Bearing in mind the requirements in terms of performance and the conditions under which the sensor has to operate, unshielded microelectrodes were the first choice for the oceanographic application. Due to the enhanced mass transport conditions, they provide a rapid response with quickly established diffusion limited steady-state currents. The absence of a membrane makes the sensor amperometric response insensitive to pressure and greatly reduces maintenance and fouling problems associated with Clark type devices. Another reason for using microelectrodes is their small electroactive area which yields very small current, typically pA to μA, sufficiently small to keep the reference electrode ideally polarised and allow the use of two-electrode arrangements. This simplifies the electronics and results in low power consumption, an essential feature in field applications.

In course of this work several fundamental issues concerning the ORR on microelectrodes were also addressed. In particular the dependence of the ORR on temperature was investigated as well as the variation of n_{app} on mass transport conditions. Earlier data on the steady-state oxygen reduction current dependence on the mass transfer coefficient is available [108, 158]. In this study the investigation was extended to the analysis of transient response and the variation of n_{app} with the timescale of experiment.

1.7 Structure of the thesis

Chapter 2 gives details on the reagents, instruments and techniques that were used on the regular basis throughout this work. Standard procedures for electrodes preparation and characterisation are described.

Chapter 3 presents the results of voltammetry and potential step studies of oxygen reduction at microelectrodes. Gold, platinum and nanostructured platinum are evaluated as potential cathode materials for the dissolved oxygen sensor.

Chapter 4 describes the system developed to calibrate the sensor. The analytical performance of the microelectrode is presented, including calibration and error estimates. Also, the data on n_{app} as a function of mass transfer coefficient and temperature is presented. This data is used to obtain some kinetic and mechanistic information on the ORR.

Chapters 5 and 6 present alternative solutions to steady-state measurements. Chapter 5 describes transient measurements, were oxygen is determined by double potential step chronocoulometry with step durations of order of milliseconds. In Chapter 6 the performance of vibrating electrodes is presented.

In Chapter 7 the sensor (based on the steady state measurements) for *in situ* oceanographic measurements is described. The algorithm for the calculation of DO concentration from the sensor output is given. The field performance is reported and results analysed.

Chapter 8 contains brief conclusion and the outline of further work, and it is followed by Appendix and the list of references.

2 Experimental

The experimental procedures presented in this chapter are general and apply to the majority of experiments. Alterations of these procedures and special arrangements for particular experiments are described in detail in the relevant results sections.

2.1 Solutions

The solutions in which the electrochemical experiments were performed were prepared using deionised water obtained from a Still Plus (Whatman) purifying system. The water had a resistance of 18 MΩ, which was frequently checked with a conductivity meter (Activon, model PTI-10). All the chemicals used in the experimental work are listed in Table 2.1. Oxygen (industrial grade, 99.5%) and argon (Pureshield Argon, 99.998%) were purchased from BOC Gases, while air was taken from the compressed air laboratory supply.

2.2 Electrodes

2.2.1 Reference electrodes

Home made saturated mercury (I) sulphate (SMSE) and calomel (SCE) electrodes were used in the experimental work. After fabrication [159], the electrodes were left for 24 h to stabilise in saturated K_2SO_4 or KCl solutions for SMSE and SCE respectively. In between experiments, the electrodes were stored in the above mentioned solutions and frequently checked against commercial reference electrodes. The potential difference did not exceed 5 mV.

Table 2.1 Chemicals used in the experimental work.

Name	Formula	Purity	Manufacturer
Reagents			
Hexaammineruthenium (III) Chloride	$Ru(NH_3)_6Cl_3$	98%	Aldrich
Manganese (II) Chloride Tetrahydrate	$MnCl_2 \cdot 4H_2O$	98%	Lancaster
Manganese (II) Chloride Tetrahydrate	$MnCl_2 \cdot 4H_2O$	ACS reag.	Riedel-de-Haën
Mercury (I) Chloride	Hg_2Cl_2	ACS 99.5%	Alfa Aesar
Mercury (I) Sulphate	Hg_2SO_4	>97%	Fluka
Potassium Chloride	KCl	Aristar	BDH
Potassium Chloride	KCl	Traceselect	Fluka
Potassium Ferricyanide	$K_3Fe(CN)_6$	Analar	BDH
Potassium Sulphate	K_2SO_4	Analar	BDH
Potassium Iodate	KIO_3	98%	Avocado
Potassium Iodide	KI	analytical reagent	M&B
Sodium Chloride	NaCl	Analar	BDH
Sodium Chloride	NaCl	Aristar	BDH
Sodium Hydroxide	NaOH	Analar	BDH
Sodium Thiosulphate Pentahydrate	$Na_2S_2O_3 \cdot 5H_2O$	analytical reagent	Timstar Laboratory Supplies Ltd.
Starch soluble	-	analytical reagent	M&B
Sulphuric Acid	H_2SO_4	Aristar	BDH
Tetrabutylammoniumtetrafluoroborate	$(C_4H_9)_4N(BF_4)$	99%	Aldrich
Metals			
Gold (wire, ϕ=10 μm)	Au	99.99+%	Goodfellow
Indium (wire, ϕ=1 mm)	In	99.99%	Aldrich
Mercury	Hg	99.9998%	Alfa Aesar
Platinum (wire, ϕ=5-50 μm)	Pt	min. 99.9+%	Goodfellow

2.2.2 Working electrodes

2.2.2.1 Fabrication

All the microelectrodes were prepared according to typical procedures described previously [160, 161]. Au or Pt microwire (a=2.5 – 25 μm) was sealed in soda glass pipette using a heating coil and under reduced pressure. The glass was previously soaked for 24 h in Decon® detergent solution, followed by a thorough rinse and soaking for 24 h in purified water. The electrical connection to a microwire was made using indium (Aldrich) and the thick connecting copper wire was immobilised at the end of the pipette with quick set epoxy resin (RS, UK). Subsequently, the glass tip was polished off to reveal the microdisc using silicon carbide abrasive papers of decreasing grain size (grades: 320, 600, 1200), followed by polishing with alumina suspentions (grain size: 1.0 and 0.3 μm, Buehler) on a moist polishing cloth (Buehler). Modifications of the procedure are mentioned in the relevant sections, where application specific electrodes had to be prepared.

2.2.2.2 Characterisation

Cyclic Voltammetry in sulphuric acid

Cyclic voltammetry in deoxygenated 1 M H_2SO_4 was used to characterise the surface of the electrodes. The shape, position and magnitude of the peaks were observed to assess the electrode roughness and detect any contaminants present on the surface. A typical voltammogram of a Pt microdisc is shown in Figure 2.1. The chosen scan limits are onsets of oxygen (D) and hydrogen (G) evolution. Several features, characteristic for clean platinum surface are visible: hydrogen monolayer adsorption (strong – F', weak – F) and desorption (strong – A', weak – A), Pt oxide formation (C) and reduction (stripping, E). Recording an acid voltammogram with well separated hydrogen adsorption/desorption peaks and shape consistent with literature [162, 163] was a prerequisite to any electrochemical experiment.

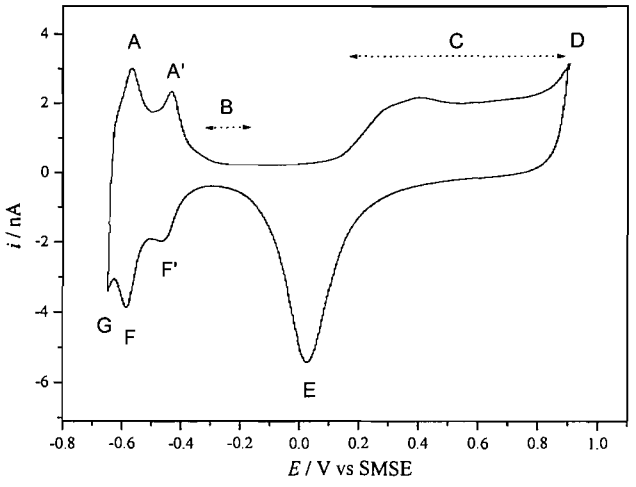

Figure 2.1 Cyclic voltammogram of a Pt microdisc (a=12.5 μm) in deoxygenated 1 M H_2SO_4, scan limits: -0.65 to 0.9 V vs. SMSE, v=200 mV s^{-1}. A, A' – hydrogen desorption, B – double layer region, C – platinum oxide formation region, D – onset of oxygen evolution, E – platinum oxide reduction (stripping), F, F' – hydrogen adsorption, G – onset of hydrogen evolution.

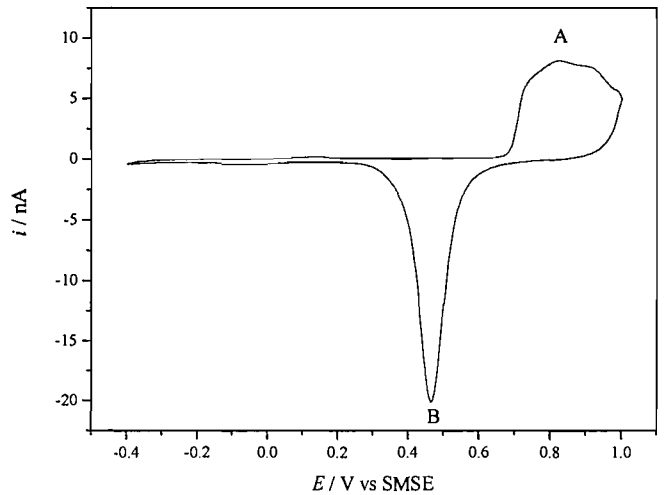

Figure 2.2 Cyclic voltammogram of Au microdisc (a=12.5 μm) in deoxygenated 1 M H_2SO_4, scan limits: -0.4 to 1.0 V vs. SMSE, v=200 mV s^{-1}. A – oxide formation region, B – oxide stripping peak.

Similarly, gold electrodes were characterised in sulphuric acid to get information on the surface state (Figure 2.2). In addition, any distortions in the shape of the voltammogram could indicate imperfect seal between the glass and the microwire or other defects.

Radius determination in purely diffusion controlled system

The radii of microelectrodes were determined by means of steady state voltammetry in purely diffusion controlled systems, i.e. the electrode reaction was a very fast outer sphere electron transfer and the number of electrons was known as well as the diffusion coefficient of the mediator. The reaction routinely used was the one-electron reduction of hexaammine ruthenium chloride, $Ru(NH_3)_6Cl_3$ (in 250 mM KCl aqueous solution – excess of supporting electrolyte assures the absence of migration current). Steady state voltammograms in this system are shown in Figure 2.3.

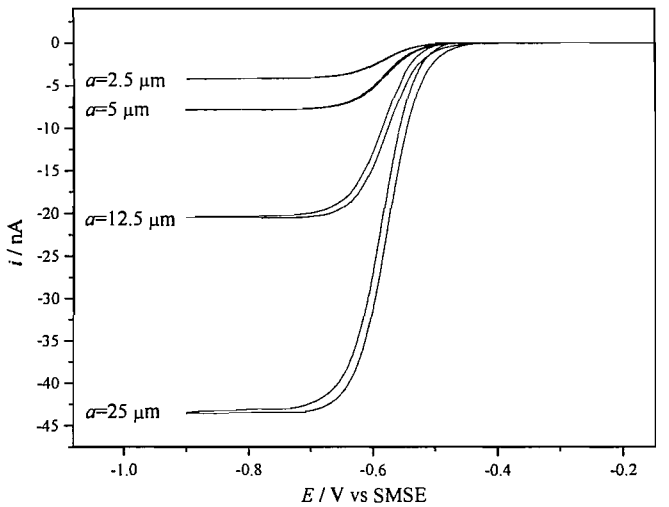

Figure 2.3 Steady state voltammograms in deoxygenated 5 mM $Ru(NH_3)_6Cl_3$, 250 mM KCl aqueous solution at 25 °C. Electrodes: Pt microdiscs with radii as indicated, v=5 mV s^{-1}.

Similar results were also obtained for reduction of ferricyanide, $K_3Fe(CN)_6$ to ferrocyanide, $K_2Fe(CN)_6$. This system was later abandoned due to the ferricyanide

and ferrocyanide adsorption on the electrode surface, particularly when relatively large cycling potential range is used [164, 165]. This film formation can affect the heterogeneous electron transfer rates and impair the activity towards ORR.

The electrode radius, a, can be calculated from the expression for the limiting current (i_{ss}) at microelectrodes (2.1)

$$i_{ss} = 4nFDca \tag{2.1}$$

where n is the number of electrons transferred, F the Faraday constant, D the diffusion coefficient of electroactive species and c the species concentration. D used for calculations was determined in a separate experiment using ten electrodes of various radii (Figure 2.4), which were determined by scanning electron microscopy imaging (XL ESEM, Philips). The diffusion coefficient of $Ru(NH_3)_6^{3+}$ in 250 mM KCl aqueous solution at 25 °C was found to be 8.8×10^{-6} cm^2 s^{-1}, which is in good agreement with values found by other researchers [166-168].

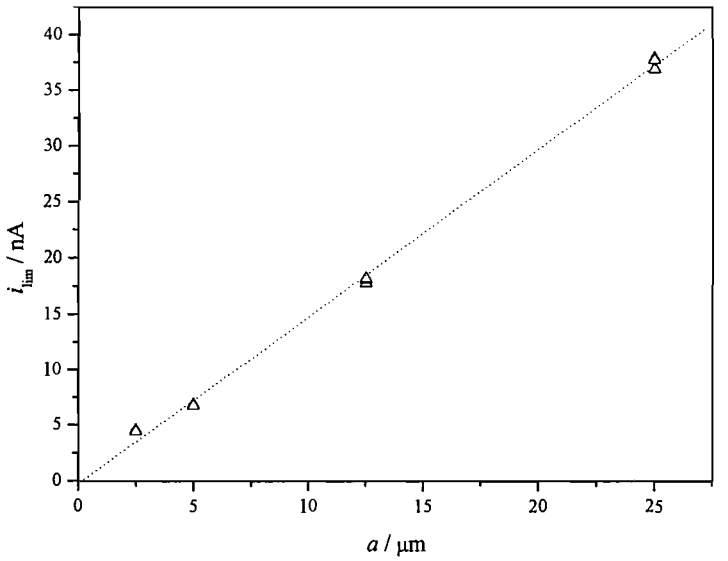

Figure 2.4 Limiting currents for the reduction of 5 mM $Ru(NH_3)_6^{3+}$ in 250 mM KCl at 25 °C as a function of the microdisc radius.

2.3 Experimental cells and instrumentation

All cells were made of glass and were equipped with a water jacket for temperature control. Cells were thermostated using a waterbath (model W14, Grant). Electrodes, gas feeds, thermometers etc., were introduced to the cell via quick-fit necks, which allowed sealing the experiment environment if needed. For the general purpose of gas transport a low gas permeability Tygon® R3603 (Saint Gobain) tubing was used. In some experiments it was replaced by glass tubes to prevent any gas exchange between the transported gas or solution and environment. The whole experimental assembly was contained in earthed aluminium Faraday cage for noise reduction.

A typical instrumentation for electrochemical experiments consisted of a PPR-1 waveform generator (HI-TEK Instruments, England) and a custom built current follower. The current follower was battery operated for maximal noise reduction. Its A/V gain was adjustable between 10^{-5} and 10^{-10} and the response time was <200 μs. In several experiments, where high frequency waveforms had to be generated, a 1250 Frequency Response Analyser (Solartron, UK) was used. The data was acquired with a PC equipped with an acquisition card with the resolution of 16 bit and adjustable sampling rate. LabView software was used for data acquisition and instrument control.

3 Steady state oxygen reduction on microelectrodes

3.1 Chapter overview

In this chapter, voltammetry and potential step investigations of oxygen reduction on microelectrodes are presented. Electrode materials are assessed in order to choose a cathode for the sensor. An attempt is made to find an optimal potential waveform, which would result in stable and reproducible response over extended period of continuous operation. Other processes occurring on the electrode surface in conditions similar to seawater environment are investigated. The effect of chloride ions on the electrode behaviour and oxygen reduction is assessed. The majority of experiments were conducted in 500 mM NaCl, which corresponds to standard salinity seawater with respect to the chloride concentration. The following pages deal only with the determination of DO on the basis of limiting current measurements in stagnant solutions.

3.2 Gold

3.2.1 Voltammetry in sodium chloride solutions

In order to design a waveform for continuous operation of the sensor, processes occurring in the accessible potential window were evaluated. A cyclic voltammogram recorded on a gold microdisc electrode in air saturated 1 mM NaCl solution is shown in Figure 3.1. The oxygen reduction wave commences at -0.35 V (vs SMSE) and the plateau at around -0.8 V; however it is poorly defined and corresponds to the two-electron reduction of oxygen. At more positive potentials one can observe the formation of gold oxide species (onset at 0.6 V) and their stripping on the cathodic scan at 0.37 V. The anodic behaviour of gold electrode was further

investigated separately from the ORR. Voltammetric measurements were performed in the potential range from -0.2 to 1.0 V in solutions containing 0-500 mM of NaCl.

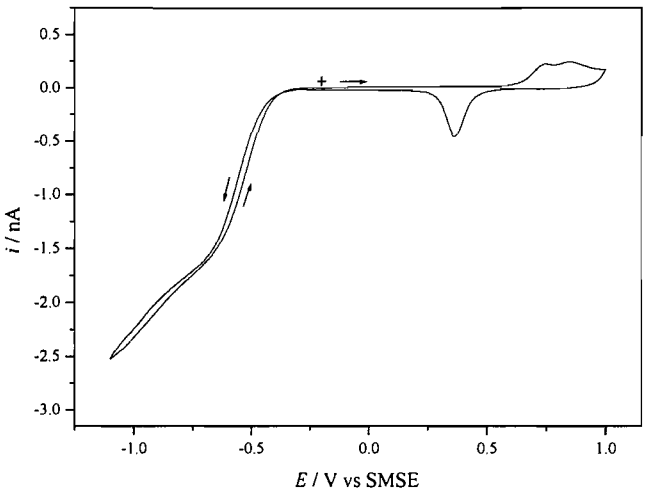

Figure 3.1 Cyclic voltammogram on a gold microdisc electrode (a=5 μm) in air saturated 1 mM NaCl solution at 25 °C. v=100 mV s^{-1}, '+' denotes the starting point, arrows show scan directions. Stable response obtained after 5-10 cycles.

A family of cyclic voltammograms is presented in Figure 3.2. In the oxide formation region a peak appears at 0.72 V and grows as the chloride content increases. The magnitude of this peak is clearly correlated with the chloride concentration (Table 3.1, Figure 3.3), while the more positive part (0.8 to 1.0 V) seems to be independent of Cl^- concentration up to 10 mM. Interestingly, the magnitude of the oxide stripping peak is little affected in this concentration range. The peak position also changes slightly but without a clear correlation to the concentration of salt. For higher Cl^- concentrations and especially in 500 mM NaCl solution we observe increased anodic currents at the most positive (> 0.8 V) potentials as well as a growing cathodic current in region more negative than 0.2 V. In 500 mM NaCl solution it forms a broad reduction signal at *circa* 0.1 V. The observed voltammetric features are in agreement with earlier study of the anodic behaviour of gold in neutral sulphate solutions containing chloride at lower concentrations (up to 100 mM) [169].

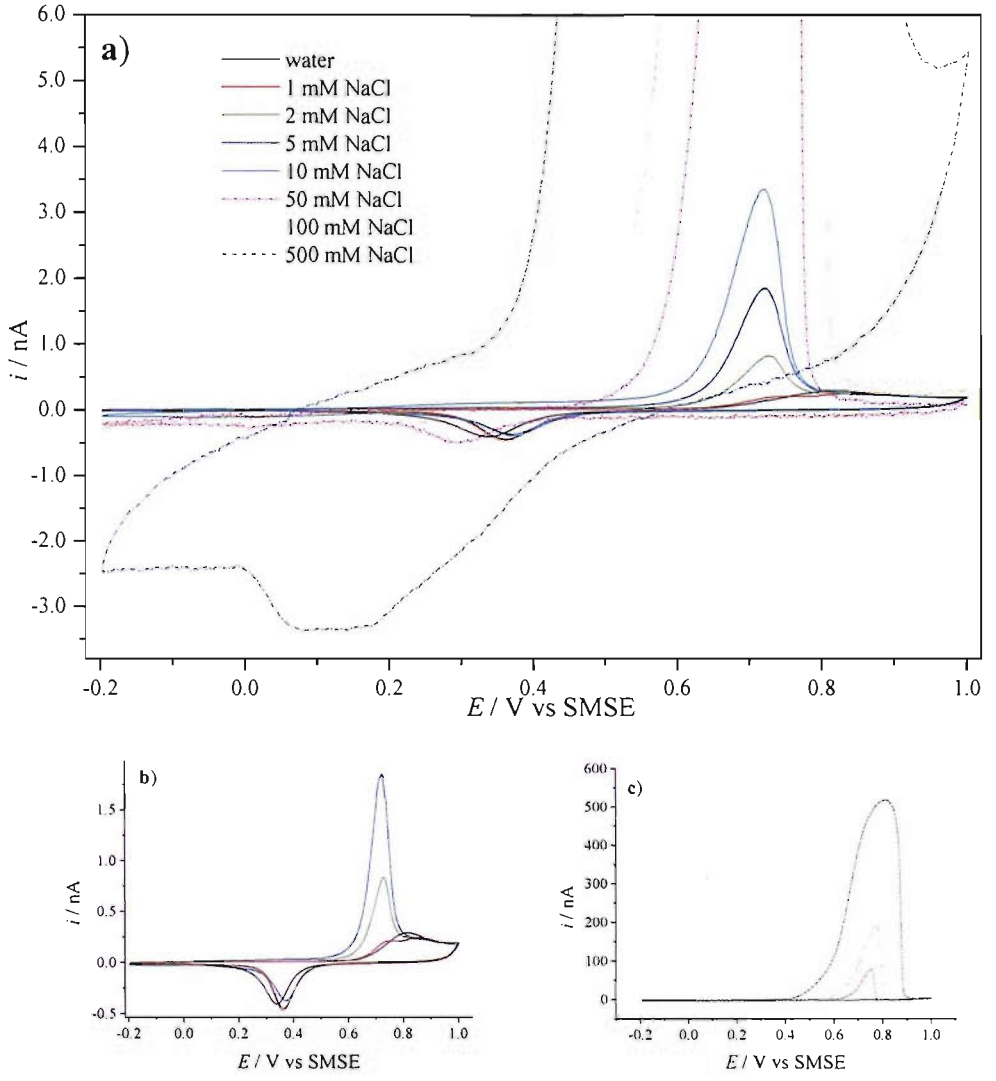

Figure 3.2 a) Cyclic voltammograms on a gold microdisc (a=5 μm) recorded in air saturated NaCl solutions at 25 °C; NaCl concentrations as indicated on the graph, scan range -0.2 to 1.0 V vs SMSE, v=100 mVs^{-1}. For clarity, the voltammograms obtained in low and high NaCl concentration ranges are also shown separately in **b)** and **c)**, respectively. The voltammograms are stable responses obtained after 5-10 cycles.

Table 3.1 Dependence of the anodic charge density (Q_a) of the gold voltammograms in Figure 3.2 on NaCl concentration.

c_{NaCl} / mM	0	1	2	5	10	50	100	500
Q_a / C cm^{-2}	8.2×10^{-4}	8.3×10^{-4}	1.5×10^{-3}	2.6×10^{-3}	4.6×10^{-3}	7.0×10^{-2}	0.25	1.46

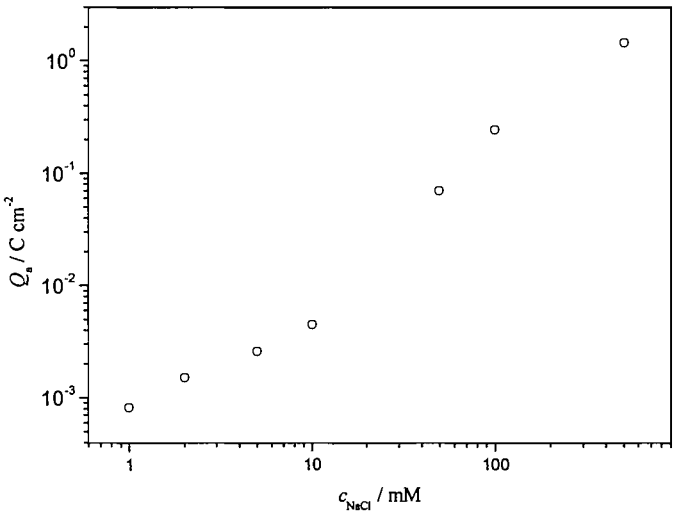

Figure 3.3 Dependence of the anodic charge (Q_a) of the gold voltammograms in Figure 3.2 on NaCl concentration. The charges were obtained by integration of the anodic sweep of the corresponding voltammogram over the range 0.4 to 1.0 V.

The peak at 0.72 V is ascribed to the oxidation of gold to soluble Au(III) species. One can conclude to the dissolution of the electrode from the fact that the anodic charge on the voltammogram is always much greater than the cathodic charge. The chloride induced dissolution appears to occur in parallel with 'gold oxide' formation on the surface and is thought to yield tetrachloroaurate ($AuCl_4^-$; (3.1)) as the main product [169-173].

$$Au(s) + 4Cl^- \rightarrow AuCl_4^- + 3e^- \qquad (3.1)$$

(*s*) in the reaction scheme denotes the solid phase. The literature suggests a competition for the adsorption sites between chloride and oxygen species, which takes place in the beginning of the oxide formation region, i.e. when the oxide has only monolayer or submonolayer thickness. At more positive potentials the surface is completely passivated by gold-oxygen species, which in neutral media are most probably $Au(OH)_3$, AuO(OH) or AuOH [169, 172]. This prevents further dissolution and indeed can be clearly seen on the voltammogram. However, significant anodic current is observed positive to 0.8 V for the highest chloride concentration, revealing that gold is being complexed by chloride despite high oxide coverage, providing the activity of Cl^- is sufficiently large. Also, in solution of 500 mM NaCl a large cathodic signal is recorded on the negative scan. The precise origin of this current is not known. Presumably, it is due to the reduction of anodically formed soluble gold species.

The observed dissolution of gold is in agreement with the thermodynamic model of gold-chloride-water system [174, 175]. From the potential-pH diagram (Figure 3.4) of the system it can be seen that the dissolution can also proceed through the formation of Au(I) species, namely $AuCl_2^-$. The formed dichloro gold(I) is however stable only at high chloride/gold activities ratio. With less chloride available in the system it undergoes disproportionation to metallic gold and $AuCl_4^-$ (3.2).

$$3AuCl_2^- \rightarrow 2Au(s) + AuCl_4^- + 2Cl^- \qquad (3.2)$$

Although the possibility of Au(I) species formation is assumed by the majority of researchers, Ye *et al.* [173] found no evidence of Au(I) compounds presence in their EQCM study in perchloric acid with chloride additives at Au(111) surfaces. Lovrecek *et al.* [169] suggest that the dissolution in neutral solutions proceeds by the reaction of chloride with $Au(OH)_3$ forming mixed chlorohydroxo gold complexes (3.3), which subsequently exchange hydroxyl ligands to eventually form $AuCl_4^-$.

$$Au(OH)_3(s) + Cl^- \rightarrow AuCl(OH)_3^- \qquad (3.3)$$

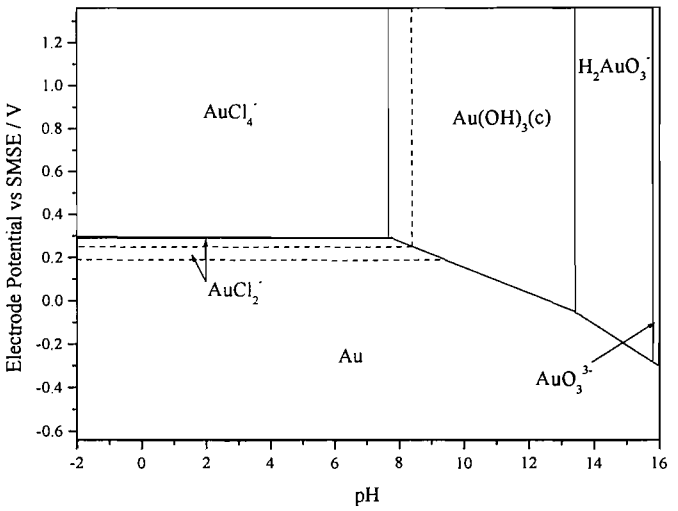

Figure 3.4 Potential – pH diagram for a gold-chloride-water system at 298.15 K for $a_{Au}=10^{-3}$ and $a_{Cl^-}=1$ (solid line), $a_{Cl^-}=5$ (dashed line), where a_i denotes the activity of species i. Taken from reference [175]; for the ease of comparison the potential axis was converted from NHE to SMSE.

After cycling the potential in the range -0.2 to 1.0 V in 100 mM NaCl solution the electrode surface was again examined in sulphuric acid. A stable response recorded after approximately ten cycles is shown in Figure 3.5. It differs significantly from the one recorded on freshly polished electrode, which suggests permanent changes to the electrode surface. Significantly higher currents are observed in the oxide formation region and a large peak appears on the negative scan at ~0.3 V. The oxide stripping peak can be seen only as a small shoulder on the right side of this peak. The presence of these features in chloride free acid solution suggests that stable gold chloride species were formed on the electrode in the preceding experiment in NaCl solution. This seems to be confirmed by other authors who reported a reproducible procedure of obtaining gold chloride films by cyclic voltammetry over corresponding potential range in hydrochloric acid [176]. The large cathodic peak is believed to be due to the reduction of the film. Its position corresponds well with the reduction of $AuCl_4^-$ in chloride containing H_2SO_4 (~0.35 V) [170] and $HClO_4$ (~0.25 V) [173]. The increased capacitive current observed on

the voltammogram is believed to result from an increased electroactive area caused by oxidative roughening of gold in Cl^- containing solutions [177].

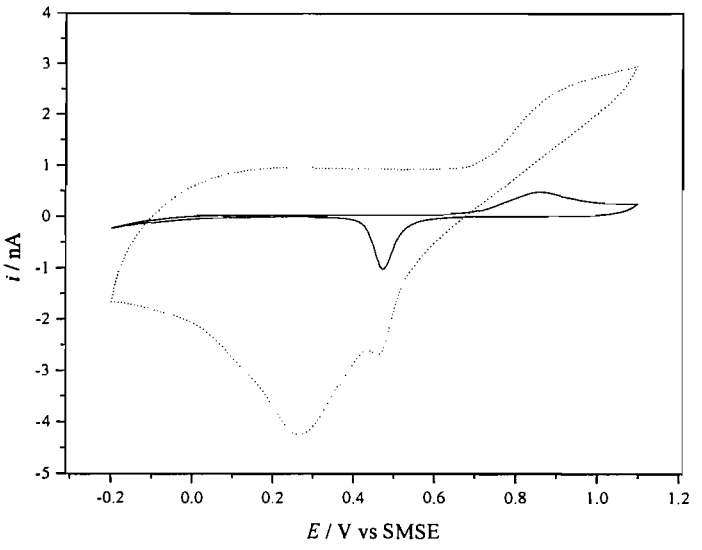

Figure 3.5 Cyclic voltammograms at gold microdisc (a=5 μm) recorded in deoxygenated 1 M H_2SO_4 before (solid line) and after (dotted line) cycling in 100 mM NaCl (range -0.2 to 1.0 V). Scan rate v=100 mV s^{-1}, T= 25 °C. Stable response after 5-10 cycles.

The anodic behaviour of gold puts constraints on the design of the waveform for the continuous operation of the sensor. As can be seen in Figure 3.2 the dissolution of gold in 0.5 M NaCl starts at around 0.1 V. This sets a positive limit for the potential for the cleaning step that can be applied to a gold cathode under seawater conditions. Dissolution of the electrode would result in a continuous loss of material, leading eventually to recess creation and changing of the diffusion field geometry. Moreover, at the cathodic measuring potential some of the gold soluble or adsorbed gold species could be reduced and form rough deposits on the surface. The high roughness of the electrodeposited gold may lead to unusual oxygen reduction, where the n_{app} is greater than 2 [178].

3.2.2 Oxygen reduction in NaCl solutions - voltammetry

Oxygen reduction on gold was investigated by cyclic voltammetry in solutions containing 0-500 mM NaCl. The experiments were performed in an open cell thermostated at 25 °C and the solution was saturated with ambient air. Before recording a steady-state oxygen reduction wave the potential was cycled at 50 mV s^{-1} between -1.2 and -0.2 V until a stable response was observed. Subsequently, cyclic voltammogram was recorded at 5 mV s^{-1}. Usually 3 to 4 cycles were needed for the response to stabilise. A cyclic voltammogram recorded in air saturated 5 mM NaCl is shown in Figure 3.6.

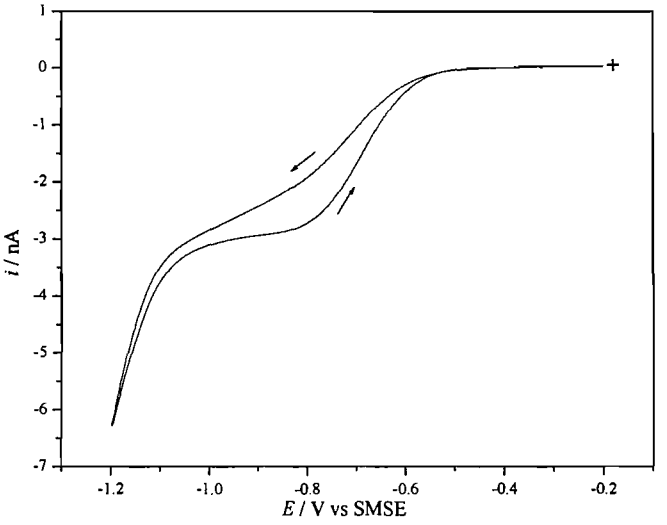

Figure 3.6 Oxygen reduction on a gold microdisc (a=5 μm) recorded in air saturated 5 mM NaCl at 25 °C; v=5 mV s^{-1}, '+' denotes the starting point, arrows show scan directions. Stable response after 5 cycles; before the slow scan the potential was cycled at 50 mV s^{-1} until stable response.

It can be seen that the limiting current on the positive scan is larger and that the plateau is better defined than on the cathodic scan. This feature is observed irrespectively of the chloride concentration. A possible explanation of this phenomenon may be found in the paper by Strbac and Adzic [179]. In their study on gold single crystal surfaces in alkaline media they observed an enhanced catalytic

activity towards oxygen reduction when the electrodes were covered with chemisorbed OH^-. It was suggested by these authors that adsorbed and partially discharged OH^- can promote four-electron oxygen reduction by either: facilitating the dissociative adsorption of oxygen (3.4)

$$O_2 \rightarrow 2O_{sa} \tag{3.4}$$

which is followed by reduction of oxygen atoms (subscript 'sa' denotes here strongly adsorbed species), or by lowering the energetic state of intermediate HO_2^-, allowing its reduction at relatively low overpotentials (mixed control region):

$$HO_{2,a}^- \rightarrow HO_{2,sa}^- \tag{3.5}$$

$$HO_{2,sa}^- + e^- \rightleftarrows O_{sa}^- + OH^- \tag{3.6}$$

$$O_{sa}^- + e^- + H_2O \rightarrow 2OH^- \tag{3.7}$$

In the case where the voltammogram is recorded in neutral solution, the OH^- is formed (and adsorbed) in the first two-electron ORR step by the deprotonation of water molecules, and also at potentials negative to the diffusion controlled region, where further reduction of peroxide species is possible. The ORR was shown to proceed with transfer of 2 to 4 electrons (also depending on potential) on several orientations of Au single crystals [179]. It is therefore reasonable to expect some of these effects also on polycrystalline gold. Indeed, later potential step experiments often point to n_{app} higher than 2 as could be expected solely from the first step of the series mechanism.

In Figure 3.7 a family of steady-state oxygen reduction voltammograms recorded in air saturated solutions of varying NaCl concentration is presented. Two trends can be clearly observed with increasing chloride concentration. In terms of the magnitude of the limiting current a constant decrease can be seen. At the same time the half-wave potential shifts to more cathodic values. The first feature is caused predominantly by the decreasing oxygen concentration in more concentrated salt solutions (c_{O2} drops from 258 μM in water to 222 μM in 500 mM NaCl). The current magnitude also decreases due to lower values of the oxygen diffusion coefficient.

This effect is however small as D_{O2} changes just slightly over the examined NaCl concentration range (from 2.26×10^{-5} cm^2 s^{-1} in water, to 2.16×10^{-5} cm^2 s^{-1} in 0.5 M NaCl, as calculated from (1.37)).

The shift in the position of the wave appears to be associated more directly with chloride concentration and its effect on the oxygen reduction on gold. The trend appears consistent over the whole range of NaCl concentration. No attempt was made to quantify the half-wave potential as a function of chloride concentration due to poorly defined plateaux and therefore inability to precisely measure $E_{1/2}$. On the basis of the literature reviewed in section 1.4.3 the potential shift can be interpreted as the effect of the competition for the adsorption sites on the electrode between Cl^- and oxygen. As the amount of adsorbed chloride depends both on its concentration and potential, the oxygen reduction appears to onset only when the surface coverage by chloride drops to a certain level. The effect of specifically adsorbed spectator species on the kinetics of the ORR was investigated by Blizanac *et al.* [180] in their study on gold single crystal RDE in Cl^- containing $HClO_4$. According to these authors, the rate determining step of the ORR is the first electron transfer with the formation of weakly chemisorbed O_2^- and free metal sites are necessary for it to occur. It was shown that the overall rate is controlled by the term $(1-\theta_{tot})$ where θ_{tot} is the total coverage by adsorbates, hence introduction of specifically adsorbing chloride causes a shift in the onset of oxygen reduction wave.

The dependence of the wave position on the amount of adsorbates has some vital implications for the sensor that would employ a gold cathode for oxygen detection. Significant differences in chloride concentration in the environment where the sensor is deployed (e.g. deep ocean or estuaries) would result in the shift of the oxygen reduction wave and appreciable changes in the measured limiting current. Thus the operating potentials would have to be adjusted or the sensor recalibrated depending on the measurement environment.

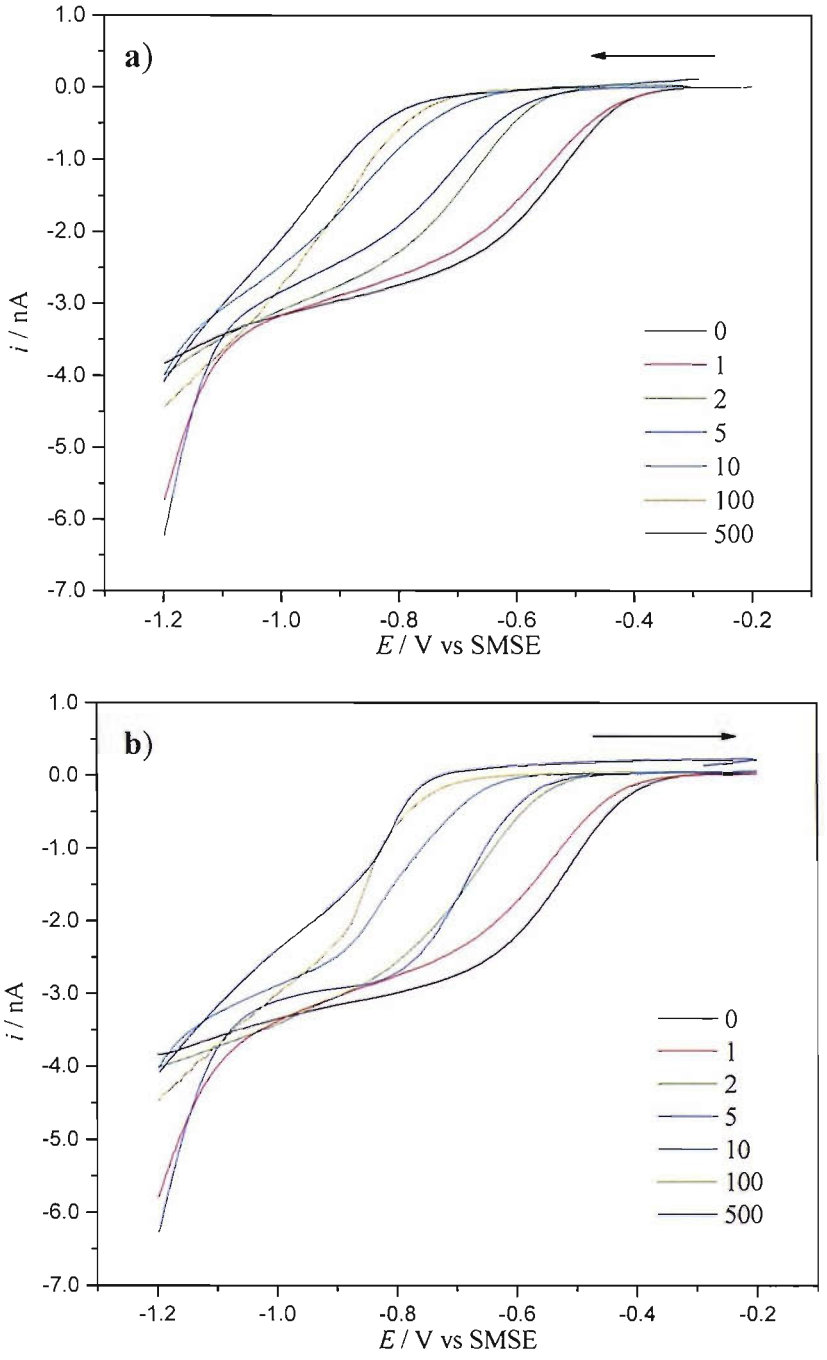

Figure 3.7 Steady state oxygen reduction waves at Au microdisc (a=5 μm) in air saturated NaCl solutions at 25 °C. NaCl concentration as indicated on the graphs. **a)** scans towards negative potentials, **b)** scans towards positive potentials; v=5 mV s^{-1}. In each case, before recording the steady state voltammogram the potential was cycled in the same range at 50 mV s^{-1} until stable response. The voltammograms shown are stable responses after 3-5 cycles.

3.2.3 Potential step experiments

On the basis of the voltammetric data presented earlier, the potential value of -1.0 V for the measuring step of the sensor operational waveform was chosen. Regardless of the NaCl concentration the potential falls within the oxygen reduction wave plateau. Attempts were made to find optimal duration and potential value for reconditioning of the electrode surface. This step will be later referred to as the cleaning step.

Long term stability tests utilising various potential waveforms were conducted in 0.5 M NaCl in order to assess them as potential operational waveforms for the sensor in seawater. In these tests the potential waveform was applied to the electrode continuously for the duration of experiment. The DO concentration was kept constant and the limiting current was monitored to identify any long term drift of the response. A general shape of the waveform is shown in Figure 3.8. It was adopted from the previous work [49, 158] and consists of only two steps. During the short cleaning step the potential is held more positive to recondition the electrode surface by e.g. stripping any metals that could be electroplated during the preceding long negative step. The measuring step potential is sufficiently negative to reduce oxygen at the diffusion limited rate. The step duration is a compromise: it is sufficiently long to achieve a steady state, but short enough to avoid the influence of natural convection on the observed current (observed as a steady increase of i_{lim}).

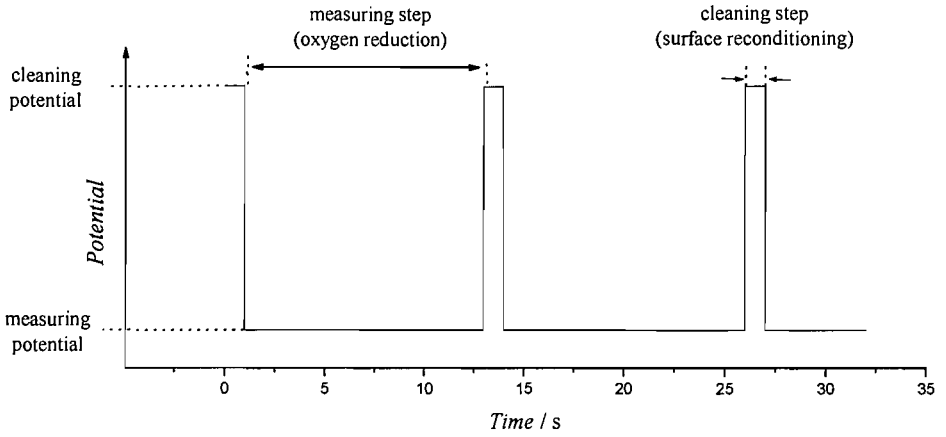

Figure 3.8 The general shape of the waveform for long term oxygen sensor operation.

The experimental arrangement for the stability tests is shown in Figure 3.9. The cell had a volume of approximately 250 ml and was equipped with gas purging ducts. Prior to the experiment the solution was purged for around 90 min. with air humidified in a separate vessel. Later, the constant oxygen concentration was assured by directing the gas stream above the solution surface. The assembly was thermostated at 25 °C and the measurement vessel was equipped with a plastic T-shaped cell and a solenoid pump (Model 120SPI, Bio-Chem Valve Inc., USA) to simulate measurement conditions as met when using the field sensor prototype (see chapter 7). The pump activation was synchronised with the beginning of the cleaning step in order to eliminate steady state current disruption due to forced convection and electrical noise resulting from pump work.

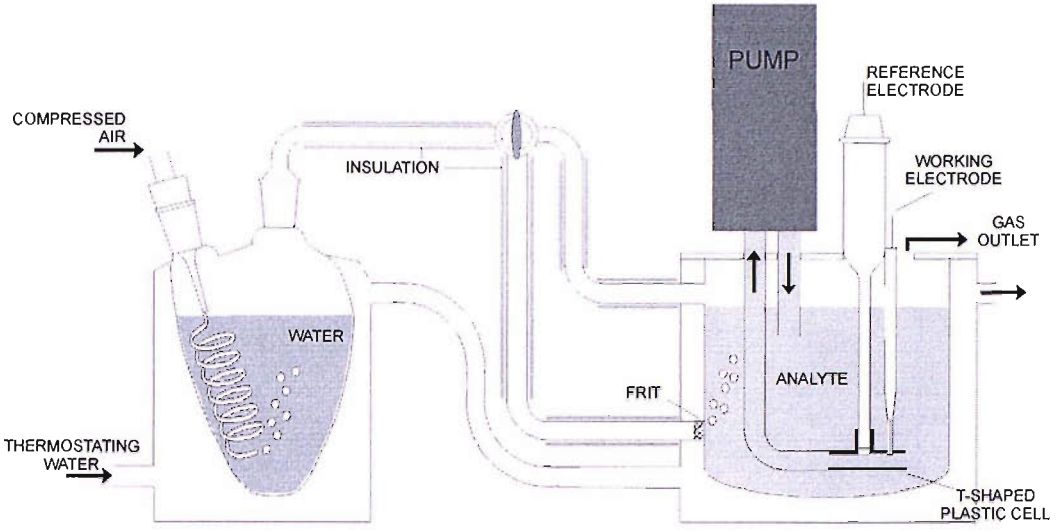

Figure 3.9 Experimental setup for the long term stability test of the microelectrode oxygen sensor.

Bearing in mind the chloride induced gold dissolution the potentials for the cleaning step, E_{cl} were chosen more negative than 0.1 V vs SMSE. The results of the stability experiments are shown in Figure 3.11 and include multiple tests of waveform with the cleaning potential set to 0.0 or -0.1 V. The duration of the cleaning step was 1 s (with a single exception of 0.4 s duration), while the measuring step was set to last 12 s. The waveform was applied to the working electrode continuously and a snapshot of the current response was recorded at regular intervals (Figure 3.10). The limiting currents were calculated as the mean values of the last 5 s of four consecutive oxygen reduction transients.

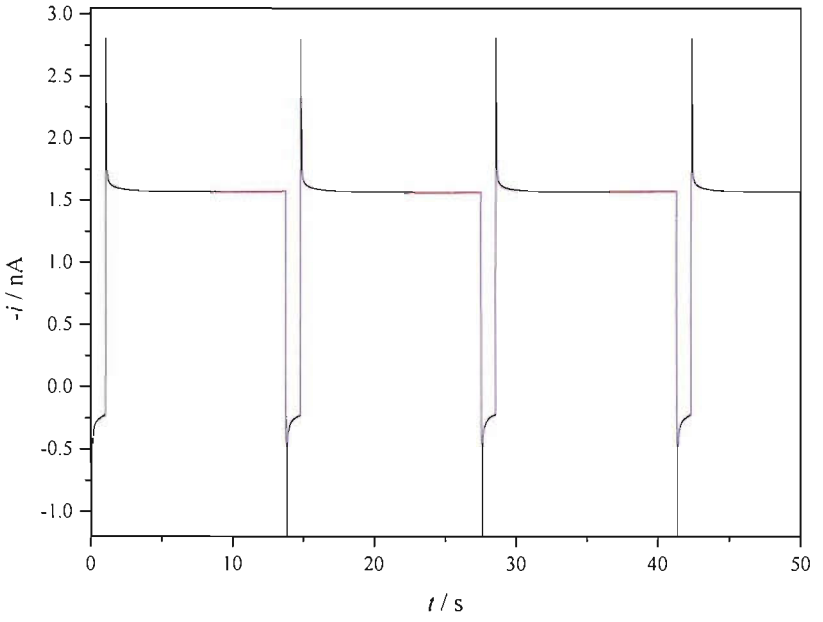

Figure 3.10 A snapshot of a gold microdisc (a=5 μm) response in air saturated 0.5 M NaCl. The potential waveform applied continuously to the working electrode consisted of the cleaning step at 0.0 V (1 s) and the measuring step at -1.0 V (12 s). Potentials vs SMSE. The fragments of the transients plotted in red were used to extract the limiting current value from the response snapshot.

As can be seen in Figure 3.11 the limiting current recorded over a period of several hours is highly unstable and irreproducible when the electrode is cleaned at 0.0 V. Setting the cleaning potential even lower to -0.1 V results in most cases in slow deactivation of the surface towards oxygen reduction. A smooth decrease in activity is observed regardless of the duration of the cleaning step. At the beginning of the experiments, when the electrode is freshly polished, the limiting current values correspond well with the expected two-electron reduction of oxygen. Later the oxygen reduction current decreases pointing to poisoning of the gold surface.

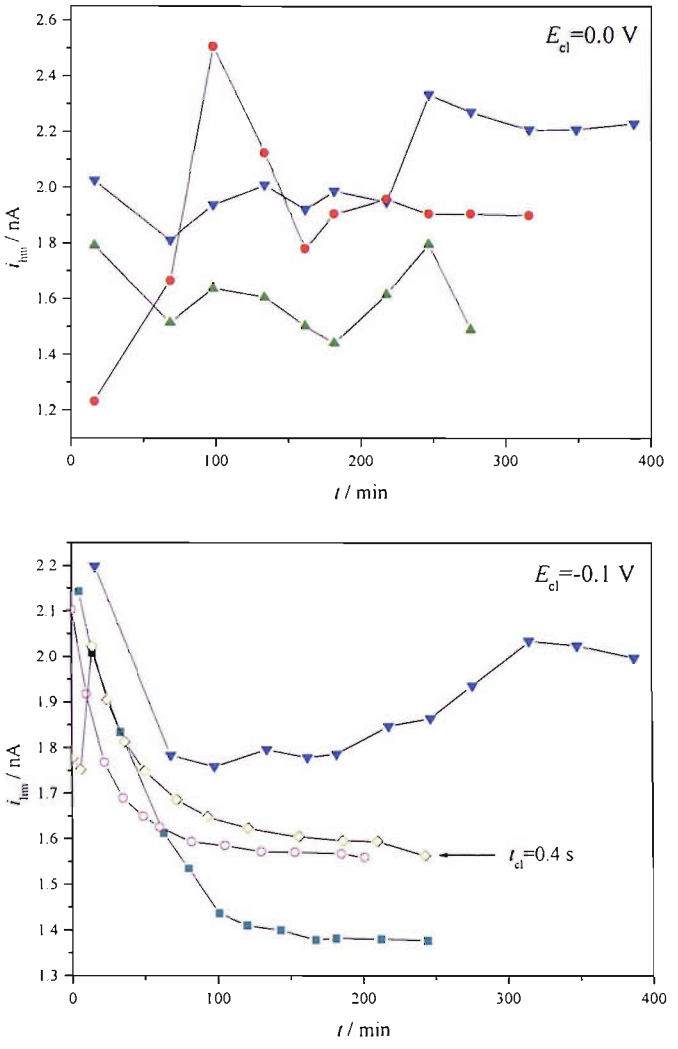

Figure 3.11 Long term performance of gold microelectrodes (a=5 μm) in air saturated 0.5 M NaCl at 25 °C. The limiting currents, i_{lim} were calculated as the mean value of the last 5 s of four consecutive oxygen reduction transients. The waveform applied to the electrode consisted of measuring step at -1.0 V (12 s) and a cleaning step at potential E_{cl} as indicated on the graph and duration of 1 s except single experiment with shorter cleaning step of 0.4 s (indicated by an arrow on the graph). Traces of different colours are repeats of the same experiment.

Since the pump action was synchronised with the cleaning step, part of the cleaning procedure was taking place in the environment containing some of the oxygen reduction step products. To eliminate the possible contribution of the

reaction products to the deactivation of the electrode, an alternative pump/potential synchronisation was tested. The solution in the vicinity of the electrode was fully replaced at the end of each measuring step, before the potential was switched to the cleaning value. Thus, each time the electrode was cleaned in the fresh portion of solution, which did not contain the products of the ORR. No improvement in the long term response was achieved and a slow decay of the measured limiting current was still observed.

Optimal parameters that would result in a stable response of unshielded gold electrode in seawater were not found. A slow decay of the oxygen reduction limiting current values was commonly observed over extended periods of continuous sensor operation.

3.3 Platinum

A similar approach to that taken for assessing gold was adopted when investigating platinum as a potential material for the oxygen reduction cathode. Platinum electrode surface processes and oxygen reduction on Pt, particularly in the presence of chloride, were characterised by cyclic voltammetry. Potential step experiments were conducted to find the optimal conditions for the continuous operation of a Pt microdisc based oxygen sensor.

3.3.1 Voltammetry in sodium chloride solutions

Cyclic voltammograms on a Pt microdisc in deoxygenated solutions with varying sodium chloride concentrations are presented in Figure 3.12. One can distinguish features typical of platinum voltammetry: an oxide formation region between -0.1 and 0.8 V on the positive scan, the corresponding oxide stripping peak at around -0.5 V and hydrogen adsorption and desorption peaks at more negative potentials. Unlike in typical adsorbed species voltammetry, the hydrogen adsorption and desorption peaks do not have the same position on the potential axis. This is due to the fact, that these processes are pH dependent. Since the measurements are performed in an unbuffered solution, the hydrogen adsorption and desorption reactions take place in the local environment where pH is a result of the preceding processes (e.g. oxides reduction) [181].

Several features of the voltammogram change as sodium chloride is introduced into the solution, and when its concentration is gradually increased. The early part (around 0.0 V) of the oxide formation region is significantly suppressed, while an increased charge is observed at more positive potentials (0.3 to 0.6 V). Further positive a new signal appears due to chloride oxidation. As the concentration of chloride grows the oxide stripping peak decreases in height but at the same time develops a broad shoulder stretching up to 0.4 V for the highest chloride concentration. Finally, the shape and position of hydrogen adsorption (-0.7 to -1.1 V

on cathodic scan) and desorption (-0.9 to -0.4 V on the anodic scan) peaks are altered. Also, one can observe a systematic increase in the double layer charge.

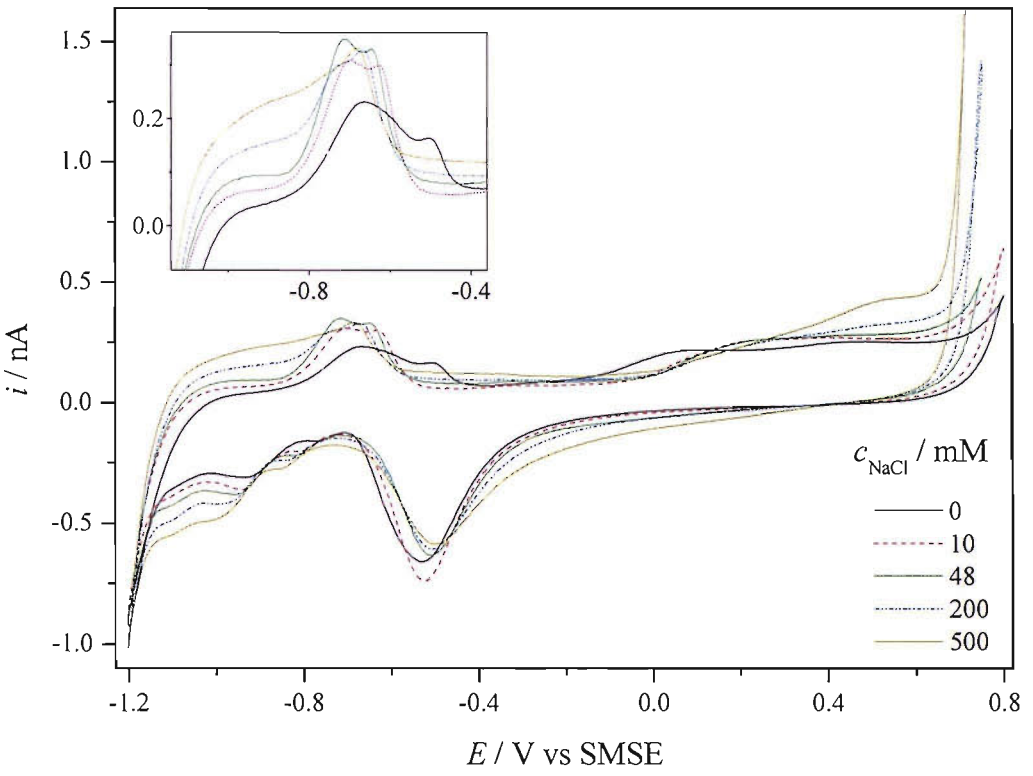

Figure 3.12 Cyclic voltammograms on Pt microdisc (a=5 μm) in deoxygenated NaCl solutions (concentrations as indicated on the graph); v=200 mV s^{-1}, T=25 °C. The inset shows the magnification of the hydrogen desorption peaks.

The observed changes can be explained in terms of specific adsorption of chloride ions on the platinum surface. Similarly to earlier investigations in acidic solutions containing Cl^- [182-184], the hydrogen adsorption and desorption peaks shift towards negative potentials. Higher overpotentials are needed for hydrogen ions to adsorb when the chloride concentration increases, as at a fixed potential the Cl^- coverage increases with its increasing concentration [110]. For the same reason, Cl^- competing for the adsorption sites with hydrogen will facilitate its desorption and

make the peaks potentials less positive. Also the separation of the desorption peaks changes with Cl^- concentration (see inset in Figure 3.12). The peak at -0.5 V corresponding to strongly bonded hydrogen appears to be more sensitive to Cl^- and its negative shift is greater than the shift of the peak corresponding to weakly bonded hydrogen (-0.65 V in water). As a result the peaks overlap increases correspondingly with Cl^- concentration. Eventually, in 0.5 M NaCl it is very hard to distinguish two separate peaks. This behaviour shows that the difference between strongly and weakly adsorbed hydrogen binding energies is decreasing, which in turn suggests a higher degree of homogeneity of the sites on the electrode surface. Interestingly, the effect is insignificant during hydrogen adsorption, where the peak potentials are ~200 mV more negative than corresponding desorption signals. As shown by other authors [110, 185] the chloride coverage at such negative potentials is much smaller and the hydrogen behaviour does not differ markedly from a clean platinum surface.

The site blocking mechanism also causes the suppression of the oxide formation on platinum. The currents are lowered with increasing Cl^- concentration in the early part of the oxide region, just before they reach the same value at ~0.3 V. Similar effect was observed by other researchers in 0.1 M H_2SO_4 with various amounts of chloride [186]. Later, with the use of electrochemical quartz-crystal nanobalance (EQCN) the isopotential point was identified as corresponding to half coverage of the surface by oxide, where each oxygen atom is coordinated by two platinum atoms [187]. Beyond this potential value oxygen atoms undergo place exchange and more water molecules are discharged on the surface to form platinum oxide. At the same time additional current is observed from the discharge of adsorbed Cl^-. Eventually, simultaneously with formation of thicker oxide layers, chloride ions are oxidised to chlorine at 0.7 V.

For further potential step experiments the potentials in the range 0.0 to 0.5 V were chosen for the cleaning step, i.e. the potentials between the onset of oxide formation and chloride oxidation.

3.3.2 Oxygen reduction voltammetry

The cathodic reduction of oxygen in neutral sodium chloride solutions was investigated by cyclic voltammetry and the influence of a range of experimental parameters was assessed. A typical voltammetric response is shown in Figure 3.13. While a well defined diffusion limited current is easily obtained, one can observe that unlike for purely diffusion controlled reactions the forward and back scans differ and cross over in several places. The number of cross-overs and the hysteresis between the scans reflect the sensitivity of oxygen reduction to the surface state of the platinum electrode. This sensitivity results from the initial step of oxygen adsorption and from the presence of adsorbed reaction intermediates [188, 189].

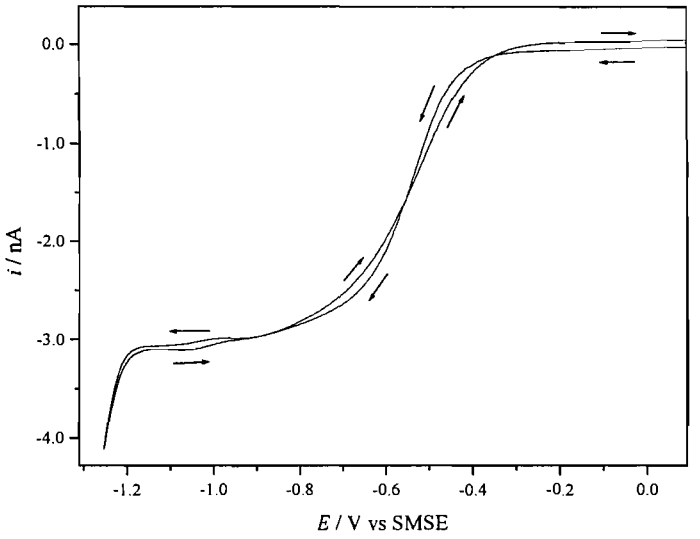

Figure 3.13 Oxygen reduction at polished Pt microdisc (a=5 μm) in air saturated 0.5 M NaCl, T=25 °C. v=20 mV s^{-1}, the potential was ramped from 0.0 V towards positive potentials with limits +0.7 and -1.25 V. Stable response obtained after 3 cycles. Before recording of the voltammogram the potential was cycled in the same range at 200 mV s^{-1} until stable response.

Three major factors contribute to the observed voltammetric behaviour: a) a clean platinum surface is a better catalyst for oxygen reduction than oxide covered platinum [85, 87], b) the contribution of the platinum oxide species reduction to the observed current (in the examined solution the oxide stripping peak is located at around -0.6 V and coincides with the oxygen reduction wave), c) the presence of adsorbing spectator species, which can alter the oxygen reduction wave position and magnitude. Since both diffusion and surface processes are involved, it is to be expected that the recorded voltammograms will be sensitive to parameters like scan rate, potential limits, surface roughness and the total adsorbates concentration.

The effect of the positive potential limit is shown in Figure 3.14. In each case a stable response obtained after 5 – 10 full cycles is shown. The hysteresis between the negative and the positive scan decreases as the positive limit is lowered, i.e. as the amount of oxide on the electrode surface decreases. For clarity only curves for three values of the positive limit are shown, however the effect is consistent over the whole range tested. The magnitude of the limiting current also changes considerably on the negative scan, while it is far more reproducible on the positive direction. The distortion of the oxygen reduction plateaux and the amount of hysteresis are due to surface processes, thus their contribution to the overall response is significantly diminished when low scan rates are used (compare Figure 3.13 and solid curve in Figure 3.14).

In conclusion, for quantitative analysis of voltammetric curves the responses obtained on clean (oxide free) platinum surfaces should be used. The scans towards more positive potentials are more reproducible as all the oxide is reduced when the potential reaches the negative limit.

The role of the chloride ion concentration was also investigated. A family of voltammograms in air saturated solution containing between 10 and 500 mM NaCl is shown in Figure 3.15. The decrease in the limiting current reflects the lower solubility of oxygen as the salt concentration increases and to lesser extent the effect of ionic strength on D_{O2}. A negative shift of the reduction wave is observed, however it is not very significant when compared to the effect of chloride on the ORR on gold as presented earlier. On Pt, the $E_{1/2}$ difference between the waves recorded in solutions of the highest and lowest Cl^- concentration does not exceed 50 mV, while

with Au microelectrode the shift was up to 300 mV. The shift of 50 mV is in good agreement with work of Kaska *et al.* [107] who observed 30-40 mV difference in $E_{1/2}$ between 0.5 M $NaClO_4$ and 0.5 M NaCl borate buffered solutions. A small shift has an important implication for the sensor. Since the wave position shows little dependence on Cl^- concentration the measuring potential does not have to be adjusted for salinity as it corresponds to the reduction plateau irrespective of the Cl^- concentration in the analyte.

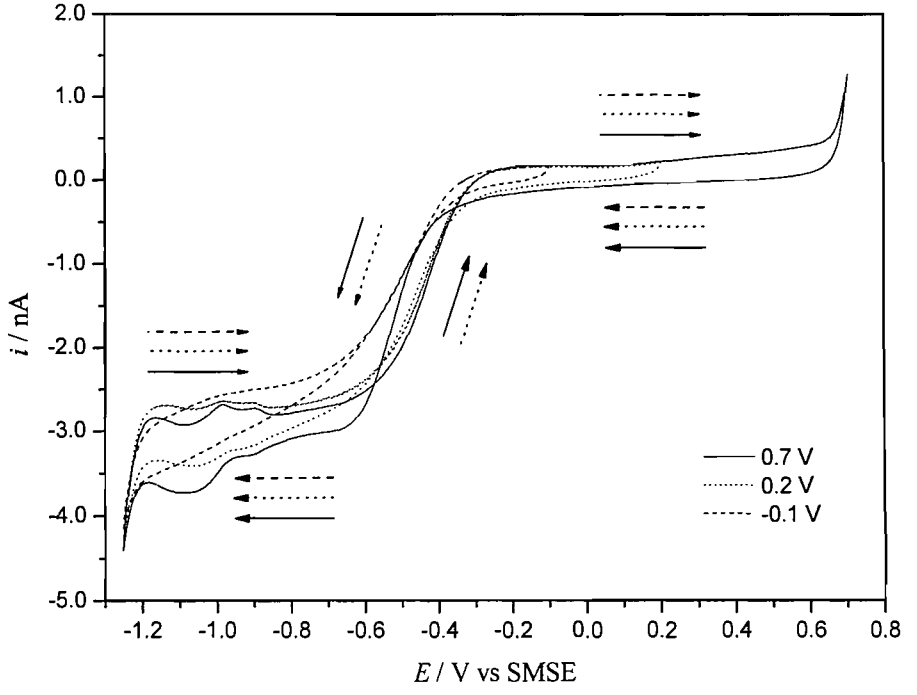

Figure 3.14 Cyclic voltammograms on a polished Pt microdisc (a=5 μm) in air saturated 0.5 M NaCl solution for various positive sweep limits (as indicated on the graph), v=200 mV s^{-1}, T=25 °C. Stable responses obtained after up to ~5 cycles.

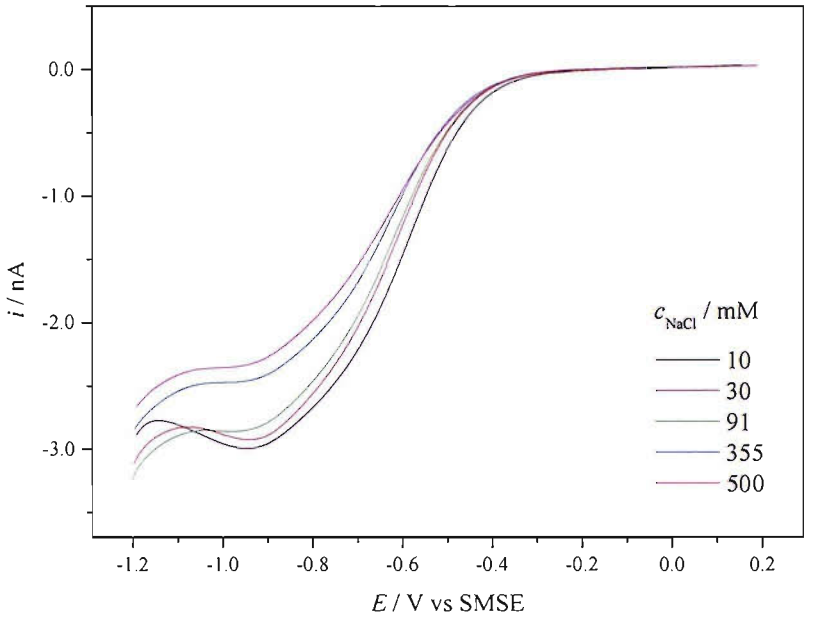

Figure 3.15 Oxygen reduction voltammograms in on Pt microdisc (a=5 μm) air saturated NaCl solutions (concentrations as indicated on the graph) at 25 °C, v= 10 mV s^{-1}, scans in positive direction. The electrode was polished in between the measurements and cycled at 100 mV s^{-1} in the same range until stable prior to recording slow scan voltammograms. The curves shown are stable responses obtained after 3-4 cycles.

The absolute wave position has to be considered only for a given electrode size as it is found to depend also on the mass transfer coefficient. When the voltammetric response is normalised by the electrode radius a shift towards more negative potentials is observed when smaller electrodes are used. Voltammograms where the current is divided by the electrode radius are shown in Figure 3.16 for microdisc radii ranging from 3 to 24.5 μm. In purely diffusion controlled reversible system the curves should overlap. In case of oxygen reduction not only the half wave potentials differ but also the magnitude of the limiting current varies depending on the electrode radius.

The changes in wave position are ascribed to the increasing irreversibility of oxygen reduction and were observed before by other researchers [102, 120]. Lower values of the limiting current suggest that n_{app} decreases when the mass transfer

coefficient increases on smaller electrodes. This behaviour is readily explained by considering the series pathway of the ORR with peroxide intermediate. Under enhanced mass transport some of the intermediates can diffuse away from the surface before further reduction to water, therefore lowering the observed net number of transferred electrons. n_{app} calculated with the equation for the limiting current at a microdisc electrode (1.5) using currents read at -1.05 V are 2.2, 2.6, 3.1, and 3.4 for the electrode radii 3.0, 4.7, 12.4 and 24.5 respectively. This issue will be treated in a more quantitative way in next chapter, where n_{app} is determined with better precision in calibration experiments.

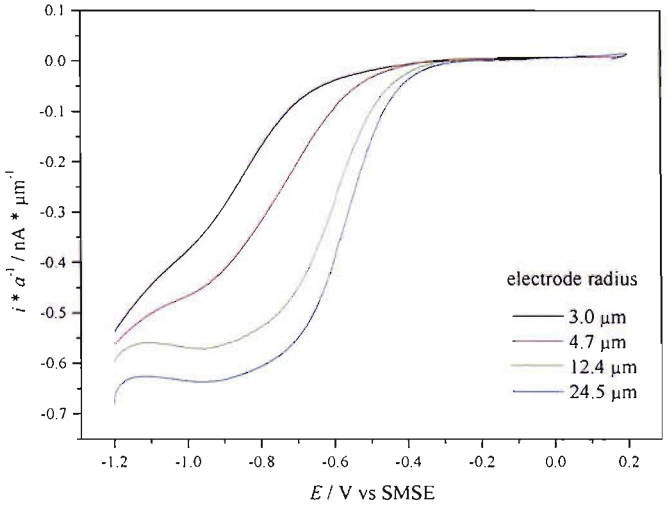

Figure 3.16 Oxygen reduction on various sizes of Pt microdiscs in air saturated 0.5 M NaCl at 25 °C. The current is normalised by the electrode radius. v=10 mV s^{-1}, scans in the positive direction.

3.3.3 Potential step experiments

An attempt was made to find the optimal cleaning potential for the continuous operation of the sensor. A series of long term experiments (usually 24 h) was conducted. In each case a potential waveform as depicted earlier (Figure 3.8) was used. It consisted of the measuring step (15 s, -1.1 V) and the cleaning step (1 s, variable potential) repeated in cyclic manner. The measuring potential was chosen well within the oxygen reduction plateau, while the cleaning step potentials were set in the region of the onset of platinum oxide formation (0.1 to 0.5 V). The electrodes operated continuously and a snapshot of the current response was recorded at regular intervals. The results are shown in Figure 3.17.

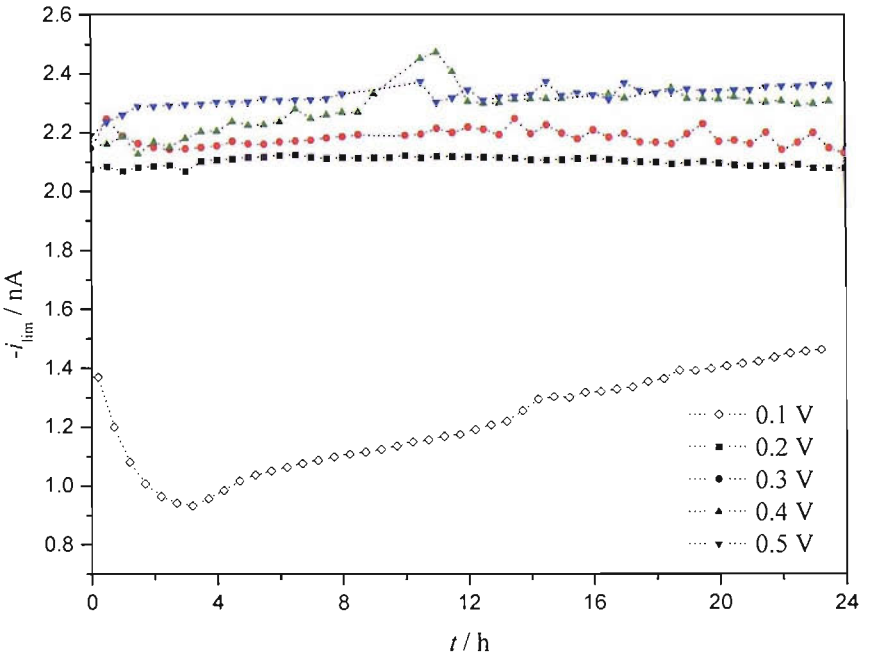

Figure 3.17 24 hours stability experiments in air saturated 0.5 M NaCl at 25 °C and ambient pressure. The working electrode (Pt microdisc, a=5 μm) was constantly subjected to a potential waveform consisting of a measuring step at -1.1 V (15 s) and a 1 s cleaning step (potentials indicated on the graph). The limiting currents, i_{lim} were calculated as the mean value of last 5 s of four consecutive oxygen reduction transients.

For the three highest cleaning potentials (0.3 to 0.5 V) one can observe appreciable instability over the duration of the experiment. Moreover the responses obtained when using 0.4 and 0.5 V cleaning steps show slow positive drift over 24 h of continuous operation. When the electrode is cleaned at 0.1 V, its activity decreases rapidly (the limiting current drops 25 % within the first 15 min of operation) and slowly recovers in later stages. When higher cleaning potentials are used, the plots show a slight increase in the limiting current. It appears analogous to the earlier voltammetric data, where the limiting current magnitude depended on the positive scan limit (see Figure 3.14 in section 3.3.2). The best results were obtained for the waveform with 0.2 V cleaning potential. The stability is excellent – the standard deviation of the limiting current over 24 h is 0.7% (corresponding to 1.6 μM in DO concentration at air saturation, 221 μM) with mean difference of only 4×10^{-5}% (8×10^{-5} μM). The maximum deviation does not exceed 1.5% (3.2 μM in DO). This 24 h trace is shown in more detail in Figure 3.18 together with the characterisation of the changes to the electrode surface that occurred during the test.

All the electrodes were characterised by cyclic voltammetry in 1 M H_2SO_4 before and after each stability experiment to evaluate the influence of the cleaning step on the electrode surface state. The roughness factor was calculated using the real surface area estimated from the charge under hydrogen monolayer adsorption peaks using a conversion constant of 210 μC cm^{-2} [190]. Table 3.2 summarises the calculations together with the key parameters of the stability experiments.

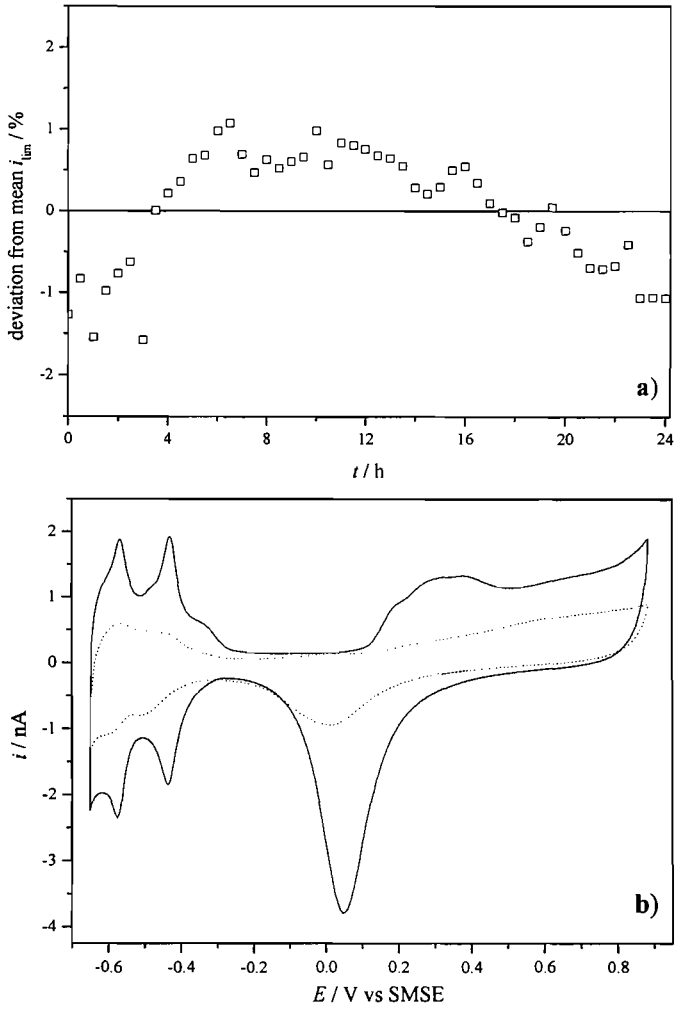

Figure 3.18 a) Limiting current variations during a 24 h stability test in air saturated 0.5 M NaCl. A waveform consisting of two steps: -1.1 V (15 s) and 0.2 V (1 s) was applied continuously to the working electrode (Pt microdisc, a=5 μm), **b)** cyclic voltammetry in deoxygenated 1 M H_2SO_4 before (dotted line) and after (solid line) the stability experiment; v=200 mV s^{-1}.

Table 3.2 Comparison of the electrode roughness changes due to extended operation using various cleaning potentials.

Measuring potential (15 s) / V vs. SMSE	Cleaning potential (1 s) / V vs. SMSE	Experiment duration / h	Roughness factor before the experiment*	Roughness factor after the experiment	Roughness factor gain
-1.1	0.1	24	22.9	28.9	1.3
-1.1	0.2	24	3.7	11.7	3.2
-1.1	0.3	72	8.6	52.9	6.1
-1.1	0.4	24	1.9	48.4	25.5
-1.1	0.5	24	0.9	27.2	30.2

* In some experiments the electrodes were not polished beforehand and their history differed (i.e. some where already roughened in earlier experiments).

As can be seen in the table the use of cleaning potentials up to 0.3 V does not cause a significant increase in roughness of the electrode surface. When the electrode is cleaned at potentials lying further into oxide formation region (where the place exchange mechanism is in operation and the oxide coverage is higher [187], see section 3.3.1) the roughness gain due to long term continuous operation is noticeably higher. A significant increase in the electrode real surface area may to a certain extent alter the catalytic properties of Pt surface towards oxygen reduction. This was shown earlier with high surface area mesoporous platinum microelectrodes [191], where the oxygen reduction limiting current was shown to be larger compared to that with polished Pt microdisc. The roughness factors obtained here are much lower than those of the mesoporous films, however some changes with respect to smooth platinum can be observed. In Figure 3.19 oxygen reduction voltammetric waves on smooth and roughened platinum microdiscs are compared. The electrode was roughened as a result of 24 h stability test with cleaning at 0.5 V (see: Figure 3.17, blue plot). A clear indication of increased real surface area comes from the voltammogram in sulphuric acid (Figure 3.19, inset). Surface features are also pronounced on the voltammogram in aerated 0.5 M NaCl. At -0.6 V on the negative scan we can observe the oxide stripping peak interfering with the oxygen reduction wave and further negative the oxygen reduction plateau is distorted by the hydrogen

adsorption and desorption signals, which are barely distinguishable on smooth platinum. More importantly the oxygen reduction wave is shifted towards positive potentials and the limiting current is slightly increased in agreement with the potential step experiment (Figure 3.17).

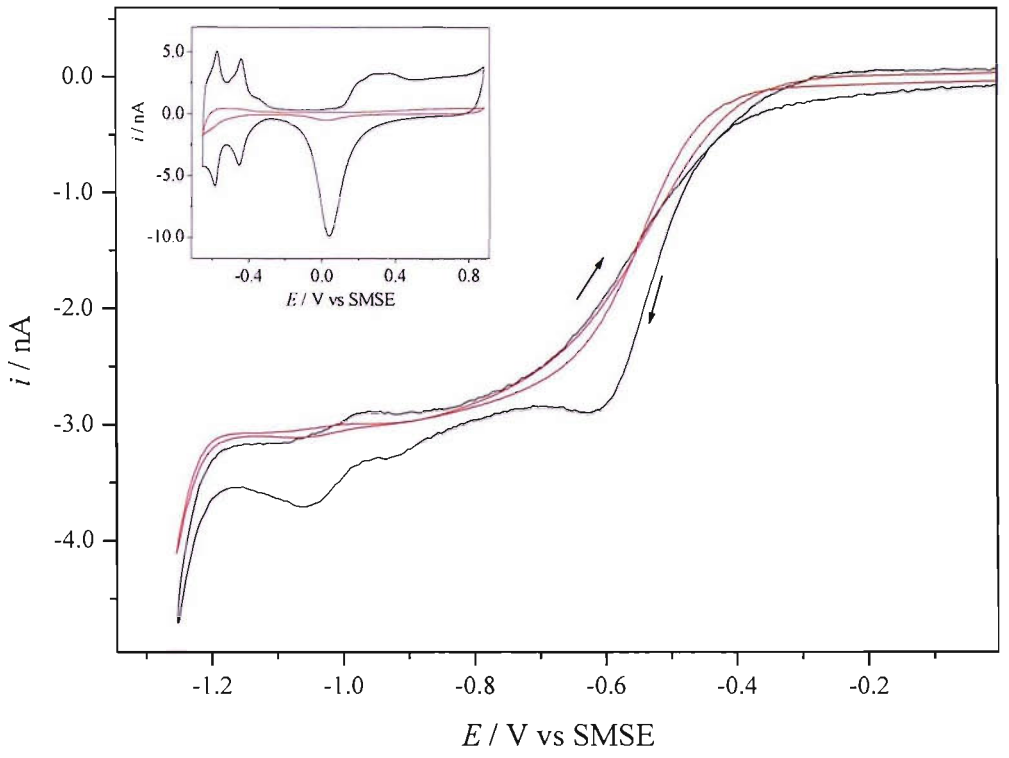

Figure 3.19 Oxygen reduction voltammograms on Pt microdisc (a=5 μm) at v=20 mV s^{-1} in air saturated 0.5 M NaCl before (red line) and after (black line) 24 h stability experiment (where the potential was continuously switched between -1.1 V, 15 s and 0.5 V, 1 s). The inset shows the corresponding voltammograms on smooth and roughened Pt in deoxygenated 1 M H_2SO_4, v=200 mV s^{-1}.

It is important that the limiting currents measured after applying a potential step agree quantitatively with the voltammetric response. The comparison of cyclic voltammograms and limiting currents obtained in transient experiments (sampled voltammograms) is presented in Figure 3.20. In the potential step approach the current was calculated as the mean value of the last 5 s of the transient (12 s in

duration). The agreement in the plateau region is very good, therefore validating the method of the limiting current extraction.

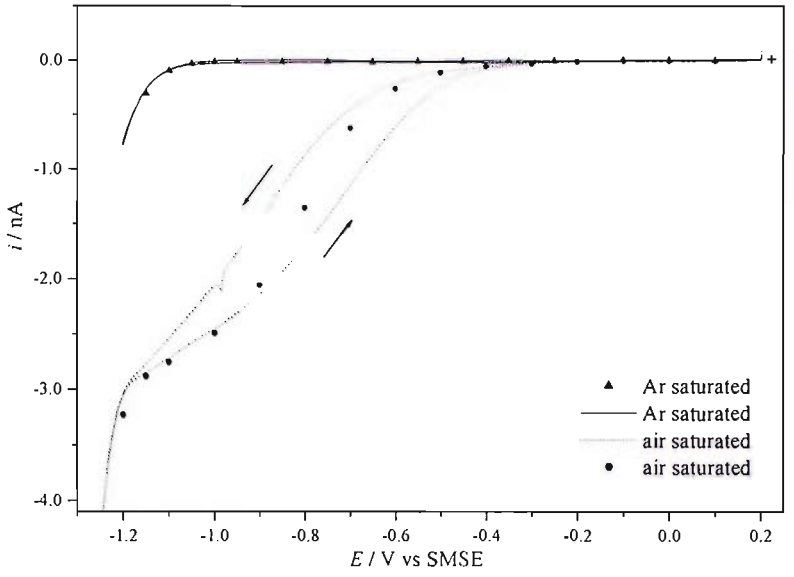

Figure 3.20 Comparison of cyclic and sampled voltammetry on Pt microdisc (a=5 μm) in 0.5 M NaCl at 25 °C. The potential sweep experiment (lines) was recorded at v=10 mV s^{-1}; in the potential step experiment (points) the potential was stepped from +0.2 V (1 s) to the target potential (12 s) and the current represents the mean value of last the 5 s of the current transient.

3.4 Nanostructured platinum

As a comparison to polished electrodes, oxygen reduction on nanostructured microelectrodes was investigated. The preparation of nanostructured metallic films produces very high real surface area electrodes while retaining mass transport properties intrinsic to microelectrodes. Since ORR is sensitive to adsorption conditions, the enhancement of the electroactive surface area is expected to have an influence on ORR. An attempt is made to assess this influence on the kinetics and the limiting current for oxygen reduction on nanostructured microelectrodes.

3.4.1 Nanostructured film preparation and characterisation

Nanostructured platinum films were obtained by deposition from lyotropic liquid crystalline phase. The principles of the true liquid crystal templating method and properties of the obtained films can be found in references [192-194]. The plating mixture composition shown in Table 3.3 was used. It consisted of the non-ionic surfactant (octaethyleneglycol monohexadecyl ether, $C_{16}EO_8$), water and hexachloroplatinic acid (H_2PtCl_6, HCPA). With this particular mass balance of the constituents, at room temperature the surfactant molecules aggregate as rods (hexagonal phase, H_1). The surfactant aggregates are present on the electrode in hexagonal arrangement and the electrodeposition of metal from this mixture yields metallic films with similarly arranged pores. The electrodeposited Pt films are therefore referred to as H_1-ePt to indicate the liquid crystal phase they were deposited from.

Table 3.3 Composition of the plating mixture used for the preparation of the nanostructured Pt films.

Chemical	Manufacturer	Weight /g	Weight %
H_2PtCl_6	Aldrich	0.291	29
$C_{16}EO_8$	Nikko Chemicals	0.421	42
H_2O		0.294	29

The plating mixture constituents were mixed using a glass rod until the mixture was uniform and placed in the drying oven set to 40 °C for 10 min. The procedure was repeated to ensure homogeneity. Before each deposition the platinum microdisc electrodes were polished with 0.3 μm alumina paste and cycled in deoxygenated 1 M sulphuric acid until a stable response was obtained. The electrodes were disconnected in the double layer region of the positive scan of the voltammogram, rinsed with water, dried and transferred into the plating solution. The deposition was carried out at 25 °C by stepping the potential from +0.6 to -0.1 V (vs saturated calomel electrode, SCE) and the corresponding deposition current transient are shown in Figure 3.21. Following the deposition the electrodes were placed in stirred water to remove the surfactant used in the plating procedure.

Nanostructured films were characterised by voltammetry in 1 M H_2SO_4 and Scanning Electron Microscopy (SEM) (Philips XL30 ESEM operating in wet mode). The acid voltammograms are shown in Figure 3.22 and served to determine the roughness factor of the obtained electrodes. The real surface area of the film was estimated from hydrogen desorption peaks as described earlier for polished and roughened Pt electrodes (see section 3.3.3). Figure 3.23 shows examples of the SEM photographs of nanostructured microdiscs. From the photographs the film radius was measured as well as the film thickness (see Appendix 9.1 for details). The films appear uniform, except at smaller microdiscs where thicker deposits are observed on the edges due to higher current densities caused by increased contribution of radial diffusion [13]. Growth of the film also results in the slight increase in the microdisc radius. The key features of the obtained nanostructured microelectrodes are summarised in Table 3.4.

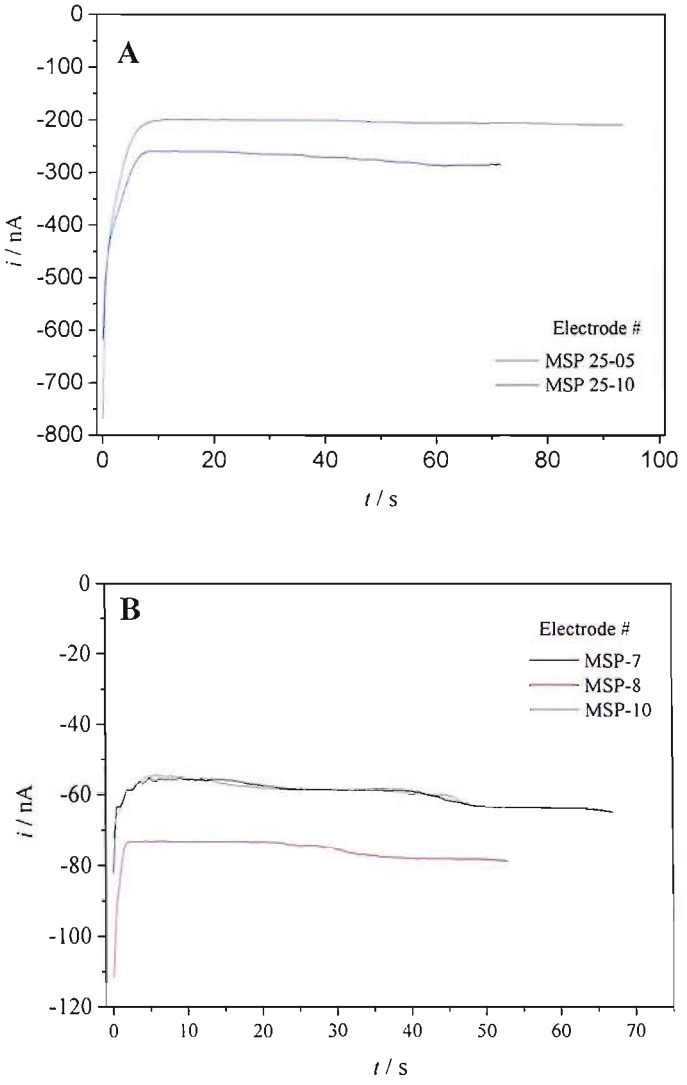

Figure 3.21 Nanostructured Pt film deposition transients for 12.5 μm (**A**) and 5 μm radius Pt microdiscs (**B**). Plating mixture composition as specified in Table 3.3, the responses were recorded after a potential step from +0.6 to -0.1 V vs SCE.

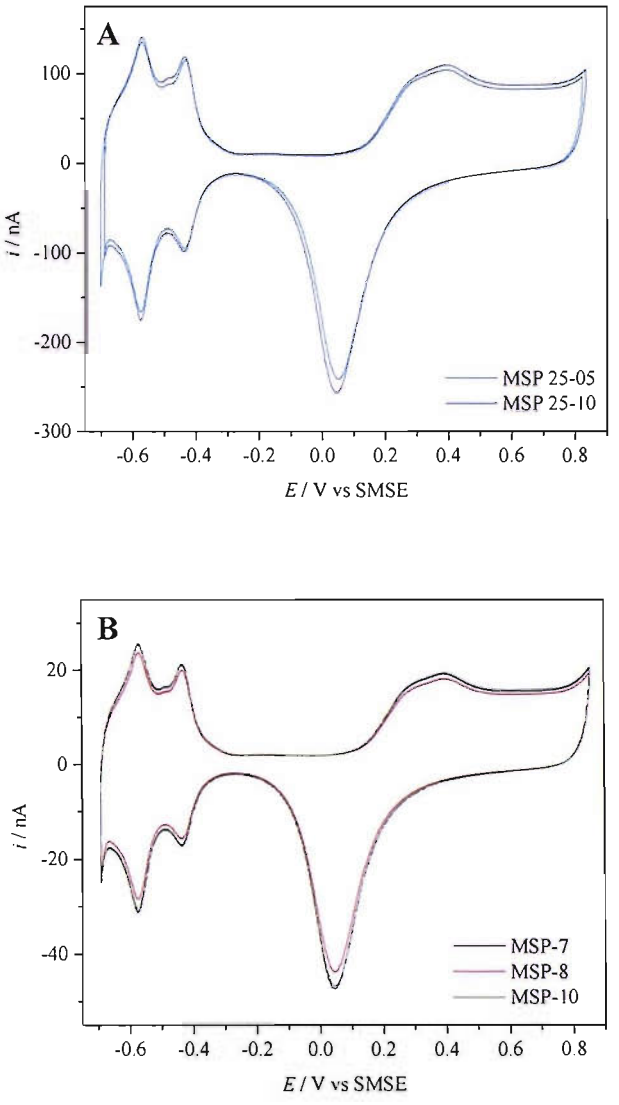

Figure 3.22 Cyclic voltammograms in deoxygenated 1 M H_2SO_4 at nanostructured microdisc electrodes: A – 12.5 μm, B – 5 μm radius. v=200 mV s^{-1}.

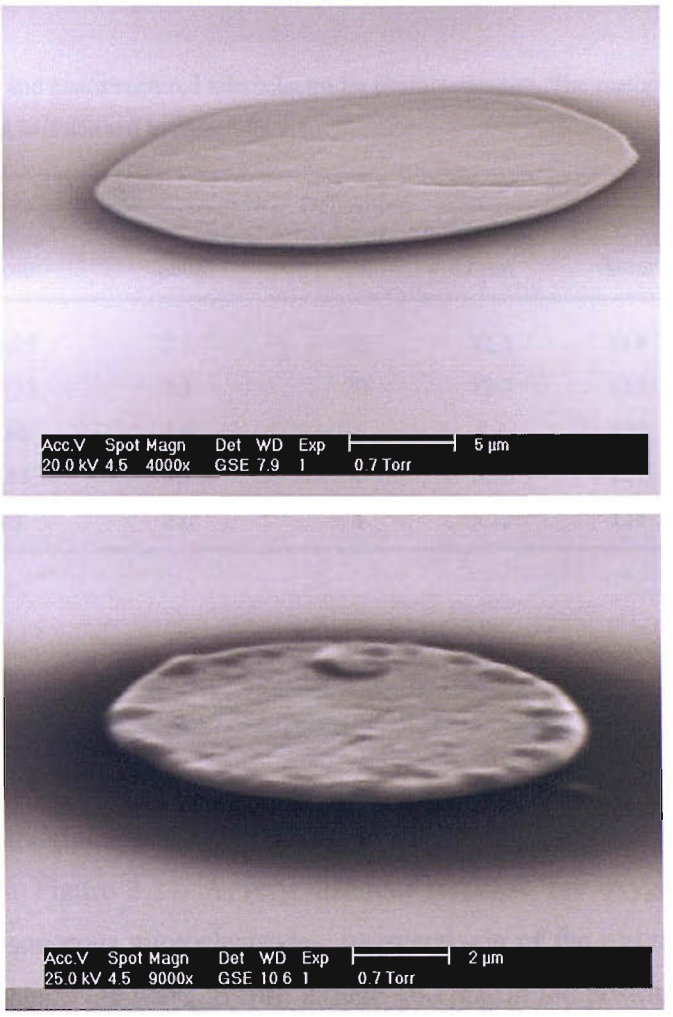

Figure 3.23 SEM images of nanostructured platinum films: electrode MSP 25-05, a=12.5 µm, deposition charge 20 µC (top), electrode MSP-7, a=5 µm, deposition charge 4 µC (bottom).

Table 3.4 Polished and nanostructured microelectrodes characterisation. The method of determination of the film thickness is described in Appendix 9.1.

Electrode #	Polished		Deposition charge / μC	Nanostructured film		
	Radius / μm	Roughness factor		Radius / μm	Roughness factor	Film thickness / nm
MSP 25-05	12.25	2.1	20	12.8	114	380
MSP 25-10	12.35	2.3	20	12.7	123	410
MSP-7	4.65	1.6	4	5.4	127	340
MSP-8	4.65	2.1	4	5.35	121	410
MSP-10	4.7	2.6	4	5.35	124	390

3.4.2 ORR at mesoporous Pt electrodes in 0.5 M NaCl

Voltammograms obtained on nanostructured and polished microelectrodes are compared in Figure 3.24. A very different response for oxygen reduction is observed on mesoporous microelectrodes. Irrespectively of the electrode radius, the deposited film causes the wave to shift around 200 mV in the positive direction and the magnitude of the limiting current to increase significantly. The parameters obtained from the voltammograms recorded in air saturated 0.5 M NaCl (Figure 3.24) are shown in Table 3.5.

The very high surface area of the mesoporous electrode improves greatly the catalytic properties of platinum towards ORR. n_{app} at 12.5 μm radius electrode increases from a typical value of *ca.* 3 to 4. Similarly larger n_{app} values were also observed by Birkin *et al.* [191] in phosphate buffer (pH=7): 3.82 to 4.4 depending on the film thickness. Jiang and Kucernak [195] used 40-50 μm thick mechanically deposited H_1-Pt and found n_{app} of 4.4 in 0.5 M H_2SO_4. It is difficult to judge solely on the basis of voltammetric data whether the increase is caused by improved peroxide species reduction, or by the promotion of the direct four-electron reduction of oxygen at nanostructured platinum. The results with smaller electrodes suggest

that the series mechanism is in operation. With the 5 μm radius microdisc n_{app} values far below 4 are observed, presumably due to the removal of reaction intermediates under enhanced mass transport conditions.

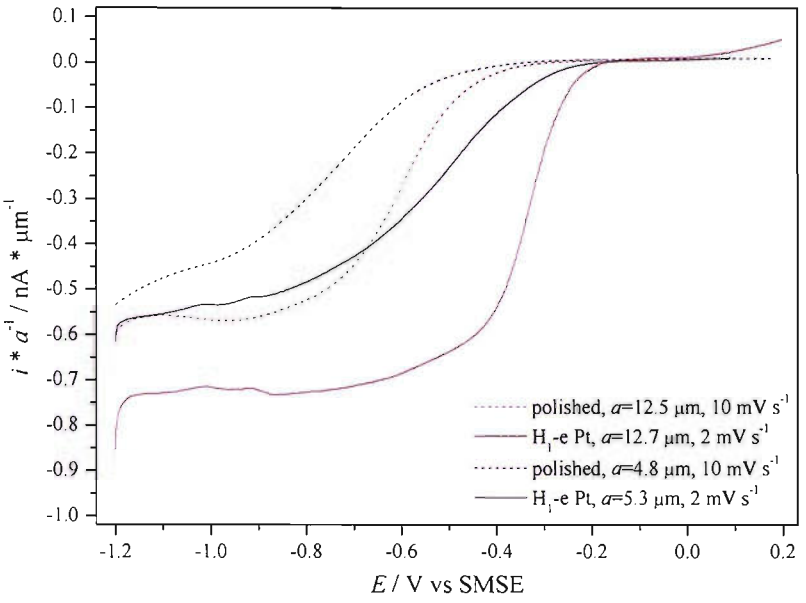

Figure 3.24 Oxygen reduction voltammograms in air saturated 0.5 M NaCl on polished (dotted lines) and nanostructured (solid lines) Pt microdisc electrodes. The nominal electrode radii used were a=5 μm (black curves) and a=12.5 μm (red curves). Scan rates are indicated on the graph, only the positive scans of the cyclic voltammograms are plotted. Before recording the voltammogram the electrode surface was electrochemically preconditioned by holding the potential at -1.25 V for 4 s, followed by 1 s at +0.2 V.

Table 3.5 Parameters obtained from voltammograms on polished and mesoporous microdisc electrodes in air saturated 0.5 M NaCl. The limiting currents were sampled at -1.05 V. n_{app} estimated using D_{O2}=2.16 cm^2 s^{-1} and c_{O2}=221 μM.

	a / μm	i_{lim} / nA	$E_{1/2}$ / mV	n_{app}	a / μm	i_{lim} / nA	$E_{1/2}$ / mV	n_{app}
polished	4.75	2.3	-730	2.62	12.45	7.0	-600	3.06
H_i-ePt	5.30	2.9	-530	2.95	12.70	9.3	-340	3.97

The nanostructured films also have a pronounced kinetic effect on the ORR as a very significant (~200 mV) positive shift of the wave is observed. The additional surface area of H_1-ePt microelectrodes resulting from the presence of pores was shown to be electrochemically accessible and the mesoporous electrodes exhibit higher exchange currents compared to polished platinum [195]. These conditions appear favourable for the initial adsorption of oxygen and the transfer of the first electron, which is the rate determining step. Moreover, studies of ORR on small Pt particles have shown that when the particle size is less than 6 nm the (111) faces dominate on the crystallite and these faces are more active than others [196]. The nanostructured films as prepared here were reported to have the pores of ~2.5 nm diameter, separated by walls of roughly the same thickness [192]. It is therefore possible that increased (111) faceting takes place resulting in lowered ORR overpotentials. However, this theory lacks experimental confirmation, and in addition the film acid voltammetry shows features usually observed with polycrystalline Pt surfaces.

3.4.3 Potential step experiments

The stability of the H_1-ePt microelectrodes response towards oxygen reduction was tested by long term experiments as well as using them repeatedly over periods of weeks (during intervals the electrodes were kept in water). Some of the films were found to lose their activity, yielding oxygen reduction currents even lower than with a polished microdisc. This behaviour was not improved by cycling the electrode in sulphuric acid prior to measurements.

An example of a stability test in oxygen saturated 0.5 M NaCl performed several days after the film deposition is shown in Figure 3.25. The potential program was modified to account for the oxygen reduction wave shift: the measuring step was set to -0.8 V and the cleaning step to +0.25 V vs SMSE. The measured limiting currents were much lower than expected at the beginning and the response appeared to recover over the 24 h test period. While the voltammetric data gave n_{app} of ~3 for a=5.3 μm H_1-ePt microdisc, the values of n_{app} extracted from the limiting currents

measured on the transients changed smoothly from 1.3 at the beginning to 2.2 at the end of the experiment. Such low values clearly indicate deactivation of the electrode, and correspond to an activity much lower than with a standard polished microdisc. The activity was not reproducible between several nanostructured electrodes. No successful recovery procedure or explanation for the observed phenomena was found.

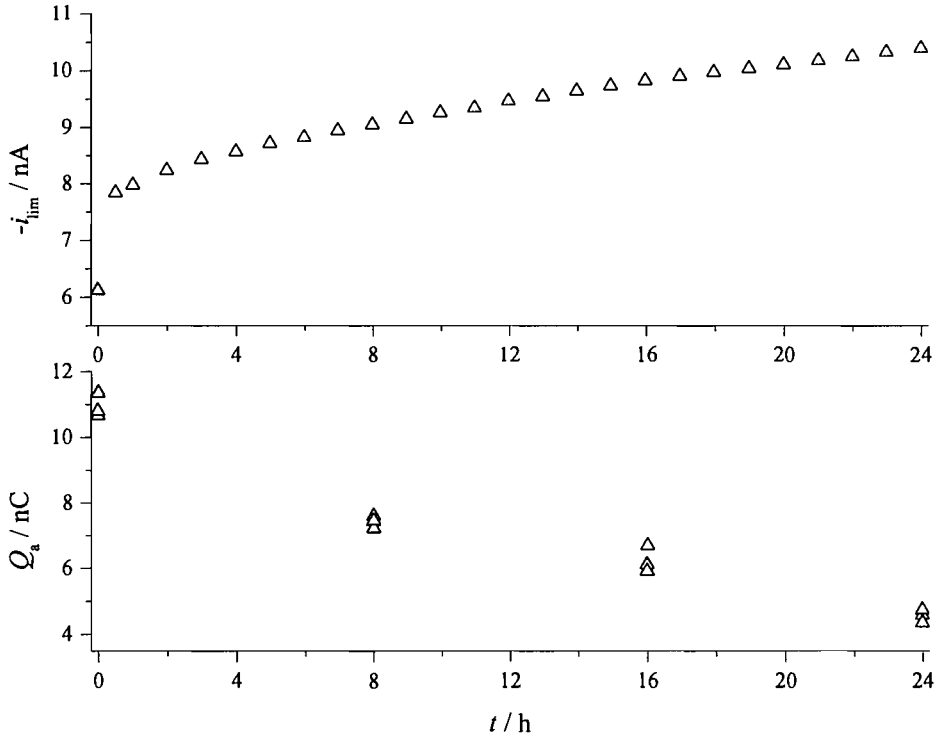

Figure 3.25 Top: Long term performance of H_1-ePt microelectrode (a=5.4 μm) in oxygen saturated 0.5 M NaCl (24.8 °C). The potential waveform consisted of measuring step at -0.8 V (29 s) and cleaning step at +0.25 V (1 s). Bottom: charges recorded during the cleaning step.

Additionally, in the long term experiment the charge during the cleaning step was monitored. This charge corresponds to the double layer charging and to oxide formation; both are proportional to the real surface area of the electrode. Thus, it reflects the changes that the film undergoes during extended operation. The charge

was found to decrease as the electrode is continuously polarised between the two potentials (Figure 3.25). This behaviour is interpreted as a slow degradation of the film architecture by the formation and reduction of platinum oxides. A serious erosion of the nanostructured film was also observed in the earlier study, where the electrode was operating for a period of three weeks in sea water [197]. Further indication of the surface area loss comes from the characterisation of the film by acid voltammetry (Figure 3.26). Clearly lower charges are recorded in the hydrogen region and for surface oxides formation and stripping, however the decrease in the real surface area appears much smaller than could be concluded from the data presented in Figure 3.25 (bottom graph).

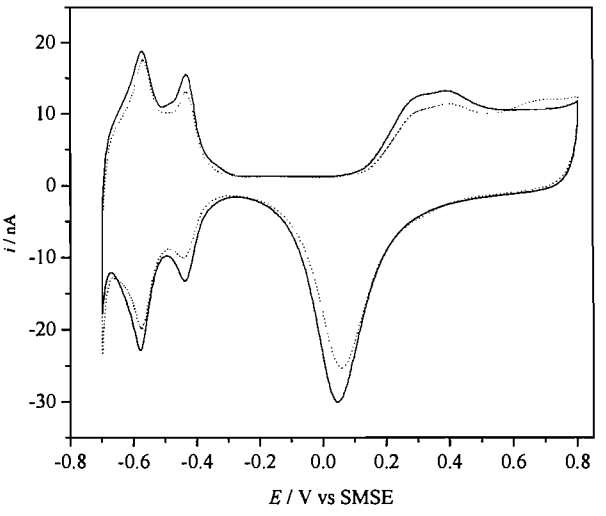

Figure 3.26 Cyclic voltammograms in deoxygenated 1 M H_2SO_4 on H_1-ePt microelectrode before (solid line) and after (dotted line) the stability experiment presented in Figure 3.25. v=200 mV s^{-1}.

3.5 Summary

Gold, platinum and mesoporous platinum microelectrodes were evaluated as cathodes for oxygen reduction in 0.5 M NaCl solution. Cyclic voltammetry was used to characterise the processes occurring on the electrode surface and to assess the influence of the experimental parameters on the materials activity towards ORR. Long term experiments were used to test material stability.

Gold was found to be very sensitive to chloride, and undergos dissolution at potentials more positive than 0 V vs SMSE in 0.5 M NaCl. Moreover, chloride appeared to form stable films on gold electrodes. Oxygen reduction wave shifted negatively in presence of chloride. The shift was as high as 300 mV for 0.5 M NaCl solution comparing to water. Constraints put by the gold anodic behaviour resulted in failure to find an optimal potential program for long term operation of the gold cathode. The response showed a constant decay (up to 50% over 6 h) and a high degree of instability (8 to 17% standard deviation from the mean i_{lim} over 6-8 h) and irreproducibility.

The behaviour of platinum electrodes was shown to be far less affected by chloride than gold electrodes, both in terms on the Pt surface electrochemistry and the performance as a cathode for oxygen reduction. Noticeable differences were observed in oxide formation and hydrogen adsorption regions, however appreciable permanent changes to the electrode surface occurred only after prolonged continuous operation. Oxygen reduction was found to depend little on the Cl^- concentration, while at the same time being strongly influenced by mass transport conditions (electrode radius). The mass transfer coefficient was found to affect both wave position and the limiting current (through changes in n_{app}). An optimal potential waveform was found for long term measurements, which yielded excellent response stability: the standard deviation of i_{lim} over 24 h was found 0.7% (corresponding to 1.6 μM at c_{O2}=221 μM). The mean difference was found to be very close to zero (4×10^{-5} %), which suggests that the variations were mainly random, with no long term drift of the response. In addition, the cleaning conditions were optimised to

keep the Pt surface roughening to minimum (roughness factor increases three fold over 24 h of continuous operation).

Mesoporous Pt films were deposited and characterised on standard Pt microdiscs. Their extraordinary high surface area causes a significant decrease in the oxygen reduction overpotential and produces higher limiting currents suggesting favourable effects of the nanostructure on both hydrogen peroxide reduction and initial rate determining electron transfer. Difficulties were encountered regarding some of the H_{ads}-ePt films long term performance (loss of activity over periods of days).

In the light of the above presented results, polished platinum microelectrodes appeared as the most suitable for the application as a sensor for oceanographic measurements. Pt was found to be a robust material, capable of stable performance over extended periods of operation. High concentration of chloride does not have damaging effect on the electrode nor does it influence significantly Pt activity towards the ORR. Most importantly, it was demonstrated that the sensor is capable of reliable performance without the need of additional maintenance on top of the electrochemical cleaning.

4 Microelectrode calibrations and the behaviour of n_{app} as a function of mass transport and temperature

4.1 Chapter overview

The chapter describes the calibration system developed to accurately test the microelectrode sensor. The design and principles are explained and the performance validated by an independent optical sensor. The calibration results for a range of electrode radii are presented and the accuracy of determination of c_{O2} from the limiting current is critically assessed. In addition, error estimates are calculated for c_{O2} derived from the microelectrode response purely on the basis of analytical expression (without the need of calibration).

Since the calibration allows a straight forward estimation of n_{app}, its values are determined for a range of electrode sizes and temperatures. An attempt is made to obtain a number of the ORR kinetic parameters and mechanistic information from the steady state values of n_{app}.

4.2 Introduction

A reliable method of oxygen calibration is crucial for the consistency of the measurements. Common approaches employ calibration standards e.g. inert gas, air, oxygen saturated solutions and commercially available gas mixtures. Unless an independent analysis (Winkler titration) can be performed, the preparation of these standards relies on the precise knowledge of the solubility of oxygen in the test solution. The availability of gas mixtures also limits significantly the number of points on the calibration curve which increases the calibration errors. The issue can only be resolved by using costly gas mixing equipment. Other approaches generate oxygen *in situ*, e.g. by electrogeneration [198, 199] or catalytic decomposition of hydrogen peroxide [200]. These methods however require the exact knowledge of the reactions efficiency and are complicated by the need to introduce additional

instrumentation to the system or chemical agents to the solution. In this work a calibration system (which can be used for any oxygen sensor) based on the 'physical method' (introduced by LeFevre [201] and Fatt and St. Helen [202]) was developed. Later this method was successfully employed by Rasmussen and Rasmussen [136] to simultaneously calibrate an oxygen electrode and to determine the oxygen solubility in various media used in respiration measurements. Their approach involved the use of calibrated and thermostated syringes to adjust the DO concentrations. In this work a highly automated system was developed, which improves the precision and accuracy of the DO sensors calibration.

4.3 Calibration: an experimental design for the control of oxygen concentrations

A schematic of the calibration system is shown in Figure 4.1. It consists of three vessels (all filled with the same test solution): a humidifier (A), an oxygen saturated solution reservoir (B) and a measurement cell (C). The ensemble is made of glass, including the tubing connecting the vessels, which is critical and enables transport of solutions without loss or gain of oxygen. The solutions are maintained at a constant temperature using a thermostatic bath (Grant, W14). The measurement cell containing the working and reference electrodes is completely filled (it is imperative to remove all bubbles) with the test solution and sealed to prevent any contact with a gaseous phase. It is also equipped with a glass coated stirring bar. Teflon stirring bars were not used due to the reported [136] oxygen uptake/release by Teflon. The inlet and outlet of the measurement cell are a thin capillary (D) and a thin channel glass connector (E), respectively. Both have a diameter of approximately 0.5 mm which prevents mixing of the contained solution with the solution in the measuring cell. Finally, downstream of the measuring cell a software controlled solenoid pump (Model 120SPI, Bio-Chem Valve Inc., USA) is fitted. This removes a fixed volume from the measurement cell and so draws an identical volume from the saturated solution into the measurement cell. The volume transferred by a

single piston movement, determined by weighing deionised water pumped through during 30 minutes of continuous operation, was found to be 51.3 μl.

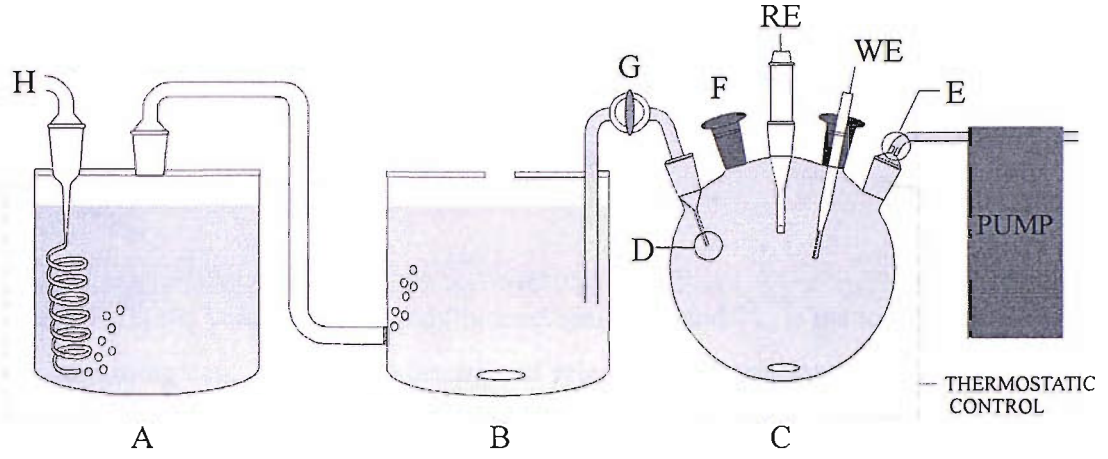

Figure 4.1 Schematic representation of the calibration system. A – humidifier, B – saturated solution reservoir, C – measurement cell, D – inlet capillary, E – outlet connector, F – argon feed neck, G – valve, H – oxygen feed, WE – working electrode, RE – reference electrode.

The initial step of the calibration procedure is the saturation of solution B by bubbling oxygen saturated with water vapour in the humidifier (A). When the saturation is complete, a sample of solution B is taken and its oxygen concentration is determined by a modified Winkler method [203]. Valve (G) is then opened and the tubing is filled with the oxygen saturated solution by activating the pump. Once the tubing is filled with solution B, valve (G) is closed and solution C is deoxygenated by purging with argon. After deoxygenation the argon feed is withdrawn and the cell is sealed ensuring no bubble is left in the cell.

The calibration of the sensor is then performed by adding volumes of solution B to solution C (which initially contains no oxygen). Each time the pump is activated, it removes a certain volume from the cell and this volume is replaced by the oxygen saturated solution. After each addition the solution is homogenised by stirring. The effectiveness of stirring was confirmed by adding a small amount of ink into the cell. The argon feed neck (F) can also be used to introduce another capillary

inlet connected to a vessel containing oxygen free solution, which allows performance of a 'backwards' calibration i.e. from high to low oxygen concentrations.

The concentration of oxygen depends on the number of additions (i) and the concentration of oxygen in the oxygen saturated solution (c_{sat}). After the first addition, assuming c_0=0, the oxygen concentration is

$$c_1 = c_{sat}\frac{V_{ex}}{V_{tot}} \tag{4.1}$$

where V_{ex} is the volume exchanged (injected/removed) and V_{tot} is the total volume of the measuring cell. The latter is determined prior to the experiment by weighing the fully assembled measurement cell both empty and filled with a solution of known density. After the second addition:

$$c_2 = c_1 + \frac{c_{sat}V_{ex}}{V_{tot}} - \frac{c_1 V_{ex}}{V_{tot}} \tag{4.2}$$

The second term in equation (4.2) represents an increment in concentration due to the injected oxygen saturated solution and the third term accounts for the loss of oxygen contained in the volume removed from the cell. After the i-th addition:

$$c_i = c_{i-1} + \frac{c_{sat}V_{ex}}{V_{tot}} - \frac{c_{i-1}V_{ex}}{V_{tot}} \tag{4.3}$$

or generally

$$c_i = c_{sat}\frac{V_{ex}}{V_{tot}}\sum_{k=0}^{k=i-1}\left(1-\frac{V_{ex}}{V_{tot}}\right)^k \tag{4.4}$$

where k is the number of additions made. The number of points to construct a calibration curve can be freely chosen by programming the number of piston cycles

during a single pumping action. It has to be stressed however, that in order to rely on the above equations the exchanged volume has to be sufficiently small, so that none of the oxygen added from the saturated solution is removed from the system during one pumping action. Also great care must be taken not to trap any bubbles in the measuring cell and the connecting tubing, while filling or purging the cell with argon. Any bubble trapped inside would impair the solution volume and cause some of the oxygen to diffuse from the solution into the inert gas bubble.

4.4 Calibration: experimental results and analysis

The performance of the developed calibration system was validated with an independent oxygen sensor. An optical sensor based on the fluorescence quenching by DO was employed. It was developed by Ed Austin (Optoelectronic Research Centre, University of Southampton) [204] and utilised a commercial sensing membrane (Presens, Germany). The microelectrode was replaced by the optode in the calibration assembly and the experimental procedure as described earlier was followed. Additionally the experiment was conducted in the dark to ensure the excitation of the indicator comes solely from the internal light source. The calibration curve of the optode is shown in Figure 4.2.

A linear response (R=0.9994) was found over the DO concentration range tested (up to air saturation), thus proving that the DO concentration is incremented as predicted by equation (4.4). Further details on the optode performance including the raw fluorescence decay curves can be found in the internal report describing the trials [205].

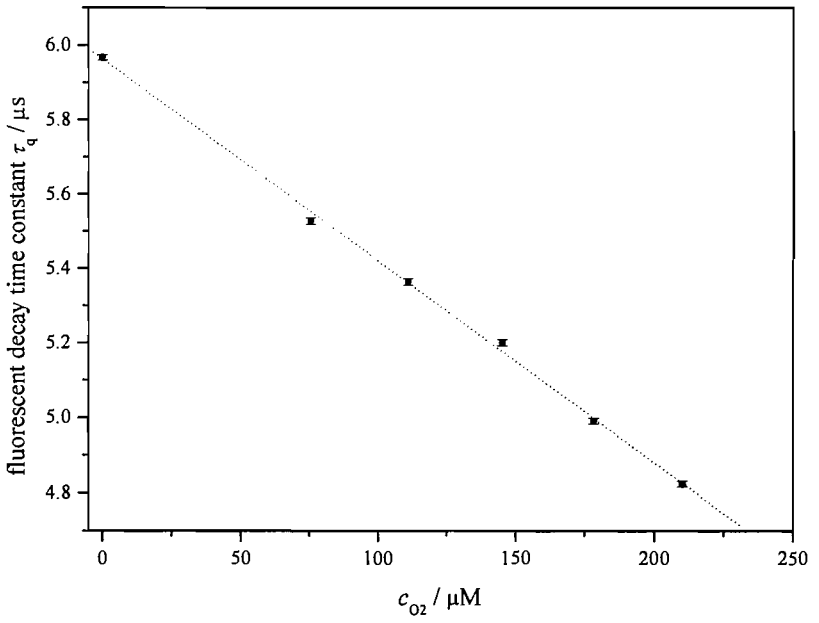

Figure 4.2 Optode fluorescence decay time constant as a function of oxygen concentration. Experiment conducted in 0.5 M NaCl at 25 °C.

The microelectrodes calibration curves in 0.5 M NaCl (Analar grade) at 25 °C are shown in Figure 4.3. Throughout the calibration experiments the electrodes were continuously operated as described in Chapter 3 (1 s cleaning step at +0.2 V and 12 s measuring step at -1.05 V). Each i_{lim} value represents the mean of the last 7 s of four consecutive oxygen reduction transients in a stagnant solution. The absolute DO concentrations are calculated on the basis of the Winkler titration of the sample taken from the oxygen saturated solution reservoir. Before the calibration a single measurement is taken in the reservoir and the i_{lim} values obtained are shown in the inset of Figure 4.3.

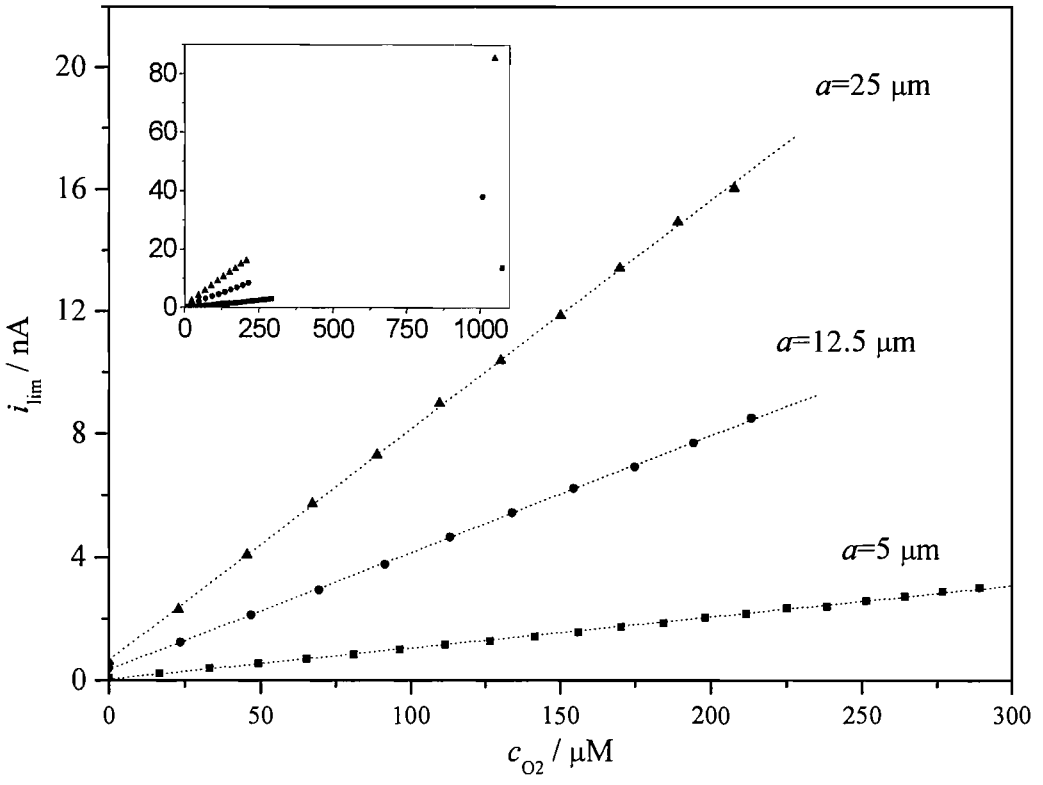

Figure 4.3 Calibration curves in 0.5 M NaCl at 25 °C using various sizes of Pt microdisc electrodes. The inset includes electrodes responses in oxygen saturated solutions.

Irrespectively of the electrode radii an excellent linearity between i_{lim} and c_{O2} is found (R>0.999 in each case). Moreover, the responses in oxygen saturated solution agree well (within experimental error) with the extrapolated fits. Although the intercepts (i_0) are very close to zero, the sensor response shows an appreciable residual current in absence of oxygen. This can be due to several reasons, e.g.: 1) residual oxygen due to imperfection (or limits) of deoxygenation procedure (argon purging), 2) reducible impurities from the salt used (the residual currents correspond to 3.2, 2.7 and 1.2 % of air saturation in Analar NaCl, Aristar NaCl and pure water, respectively). Table 4.1 summarises the key quantities obtained from linear fits of the calibration curves for various radii microelectrodes at 25 °C, which allow calculation of the oxygen concentration directly from the microelectrode limiting current.

Table 4.1 Parameters obtained from the calibrations of microelectrode sensors.

Radius / μm	Slope, B (sensitivity) / pA μM^{-1}	Intercept, i_0 / pA	Detection limit / μM
4.7 ± 0.2	10.3 ± 0.1	29 ± 14	8.1
12.1 ± 0.4	32.8 ± 0.2	340 ± 3	2.9
24.5 ± 0.7	74.0 ± 0.1	640 ± 1	0.9

The detection limit (DL) was calculated from equation (4.5) [206]:

$$DL = \frac{i_{\lim(c=0)} + 2\Delta i_0}{B} \tag{4.5}$$

where $i_{\lim(c=0)}$ is the limiting current in oxygen free solution, Δi_0 is the absolute error on the intercept of the calibration curve linear fit and B is the slope of the fit. Commercial Clark type probes usually present better detection limits, due to the presence of the membrane which makes the sensor more selective. The detection limits are usually lower than 1 μM (e.g. Unisense needle sensor 0.3 μM).

4.5 Error treatment

4.5.1 Errors in the determination of the DO concentration

The error on c_{O2} measured by the electrode was estimated for two cases: when c_{O2} is calculated from the calibration performed before the measurement and when c_{O2} is calculated directly from an analytical expression for the limiting current. The total differential method was used in both cases and the general expressions and results are presented here. A detailed error treatment can be found in the Appendix (see section 9.2).

Calibration approach

Calibration of the microelectrode in a medium with similar salinity before the measurement results in significant reduction of errors due to fewer parameters, when compared to the analytical expression for c_{O2} (see equation (4.10)). A linear fit of the calibration data yields:

$$c_{O2} = \frac{i_{lim} - i_0}{B} \tag{4.6}$$

where i_{lim} is the measured limiting current, i_0 is the intercept and B the slope of the linear fit. The error of DO determination can be calculated as

$$\Delta c_{O2} = \left|\frac{\partial c_{O2}}{\partial i_{lim}}\right| \Delta i_{lim} + \left|\frac{\partial c_{O2}}{\partial i_0}\right| \Delta i_0 + \left|\frac{\partial c_{O2}}{\partial B}\right| \Delta B \tag{4.7}$$

The total differential of (4.6) has the following form:

$$\Delta c_{O2} = \frac{1}{B}\left(\Delta i_{lim} + \Delta i_0 + \frac{i_{lim} - i_0}{B}\Delta B\right) \tag{4.8}$$

Taking the value Δi_{lim} as 2% (see page 104) and Δi_0, ΔB from the relevant calibration curve, the errors were calculated for three electrode radii and are presented in Figure 4.4. The obtained errors are relatively small for concentrations higher than ~50 μM. For the two larger electrodes the errors are below 4 % level and somewhat higher, up to 6% for the smallest electrode, which is remarkable for microelectrode experiments and indicates the effectiveness of the preconditioning procedure.

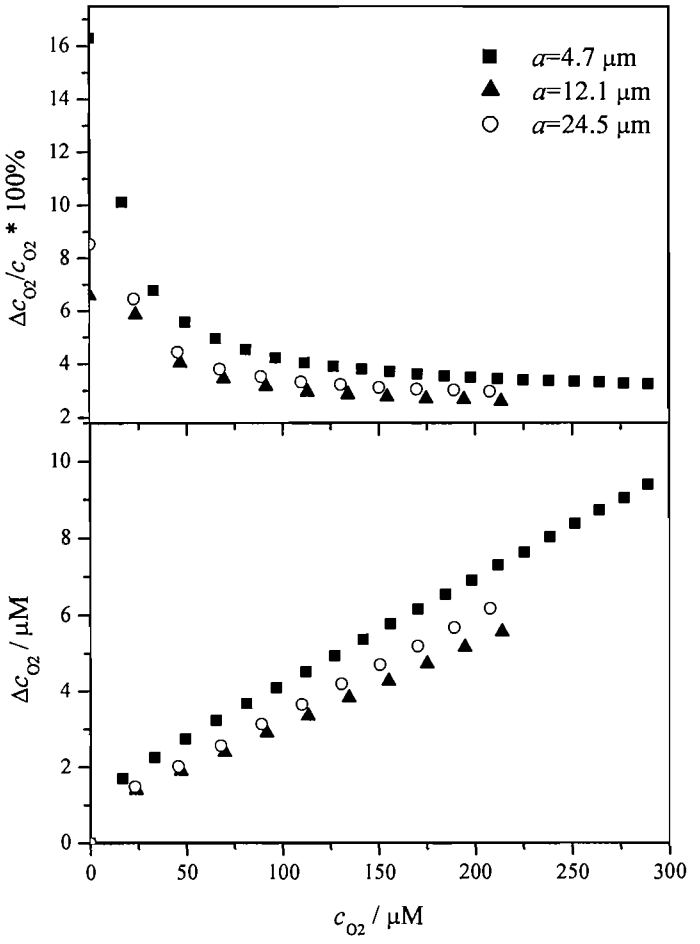

Figure 4.4 Relative (top) and absolute (bottom) errors of c_{O2} determination as a function of oxygen concentration for a range of electrodes radii. Errors are based on the calibrations of microelectrodes in 0.5 M NaCl at 25 °C.

Analytical approach

The analytical expression for c_{O2} is simply derived from the equation for the limiting current at a microdisc electrode:

$$c_{O2} = \frac{i_{lim}}{4n_{app}FD_{O2}a} \tag{4.9}$$

where D_{O2} is derived from equations (1.34) - (1.38) described in section 1.5.2.
The following uncertainties have to be taken into account to calculate the total error:

- Δi_{lim} – the error on the limiting current is taken as the variation of i_{lim} from its mean value within the last 5 s of the oxygen reduction transient. It was found to be 1.8 – 2.0% depending on concentration. All later calculations will use a 2% uncertainty.
- Δn_{app} – the error on the apparent number of electrons was estimated separately for all the electrode radii used and is presented in the following section. n_{app} is also assumed to be temperature independent.
- Δa – the error on the electrode radius. It was estimated statistically on the basis of all the radius determinations as 0.17, 0.34 and 0.71 μm for electrodes with nominal radii of 5, 12.5 and 25 μm, respectively.
- ΔT – temperature uncertainty taken as 0.2 K.
- ΔD_w – the error on the diffusion coefficient of oxygen in water. The literature values of D_w are very scattered and the error estimates vary significantly, therefore a 5% uncertainty is assumed.

The uncertainties related to the salt concentration were neglected for the following reasons: laboratory experiments were performed in 0.5 M NaCl solution, which was prepared in large quantities (usually 2 dm^3), therefore minimising the error; in field measurements the salinity is determined with a precision of six decimal places by conductivity measurements. Since D_w varies by less than 1% with a 0.1 M change in c_{NaCl}, neglecting the errors is justified. Also, the components of activation energy of of diffusing solute as defined in equation (1.36) where taken as constants in the overall error equation. Moreover, since DO concentration is always much

smaller than the concentration of the supporting electrolyte, D_{O2} is assumed to be independent of c_{O2}. Also, n_{app} is treated as not dependent on c_{O2}. The validity of these assumptions is confirmed by the excellent linearity of the calibration curves.

By combining equation (4.9) with equations (1.37) and (1.38) we obtain the equation binding c_{O2} with all the variables that may be the source of errors:

$$c_{O2} = \frac{i_{lim}}{4n_{app}FaD_w\left(\frac{V}{V_w}\right)^{2/3}\exp\left(-\frac{\Delta\alpha x_+ + \Delta\beta x_-}{RT}\right)} \tag{4.10}$$

Thus, the maximal absolute error on c_{O2} can be quantified as

$$\Delta c_{O2} = \left|\frac{\partial c_{O2}}{\partial i_{lim}}\right|\Delta i_{lim} + \left|\frac{\partial c_{O2}}{\partial n_{app}}\right|\Delta n_{app} + \left|\frac{\partial c_{O2}}{\partial a}\right|\Delta a + \left|\frac{\partial c_{O2}}{\partial D_w}\right|\Delta D_w + \left|\frac{\partial c_{O2}}{\partial T}\right|\Delta T \tag{4.11}$$

where $\frac{\partial c_{O2}}{\partial x}$ is a partial derivative of c_{O2} with respect to variable x. Accordingly, the total differential calculated with equation (4.11) related to expression (4.10) allows estimation of the relative error as:

$$\frac{\Delta c_{O2}}{c_{O2}} = \frac{\Delta i_{lim}}{i_{lim}} + \frac{\Delta n_{app}}{n_{app}} + \frac{\Delta a}{a} + \frac{\Delta D_w}{D_w} + \frac{\Delta T}{T^2} \tag{4.12}$$

(see Appendix, section 9.2 for details).

For electrodes of nominal radii 5, 12.5 and 25 μm and at 25 °C the maximal relative errors were calculated to be 15, 14 and 11%, respectively. In this approach the errors are usually 3-4 times higher compared with the calibration. The dissolved oxygen concentration and the corresponding accuracy of the measurement can thus be determined directly from the analytical expression provided the temperature, water density, salinity and D_w are known. The values of a, and n_{app} are listed in Table 4.2 (see section 4.3). For other electrode radii the data can be interpolated.

4.5.2 Determination of errors on n_{app}

The maximal errors on n_{app} were calculated using the total differential method (for complete calculations see Appendix 9.3). When the calibration approach was used, the following uncertainties were taken into account: the error on the fit of the slope, the error on the diffusion coefficient and the error on the electrode radius (calculated as described in section 4.5.1):

$$\Delta n_{app} = \left|\frac{\partial n_{app}}{\partial B}\right| \Delta B + \left|\frac{\partial n_{app}}{\partial D_{O2}}\right| \Delta D_{O2} + \left|\frac{\partial n_{app}}{\partial a}\right| \Delta a \tag{4.13}$$

In the course of obtaining a calibration curve, the Winkler titration was performed on a sample of the oxygen saturated stock solution. The samples were taken in 50 ml bottles, and titrated using thiosulphate solution. Potassium iodate was used as the primary standard, and standardisation procedure was always repeated on the day of oxygen determination. With starch used as an indicator and visual end point detection the accuracy of oxygen determination is ±1.3 μM [207]. With DO concentrations between 1000 and 1400 μM the resulting errors were smaller than the deviation of experimental calibration data from the linear fit. In consequence, the larger value of the slope error was taken to estimate the overall error. The major contribution (~60%) to the error is from the diffusion coefficient term and later from the uncertainty in a. The maximal errors were calculated to be 0.27, 0.33, and 0.27 for 5, 12.5 and 25 μm radius electrode respectively. This corresponds to relative error in n_{app} of 9.1, 10.1 and 8.3%.

Higher errors were calculated for n_{app} extracted from a single potentials step, where the limiting current error replaced usually much smaller error on the slope of the calibration curve:

$$\Delta n_{app} = \left|\frac{\partial n_{app}}{\partial c_{O2}}\right| \Delta c_{O2} + \left|\frac{\partial n_{app}}{\partial i_{lim}}\right| \Delta i_{lim} + \left|\frac{\partial n_{app}}{\partial D_{O2}}\right| \Delta D_{O2} + \left|\frac{\partial n_{app}}{\partial a}\right| \Delta a \tag{4.14}$$

Oxygen concentration in this approach was calculated on the basis of data given by Rettich *et al.* [135] and Tromans [134], which predict c_{O2} with 0.1 μM accuracy. The error is negligible compared to other uncertainties and was not taken into account in the calculations.

4.6 Variation of n_{app} with the mass transfer coefficient

The microelectrode calibration provides an easy way to assess the apparent number of electrons (n_{app}) in the oxygen reduction. The electrode radius is determined earlier and the diffusion coefficient D_{O2} is calculated as described in section 1.5.2, thus the n_{app} is extracted directly from the slope (B) of the calibration curve:

$$n_{app} = \frac{\mathrm{d}\, i_{lim}}{\mathrm{d}\, c_{O2}} \times \frac{1}{4FD_{O2}a} = B \times \frac{1}{4FD_{O2}a} \tag{4.15}$$

Values of n_{app} obtained from the calibration curves at 25 °C in 0.5 M NaCl are presented in Table 4.2 and compared with earlier data [158] obtained from voltammetry at Pt microdisc electrodes in 0.1 M NaCl. The agreement is good and the differences are attributed to slightly different conditions and different value of D_{O2} used in the calculations. Both sets of data show clearly a similar trend. Higher rates of mass transport (the mass transfer coefficient at a microdisc, as defined in equation (4.16), increases as the electrode radius gets smaller) cause n_{app} to decrease, due to the removal of the peroxide intermediates from the electrode surface before the next two electrons can be transferred to yield water as the final product.

$$m_i = \frac{4D_i}{\pi a} \tag{4.16}$$

Table 4.2 Comparison of n_{app} values obtained in calibration experiments with earlier data [158]. The quoted errors are based on the standard error of the calibration curves and the error from the electrode radius determination. Due to a lack of data on error estimates on D_w, the D_{O2} uncertainty is not taken into account.

This work (0.5 M NaCl, $D_{O2(25°C)} = 2.16\times10^{-9}$ m^2 s^{-1})		**Sotiropoulos** [158] (0.1 M NaCl, $D_{O2} = 2.29\times10^{-9}$ m^2 s^{-1})	
radius / μm	n_{app}	**radius / μm**	n_{app}
3.00	*2.2		
4.68 ± 0.17	2.64 ± 0.12	5	2.8 ± 0.1
12.08 ± 0.37	3.26 ± 0.13	12.5	3.3 ± 0.1
24.54 ± 0.71	3.62 ± 0.09	25	3.7 ± 0.1

* Obtained from voltammetric data

Chen and Kucernak [120] investigated the dependence of n_{app} on mass transfer coefficients using submicrometer sized electrodeposited Pt single particles. Very small electrodes (down to several tens of nanometers) allowed them to extend the range of m studied to high values, which are inaccessible to conventional microdisc electrodes. The authors kinetically modelled the experimental data using analytically derived expressions. The analysis was made according to the parallel mechanism of oxygen reduction proposed by Wroblowa *et al.* [88], simplified by disregarding the oxidation of H_2O_2 (4.17):

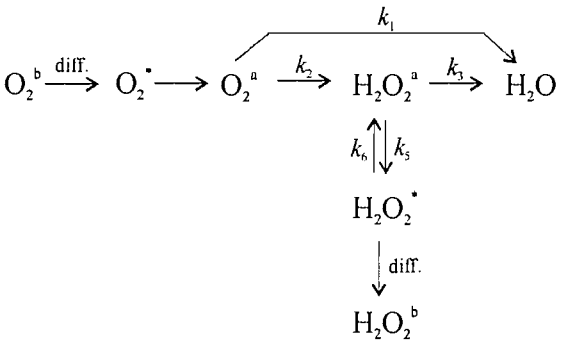

(4.17)

From the comparison of the expressions for the steady state current density and the theoretical limiting current density when n_{app}=4 (i.e. when current densities of steps controlled by k_2 and k_3 equal), the equation relating n_{app} to kinetic parameters of the

reaction is derived (4.18). The full derivation of this equation can be found in reference [120].

$$n_{app} = 4 - \frac{2}{\left(1+\frac{k_1}{k_2}\right)\left(1+\frac{k_3}{k_5}\left(1+\frac{k_6}{m_{H_2O_2}}\right)\right)} \tag{4.18}$$

In the above equation k_6 is in fact a product of the real rate constant and the relative number of surface sites available for H_2O_2, $k_6 \times (1-\theta)$, where θ is the total relative surface coverage by spectator species. After substitution of (4.16) to (4.18) we obtain n_{app} as a function of the microdisc radius

$$n_{app} = 4 - \frac{2}{\left(1+\frac{k_1}{k_2}\right)\left(1+\frac{k_3}{k_5}\left(1+\frac{\pi a k_6}{4D_{H_2O_2}}\right)\right)} \tag{4.19}$$

The experimental data were fitted with equation (4.19) and kinetic parameters: k_1/k_2, k_3/k_5 and k_6 were obtained. Four sets of data of $n_{app}=f(a)$ were used: from steady state cyclic voltammograms (read at -1.05 V), from calibration curves, from steady state currents after a potential step in air saturated solution (experiment presented later in Figure 4.7) and the voltammetric data reported by Sotiropoulos [158]. Figure 4.5 shows all the datasets and the best fit compared with the fit obtained by Chen and Kucernak [120].

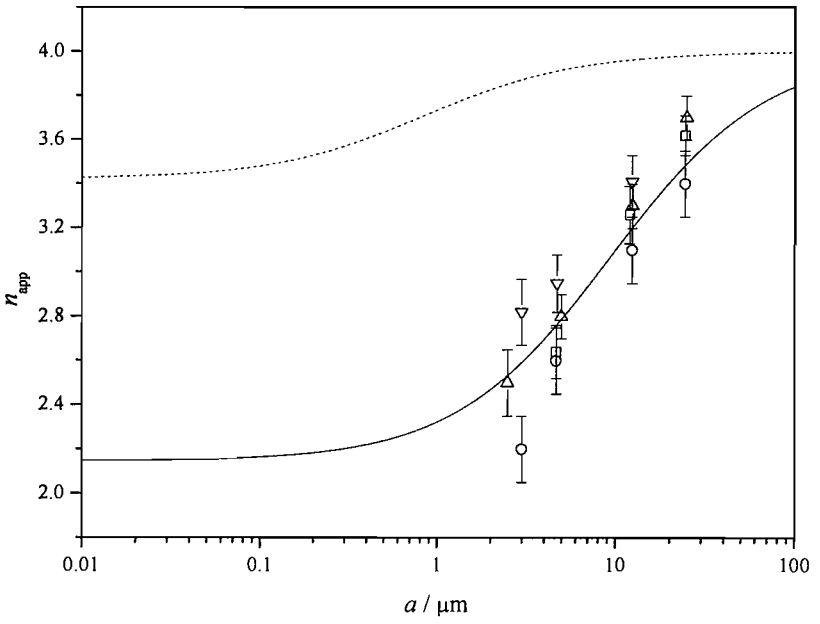

Figure 4.5 n_{app} as a function of electrode radius. Data sets obtained from calibration experiments (□), voltammetry (○), potential step (▽) (all in 0.5 M NaCl at 25 °C) and data obtained by Sotiropoulos in 0.1 M NaCl (△). Solid line represents the fit of the data using equation (4.19) with the following parameters k_1/k_2=0, k_3/k_5=0.078 and k_6=0.27 cm s^{-1}. $D_{H_2O_2}$ was taken as 1.45×10^{-5} cm^2 s^{-1} [208]. For comparison, the fit of the data of Chen and Kucernak [120] is presented (dotted line). Their experimental data was recorded in 0.1 M H_2SO_4 on electrodeposited Pt particles. The fit was obtained using the following parameters: k_1/k_2=1, k_3/k_5=0.72 and k_6=0.4 cm s^{-1}, while $m_{H_2O_2} = D_{H_2O_2} / a$. The error bars of n_{app} are calculated from equations given in section 4.5.2 and appendix 9.3.

One can notice a significant difference between the two fits presented. The values of n_{app} obtained in this work are much lower compared to Chen's work, where n_{app} is always larger than 3.4. Several factors are most likely behind such significant discrepancy:

a) Chen and Kucernak assumed on the basis of equivalent mass transfer rate between the microelectrode and RDE, that n_{app}=4 at a 12.5 μm radius microdisc. All their n_{app} were extracted from the limiting currents using the product $c_{O2}\times D_{O2}$ which was obtained on the basis of the abovementioned

assumption. In the light of the observations in this work and by other researchers [108] this assumption does not appear to be valid, as n_{app} at 12.5 μm radius microdisc is usually observed to be between 3.2 and 3.4. ORR involves several surface processes requiring available adsorption sites. In RDE experiment the number of adsorption sites is far greater than with a microelectrode, therefore the reaction cannot proceed at the same rate despite the same mass transfer coefficient. Such dependence on the surface sites availability was shown by Evans [209] for H_2O_2 oxidation using polished and nanostructured Pt microelectrodes. The range of linearity of i_{lim} vs c_{H2O2} plots was extended each time the thickness of the deposited mesoporous film (i.e. the number of surface sites) was increased. At the same time the mass transport conditions to the microdisc remained practically unaltered whether the nanostructured film was present or bare Pt microdisc was used.

b) An appreciable contribution to lower values of n_{app} can also originate from high concentration of adsorbing chloride and therefore lower values of $k_6 \times (1-\theta)$.

c) The experiments were conducted in notably different conditions. 0.1 M H_2SO_4 was used as an electrolyte in the work of Chen, while this work employed neutral 0.5 M NaCl solution. Different adsorption properties of sulphate and chloride and different pH are bound to alter the rate constants of ORR. The vast majority of literature on ORR is for acidic and alkaline media, which makes any comparison particularly difficult.

d) The mass transfer coefficient in this work is defined as for a microdisc (4.16), while Chen's study employed approximately hemispherical particles and correspondingly a diffusion model for uniformly accessible electrode was employed, where $m_{H_2O_2} = D_{H_2O_2} / a$. Consequently, for microdisc the denominator in equation (4.18) will be smaller and lower n_{app} will be observed.

The best fit of the experimental data yielded $k_1/k_2=0$, $k_3/k_5=0.078$ and $k_6=0.27$ cm s^{-1}. $D_{H_2O_2}$ was taken as 1.45×10^{-5} cm^2 s^{-1} [208]. It has to be stressed that due to the very limited number of electrode radii and significant variations in n_{app}

(especially for the smallest microelectrodes), the kinetic parameters obtained from the fit carry very significant errors. Nevertheless, the data provides some insight into the mechanism of ORR on Pt in the conditions employed. A reasonably good fit could only be obtained with k_1/k_2 set to zero, which suggests that oxygen reduction proceeds exclusively via the series mechanism, i.e. no direct four-electron reduction takes place. This stands in contrast to the mechanism of ORR on Pt established in the literature. However, numerous researchers postulated a significant contribution of the series pathway in the overall mechanism of ORR on Pt [107, 108, 112, 120]. Chen and Kucernak reported that reasonable fits could only be obtained for $k_1/k_2<1.5$. The series pathway of the ORR will also be favoured in cases with high chloride coverage as described in section 1.4.3.

4.7 Temperature dependence of the microelectrode response

The sensor is designed to operate in the water column, where temperature can vary from around 25 °C close to the surface to 0 °C in deep regions. Even more extreme conditions can be met on board of the research ship. Therefore, the current concentration relationship was examined in a range of temperatures 5 – 35 °C to derive a possible correction for the algorithm used to obtain c_{O2} from the sensor output.

A series of calibration experiments were conducted in order to extract n_{app} at various temperatures. The values of n_{app} were extracted from the calibration slopes using temperature corrected D_{O2} values calculated with $D_w=2.11\times10^{-5}$ cm^2 s^{-1} at 22 °C [146] according to the equations presented in section 1.5.2. The extracted values of n_{app} for a range of electrode radii are shown as Arrhenius plots in Figure 4.6. Essentially very little temperature dependence is observed over the examined temperature range. With 12.5 μm radius microdiscs the scatter is larger than with other sizes. The poorer reproducibility of the underlying calibration slopes results presumably from the fact that the electrodes where not polished between

experiments. The obtained n_{app} values for a range of temperatures and electrode radii are presented in Table 4.3.

Table 4.3 n_{app} extracted from calibration curves at various temperatures, T_C (°C).

a=5 μm		a=12.5 μm		a=25 μm	
T_C	n_{app}	T_C	n_{app}	T_C	n_{app}
6.2	2.42	6.1	2.59	12.0	3.48
10.0	2.63	7.2	2.58	25.5	3.63
11.0	2.46	8.8	2.78	29.6	3.63
15.3	2.57	16.2	3.13	33.8	3.73
20.5	2.67	20.5	3.19		
24.5	2.58	25.8	3.04		
26.0	2.63	27.5	3.00		
26.0	2.73	30.0	3.64		
27.2	2.60	30.6	3.11		
27.4	2.55	33.7	3.41		
28.4	2.67	34.0	3.70		
29.6	2.65				
34.8	2.68				
34.8	2.80				

The data was fitted with the Arrhenius type function (4.20) and the slope was used to calculate the activation energy E_a.

$$\ln n_{app} = const. + \frac{E_a}{R}\frac{1}{T} \tag{4.20}$$

The E_a values of 2.2, 6.5, and 2.1 kJ mol^{-1} where obtained with 5, 12.5, and 25 μm radius electrodes respectively.

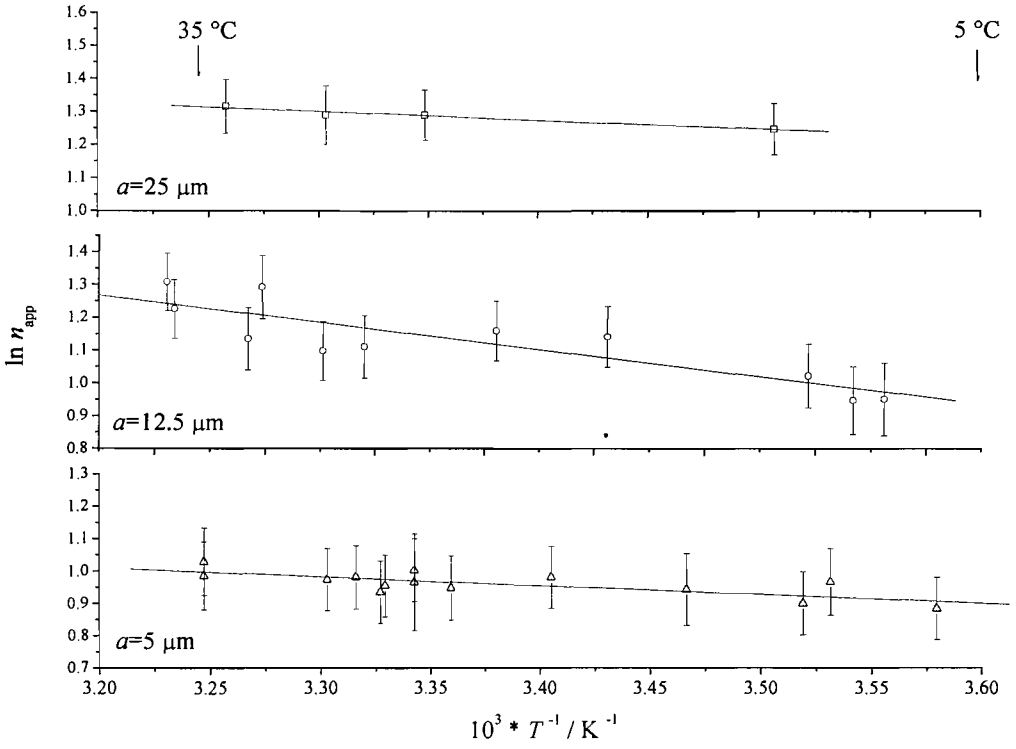

Figure 4.6 ln n_{app} as a function of $1/T$ for a range of electrode radii: a=5 μm (△), 12.5 μm (○), 25 μm (□) and temperatures 5 to 35 °C. The values of n_{app} are extracted from the calibration curves. Solid lines represent linear fits of the experimental data. The error bars are calculated as described in section 4.5.2.

In addition, a more rapid but less accurate approach to obtain $n_{app}=f(T)$ was employed. In this type of experiments the measurements were performed in a solution with constant DO concentration (air saturation) in a sealed thermostated cell. The temperature was incrementally varied over a range 5 to 35 °C, while the potential waveform was continuously applied to the electrode. The larger error in n_{app} is a consequence of its extraction from single measurements in contrast to obtaining it from the slope of the calibration curve. The n_{app} data are presented in Table 4.4 and the resulting Arrhenius plots are shown in Figure 4.7 and compared with the fits of $n_{app}=f(T)$ from calibrations where available.

Table 4.4 n_{app} extracted from the potential step experiments at various temperatures, T_C (°C)

a=2.5 μm		a=5 μm		a=12.5 μm	
T_C	n_{app}	T_C	n_{app}	T_C	n_{app}
6.9	2.27	5.2	2.45	7.0	2.79
8.9	2.34	9.7	2.58	10.7	3.00
10.7	2.32	14.8	2.76	14.9	3.19
12.8	2.38	20.0	2.86	21.0	3.39
15.8	2.47	24.8	2.98	25.2	3.52
20.5	2.69	29.8	3.06	30.6	3.59
25.2	2.87	34.9	3.14	36.2	3.60
30.2	3.01				
34.7	3.13				

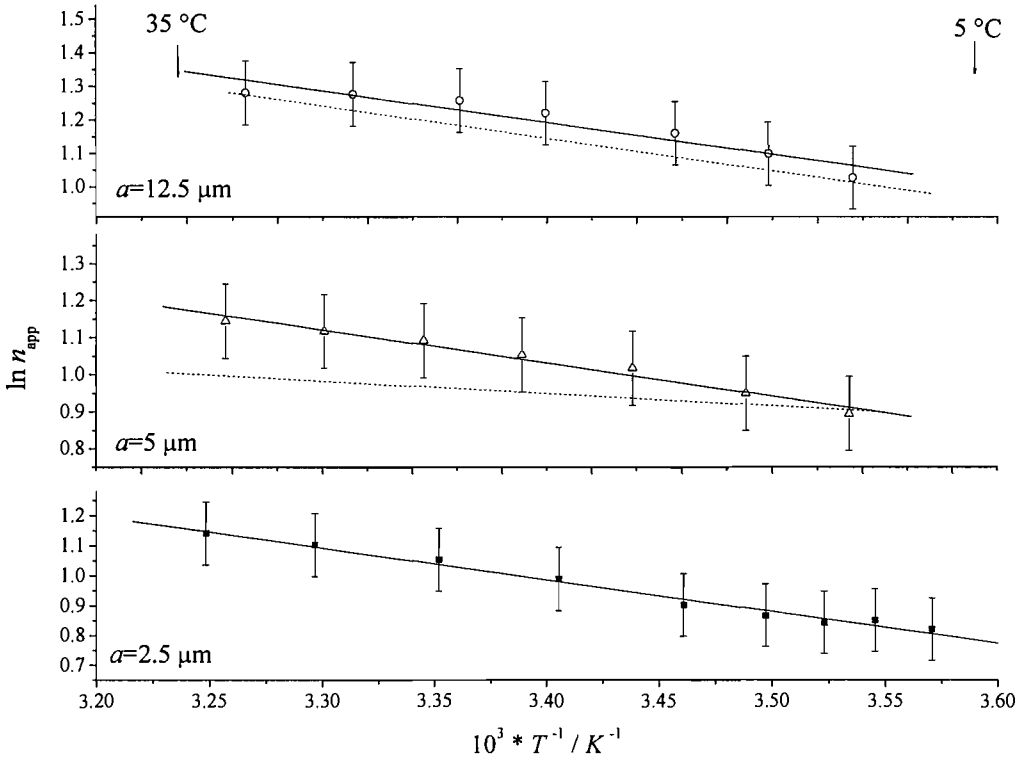

Figure 4.7 ln n_{app} as a function of $1/T$ for a range of electrode radii: a=2.5 μm (■),5 μm (△), 12.5 μm (O) and temperatures 5 to 35 °C. The values of n_{app} were obtained from the limiting currents in potential step experiment in air saturated 0.5 M NaCl. Solid lines are linear fits of experimental data. For comparison, the linear fits of data obtained in calibration experiments (Figure 4.6) are also plotted (dashed lines). The error bars are calculated as described in section 4.5.2.

The n_{app} values obtained in these experiments are few percent higher, but well within the experimental error and reproducibility of the measurements. The activation energies calculated from the linear fits here are 8.8, 5.9, and 6.3 kJ mol^{-1} for 2.5, 5 and 12.5 μm microdiscs radii respectively. When compared to the corresponding calibration data, E_a is almost identical for 12.5 μm and slightly higher for 5 μm radius electrodes.

In general, the observed E_a range from 2 to 9 kJ mol^{-1}, which is very low when compared to activation energies for diffusion processes (~15 kJ mol^{-1}) or chemical reactions (tens to hundreds kJ mol^{-1}). It is possible that the temperature effects on different parameters determining n_{app} cancel each other and the overall change is not significant. However, one can only speculate about the true value of E_a due to large experimental errors. The major sources of the error are the uncertainty in the value of D_{O2} and also the dependence of this diffusion process on temperature. Since the steady state current on microdisc is directly proportional to D_{O2}, its temperature dependence will directly influence the value of n_{app}. E_a of 13.8 kJ mol^{-1} for diffusion of oxygen in water is used in all the calculations of n_{app}, but literature data are quite scattered and give values from 13.7 to 18.4 kJ mol^{-1} [142, 150, 153, 154]. Thus, from the obtained data and taking into account the accuracy of measurements, it can be concluded that the change of n_{app} over the range of temperatures tested is negligible.

It is difficult to ascribe a precise physical meaning to E_a in the case of $n_{app}=f(T)$ for oxygen reduction. The n_{app} is a complex function of several rate constants, including adsorption and desorption rates, surface coverage of spectator species and diffusion processes (see equation (4.19)). All these parameters are temperature dependent: the diffusivity and electron transfer rate constants are expected to increase and at the same time the desorption processes would be favoured with increasing temperature. Thus, the overall behaviour of n_{app} will result from the interplay of all these parameters.

4.8 Summary

A simple system for oxygen microelectrode calibration was developed and successfully used. The system utilises the dilution method and essentially can be used to characterise any oxygen sensor. The procedure involves just initial saturation of a stock solution and a Winkler titration on its sample, which are followed by automated c_{O2} increments. A software controlled pump allows precise control over the DO concentration increments and range.

A range of microelectrodes radii were calibrated against DO concentration in 0.5 M NaCl solution and the responses were found to be linear in range up to full oxygen saturation. Significant residual currents were observed determining the detection limits of 8.1, 2.9 and 0.9 μM for 4.7, 12.1 and 24.5 μm electrodes radii, respectively. Calibration curves also served to determine n_{app} for various sizes of microdiscs.

The parameters obtained from calibrations allow calculation of DO concentration form the limiting current with errors not exceeding 4% at microdiscs of 12.5 and 25 μm radius and under 5% for 5 μm radius for concentrations >50 μM. At lower concentrations the errors are larger due to residual currents. The possibility of obtaining DO concentration solely on the basis of analytical equation and determined values of n_{app} was also demonstrated. This approach yields more significant errors: 15, 14 and 11% for 5, 12.5 and 25 μm nominal electrode radius respectively.

n_{app} was examined as function of electrode radius and temperature. $n_{app}=f(a)$ was modelled with the equation relating it to the kinetic parameters of the ORR. Despite large errors on n_{app} it was possible to conclude that the ORR in examined conditions proceeds primarily via the series mechanism i.e. with two two-electron steps.

5 Non-steady state measurements

5.1 Chapter overview

This chapter describes the evaluation of double potential step chronocoulometry as a possible method for very rapid determination of DO concentration. The considered step duration is of the order of milliseconds for improved sensor response time and high immunity to external flow, which could result in the microelectrode working directly in the water column without the stop flow system. The rationale for the approach is presented, including the interplay of the diffusion layer and the flow related boundary layer.

Further, the principles of the double potential steps approach are given together with the initial data on DO detection. Calibrations of the sensor for a range of step durations and long term stability data are presented. Preliminary assessment of the performance of the method under flow conditions is also included.

5.2 Introduction

Although the microelectrode response is rapid, the steady state still requires an appreciable amount of time to be established ($t \gg a^2 / \pi D$). For the considered application – obtaining a vertical DO concentration profile – where the probe is descending at around 1 m s^{-1} this response time translates to sampling c_{O2} every 10 m. While it is a significant improvement to presently employed methods (water sampling followed by on-board analysis, Clark type devices) a better spatial resolution (< 1 m) is desirable. In addition, even at smaller microelectrodes the limiting current is sensitive to convection, which requires measurements in stagnant sample, i.e. the necessity to employ a stop-flow system on the constantly moving probe. The system consumes additional power and space, both very limited on oceanographic rigs.

For the above reasons it would be beneficial to perform the measurements directly in the water column, without the need for a stop-flow cell. Even more important is improving the response time to sub-second values. Both targets can potentially be achieved by non-steady state measurements, i.e. measurements at very short times after a potential step, when the diffusion layer at the microdisc is not fully established. Fast potential step techniques at microelectrodes were shown to be very useful when investigating kinetically fast reactions (e.g. [210]) or continuously monitoring oxygen in aprotic media, where cross interfering reactions of superoxide radicals with CO_2 need to be avoided (e.g. [211, 212]). With microelectrodes faradaic information can be obtained for step duration down to submicrosecond [213].

The choice of the potential step duration translates directly into the response time and has significant implications on the flow sensitivity. To evaluate the effect of flow on the microdisc response the relationship between the diffusion layer and the flow related boundary layer has to be established. It is assumed that the flow is laminar and that the microdisc is inlaid within an infinite plane. For the microelectrode mounted on the CTD moving in one direction it would be most appropriate to use the model describing the flow across a flat moving plate [214]. In this model however, the boundary layer thickness is dependent on the distance from the leading edge of the plate and exact solutions are difficult due to more complicated flow patterns around the CTD package. Thus, it is convenient to use the flow model in a confined channel, where the microelectrode is inlaid in the channel wall. The principles for this model are well established in the literature, e.g. [214-216]. Also, later in this chapter the flow dependence of the microelectrode response is assessed in the channel arrangement.

For laminar flow in a rectangular channel a parabolic velocity profile is established (Figure 5.1)

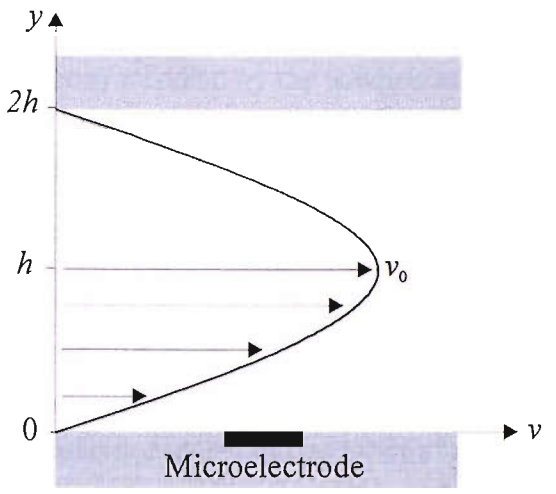

Figure 5.1 A schematic representation of solution steady state velocity profile in laminar flow in a rectangular channel.

The solution velocity v in a rectangular channel with the width of $2h$ can be estimated at any given distance y from the wall as a function of the maximal velocity v_0 in the centre of the channel [214]:

$$v = v_0\left[1-\frac{(h-y)^2}{h^2}\right] \tag{5.1}$$

At the same time the thickness of the diffusion layer δ_D of the microelectrode at time τ after the potential step can be calculated from equation (5.2). More conservatively, equation (5.3) can be used to estimate the distance δ_{bulk} from the electrode where the concentration reaches 0.99998 of the bulk concentration [13], thus at this distance the diffusion layer is fully contained. Although these equations are valid only for planar diffusion, it is justified to use them for microdisc when the value of τ is small (few milliseconds), i.e. when the contribution of radial diffusion is not significant.

$$\delta_D = \sqrt{\pi D\tau} \tag{5.2}$$

$$\delta_{bulk} = 6\sqrt{D\tau} \tag{5.3}$$

It is possible now to assess the deformation of the diffusion layer by calculating the distance z (determined by v) travelled by the solution at $y=\delta_D$ or $y=\delta_{bulk}$. Table 5.1 compares values of δ_D, δ_{bulk} and z at different times calculated for a rectangular channel with wall distance of 1 cm and v_0=100 cm s^{-1} (approximate CTD velocity).

Table 5.1 Diffusion layer thickness (δ) at different timescales and the liquid velocity (v) at δ with corresponding distance z travelled by the liquid flowing with velocity v over time τ. The values are calculated for a flow in rectangular channel (h=1 cm), v_0=100 cm s^{-1} and D=2.16×10^{-5} cm^2 s^{-1}.

τ / ms	$\delta_D = \sqrt{\pi D\tau}$			$\delta_{bulk} = 6\sqrt{D\tau}$		
	δ_D / μm	v at δ_D / cm s^{-1}	z / μm	δ_{bulk} / μm	v at δ_{bulk} / cm s^{-1}	z / μm
0.5	1.8	0.01	0.05	6.2	0.12	0.6
1	2.6	0.02	0.20	8.8	0.18	1.8
2	3.7	0.04	0.80	12.5	0.25	5.0
5	5.8	0.10	5.00	19.7	0.39	19.7
10	8.2	0.20	19.99	27.9	0.56	55.7
20	11.6	0.40	79.92	39.4	0.79	157.4
50	18.4	1.00	498.75	62.4	1.24	621.6

For very short times (1 ms and 0.5 ms) the diffusion layer does not extend further than 3 μm into the bulk of the solution. At this distance the solution velocity is small and the total displacement over time τ is of order of fractions of micrometer. The ratio of z to the microelectrode size (e.g. a=5 μm) suggests that the diffusion layer should not be significantly deformed by the motion of the solution. For larger values of τ the displacement z increases very quickly compared to the diffusion layer dimensions. Thus, for measurements in flowing conditions the potential pulse duration should be restricted to 1 ms or shorter. The deformation of the diffusion layer on this timescale will be insignificant to alter the measured currents.

5.3 Double potential step chronocoulometry: high frequency oxygen measurements

5.3.1 Principles

When switching the potential between the cleaning and the measuring value, several additional processes occur on top of the oxygen reduction. These processes involve the charging of the double layer and different faradaic processes, such as platinum oxide formation and reduction and impurities redox reactions. In general, the charge observed during the cathodic (Q_C) and anodic (Q_A) steps will be the sum of all the constituting charges (equations (5.4), (5.5)). Due to the irreversibility of the ORR the corresponding charge Q_{O2} is only present during the cathodic step.

$$Q_C = Q_{dl} + Q_{\substack{oxide \\ reduction}} + Q_{\substack{impurities \\ reduction}} + Q_{O2} \tag{5.4}$$

$$Q_A = Q_{dl} + Q_{\substack{oxide \\ formation}} + Q_{\substack{impurities \\ oxidation}} \tag{5.5}$$

Since the electrode roughness can change with time, so will the double layer charge (Q_{dl}) and the charge due to oxide formation/reduction. These variations would prevent obtaining a reliable oxygen reduction charge from a single potential step chronocoulometric measurement. A simple solution to this is to apply measuring and cleaning steps of equal duration and measure the total charge Q_{tot}. In this case the double layer charge and charges related to the surface processes cancel each other and the remaining charge is only due to oxygen reduction and the reactions involving impurities (equation (5.6)). The magnitude of the additional charge due to impurities will largely depend on the reversibility of the redox processes that they undergo. This background charge will be small for reversible couples (appropriate equations describing chronocoulometric response to the double potential step at a microdisc for diffusion controlled reversible reactions are available in the literature, e.g. [217, 218]), and larger as the degree of irreversibility increases (the difference between the charges of forward and backward reactions increases).

$$|Q_{tot}| = |Q_{O2}| + \left|Q_{\substack{impurities \\ reduction}}\right| - \left|Q_{\substack{impurities \\ oxidation}}\right| \tag{5.6}$$

The general idea of the double potential step chronocoulometry for oxygen detection is depicted in Figure 5.2.

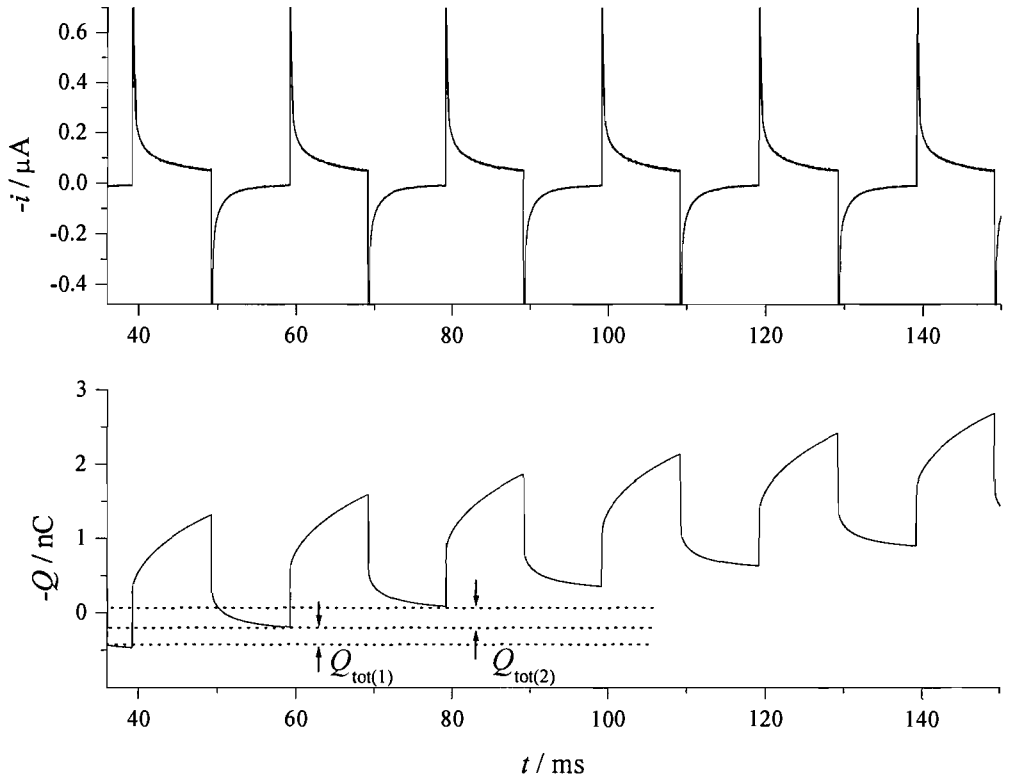

Figure 5.2 Double potential step chronoamperometry (top) and the corresponding chronoulometric curve (bottom) at Pt microdisc (a=12.5 μm) in 0.5 M NaCl containing 70 μM O_2. The potential was stepped between +0.2 and -1.05 V (vs SMSE) with step duration of 10 ms. $Q_{tot(i)}$ indicate subsequent double step charges used to extract the DO oxygen concentration.

The most convenient way to obtain the relationship between the charge and DO concentration is to perform a calibration experiment. This approach (presented in the following section) was found to yield linear dependence and therefore a straight forward way to determine DO concentration. However, in principle it should be

possible to predict the charge due to oxygen reduction analytically. While the theoretical current response can be integrated analytically or numerically to obtain a model chronocoulometric curve, a complication arises due to the behaviour of n_{app}. It was shown in section 4.6 that n_{app} is strongly dependent on mass transport conditions (n_{app} decreases as the microdisc radius decreases). One can expect that n_{app} will also vary as the diffusion changes from semiinfinite linear diffusion to pseudo-hemispherical at larger τ. Indeed, such variation is observed when the experimental data is compared to simulated current transients or chronocoulograms where n_{app} was assumed constant. Thus, to predict the charge analytically the $n_{app}(t)$ function has to be determined. Alas, the attempts to establish this relationship gave inconsistent results and the problem should be reinvestigated. The methodology and some of the findings are reported in the Appendix (section 9.4).

5.3.2 Calibration

To test whether this approach can give quantitative data on oxygen concentration, a series of calibrations were performed for various step durations. The experiments were conducted as described in Chapter 4 and the high frequency potential waveform was applied to the working electrode continuously throughout the duration of the experiment. The results for τ ranging from 1 to 20 ms are shown in Figure 5.3 and Figure 5.4.

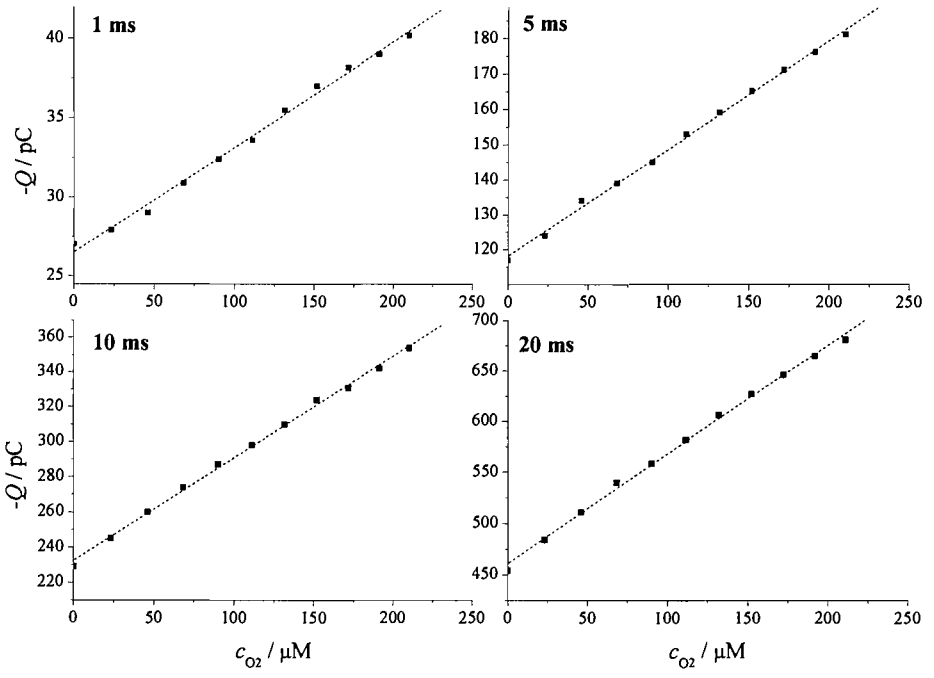

Figure 5.3 Total charge during double potential steps as a function of DO concentration in 0.5 M NaCl at 25.5 °C. The working electrode was Pt microdisc (a=12.5 μm) and the potential was stepped between +0.2 and -1.05 V vs SMSE. Potential step durations τ are indicated on the graphs. The dashed lines represent the least square linear fits of the experimental data.

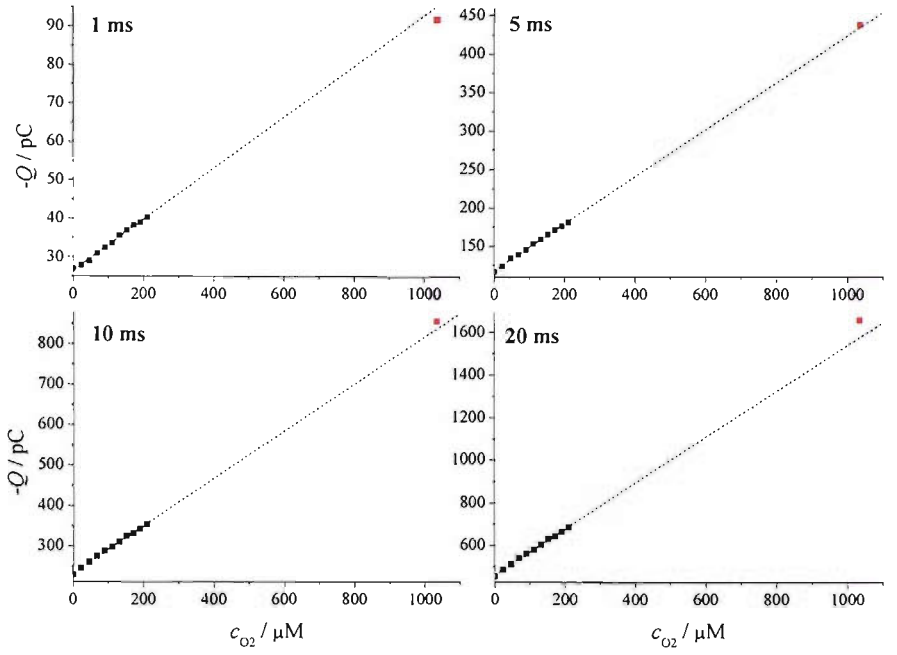

Figure 5.4 Total charge during double potential steps as a function of DO concentration in 0.5 M NaCl at 25.5 °C. The working electrode was Pt microdisc (a=12.5 μm) and the potential was stepped between +0.2 and -1.05 V vs SMSE. Potential step durations τ are indicated on the graphs. The fits (dashed lines) of the calibration data are extrapolated to show the linearity over the concentration range up to full oxygen saturation (measurement in oxygen saturated solution – red points).

In all cases a linear relationship between c_{O2} and the double step charge (Q) was obtained. The correlation coefficients of 0.9975 to 0.9988 were found with standard deviation of 1.0% for 1 ms steps and 0.7% for 5 to 20 ms (SD relative to the average charge). An extrapolation of the linear fit (over the range from zero to air saturation) corresponds very well with the charges recorded in oxygen saturated solutions. Irrespectively of the step duration, a significant background current was present. The intercepts of the calibration curves show a linear dependence (R=1) on the step duration (Figure 5.5) and consequently on the current integration period. This suggests that the underlying current is constant and independent of the time after the potential step. Thus, the residual charge cannot be ascribed to an additional faradaic process (where i should be proportional to $t^{-1/2}$), but it is most likely due the baseline

offset originating from the measurement hardware. Currents corresponding to the residual charges were estimated to be between 26.5 and 23.1 nA. Since the current follower gain was set to 10^{-5} A/V the average current of 24.1 nA corresponds to as little as 1.2 mV shift in current follower baseline.

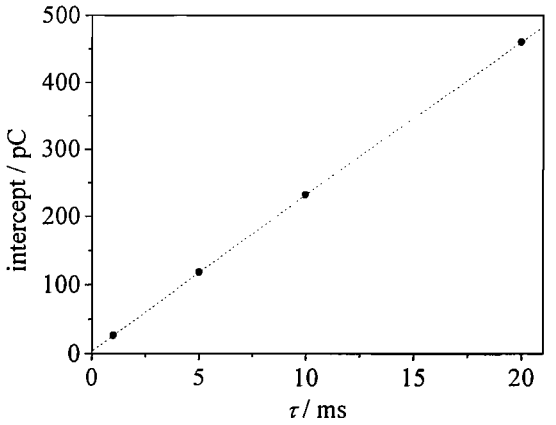

Figure 5.5 Intercepts of the calibration curves from Figure 5.3 as a function of the potential step duration.

5.3.3 Long term stability

The same methodology as for the steady state measurements was applied to test the microelectrode response stability. The potential waveform consisting of measuring and cleaning steps of equal duration (at -1.05 and +0.2 V, respectively) was applied continuously to the working microelectrode. Figure 5.6 shows the long term traces obtained with a 5 μm radius Pt microdisc in a sealed cell containing air saturated 0.5 M NaCl. The points on the graphs represent an average double potential step charge calculated from the integration of a random snapshot of the current response. The time of the snapshot always corresponded to a multiple of the waveform period. The data are shown for two waveforms of different step duration: 20 and 1 ms. A reasonably good stability was observed, with better statistical distribution for longer potential step. The key data and statistical results of the stability tests are summarised in Table 5.2

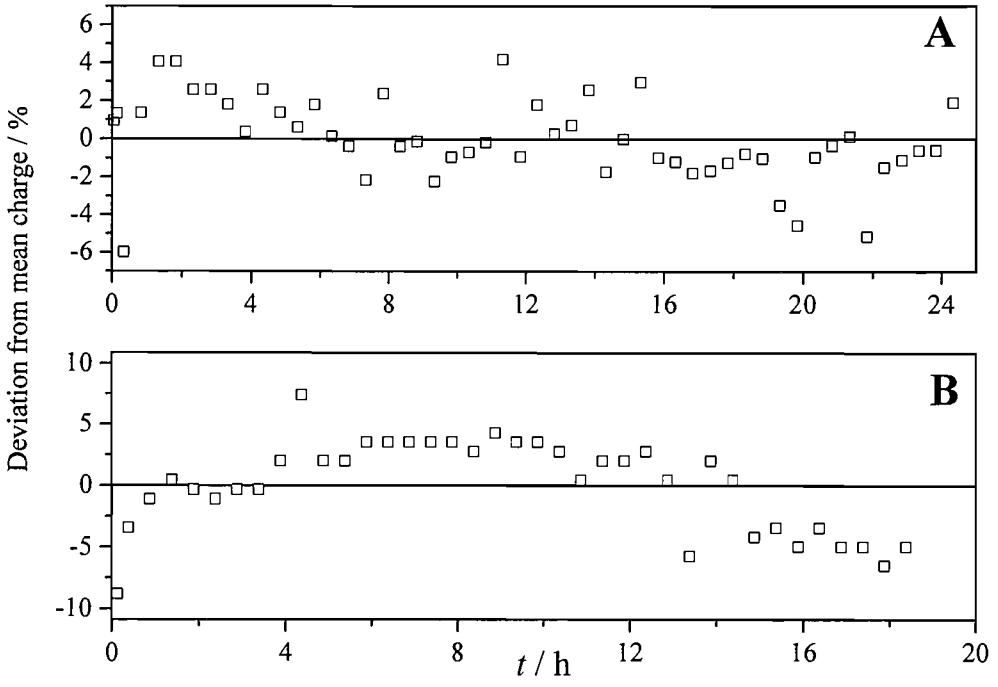

Figure 5.6 Long term stability of the microelectrode response in air saturated 0.5 M NaCl solution. In each case Pt microdisc (a=5 μm) was used and the potential was continuously stepped between +0.2 and -1.05 V (vs SMSE). The step duration was 20 ms (A) and 1 ms (B). Each point represents an average charge of at least 10 consecutive double potential steps.

Table 5.2 The key parameters of the stability experiments using double potential step chronocoulometry at a microelectrode (a=5 μm).

Step duration / ms	Number of integrated cycles	Number of points	Experiment duration / h	Standard deviation		Mean difference	
				%[a]	μM DO[b]	%[a]	μM DO[b]
20	20	51	25	2.2	4.8	5×10^{-5}	1×10^{-4}
1	10	39	19	3.7	8.2	5×10^{-6}	1×10^{-5}

[a] with respect to the mean charge over the duration of experiment,

[b] calculated for the experimental conditions, i.e. air saturated 0.5 M NaCl, 221.1 μM DO

The deviations of the total charge are noticeably larger compared to the steady state measurements (SD below 1%). This is believed to be due to much higher sensitivity to the variations of the baseline resulting from the measurement hardware. In addition, short time measurements require a high dynamic range from the acquisition system and appreciable amount of digital noise can be observed for lower currents.

The effect of continuous potential stepping during the stability experiment on the surface state of the electrode was evaluated by cyclic voltammetry in sulphuric acid (Figure 5.7). As for steady state measurements (cleaning for 1 s, measuring for 12 s) the electrode roughened with time. For the 25 h experiment with the step duration of 20 ms the roughness factor (RF) was found to increase from 1.9 (polished electrode) to 9.9. The increase in RF is comparable to the one observed with the waveform used for steady state measurements, thus indicating the dependence of this effect mainly on the value of the cleaning potential and not on its duration.

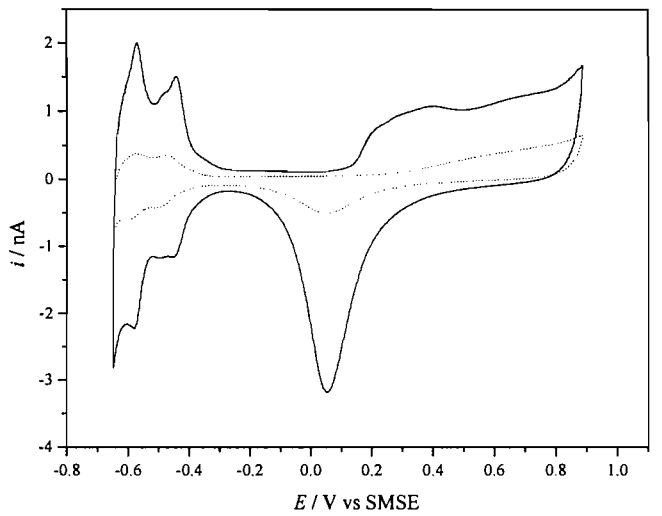

Figure 5.7 Cyclic voltammograms at Pt microdisc (a=5 μm) in 1 M H_2SO_4 before (dotted line) and after (solid line) the 25 h stability experiment in 0.5 M NaCl; v=200 mV s^{-1}. In the stability experiment the electrode potential was continuously switched between +0.2 and -1.05 V vs SMSE (20 ms at each potential).

5.4 Performance under flow conditions

5.4.1 Experimental arrangement

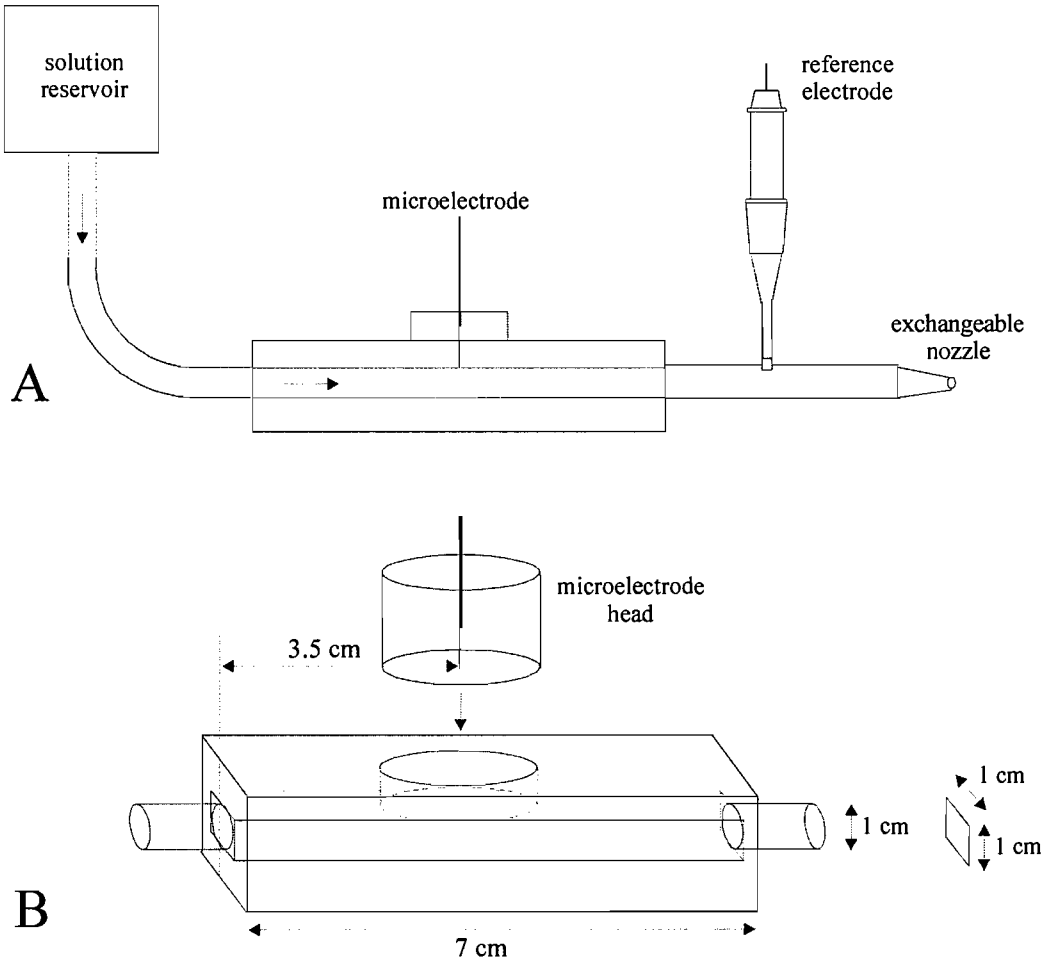

Figure 5.8 A schematic of the gravity fed flow system (A) and the magnification of the perspex flow cell (B) used for microelectrode tests under flow conditions. Parts of the schematic are not to scale.

The flow dependence of the microelectrode was investigated using the system schematically depicted in Figure 5.8. The system consisted of a Perspex flow cell with 7 cm long square channel (side length 1 cm) and a cylindrical void to fit the sensor head. The cell was connected with rubber tubing to the solution reservoir equipped with a valve and the flow was achieved simply by gravity. Another piece of tubing led from the cell outlet to the collection vessel. The reference electrode was fitted directly in the tubing downstream from the microelectrode. Different flow rates were achieved by fitting a range of nozzle sizes at the end of the flow path.

The flow rate (V_f, in $cm^3\ s^{-1}$) was measured volumetrically and subsequently the average solution velocity $\bar{v}$ was calculated:

$$\bar{v} = \frac{V_f}{A} = \frac{V_f}{4h^2} \tag{5.7}$$

where A is the area of the cross section of the channel (in this case 1 cm^2). For a parabolic velocity profile in the square channel with width $2h$ the average velocity is given by

$$\bar{v} = \frac{1}{2h}\int_0^{2h} v_0\left[1-\frac{(h-y)^2}{h^2}\right]dy \tag{5.8}$$

After integration and rearrangement we get

$$v_0 = \frac{3}{2}\bar{v} \tag{5.9}$$

Substituting equations (5.7) and (5.9) into (5.1) yields an expression allowing the prediction of the liquid velocity at any given distance from the wall (y):

$$v = \frac{3}{8}\frac{V_f}{h^2}\left[1-\frac{(h-y)^2}{h^2}\right] \tag{5.10}$$

5.4.2 Flow dependence of the microelectrode response

The flow dependence of the microelectrode response was investigated for 1 ms and 0.5 ms step durations. The waveform was applied continuously and the charge was calculated from four consecutive random snapshots lasting ten times the waveform period. In each case the microdisc was flush with the channel wall, half way down the channel length. Various flow rates were achieved by changing the nozzle at the end of the flow path. The results for a range of electrode radii are shown in Figure 5.9.

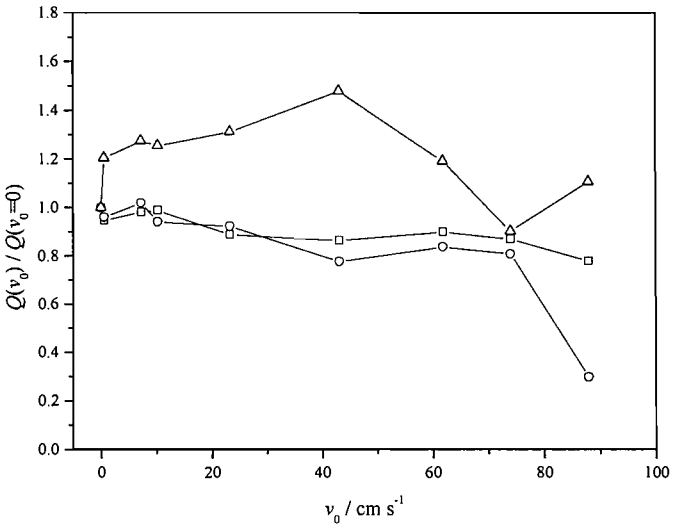

Figure 5.9 Normalised double step charges as a function of solution velocity in the centre of a square channel (1 cm width). The points represent the average values of at least two experiments. Microdisc radii: 5 μm (□), 12.5 μm (○), 25 μm (△). The potential step duration was 1 ms.

Clearly the smallest microdisc is the least influenced by the flow of solution, and the flow effect gets more pronounced for larger electrodes. However the observed trends are inconsistent. The decrease of charge with increasing flow rates is in contradiction with theory and experimental data found in the literature [216], where the microdisc currents increase consistently at higher flow rates in rectangular channel. These discrepancies were initially ascribed to a turbulent flow which was most probably generated at the inlet of the flow cell, where the circular cross section of the

connector changes to square channel. With the relatively high flow rates used, the distance of 35 mm between this transition point and the microdisc was not sufficient to re-establish a laminar flow pattern. However, this interpretation cannot be correct as any turbulent flow patterns should result in increased currents at a microdisc as well. To a certain extent the decreasing charge can be attributed to the lowering of the value of n_{app}.

Additionally, the flow dependence was assessed in a simpler arrangement. The electrodes were placed directly in a rubber tube, which was several tens of centimetres long. In this arrangement it was difficult to control the position of the microdisc with respect to the tube wall. Thus, the estimation of the linear solution velocity at the microelectrode was not possible and the results of these experiments can only be treated qualitatively. Three electrode radii were used for the trials and the flow dependence of their responses to double potential step are shown in Figure 5.10.

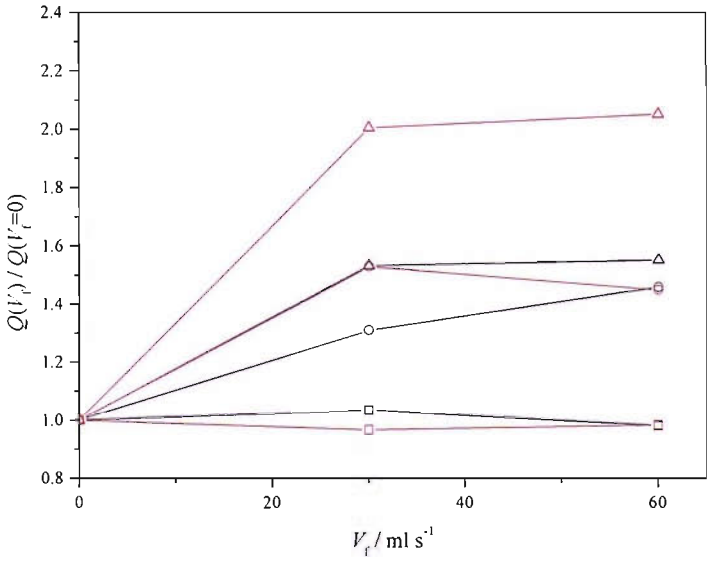

Figure 5.10 Normalised charges of double potential step in air saturated seawater as a function of flow rate. Microdisc radii: 5 μm (□), 12.5 μm (○), 25 μm (△). The potential step duration used was 0.5 ms (black) and 1 ms (red).

The flow dependence decreases with the microdisc radius. Moreover, the response is less affected for shorter steps, which is in agreement with the considerations given in the introduction of this chapter, i.e. that the thinner the diffusion layer the less it is distorted by the liquid movement. The fast measurements offer significantly smaller flow sensitivity than steady state measurements. The maximal enhancement of the response was found approximately 2× for the largest microdisc, while other researchers reported similar or higher increases in steady state current for the same size or smaller microdisc at flow rates below 1 ml s^{-1} [216, 219]. Practically no flow effect is observed for microdisc with 5 μm radius. This behaviour is very encouraging from the point of view of the sensor application directly in the water column.

5.5 Instrumental requirements

Additional attention to the instrumental and acquisition parameters has to be paid when performing fast measurements. Two sources of errors and inconsistent readings were identified during the experiments on millisecond timescales. The first one is related to the performance of the operational amplifier in the current follower, another arises from underperformance of the signal acquisition system.

If the response time of the op-amp is insufficient, the current rise immediately after a potential step is not sharp and does not reflect the electrochemistry in the investigated system. In this work, measurements as short as 1 ms were performed which required a response time of the order of microseconds. Even more important is the choice of the resistor and the capacitor in the feedback loop of the first op-amp in the current follower circuit. The *RC* constant has to be matched with the electrode impedance and a wrong choice can result in the distortion of the shape of the current transient at short times. The effect is visible as so called 'ringing' of the current signal (Figure 5.11). Similar effect is observed when an additional capacitance source is present somewhere in the current path, e.g. poor electrical connection or a discontinuity within the reference electrode. Such

distortions will certainly give erroneous charge values in coulometric measurements (the more pronounced the shorter the step duration).

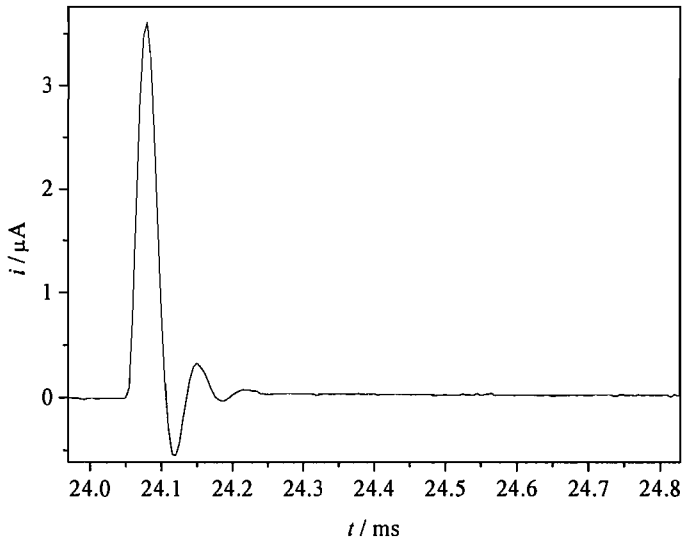

Figure 5.11 Instrumental response ("ringing") to the potential step (+0.2 to -1.05 V vs SMSE) at a Pt microdisc (a=2.5 μm).

Equally important is the choice of the acquisition parameters. Unlike in steady state measurements it is important to record complete transient including very high currents for short times. Since the signal decays very fast, the signal is a few orders of magnitude smaller at the end of the step. To be able to resolve these small currents accurately, it is essential to use acquisition system with large dynamic range. Moreover, the peak current has to be well defined to capture it in full, demanding significant speed of data acquisition. The minimal data acquisition parameters needed for reliable and reproducible measurements were found to be 200 kHz sampling with 16 bit resolution. While the appropriate instrumentation is available in the laboratory, a different solution has to be sought for field measurements. One of the options is the construction of new electronic board which would integrate the measured currents in real time. A prototype was built by co-workers in the National Oceanography Centre, Southampton (NOCS), which contains a current follower unit

with low pass filtering. This arrangement effectively integrates the current response and the output is a simple analogue voltage proportional to the charge.

5.6 Summary

Non steady-state measurements were shown to be a potential way forward to the improvement of the DO microelectrode sensor performance. A linear dependence between the double potential step charge and DO concentration was found for step duration down to 1 ms. Since no obvious relationship between the charge and oxygen concentration is available, the calibration is necessary for quantitative DO determination. The response of the sensor showed good stability for periods up to 25 h of continuous operation. Preliminary study of flow dependence of the sensor working in non-steady state regime proved very encouraging, in particular for smaller microdisc.

6 Oxygen reduction under hydrodynamic conditions

6.1 Chapter overview

As an alternative to non-steady state measurements, another method of removing the flow sensitivity of the electrode response is investigated. An attempt was made to create reproducible hydrodynamic conditions where the rate of the forced mass transport to the electrode should be much greater than that due to the external flow. This ensures that the effect of external flow on the recorded current can be neglected. Two methods of creating forced convection conditions were evaluated: high frequency vibration of the electrode in bulk solution and in the vicinity of a stationary wall. The vibration of the electrode was achieved by mounting it on a piezoelectric transducer. In the remainder of this chapter the enhancement of the limiting current caused by electrode vibration is investigated. The performance of the vibrating electrodes is characterised for purely mass transport controlled system and for oxygen reduction.

6.2 Microelectrode vibrating in the bulk

6.2.1 Fabrication and characterisation of vibrating microelectrodes

The microelectrodes were fabricated using thin soda glass capillaries as described in the Chapter 2 and subsequently mounted on a transducer using quickset epoxy resin (RS, UK). The transducers used were 27 mm / 4.2 kHz (Bell Piezo Ceramics Inc., Taiwan) of nominal resonant frequency 4.2 kHz (± 0.5 kHz, in air). Two kinds of vibrating electrodes were prepared: some vibrating perpendicularly to the microdisc surface and others vibrating parallel to it (Figure 6.1). A 1250 Frequency Response Analyser (Solartron, UK) was used to generate the AC voltage to drive the transducers.

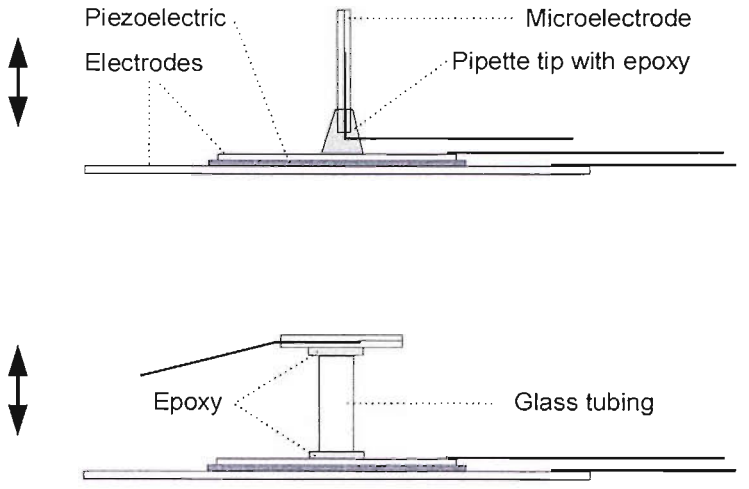

Figure 6.1 A schematic picture of vibrating electrodes in two arrangements: vibrating normal to the electrode surface (top) and vibrating parallel to the electrode surface (bottom). In each case the direction of vibration is indicated with an arrow.

The resonance frequency of the piezoelectric corresponds to the largest displacement of the electrode, which correspondingly should result in the largest enhancement in mass transport. To find the resonance frequency under the experimental conditions the piezoelectric driving voltage was kept constant (sine wave, amplitude A=3 V) and the frequency was varied. The electrode was placed in deoxygenated $Ru(NH_3)_6Cl_3$ solution and polarised at -0.85 V i.e. in the diffusion controlled plateau region. An example of a plot characterising the vibrating electrode is shown in Figure 6.2. For all vibrating electrodes, irrespectively of arrangement, the resonance frequency f=3.4 kHz was found and chosen for later experiments.

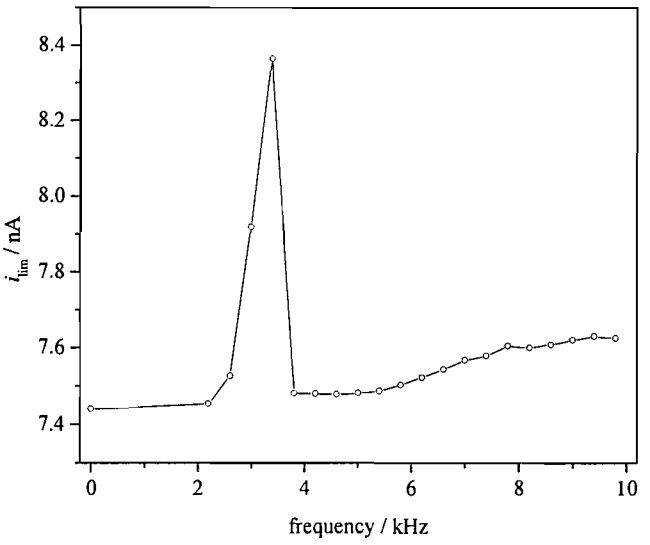

Figure 6.2 The dependence of the limiting current on transducer driving frequency. Perpendicular vibration, AC voltage amplitude: 3 V; electrode: Pt microdisc a=5 μm; solution: 4.9 mM $Ru(NH_3)_6Cl_3$ in 0.25 M KCl.

6.2.2 Vibrating electrodes performance in $Ru(NH_3)_6^{3+}$ system

The enhancement of the mass transport to the electrode was evaluated in $Ru(NH_3)_6^{3+}$ system. The vibration frequency was set to the resonant value f=3.4 kHz and the magnitude of the piezoelectric displacement was varied by altering the amplitude of the driving voltage. The results of perpendicular and parallel vibration of the microelectrode are shown in Figure 6.3 and Figure 6.4, respectively. In order to eliminate the AC component of the recorded current the raw signal was passed through a low-pass filter.

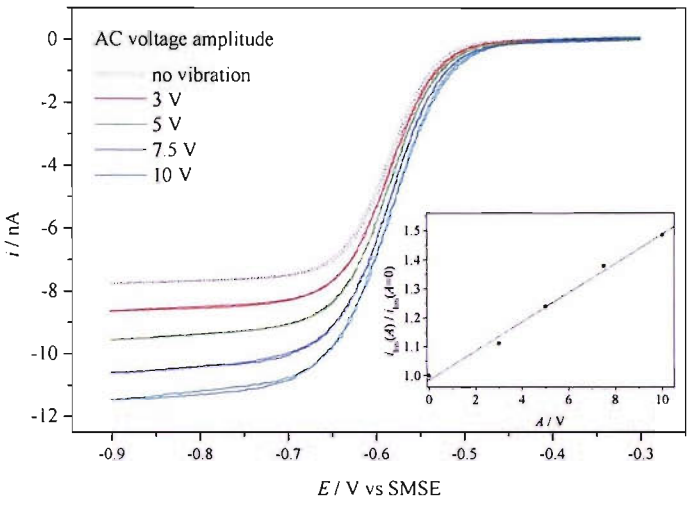

Figure 6.3 $Ru(NH_3)_6Cl_3$ reduction at vibrating Pt microdisc (a=5 μm). Transducer vibrated at f=3.4 kHz, amplitude varied, electrode vibrating in direction perpendicular to its surface. Dotted black line: the non-vibrated electrode response. The inset shows the limiting current (read at -0.85 V) as a function of the transducer driving voltage amplitude. The limiting currents are normalised with respect to i_{lim} at a non-vibrated electrode.

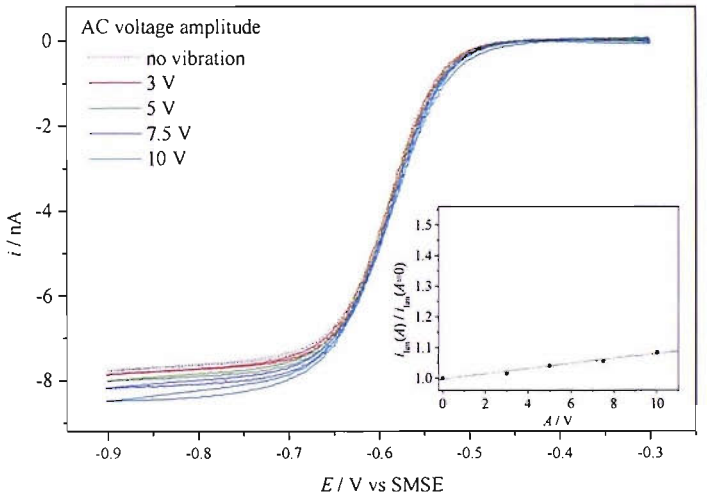

Figure 6.4 $Ru(NH_3)_6Cl_3$ reduction at vibrating Pt microdisc (a=5 μm). Transducer vibrated at f=3.4 kHz, amplitude varied, electrode vibrating in direction parallel to its surface. Dotted black line: the non-vibrated electrode response. The inset shows the limiting current (read at -0.85 V) as a function of the transducer driving voltage amplitude. The limiting currents are normalised with respect to i_{lim} at a non-vibrated electrode.

The enhancement in the limiting current can be seen in both cases, clearly being more pronounced for the perpendicular vibration arrangement, where the limiting current for 10 V amplitude is 1.65 times the limiting current at non-vibrated electrode. The increased current is explained in terms of a deformation of the diffusion layer. As the electrode moves towards the bulk the diffusion layer is "squashed" and the concentration gradient increases. The larger the amplitude the faster the electrode moves and the larger the displacement; this is analogous to increasing the rotation rate in RDE experiments. When the electrode is moving in the opposite direction a wake is probably formed and the radial mass transport towards the electrode axis is increased.

To get more insight on the observed phenomenon the raw signal was monitored while the electrode was held at a potential in the mass transport limited current plateau region (-0.85 V). The AC current should reflect the changes of the mass transport variation on the time scale of the vibration period. Although the piezoceramic was not immersed in the solution, the analysis was complicated by a very strong AC coupling of the transducer driving waveform to the microelectrode response. To eliminate the non-faradaic element of the response, the current was also recorded with the electrode held at 0.0 V, i.e. where no faradaic processes occur. Subtracting the two signals (at -0.85 and 0.0 V), under the condition that the sine waves were in phase, should have allowed observing the periodic variations of the limiting current and correlating them with the electrode movement. The resulting sinusoidal current response was however irreproducible between measurements in terms of phase shift difference with respect to the transducer driving waveform. For the parallel vibration the signal had a frequency f, instead of $2f$ as expected for a diffusion layer deformation dependent only on the magnitude of the electrode displacement and not on its direction. These observations suggest that the fine structure of the current was completely dominated by effects related to the AC voltage used to drive the transducer, which prevented obtaining any information on short time limiting current variations.

6.2.3 Oxygen reduction

With more significant enhancement in mass transport, the electrodes vibrating perpendicularly to their surface were chosen for further experiments. ORR was investigated in a similar manner and the voltammetric response of vibrating electrodes in oxygen saturated 0.5 M NaCl is shown in Figure 6.5.

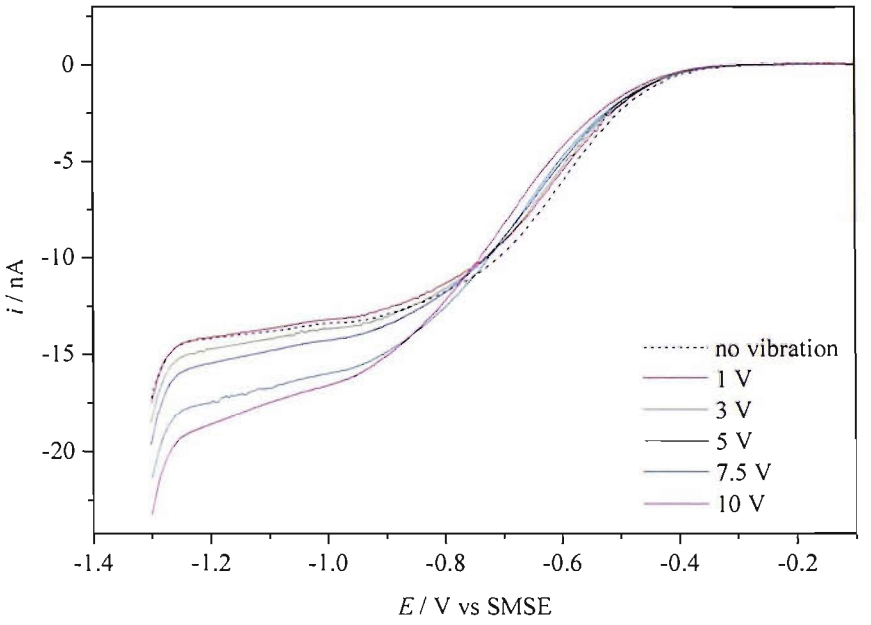

Figure 6.5 Oxygen reduction voltammograms recorded in O_2 saturated 0.5 M NaCl using vibrating Pt microdisc electrode (a=5 μm). The direction of the vibration was perpendicular to the electrode surface. The transducer was fed with a constant frequency (3.4 kHz) sine wave, whose amplitude was varied as indicated on the graph. Before recording the voltammogram the electrode was polarised at -1.3 V for 1 s, followed by a step to +0.2 V (1 s). Shown on the graph are the positive scans of the first cycles at 20 mV s^{-1}; a low pass filter was used to eliminate the AC component of the signal.

The AC component of the recorded current was eliminated with low pass filter at the output of the current follower, so only the DC component of the vibration is visible. The limiting current increases with the vibration amplitude, clearly

pointing to the enhanced mass transport to the electrode. One can also observe an appreciable shift of the half wave potential towards more negative values with increasing amplitude. This agrees well with the data presented earlier for various sizes of microelectrodes, where the increasing mass transfer coefficient resulted in a similar, though much more pronounced shift (see section 3.3.2, Figure 3.16).

A similar enhancement in i_{lim} was also observed in potential step experiments. The limiting currents are compared with those obtained from voltammetry (measured at -1.05 V vs SMSE) in Figure 6.6. Also shown are the limiting currents recorded with a 2.5 μm radius vibrating microdisc. With the smaller microelectrode there is no appreciable enhancement observed. The variations of i_{lim} with the amplitude of the transducer driving waveform can be treated in terms of the reproducibility of measurements with small microdisc electrodes. The limiting currents are normalised with respect to the limiting current recorded at a non-vibrating electrode.

While forced convection conditions undoubtedly result in higher limiting currents for oxygen reduction, the enhancement is smaller compared to the ruthenium system (with 10 V vibration amplitude i_{lim} compared to the stationary electrode is 1.25 and 1.65 for oxygen and $Ru(NH_3)_6^{3+}$ reduction, respectively). One can conclude to the lowering of the value of n_{app} for ORR under high mass transport conditions (similarly to the decrease of the stationary electrode size). This effect is not observed with a simple fast electron transfer reaction.

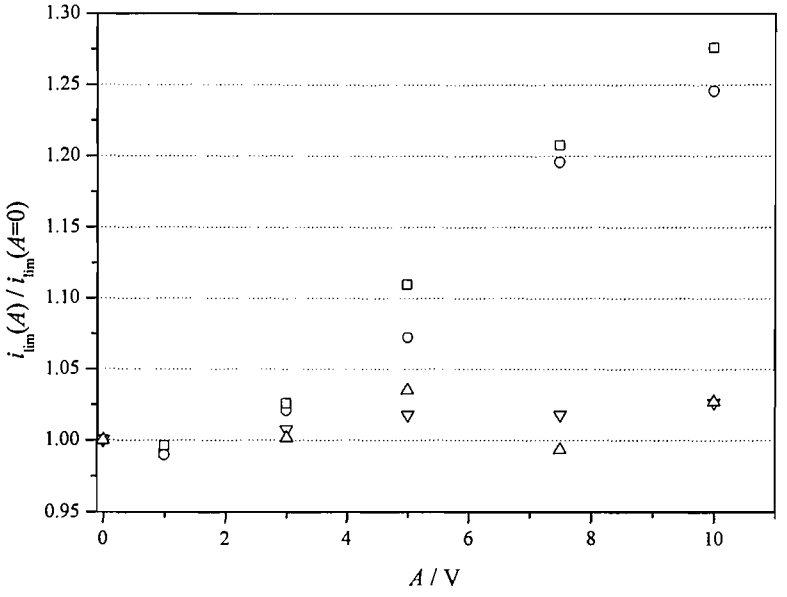

Figure 6.6 Relative limiting currents for oxygen reduction in 0.5 M NaCl at vibrating microelectrodes vs. amplitude of the transducer driving waveform (sine wave, f=3.4 kHz). The currents recorded for amplitude A, $i_{lim}(A)$ are normalised by the limiting current at non-vibrating electrode, $i_{lim}(A=0)$. The data was obtained with 5 μm radius microdisc from: voltammetry (O) and potential step (□) and with 2.5 μm radius microdisc: voltammetry (▽) and potential step (△).

6.3 Microelectrode vibrating against stationary wall

6.3.1 Experimental

The vibration of the electrode in the vicinity of a stationary wall was investigated as an alternative to the previously described experiment. In this approach the microelectrode tip is positioned very close to an insulating surface, i.e. the distance between the microdisc and the insulator is comparable to the size of the diffusion layer. In this arrangement the movement of the tip will cause an additional hydrodynamic effect (alike pumping action) compared to vibration in the bulk of solution. The experimental setup is shown in Figure 6.7. The position of the

microelectrode was fixed and the glass plate was mounted on a SECM (scanning electrochemical microscope) positioning module. This allowed precise control of the distance between the electrode and the glass wall. The electrodes used did not have a conical shape typical for SECM experiments. Standard cylindrical tips were used with 0.9 to 1.0 mm glass radius. Positioning the tip surface parallel to the glass plate was thus more difficult and even a small angle between the two surfaces would result in a diffusion path to the microdisc. To improve the contact the glass plate was additionally covered with a layer of an acetate film. Since the film adjusts its shape to certain extent, this arrangement should facilitate obtaining the "zero" distance, i.e. when the whole electrode surface is in contact with the insulator. The glass plate position was adjusted with the piezoelectric inchworms (Burleigh) connected to the microcontroller (6000 Controller, Burleigh). The electrode was vibrated in the direction normal to its surface.

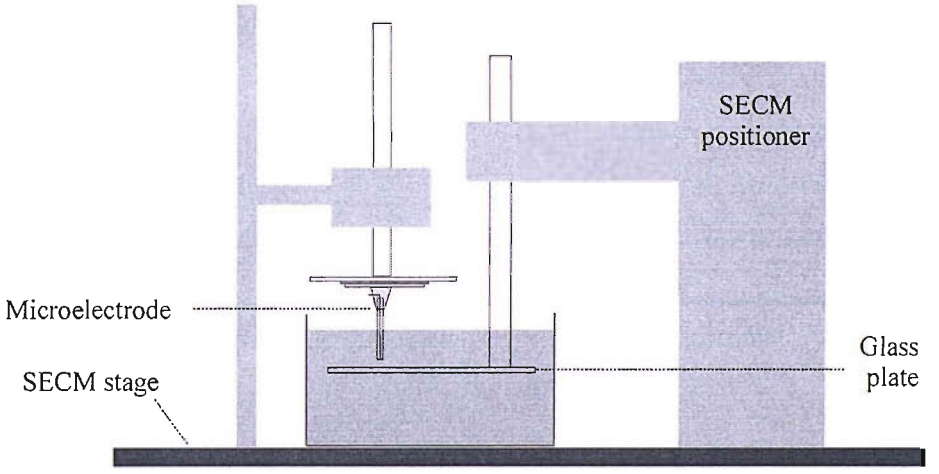

Figure 6.7 Experimental arrangement for the experiments involving an electrode vibrating against stationary wall. For clarity the gas purging system and some cell elements are omitted on the graph.

6.3.2 Experiments in the $Ru(NH_3)_6^{3+}$ system

The limiting currents for $Ru(NH_3)_6^{3+}$ reduction were measured at -0.85 V at discrete distances from the insulator surface ranging from 0 to 500 μm. The maximum distance was set at 500 μm since at this distance the recorded i_{lim} at a non-vibrated electrode was already equal to that recorded in bulk solution, i.e. the diffusion to the microdisc was not hindered by the insulating wall. The measured limiting currents served to construct approach curves. Such curves were constructed for various vibration amplitudes and are presented in Figure 6.8.

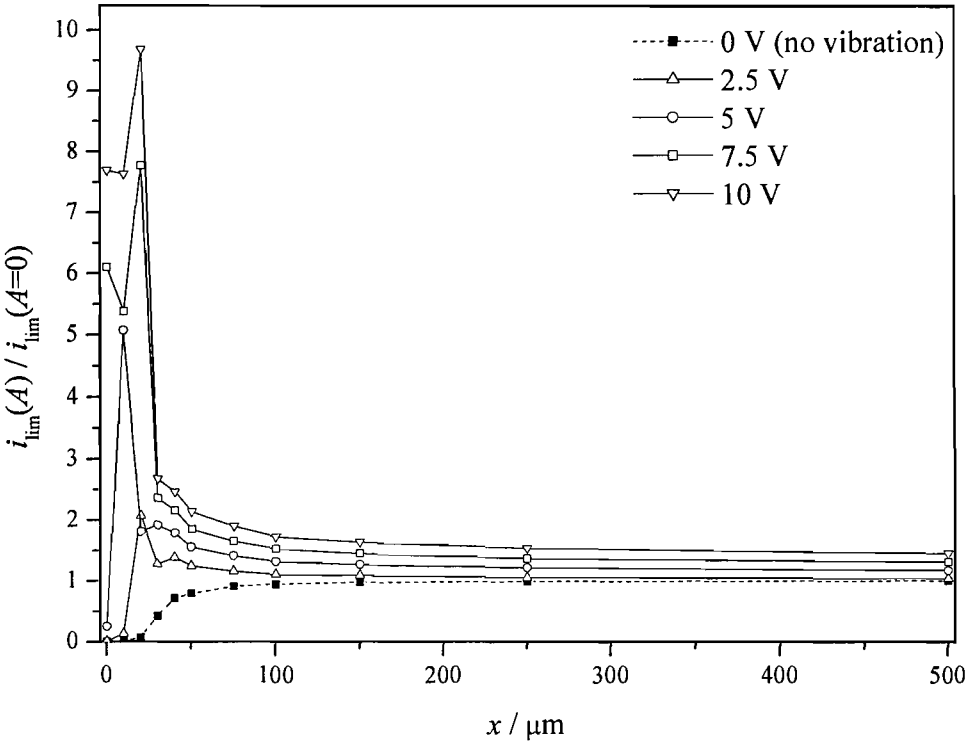

Figure 6.8 Limiting currents for $Ru(NH_3)_6^{3+}$ reduction at vibrating Pt microdisc (a=5 μm) as a function of distance from an insulating wall and of the vibration amplitude (voltages of the vibration driving waveform are indicated on the graph). The limiting currents are normalised with respect to i_{lim} in the bulk solution at a stationary electrode.

For a non-vibrating electrode the shape is consistent with an SECM approach curve under hindered diffusion [220]. The deviation appears at $x \approx 20$ μm,

where the current starts to decay slower than expected. This suggests that due to very large glass diameter the tip edge touches the insulator before the microdisc itself can reach the 'zero' distance. With the vibrated electrode i_{lim} increases as the tip is placed closer to the insulating surface. The maximal enhancement is observed at approximately 20 μm distance. The current decreases again as the electrode is nearer the insulator. Unlike with stationary electrode, the limiting current does not reach zero when the electrode touches the surface. The movement of the electrode causes convective movements of solution in between the surfaces and enhances the flux of species to the microdisc surface. The currents scale up with the magnitude of the vibration. For A=10 V i_{lim} was approximately ten times larger compared to stationary electrode in the bulk solution.

The enhancement is ascribed to two effects caused by the vibration of the tip. The tip movement forces high convective mass transport, i.e. the electrode body works as a piston pumping the solution. The pumping action also results in deformations of the diffusion layer. When the distance between the two surfaces becomes comparable with the diffusion layer thickness, an additional factor can also affect the measured i_{lim}. The diffusion layer is squeezed, therefore the concentration gradient increases resulting in higher currents. The quantitative treatment of the observed i_{lim} enhancement was not possible due to unknown displacement of the vibrating microelectrode. Similar conclusions to mixed hydrodynamic and electrochemical effects were drawn by Fushimi *et al.* [221] who investigated the behaviour of a microdisc vibrating parallel to an insulating surface. Their work involved a microdisc (200 μm glass sheath diameter) vibrated at 25-51 kHz and results showed i_{lim} maxima at *ca.* 5 μm from the surface (the maximal enhancement were between 1.2 and 2 depending on the vibration frequency).

6.3.3 Oxygen reduction

Analogous experiments were conducted for oxygen reduction in air saturated 0.5 M NaCl. The observed enhancement in the limiting current is qualitatively very similar to the reduction of $Ru(NH_3)_6^{3+}$ with the maxima observed

for the electrode-wall distances of approximately 20 μm. However the magnitude of the enhancement is much lower for oxygen reduction. When the highest vibration amplitude was used the $i_{lim}(A)/i_{lim}(A=0)$ ratio was only 1.6 compared to *ca.* 10 for the ruthenium system.

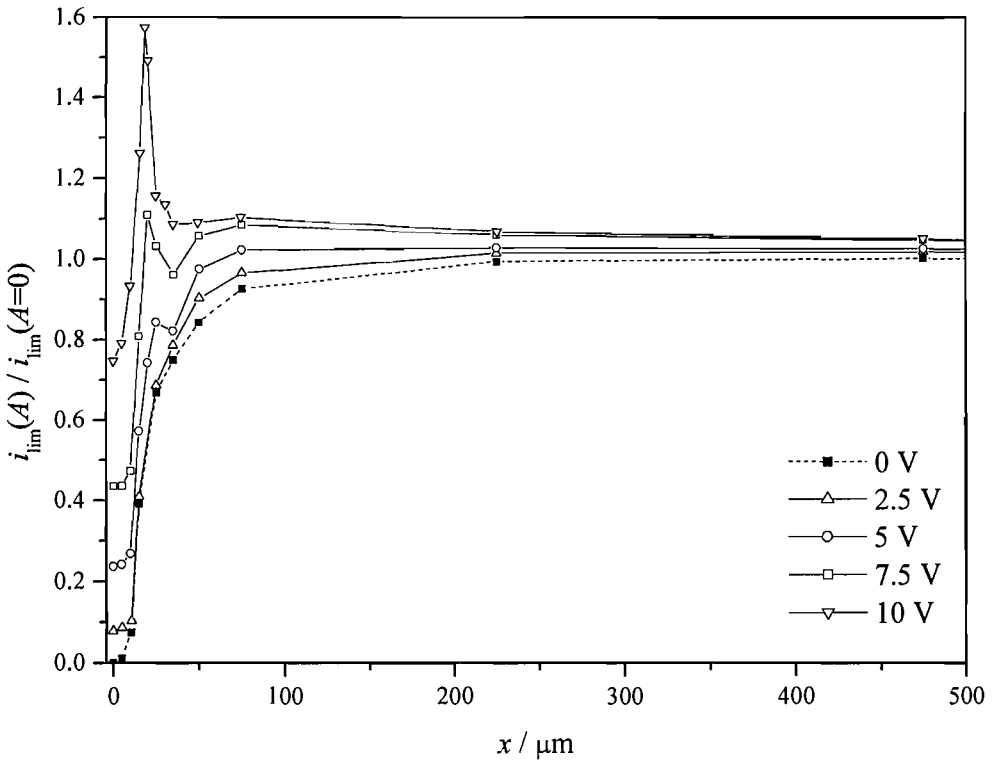

Figure 6.9 Limiting currents for oxygen reduction in air saturated 0.5 M NaCl at a vibrating Pt microdisc (a=5 μm) as function of distance from an insulating wall and of the vibration amplitude (voltages of the vibration driving waveform are indicated on the graph). The limiting currents are normalised with respect to i_{lim} in the bulk solution at a stationary electrode.

In both cases, whether the electrode was vibrated in the bulk or in the proximity of an insulating wall, an appreciable increase in the limiting current for oxygen reduction was observed. However, this enhancement was consistently smaller when compared to $Ru(NH_3)_6^{3+}$ reduction under the same conditions. This limitation is believed to be a consequence of the complex mechanism of ORR.

Firstly, the transfer of the first electron requires the adsorption of oxygen and therefore available adsorption sites. Thus, more efficient mass transport will result in increased limiting current only to a certain point, at which the surface is saturated and there are no adsorption sites available. This effectively corresponds to the situation where the surface oxygen concentration is not zero, i.e. an appreciable amount of oxygen molecules that reach the surface cannot be reduced due to lack of the free adsorption sites. Secondly, as observed before (see section 4.6) with various sizes of microelectrodes, enhanced mass transport increases the probability of removal of peroxide intermediates before their further reduction to water. This yields lower values of n_{app} and consequently lower i_{lim}. These effects can explain the different behaviour between ORR and $Ru(NH_3)_6^{3+}$ reduction where the electron transfer is instantaneous, i.e. the system is under true mass transport control

6.4 Summary

For a purely mass transport controlled process the vibration of the electrode either in the bulk or close to insulating surface result in considerably larger limiting currents. This effect is however much less pronounced for the ORR, presumably because n_{app} decreases as the mass transfer coefficient m_i increases but also because the number of active sites remains the limiting factor despite higher m_i [209]. With the piezoelectric transducers used, the enhancement is comparable to the effects of moderate stirring. This is not sufficient to overcome the influence of high rate of external flow around a bare microdisc mounted on a moving probe. The observed enhancement is very small presumably due to the aforementioned adsorption limitations, thus it is unlikely that the use of more powerful transducers would improve the performance.

7 Dissolved oxygen sensor for water column profiling

7.1 Chapter overview

In this chapter the general conditions for obtaining a vertical DO profile in the ocean environment with the platinum microelectrode sensor are presented. Details of the instrument designed for field measurements are given. The algorithm for extracting DO concentration from the sensor output utilising the readings from CTD collocated instruments is described. Finally, DO data acquired during RRS Discovery oceanographic cruise D279 are presented and the usefulness of the sensor in real working conditions is evaluated.

7.2 CTD profiling and current DO measurements methods

Vertical water column profiling is performed with a Sea-Bird 9/11 plus CTD system. The system holds a rosette with 24 Niskin bottles (10 dm^3 each), altimeter, temperature, conductivity sensors and other instrumentation. The pressure, temperature and conductivity data are acquired at 24 Hz. The whole instrumentation package is operated from an on-board winch and its velocity in the water column is between 1 and 1.5 m s^{-1}.

Oxygen measurements are performed using two methods. The first one involves collecting water samples at discrete depths (the CTD system is stopped) in the Niskin bottles and subsequent chemical DO determination. On-board oxygen analysis is made by automated Winkler titration using SIS Dissolved Oxygen Analyser, SIS DOA (SiS Sensoren Instrumente Syteme GmbH, Germany) with spectrophotometric end point detection. The water from the Niskin bottle is transferred to 100 ml sampling bottles and the whole bottle titration method is employed. Repetitive analysis using SIS DOA yields an accuracy of 0.1 % [222].

The second set of DO data is obtained with a SBE 43 dissolved oxygen sensor (Sea-Bird Electronics). This is a Clark type membrane sensor utilising a gold cathode and Ag/AgCl anode. The manufacturer claims the accuracy of the sensor is 2% of saturation [223]. The sensor shows very little deviation with respect to bottle data in the upper ocean (0-1000 m depth), however in deeper regions the pressure affects the membrane performance resulting in significant lowering of the signal.

7.3 Sensor design

The sensor for oceanographic applications including the head, stop flow cell and the electronics were designed and constructed by co-workers in the National Marine Facilities Division at NOC, Southampton. The details are included in this thesis as they are essential for the completeness of the research record.

Several issues have to be addressed when designing the sensor for the oceanographic measurements. All the elements of the sensor have to withstand the extreme pressures met in deep sea applications. This concerns mainly the glass electrode body and the electronics used to produce the voltage difference between electrodes and to amplify the recorded currents. Moreover, unshielded electrodes are sensitive to external flow and this issue has to be resolved for the sensor located on a system moving with variable velocity. Also, particular care has to be taken when choosing the anode material. The anode should maintain a stable potential and be resistant to fouling over long periods of continuous operation in the harsh ocean environment.

Microelectrodes were constructed using soda glass capillaries and the contact with the thick connecting nichrome wire was made with indium or silver loaded epoxy. Particular attention was paid not to leave any gas bubbles inside the glass that could result in electrode breaking under increased pressure. The glass body was later integrated within a block of epoxy for further pressure protection. No attempts to set the microwire directly in epoxy resin were undertaken due to the 'swelling' of epoxy at high pressures observed in early stages of the DO sensor development. This effect resulted in an increasingly recesses microdisc thus

modifying the diffusion field to the electrode. A schematic and a photograph of the sensor head are shown in Figure 7.2 and Figure 7.3, respectively.

The anode is in the form of a copper tube mounted around part of the epoxy block. Copper was chosen as an anode material for several reasons. In seawater environment Cu is resistant to corrosion thanks to the formation of a protective film on its surface. The film consists of several copper compounds and their relative quantity depends on Cl^- concentration, oxygen availability and general physical conditions [224]. The typical make up of the film on pure copper in seawater is presented in Figure 7.1. The film formation on fresh Cu is fast – the amount of dissolved copper in the surrounding solution decreases 100 fold within one hour after immersion [225]. Copper is also resistant to biofouling, which is very desirable when the electrode is routinely deployed in biologically rich waters. This anti-fouling effect is a consequence of the presence of Cu(I) and Cu(II) species which are strong cytotoxic agents [226]. In addition, the cost and the ease of Cu mechanical processing are important factors.

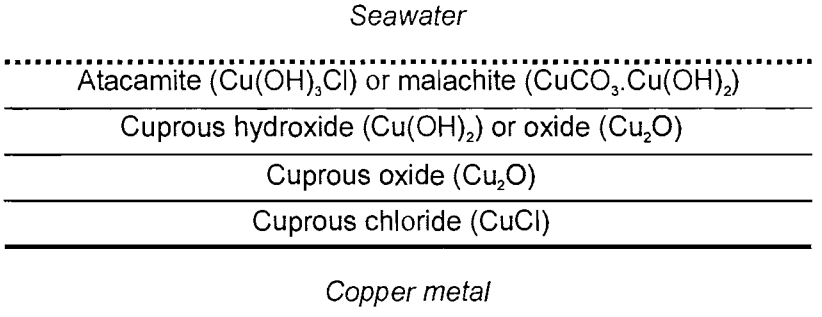

Figure 7.1 General scheme of species in a mature unalloyed copper corrosion product, after Bengough *et al.* [227].

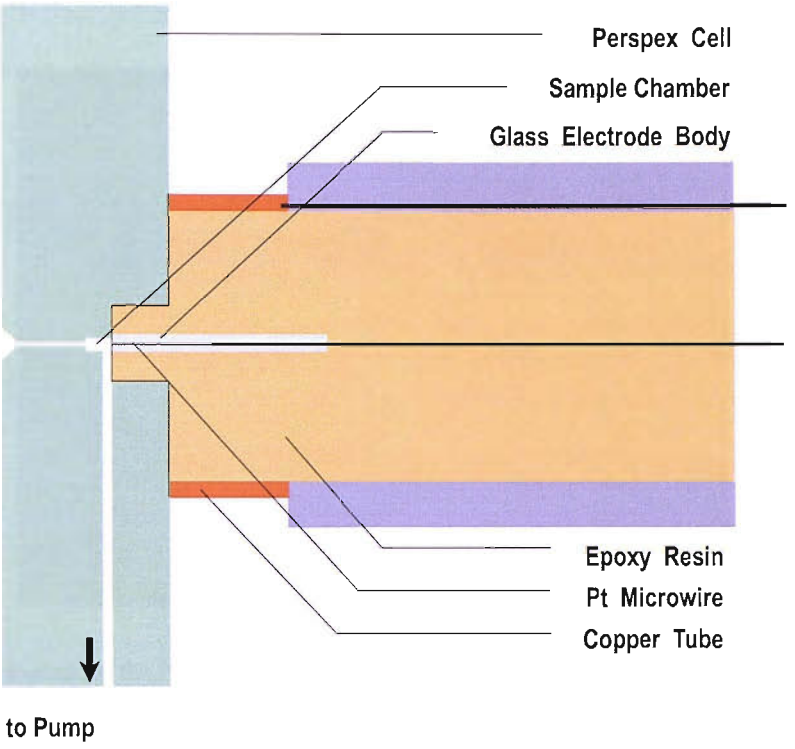

Figure 7.2 A schematic of the sensor head cross section with the stop flow cell mounted. The sensor electronics and the pump are not included in the schematic.

Figure 7.3 Photograph of a DO microelectrode sensor head.

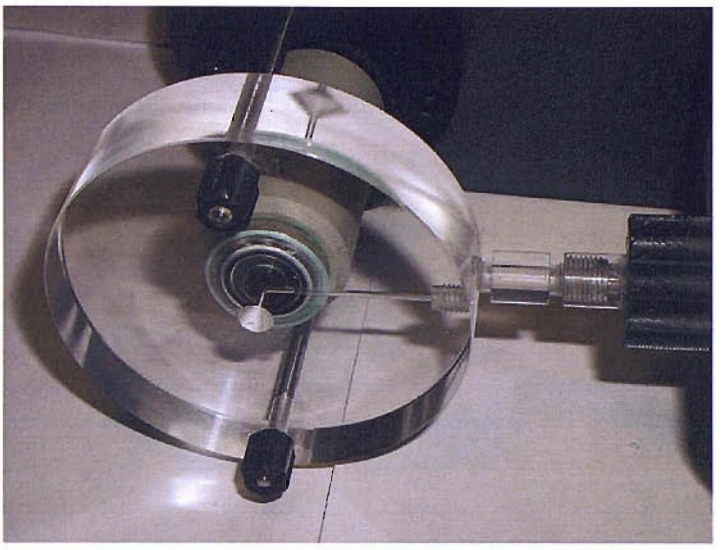

Figure 7.4 Photograph of the Perspex stop-flow cell mounted on the sensor head.

To eliminate the flow sensitivity a purpose made Perspex cell was mounted on the electrode head (Figure 7.2 and Figure 7.4). A thin channel within the Perspex block leads to the electrode and further to the solenoid pump fitted downstream (the pump is contained in the appropriate pressure balanced housing). Each time the pump is activated a fresh amount of seawater is sucked into the sample chamber adjacent to the microelectrode. When the pump is not working, it acts as a valve, the solution within the channel and the chamber is stagnant and the measurement can be performed without the influence of the convective mass transport. The fixture of the stop-flow cell makes the current path between the electrodes far from ideal. However, due to the very small currents recorded with the microelectrode and the high conductivity of the medium there are no differences in the oxygen reduction wave position and magnitude when compared to electrodes positioned very close to each other. Moreover, in this arrangement one can avoid the presence of dissolved copper species in the vicinity of the microdisc, which could be deposited simultaneously with oxygen reduction impairing the catalytic properties of platinum towards the ORR.

The sensor is completed with the electronics contained in a pressure tube. It is used to apply the potential between the electrodes and to amplify the measured current. Also, it generates a waveform to control the pump work and allows synchronisation between both electrode and pump waveforms. The whole assembly is depicted in Figure 7.5 and Figure 7.6 (while mounted on a fin of the CTD probe).

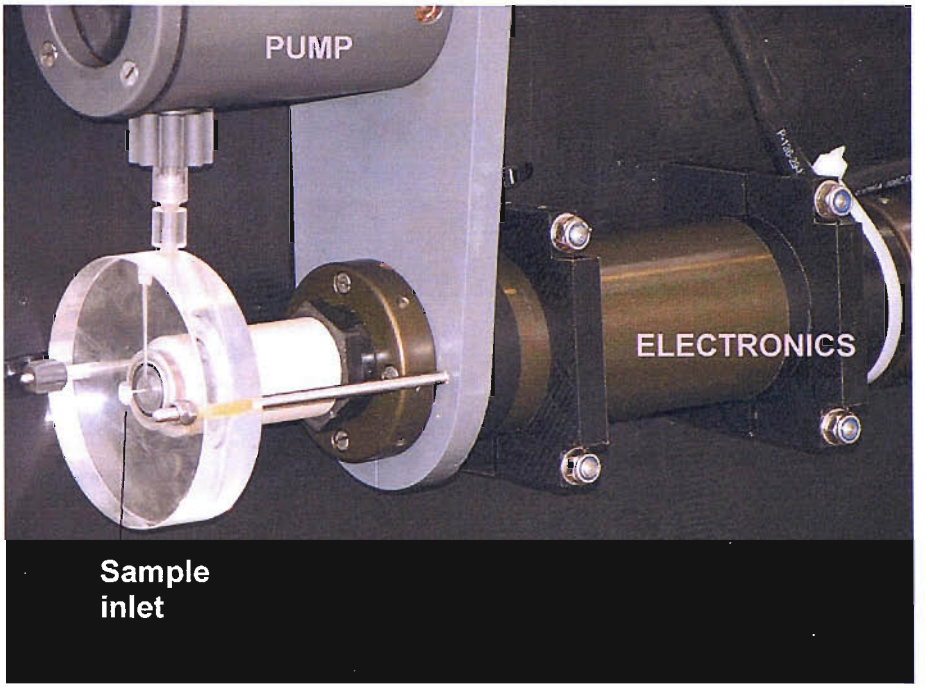

Figure 7.5 A photograph of the fully assembled DO microelectrode sensor for oceanographic measurements.

Figure 7.6 DO microelectrode sensor mounted on the CTD probe fin.

7.4 Principles of the sensor operation

The potential sequence is applied to the electrodes continuously from the moment of the CTD immersion to its retrieval on board of the research ship. After immersion, the CTD is brought to a depth of approximately 10 m and held still for 2-3 min to check for correct signals of all the instruments and to allow the stabilisation of the responses. This time is also sufficient for the microelectrode output to stabilise. Following this procedure the CTD is retracted to the surface and the profiling commences. The key features of the DO microelectrode sensor operation are shown in Figure 7.7. The electrode potential waveform consists of measuring steps (12 s) separated by short cleaning pulses (1 s). As described earlier (see Chapter 3) this duty cycle was found to yield very stable response over extended periods of continuous operation. Pump actuation is synchronised with the events occurring on the microelectrode. Each time the potential is switched to the cleaning value the pump is activated to exchange the seawater sample. Five pump cycles

lasting in total 2.5 s are sufficient to replace the volume contained in the sample chamber. The signal distorted by the pump work is discarded and only the last 2 s of the steady state current are sampled and recorded for further analysis.

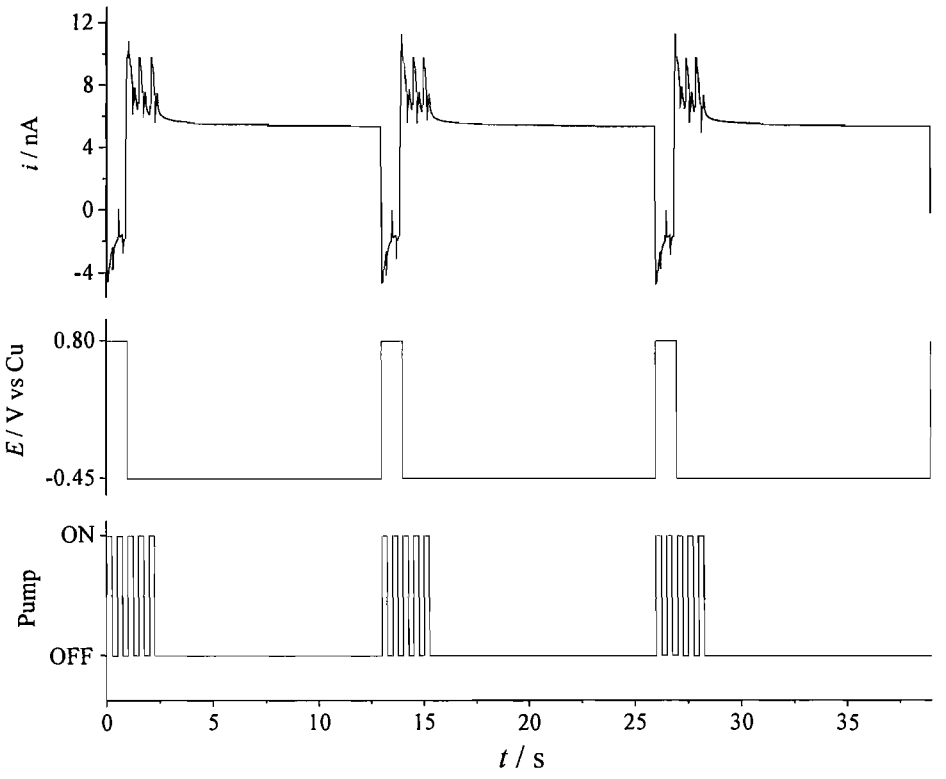

Figure 7.7 A snapshot of current response, potential and pump waveforms as used for field measurements.

The values of potentials for the cleaning and the measuring steps were chosen on the basis of the steady state voltammetry for oxygen reduction in synthetic seawater with the sensor's copper ring used as a counter/reference electrode (Figure 7.8). The measuring potential lies within the limiting current plateau (-0.45 V vs Cu) and the cleaning potential was chosen 1.25 V larger analogously to the potentials obtained vs SMSE.

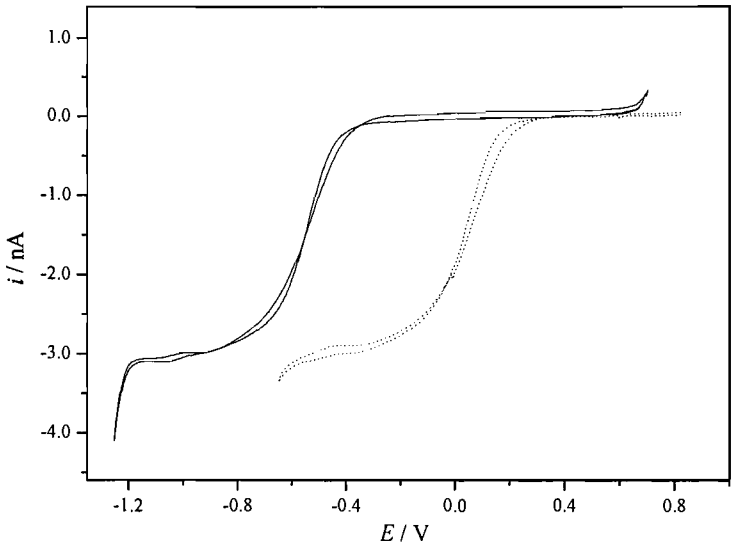

Figure 7.8 Oxygen reduction at Pt microdisc (a=5 μm) in air saturated 0.5 M NaCl with SMSE (solid line) and Cu (dotted line) used as counter/reference electrode. v=20 mV s^{-1}.

7.4.1 Calculating dissolved oxygen concentrations from the sensor output

The DO concentration can be readily determined from the limiting current at the microelectrode using the equation for steady state current at a microdisc (1.5) with a and n_{app} determined in the lab and D_{O2} calculated on the basis of readings from the instruments collocated on the CTD package.

Conductivity measurements provide a very accurate measure of the seawater salinity. Commonly used is the Practical Salinity Scale recommended by the Joint Panel on Oceanographic Tables and Standards in 1978 [228]. According to this scale the seawater salinity is determined solely on the basis of the conductivity measurements. The conductivity of seawater $C(S,T_C,0)$ is related to the conductivity of a standard KCl solution (32.4356 g in 1000.000 g of solution), $C(KCl,T_C,0)$ to yield the conductivity ratio R_T:

$$R_T = \frac{C(S, T_C, 0)}{C(\mathrm{KCl}, T_C, 0)} \tag{7.1}$$

where 0 denotes the standard barometric pressure. The salinity according to the practical salinity scale is then defined as:

$$\begin{aligned} S = {} & 0.0080 - 0.1692R_T^{1/2} + 25.3851R_T + 14.0941R_T^{3/2} \\ & -7.0261R_T^2 + 2.7081R_T^{5/2} + \Delta S \end{aligned} \tag{7.2}$$

where

$$\begin{aligned} \Delta S = {} & \left[\frac{(T_C - 15)}{1 + 0.0162(T_C - 15)}\right] + 0.0005 - 0.0056R_T^{1/2} - 0.0066R_T \\ & -0.0375R_T^{3/2} + 0.636R_T^2 - 0.0144R_T^{5/2} \end{aligned} \tag{7.3}$$

For R_T =1 the seawater salinity is 35. The precise relationship between S and the absolute salinity S_A (the total mass of dissolved matter in 1 kg of seawater) is unknown as some variations in the seawater composition may not result in conductivity changes. Nevertheless, absolute salinities estimated by chemical and other methods yield values very close to S [229]. Thus, in further data analysis it is assumed that S_A is numerically equal to S.

To obtain the value of D_{O2} the absolute salinity is used to calculate the concentration (c_{NaCl}) of the equivalent NaCl solution characterised by the same S_A (7.4). This approximation introduces negligible errors, since NaCl constitutes over 85% of dissolved matter and the variations of salinity are very small regardless of location.

$$c_{NaCl} = \frac{S_A \times \rho}{M_{NaCl}} \tag{7.4}$$

This concentration can be further used to calculate the necessary molar fractions of Na^+ and Cl^- for estimation of D_{O2} (see section 1.5.2, equations (1.33) - (1.37)). The

above equation, and the expression for D_{O2} require knowledge of the medium density, which is obtained from the salinity, temperature and pressure data using the equation of state for seawater (EOS 80) [229]:

$$\rho(S,T_C,p) = \frac{\rho(S,T_C,0)}{1-\frac{p}{K(S,T_C,p)}} \tag{7.5}$$

$\rho(S,T_C,0)$ and $K(S,T_C,p)$ are defined by equations (7.6) and (7.7) respectively:

$$\rho(S,T_C,0) = A + BS + CS^{3/2} + DS^2 \tag{7.6}$$

$$K(S,T_C,p) = E + FS + GS^{3/2} + (H + IS + JS^{3/2})p + (M + NS)p^2 \tag{7.7}$$

The coefficients A,...N in the above equations are polynomials of temperature T_C (in °C) and the coefficients of these polynomials are given in Table 7.1.

Table 7.1 Coefficients of temperature polynomials used in the equation of state for seawater [229]

	T_C^0	T_C^1	T_C^2	T_C^3	T_C^4	T_C^5
A	999.8426	6.79E-02	-9.10E-03	1.00E-04	-1.12E-06	6.54E-09
B	8.24E-01	-4.09E-03	7.64E-05	-8.25E-07	5.39E-09	
C	-5.72E-03	1.02E-04	-1.65E-06			
D	4.83E-04					
E	1.97E+04	1.48E+02	-2.33E+00	1.36E-02	-5.16E-05	
F	5.47E+01	-6.03E-01	1.10E-02	-6.17E-05		
G	7.94E-02	1.65E-02	-5.30E-04			
H	3.24E+00	1.44E-03	1.16E-04	-5.78E-07		
I	2.28E-03	-1.10E-05	-1.61E-06			
J	1.91E-04					
M	8.51E-05	-6.12E-06	5.28E-08			
N	-9.93E-07	2.08E-08	9.17E-10			

The summary of all the parameters used to obtain the DO concentration from the limiting current recorded by the sensor is presented in Table 7.2 and the data flow chart is shown in Figure 7.9. While oxygen concentration can be calculated analytically, a common procedure is to recalibrate the sensor with respect to DO concentrations determined in the bottled samples. This approach significantly improves accuracy since the product $n_{app} \times D_{O2} \times a$ is obtained from the calibration and the errors are only due to the measurement of i_{lim} and the corrections for temperature and pressure effects. Also, it has to be remembered that the current is measured approximately 12 s after the seawater is sampled. The probe is constantly moving, thus an offset with respect to depth has to be applied.

Table 7.2 The list of parameters measured and calculated on route to obtain DO concentration from the sensor output.

Parameter		Comments, (equations)
Symbol	Description	
C	seawater conductivity	measured by CTD
p	pressure	measured by CTD
T_C	temperature	measured by CTD
S	salinity	calculated using C, p, T_C; (7.1) - (7.3)
ρ	seawater density	calculated using S, p, T_C; (7.5) - (7.7)
c_{NaCl}	concentration of model NaCl solution	calculated using S, ρ; (7.4)
D_{O2}	oxygen diffusion coefficient in seawater	calculated using T_C, ρ, c_{NaCl}; (1.34) - (1.37)
n_{app}	the apparent number of electrons for ORR	determined in the lab (calibration)
a	microdisc radius	determined in the lab ($Ru(NH_3)_6^{3+}$ reduction)
i_{lim}	limiting current for oxygen reduction	measured
c_{O2}	dissolved oxygen concentration	result, calculated using i_{lim}, D_{O2}, n_{app}, a; (4.9)

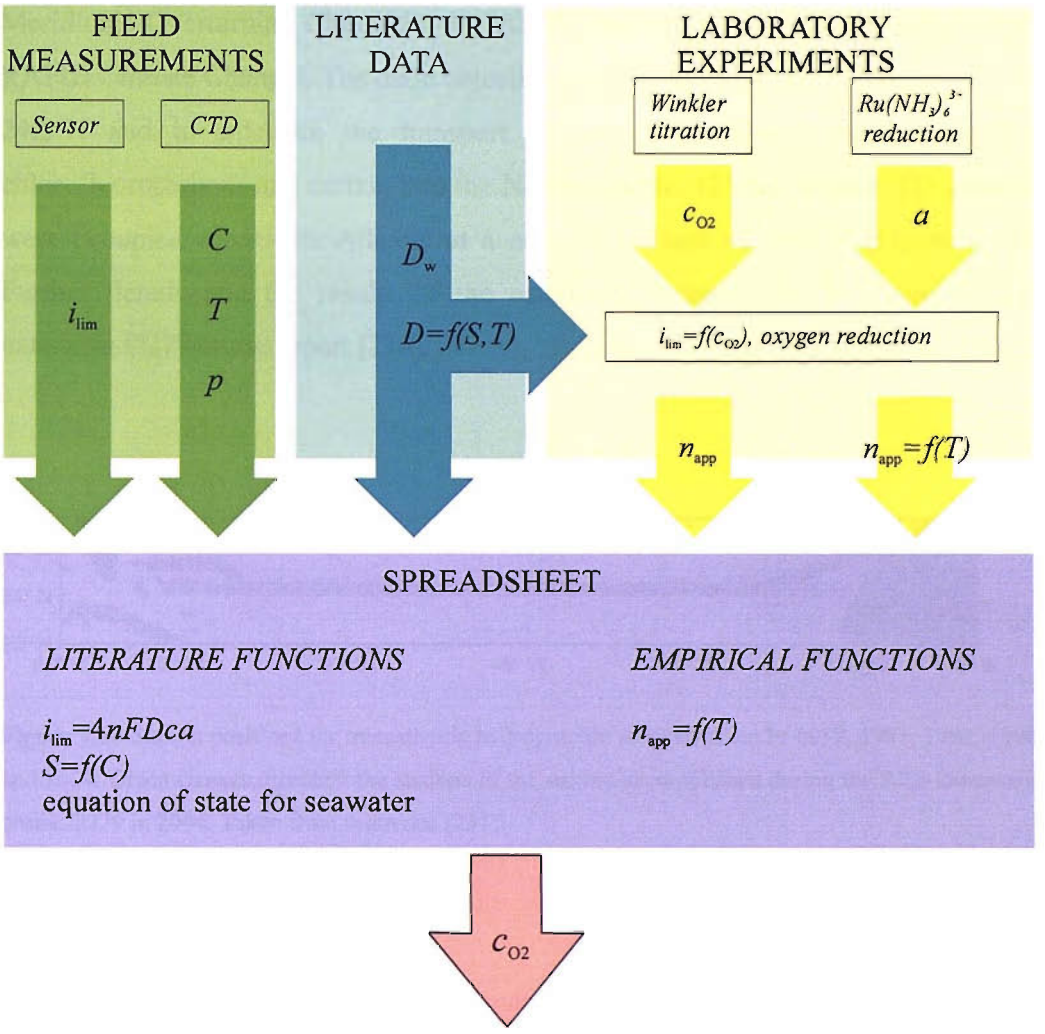

Figure 7.9 Data flow chart for obtaining oxygen concentration from probe readings and analytical expression.

7.5 Field tests

7.5.1 Cruise data

The field trials of the microelectrode DO sensor were performed during the RRS Discovery cruise D279. The cruise took place between 4th of April and 10th of May 2004 as a part of James Rennell Division Core Strategic Programme "Ocean Variability and Climate" and a contribution to the project "Monitoring the Atlantic

Meridional Overturning Circulation at 26.5°N" (part of NERC directed programme RAPID Climate Change). The main objectives were to measure the circulation across 24.5°N and to calculate the transport of heat, freshwater, oxygen, nutrients, chlorofluorocarbons and carbon into the North Atlantic. 125 full depth CTD stations were occupied across the Atlantic at a nominal latitude of 24.5°N (Figure 7.10). Further details and the results of the conducted research can be found in the extensive D279 cruise report [230].

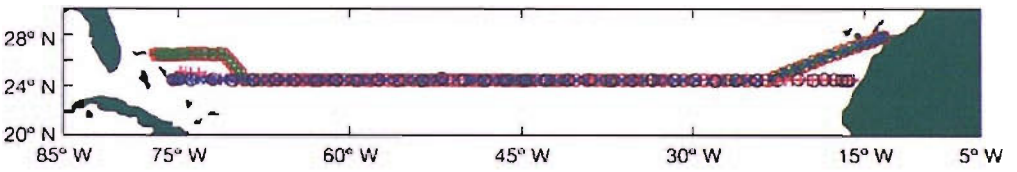

Figure 7.10 Station positions for transatlantic hydrographic sections taken in 1957, 1981, 1992, 1998 and 2004. Green crosses represent the stations of the section accomplished during the RRS Discovery cruise D279 in 2004. Taken from reference [231].

Table 7.3 CTD stations data during D279 cruise in which the DO microelectrode sensor was successfully deployed.

Station #	Date	Time	Coordinates	Maximum depth /m
118	08/05/2004	16:27	27°02'59"N, 16°07'32"W	3471
119	08/05/2004	21.40	27°14'01"N, 15°35'53"W	3130
120	09/05/2004	03:59	27°26'00"N, 14°51'62"W	2581
121	09/05/2004	09:09	27°37'24"N, 14°13'72"W	2015
122	09/05/2004	13:05	27°49'75"N, 13°49'05"W	1541
123	09/05/2004	15:42	27°51'14"N, 13°03'06"W	1081
124	09/05/2004	17:32	27°52'80"N, 13°25'19"W	598
125	09/05/2004	18:48	27°54'94"N, 13°22'24"W	344

In all the deployments during cruise D279 a sensor prototype equipped with 12.5 μm radius Pt microdisc was used. The microelectrode sensor was mounted on the CTD for station 93, but unforeseen problems (see section 7.5.4) prevented obtaining any meaningful oxygen data. Significant improvement was made starting from station 114 and successful c_{O2} – depth profiles were recorded for the subsequent CTD deployments 118-125. The time, location and maximal depths of these stations are summarised in Table 7.3.

7.5.2 Field tests results – comparison with currently used techniques

DO concentrations were calculated from the sensor output in two ways: using analytical expressions as described in section 7.4.1 and on the basis of calibration vs data from Winkler titrations on the samples taken at discrete depths during the CTD deployment (see equations (7.8), (7.9) below). In the remainder of this section the obtained DO profiles are compared to the bottle data as well as to the collocated Clark type Seabird DO sensor. A general performance of the microelectrode sensor is assessed and the variations with respect to the bottle data are treated quantitatively.

An example of a DO profile measured with the microelectrode DO sensor along with the Winkler titration data and Clark electrode is presented in Figure 7.11. Two traces for the microelectrode are plotted. One of them is constructed with DO concentrations calculated analytically and the other is calculated using a calibration curve obtained using DO values from the Winkler analysis of bottled samples.

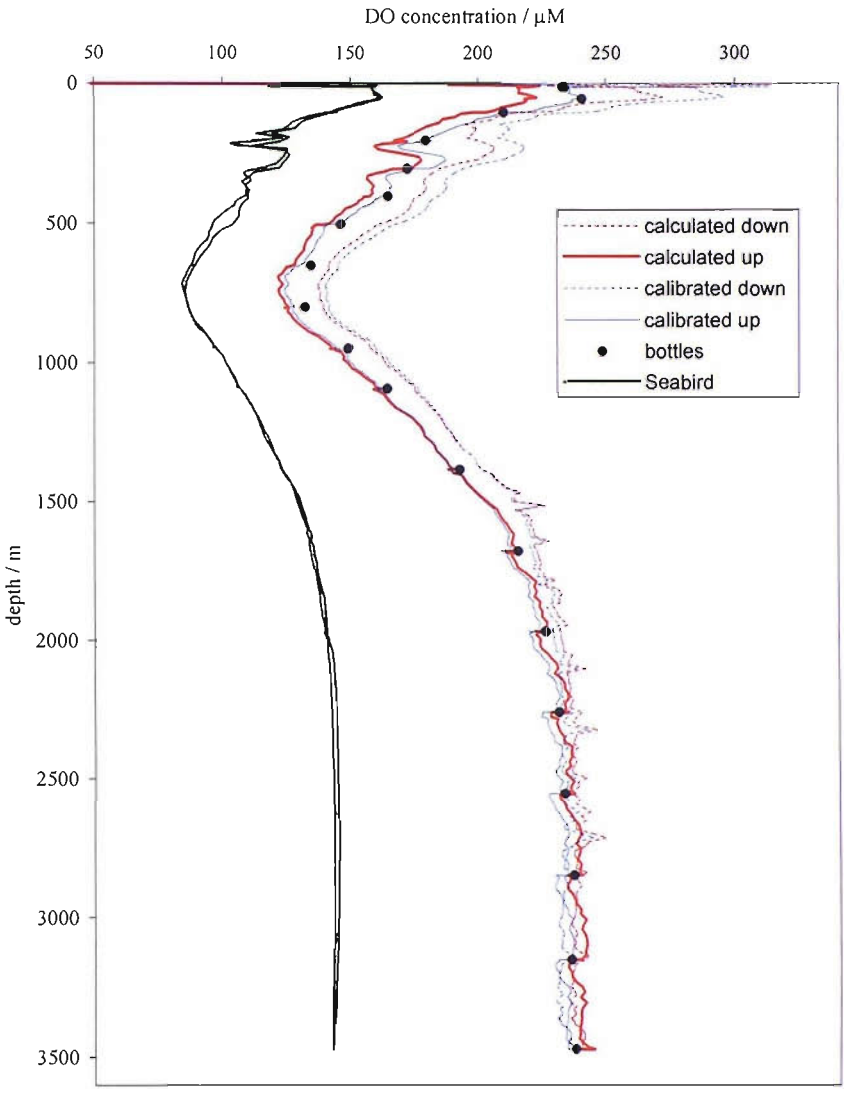

Figure 7.11 Dissolved oxygen – depth profiles from cruise D279, station 118. Winkler titration data from samples collected in Niskin bottles (black points), Seabird oxygen sensor SBE 43, Clark type (green line), microelectrode DO sensor: calculated analytically (red) and calibration based (blue); downcasts (dotted) and upcasts (solid).

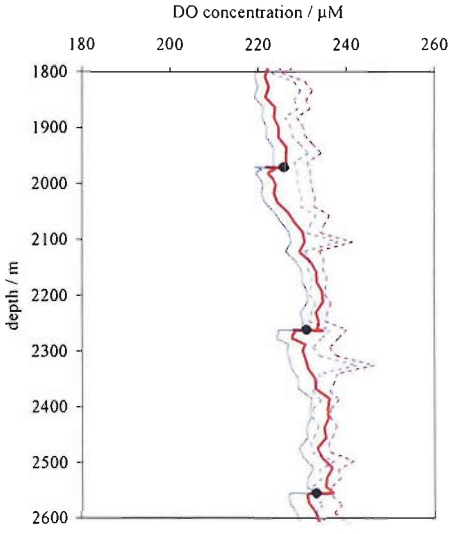

Figure 7.12 A magnification of a section of the profile from Figure 7.11 showing the effect of stopping of the CTD package (black points) on the microelectrode response: calculated analytically (red) and calibration based (blue); downcasts (dotted) and upcasts (solid).

In general, the profiles obtained with the microelectrode (both calibrated and calculated analytically) show very good agreement with the bottles data. The variations between the microelectrode and the Winkler reference are quantitatively presented in Table 7.4. Seabird sensor showed significantly lower signal than expected presumably due to a fouled membrane and its response cannot be used for direct comparison. Nonetheless, one can still observe that below 1000 m the offset between its trace and bottles data is getting larger with increasing depth. This behaviour is typical for Clark probes, where the membrane permeability is strongly affected by pressure. A closer look at the microelectrode response reveals some discrepancies regarding the shape of the profile and a significant hysteresis between the up and down casts. In Figure 7.12 a fragment of the profile is blown up to show quite significant (corresponding to 7-8 µM in DO) changes in the signal occurring when the whole CTD package is stopped to fire a Niskin bottle. The effect is not present on the downcast profile where the CTD was moving continuously without stopping. This suggests that despite the fitted stop flow cell the microelectrode is

experiencing some effects from the CTD motion and a slow stabilisation of the signal is seen when the CTD is brought to a halt. The imperfection of the flow control is also the reason for the hysteresis between the up- and down-casts. The effect was consistent in all the deployments made, where the up-casts showed very good agreement with bottles data, but the down-casts results overestimated the DO concentration. In the following analysis only the up casts will be considered.

The field calibration was performed by fitting microelectrode limiting currents to the corresponding bottles DO values. DO concentration can be generally expressed by equation (7.8):

$$c_{O2} = \frac{i_{lim}}{A \exp\left(-\frac{E_a}{RT}\right)} \tag{7.8}$$

where

$$A = 4 n_{app} F D_{O2} a \tag{7.9}$$

and $\exp\left(-\frac{E_a}{RT}\right)$ is a combined Arrhenius type correction for temperature effects on D_{O2} and n_{app}. After rearranging equation (7.8) a linear function of $\ln(i_{lim}/c_{O2})$ vs $1/T$ is obtained:

$$\ln\left(\frac{i_{lim}}{c_{O2}}\right) = \ln A - \frac{E_a}{R}\frac{1}{T} \tag{7.10}$$

The plot of equation (7.10) using the i_{lim}, c_{O2} (bottles) and temperature data from cast 118 is shown in Figure 7.13.

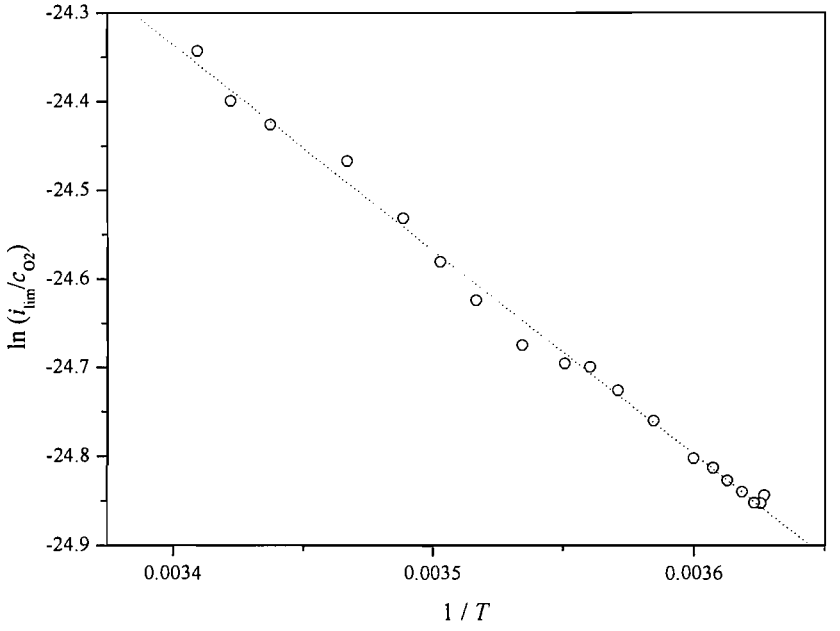

Figure 7.13 The field calibration of the microelectrode limiting currents (in amps) using c_{O2} (bottles; in μM) and temperature data from cast 118. The dotted line represents the linear fit of the experimental points.

The linear fit (R=0.997) yielded E_a=19.2 kJ mol^{-1} and A=6.94×10^{-8} these parameters were used to calculate c_{O2} at any depth for all the remaining CTD stations. This calibration method is somewhat simplified as it does not include the salinity effect on D_{O2}. This effect however can be neglected as the salinity during the cast varied between 34.91 and 36.81, which corresponds to D_{O2} variation of only 6×10^{-8} cm^2 s^{-1}. The DO concentrations for station 118 calculated as above are compared to the bottles data in Figure 7.14. The mean variation of c_{O2} of 2.5 μM and standard deviation (SD) of 3.4 μM were found for these two sets of data. Extending the analysis to casts 118 to 125 using the same parameters obtained from the calibration yielded mean variation of 0.6 μM with standard deviation of 3.8 μM. The details including DO variations and standard deviations for all the performed CTD deployments are presented in Table 7.4. The statistical data is given in μM as well as in percentage (referred to bottles DO concentrations) for both calibration based and purely analytical DO calculations. The relative deviations for all the CTD casts as a function of depth are also plotted in Figure 7.15.

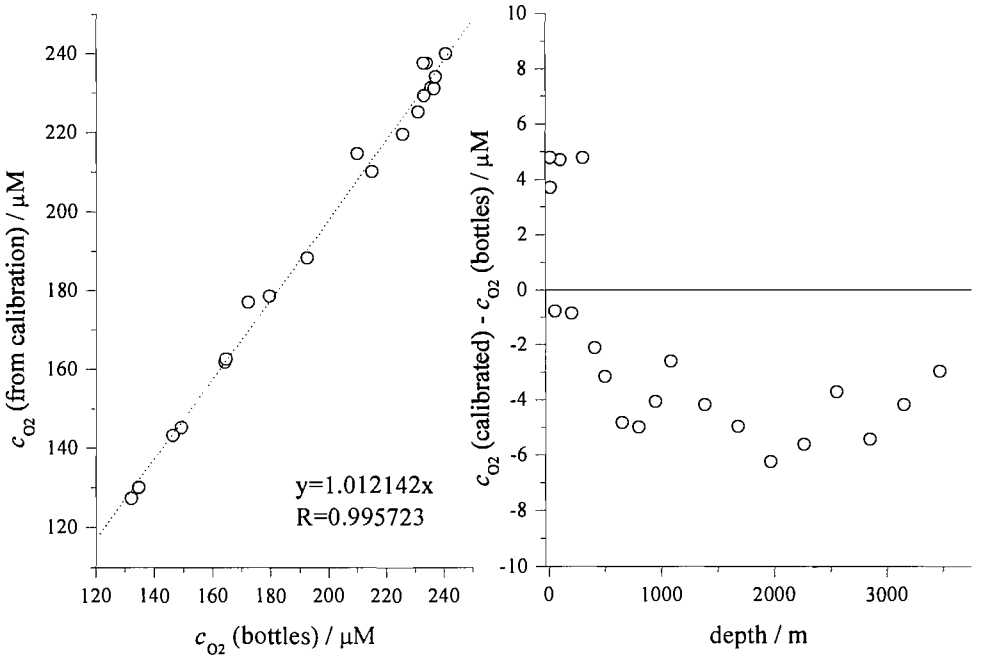

Figure 7.14 Comparison of DO concentrations from bottles (Winkler titration) and microelectrode data (calculated using calibration vs bottles) (left), variations between the two sets of DO data at discrete points on the DO – depth profile (right). The data was collected during cast 118.

Table 7.4 Mean differences and standard deviations of microelectrode DO data with respect to DO concentrations obtained from the bottled samples for CTD stations 118-125.

cast #	n	calibrated				calculated			
		mean difference		standard deviation		mean difference		standard deviation	
		µM	%	µM	%	µM	%	µM	%
118	19	-2.5	-1.4	3.4	1.8	-6.1	-3.3	5.8	2.8
119	18	-0.6	-0.5	3.4	1.9	-5.3	-3.0	7.4	3.5
120	16	1.1	0.2	4.4	2.4	-4.4	-2.6	8.0	3.9
121	14	-1.1	-0.9	4.0	2.2	-7.6	-4.2	7.0	3.1
122	12	-1.1	-0.9	3.4	2.1	-7.7	-4.1	7.4	3.3
123	11	0.3	0.0	3.1	1.9	-8.1	-4.2	7.1	3.3
124	5	-1.6	-0.6	4.0	2.7	-12.4	-5.7	10.0	4.6
125	6	0.8	0.7	4.6	2.7	-10.8	-4.9	10.2	4.5
total	101	-0.6	-0.4	3.8	2.2	-7.8	-4.0	7.9	3.6

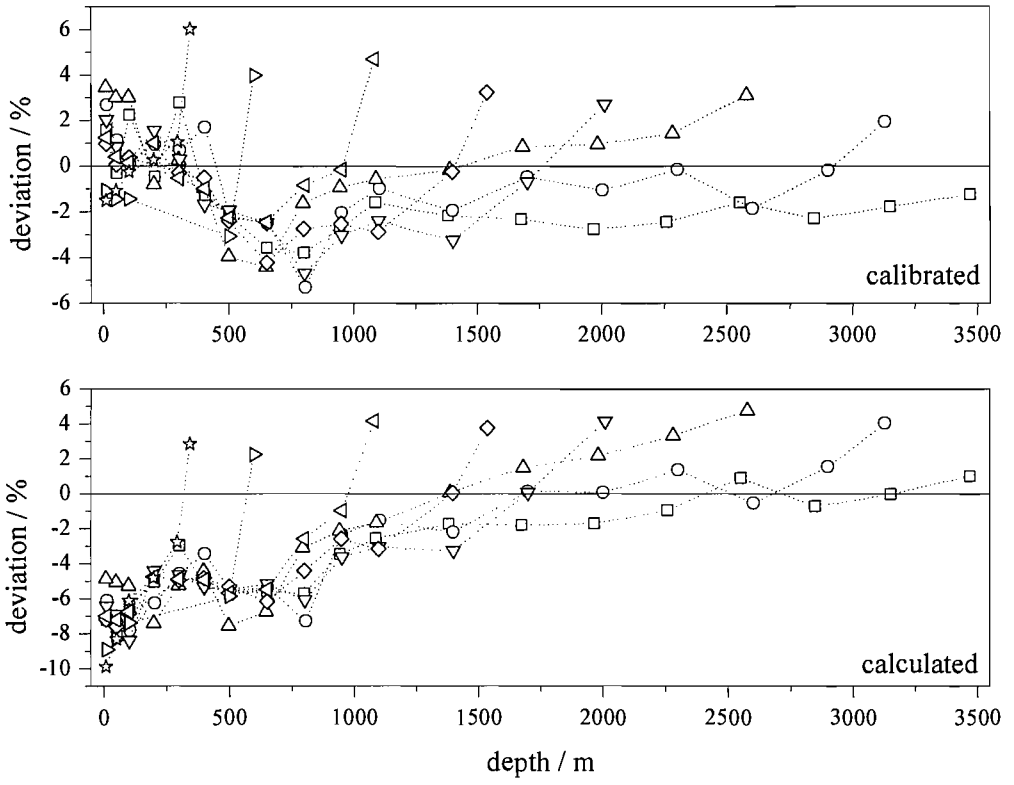

Figure 7.15 The deviation of DO concentration (from the calibration – top, and calculated analytically – bottom) from the bottles data for casts: 118 (□), 119 (○), 120 (△), 121 (▽), 122 (◇), 123 (◁), 124 (▷) and 125 (☆).

The standard deviation of the calibrated data ranges from 3.1 to 4.6 μM with an average of 3.8 μM. This can be treated as the accuracy of the microelectrode sensor, provided the field calibration was performed. Significantly lower values of the mean difference suggest that the deviation is dominated by random errors rather than systematic errors. The average of the mean difference for all casts was found to be -0.6 μM, and ranging from -2.5 to 1.1 μM. Since the DO concentration varied significantly within the cast and between deployments (100 – 300 μM) it is more convenient to use the relative deviations instead of the absolute values. The calculated average mean difference and standard deviation were -0.4% and 2.2%, respectively.

Significantly larger deviations were found when the DO concentrations were calculated solely on the basis of analytical equations and parameters obtained in the lab. The following values were taken for the calculations: $D_{w(298)}=2.16\times10^{-5}$ cm^2 s^{-1}, $n_{app(298)}=3.26$, $a=12.5$ μm. The activation energies for $D_w(T)$ (equation (1.38)) and for $n_{app}(T)$ were taken as 13.8 and 6.4 kJ mol^{-1}, respectively. It can be seen that the analytically obtained DO concentration consistently underestimated the true c_{O2} value. The mean difference (ranging from -4.4 to -12.4 μM, averaging at -7.8 μM) was observed to be correlated with the standard deviation (5.8 to 10.2 μM, averaging at 7.9 μM), which points to a systematic error resulting from the choice of parameters taken for calculations. Nevertheless, the results follow very closely the bottle DO reference. The average standard deviation of 3.6% (ranging from 2.8 to 4.6%) indicates excellent microelectrode performance when compared to the earlier presented maximal error estimates of 14% (see section 4.5.1).

7.5.3 Response stability

All the c_{O2} – depth profiles obtained with the microelectrode sensor are presented in Figure 7.16. Superimposed are the DO concentrations determined from the bottled samples at discrete depths. For ease of comparison the profiles are offset by 30 μM from each other. From station 118 to 125 the profiles decrease in depth as the research ship was approaching the African continental shelf.

From the error analysis presented in the preceding subsection (7.5.2) one can see that the deviations from the true DO values do not vary in a systematic way from cast to cast. The calibration performed initially using Winkler titration data from cast 118 held throughout all the subsequent sensor deployments. The deviations of the experimental data from the bottles as a function of station number are plotted in Figure 7.17. No evident trend is observed, indicating the absence of any long term drift of the microelectrode response.

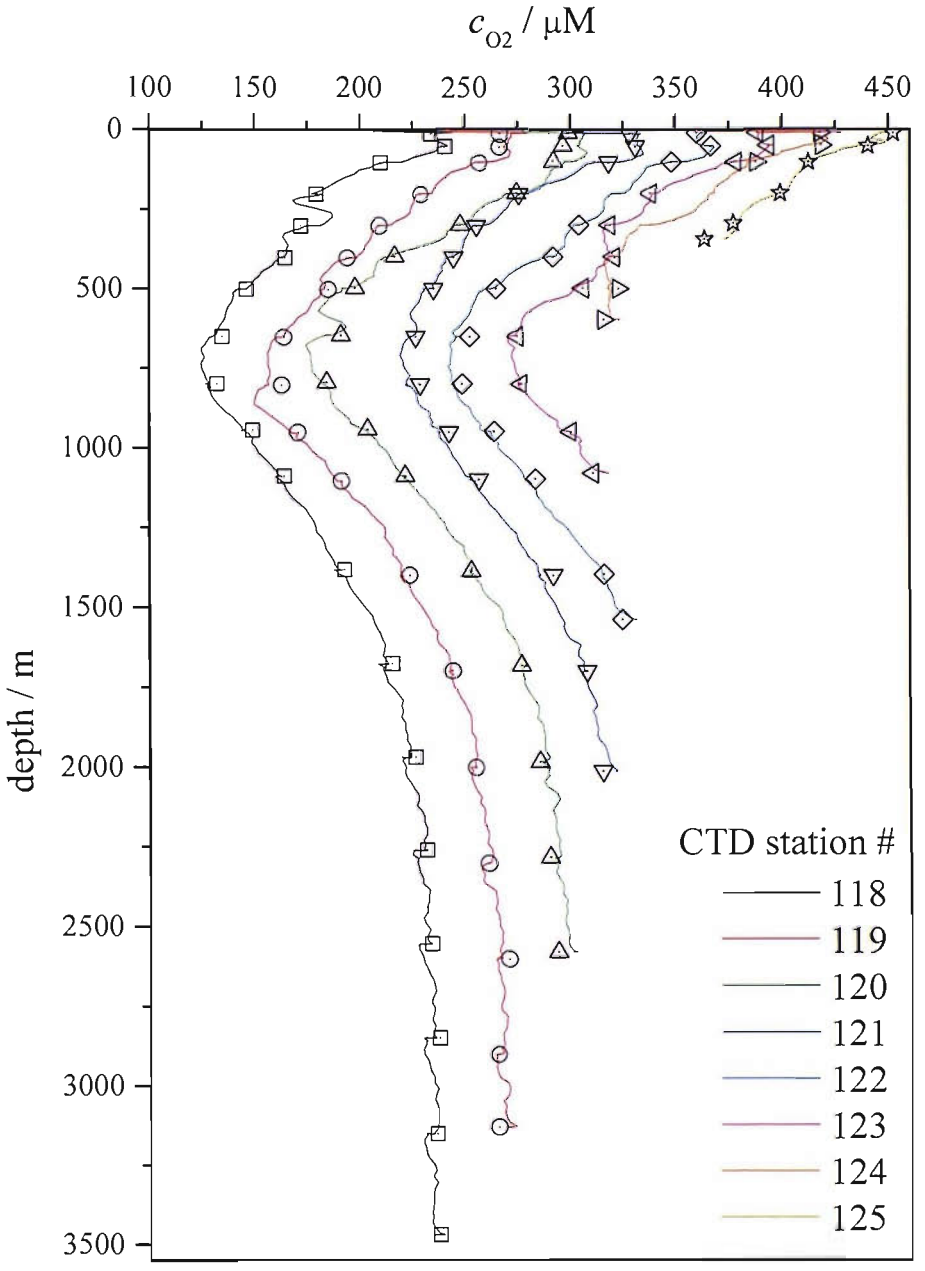

Figure 7.16 Comparison of DO – depth profiles (upcasts) obtained with the microelectrode DO sensor (calibrated vs bottles; lines) with the DO concentration determined by Winkler titration on samples taken at discrete depths (points). The profiles were recorded during the cruise D279 in eight consecutive CTD deployments: cast 118 (□), 119 (○), 120 (△), 121 (▽), 122 (◇), 123 (◁), 124 (▷) and 125 (☆). For clarity the profiles were separated by offset of 30 μM.

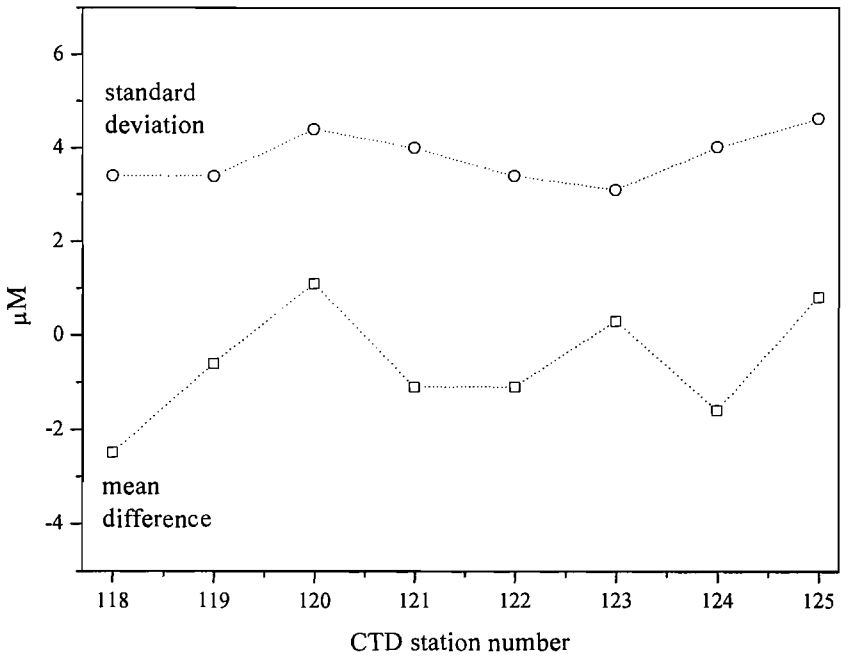

Figure 7.17 Standard deviation (O) and mean difference (□) of microelectrode response with respect to bottles data for eight subsequent CTD stations (up casts).

It has to be emphasised that the microelectrode was not treated in any way between the deployments. To maintain a consistent performance only the electrochemical cleaning (i.e. the short steps to positive potentials) was applied. When on board, the sensor was powered down and usually the electrode was left to dry. The sensor was re-powered every time the probe was submersed. An excellent cast to cast reproducibility proves that the applied pulse sequence is capable of maintaining a stable long term response (26 h deployment data).

7.5.4 Field measurements difficulties

Performing the measurements in the real ocean environment involves several complications, which are not present when operating the sensor in well

controlled laboratory conditions. The two main issues that emerged during the field trials were the point of reference of the potential applied to the working electrode and the problems related to the motion of the probe [232].

It was often observed that after submersing the CTD package the readings of the microelectrode DO sensor went off scale, i.e. the reduction current was so large that it saturated the current follower. It was later found that this phenomenon was due to the common ground reference point of the oxygen sensor electronics and other CTD instruments, as well as the sensor proximity to the rosette, which contained large quantities of stainless steel and zinc. Thus the potential difference was not applied with respect to the copper tube but to the bulk of other metals present on the CTD assembly. With large amount of zinc acting effectively as the reference electrode the applied potential corresponded not to the plateau of oxygen reduction wave, but to the hydrogen evolution region. The problem was resolved by mounting the sensor on the fin of the CTD. This increased the distance between the copper and the zinc chassis to approximately 1 m. Another option is to create a floating earth using the copper counter electrode as the earth reference by using isolation in signal and power circuits to break the link with the common ground reference.

Other problems were related to the CTD package motion. As mentioned before the current readings were altered every time the CTD was stopped. Moreover, the magnitude of the response was dependent on the direction of the probe movement, hence the hysteresis between the up- and down-casts. It was initially thought that such effect could arise if the sample inlet was pointing in one of the directions of the CTD movement. However, it was consistent during all the casts when the sample inlet was directed normally to the profiling direction and no definite explanation for this behaviour was found. A closer analysis of the current transient recorded *in situ* revealed yet another flow related issue. Figure 7.18 shows a snapshot of the microelectrode response recorded during profiling. One can observe low frequency distortions of the steady state current when the sensor is working on the CTD. These were correlated with the ship vertical movement due to waves on the surface. It appears that this motion was transferred even though the microelectrode was working inside the stop-flow cell.

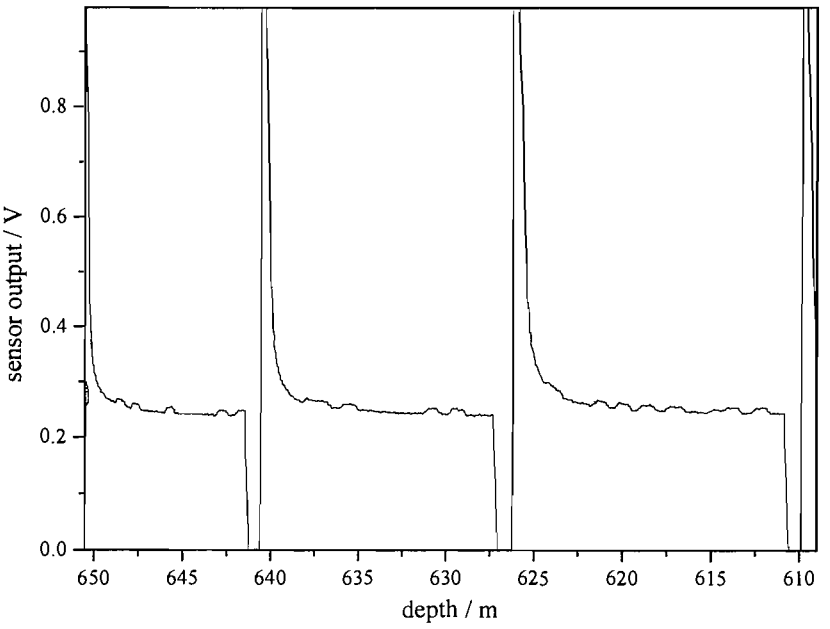

Figure 7.18 A snapshot of the microelectrode response while profiling on the CTD probe showing low frequency variations in the limiting current region caused by the vertical ship movement. The plot shows the raw signal smoothed by adjacent averaging (5 points).

7.6 Summary

A prototype of the microelectrode DO sensor employing an unshielded Pt microdisc was constructed and tested on the CTD profiler during transatlantic cruise D279. The sensor was equipped with a stop-flow cell to eliminate the effect of convective mass transport inherently present when measuring on constantly moving probe. Eight successful deployments yielded high quality DO – depth profiles. When in field calibration of the sensor was performed, the obtained DO concentrations followed very closely the reference data obtained by means of on-board Winkler titration on the bottled samples. Overall standard deviation from the bottles data was 2.2% with the mean difference of only -0.4%. The deviations were significantly larger when c_{O2} was calculated solely on the basis of analytical equations and

parameters determined in the laboratory conditions. This approach yielded DO concentrations underestimating the true value (bottles) by an average of approximately 4% (or 8 μM). The field tests show excellent cast to cast reproducibility with no long term drift of the microelectrode response. This confirmed that the periodically applied electrochemical cleaning pulse is sufficient to maintain a stable response over many days of continuous operation. The sensor response was however still significantly influenced by the probe motion. Variations in the signal following the stoppage of the CTD package and hysteresis between up and down casts remain issues to be resolved.

8 Conclusions and future work

Gold, platinum and mesoporous platinum were assessed as the cathode materials for the membrane-free dissolved oxygen sensor for oceanographic measurements. The effect of chloride on the electrode behaviour was investigated by means of cyclic voltammetry and potential step experiments were used to evaluate the long term stability of the electrode response. Gold was found unsuitable for the considered application as the prolonged operation resulted in the electrode material dissolution presumably as mixed chlorohydroxo gold complexes. Moreover, the response of continuously operated gold microelectrodes showed high degree of instability and irreproducibility. Oxygen reduction was also strongly affected by chloride. The oxygen reduction wave shifted approximately -300 mV in the investigated Cl^- concentration range from 0 to 500 mM. This effect was much smaller with platinum electrodes, where the shift in the cathodic direction did not exceed 50 mV. Pt was also found very resistant in presence of chloride ions and the only effect of long term operation was the roughening of the electrode surface. Nanostructured platinum films deposited from liquid crystal templates exhibited high activity for ORR with a pronounced kinetic enhancement. When compared to polished platinum microdisc the half-wave potentials were shifted on average 200 mV positive. In addition, the very high electroactive surface area of nanostructured microdiscs resulted in higher limiting currents due to the increase of n_{app}. Nonetheless, the films were found to be affected by continuous switching of the potential between oxygen reduction and oxide formation regions. An appreciable loss in surface area during long term experiments suggested the erosion of the film structure. Also, some of the electrodes appeared to loose their activity towards ORR over period of weeks when repeatedly tested.

Polished Pt microdiscs were found to be the best choice for the oxygen reduction cathode in the DO sensor for oceanographic application. Starting from the established principles, the parameters of sensor operation were optimised to yield accurate and reliable performance in real working conditions. The steady state response was shown to be stable (SD=0.7 %) over periods of 24 h of continuous

operation in synthetic seawater. The activity was maintained solely by means of *in situ* electrochemical cleaning, i.e. switching the potential to the onset of oxide formation region (+0.2 V vs SMSE) for 1 s. In between, the electrode was held at -1.05 V for the determination of the DO concentration from the steady state limiting current.

To obtain an accurate relationship between the electrode current and the DO concentration an automated calibration system was developed. The system provided a fine control of DO increments and range, which allowed a microelectrode characterisation superior to the two points calibration commonly used for commercial devices. The calibration procedure and the apparatus were validated by measurements using an optical sensor based on commercially available sensing membrane. Excellent linearity was found between the measured limiting current and DO concentration regardless of the microdisc radius up to oxygen saturation. Detection limit of 0.9 μM was achieved for 25 μm radius electrodes. Error estimates for calibrated microelectrodes were calculated. For DO concentrations >50 μM the relative accuracy of the determination is below 4 % for 12.5 and 25 μm radii and below 6% for a=5 μm. As an alternative to calibration an analytical approach was proposed, which accounts for salinity and temperature effects and gives a direct value of DO concentration from the measured limiting current. With more parameters needed the relative accuracy is significantly lower and ranges from 15% for the smallest to 11% for the largest microdisc.

An accurate calibration procedure also served to determine the values of n_{app}. The data obtained for a range of electrode radii were used to investigate the dependence of n_{app} on mass transport coefficient. n_{app} decreases with decreasing electrode radius, i.e. with increasing m_i. The obtained values of steady state n_{app} were fitted to the model developed by Chen and Kucernak [120], which allows extraction of a number of kinetic parameters and mechanistic information. The findings suggest that under the experimental conditions used the ORR proceeds via the series mechanism, i.e. the contribution of the direct reduction of oxygen to water is negligible and the oxygen is reduced in two two-electron reduction steps with peroxide intermediates.

A prototype of the dissolved oxygen sensor based on unshielded Pt microdisc was constructed and tested during oceanographic cruise. The sensor utilised the steady state limiting current measurements and the developed electrochemical cleaning procedure. To overcome the current distortions due to convection the sensor was equipped with a stop flow cell and a solenoid pump to periodically sample seawater and perform the measurements in stagnant solution. Several deep sea deployments yielded high quality DO-depth profiles of the water column. Excellent agreement was found between the sensor readings and the Winkler titration standard. When the sensor was calibrated in the field, the mean difference from the bottle data was only 0.4% (SD=2.2%; average for all performed casts). In addition the DO concentrations were also calculated using the analytical approach, i.e. solely on the basis of parameters determined in the laboratory. The agreement was remarkably better than to the theoretical error estimate of 14% for 12.5 μm radius microdisc. Compared to bottles standard, the oxygen concentration calculated from the electrode output differed 4.0% on average, with standard deviation of 3.6%. The performance of the microelectrode was consistent throughout all the sensor deployments, which proved the effectiveness of the electrochemical cleaning procedure. All obtained profiles were calculated on the basis of single in field calibration and the variations from the bottles data did not show any long term drift.

To improve the response time of the sensor, and potentially remove the stop-flow cell, two alternative measurement strategies were investigated. The first approach involved the creation of forced convection conditions by vibrating the microelectrode with a piezoceramic transducer. A significant enhancement of the limiting currents was observed for a purely mass transport controlled system (both for electrode vibrating in the bulk of solution and in the vicinity of an insulating surface). However, the effect was much less pronounced for oxygen reduction. The results have shown that despite the increased mass transfer to the electrode a limitation exists, most probably due to the limited number of active electrode sites. The enhancement was insufficient to compete with the effect of convection resulting from the probe movement.

The second method to improve the response time and flow immunity was based on non-steady state measurements. The double potential step chronocoulometry with step duration down to 1 ms was investigated as an alternative to the limiting current measurements. It was demonstrated that the double potential step measurements can give quantitative information on DO concentration. The calibration curves were linear for steps between 1 and 20 ms over the full range of DO concentrations (up to oxygen saturation). The electrode showed good stability over periods up to 25 h, with effects on the electrode surface state similar to those observed for steady state measurements. The initial tests of the method under flow conditions proved very encouraging, in particular for smaller microdiscs where the measured charges did not vary under flow rates up to 80 ml s^{-1}.

Further work is needed for the development of the non-steady state approach, including long term stability over periods of days and in particular the flow dependence of the response. The use of the chronocoulometry with millisecond step durations also requires developing a new electronic circuitry. It should be capable of integrating the current response in real time and outputing a simple analogue voltage corresponding to the recorded charge. The removal of the flow cell should also be followed by redesigning the sensor head to insure that the laminar flow boundary layer can be established next to the microdisc. Moreover, using a microelectrode array instead of single microdisc for improved sensitivity and reliability should also be considered.

9 Appendix

9.1 Estimation of the nanostructured film thickness

The thickness of the nanostructured films was estimated from the SEM photographs in a way described below:

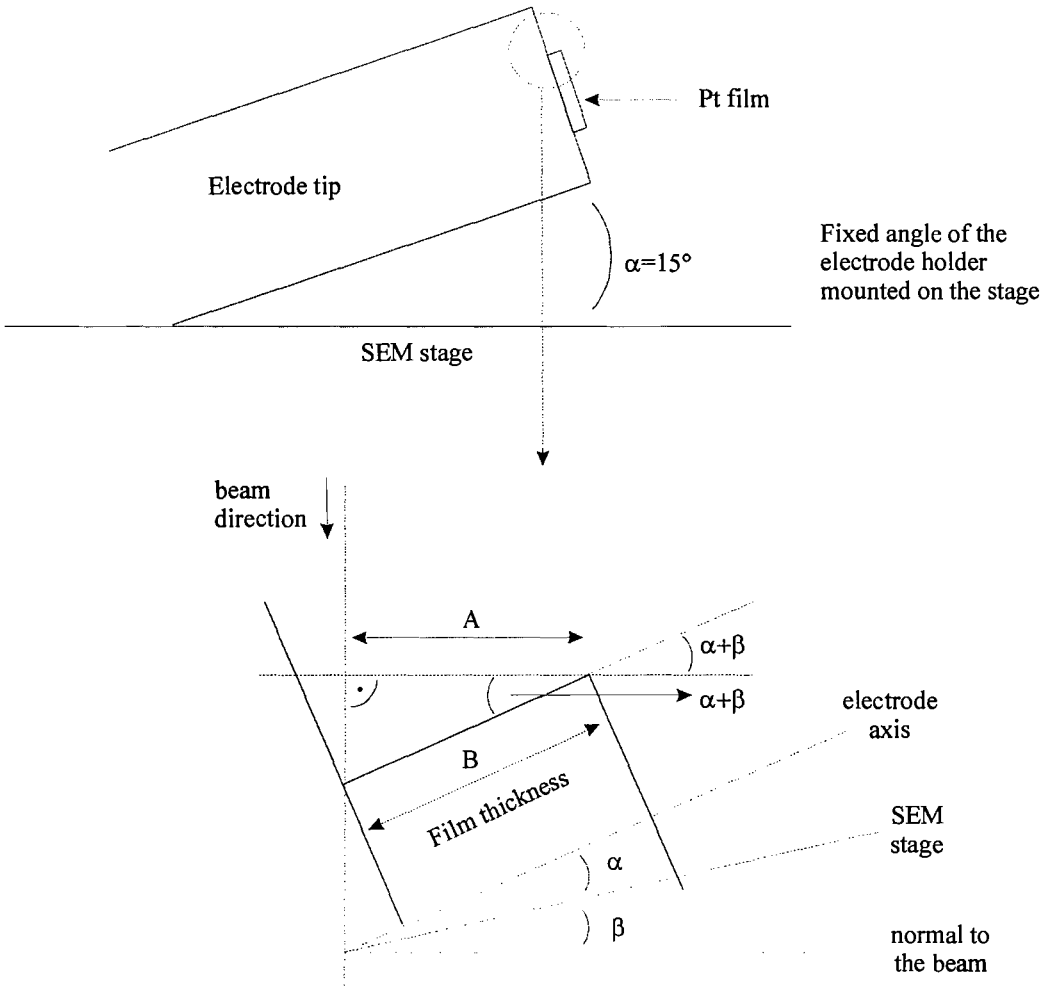

Figure 9.1 A schematic used to calculate the film thickness from a microphotograph.

β is the angle between the SEM stage and the normal to the beam direction. The stage angle β is known and A is measured from the microphotograph (Figure 9.2). Thus, the film thickness B can be calculated as follows:

$$B = \frac{A}{\cos(\beta + 15°)} \tag{9.1}$$

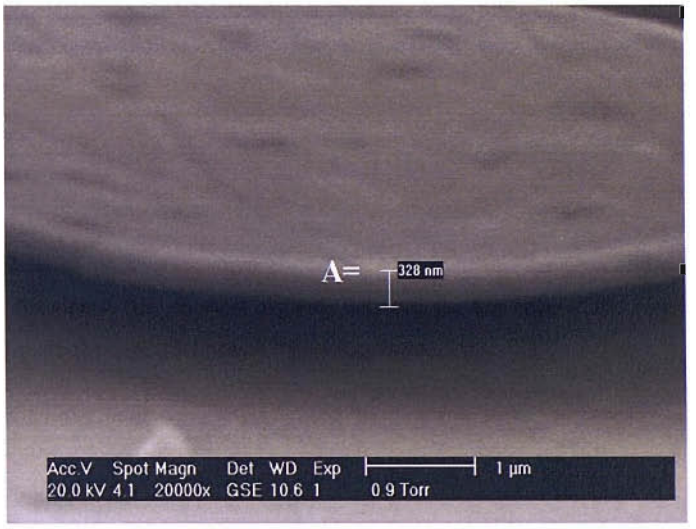

Figure 9.2 SEM photograph of a nanostructured Pt film edge. Marked on the photograph is the measured distance A (the shortest distance between the top edge of the film and the beam direction) used to estimate the film thickness.

9.2 Calculations of absolute and relative errors of oxygen concentration from the sensor reading

9.2.1 Error on DO concentration (c_{O2}) as calculated from the analytical expression

$$c_{O2} = \frac{i_{lim}}{4n_{app}FD_{O2}a} \tag{9.2}$$

where

$$D_{O2} = D_w \left(\frac{V}{V_w}\right)^{2/3} \exp\left(-\frac{\Delta\alpha x_+ + \Delta\beta x_-}{RT}\right) \tag{9.3}$$

(9.3) is substituted to (9.2) and rearranged

$$c_{O2} = \frac{i_{lim}}{4n_{app}FaD_w \left(\frac{V}{V_w}\right)^{2/3} \exp\left(-\frac{\Delta\alpha x_+ + \Delta\beta x_-}{RT}\right)} = \frac{i_{lim} \exp\left(\frac{\Delta\alpha x_+ + \Delta\beta x_-}{RT}\right)}{4n_{app}FaD_w \left(\frac{V}{V_w}\right)^{2/3}} \tag{9.4}$$

Absolute error on c_{O2}

$$\Delta c_{O2} = \left|\frac{\partial c_{O2}}{\partial i_{lim}}\right| \Delta i_{lim} + \left|\frac{\partial c_{O2}}{\partial n_{app}}\right| \Delta n_{app} + \left|\frac{\partial c_{O2}}{\partial a}\right| \Delta a + \left|\frac{\partial c_{O2}}{\partial D_{O2}}\right| \Delta D_{O2} \tag{9.5}$$

Since $D_{O2} = f(D_w, T)$

$$\Delta c_{O2} = \frac{\partial c_{O2}}{\partial i_{lim}} \Delta i_{lim} + \frac{\partial c_{O2}}{\partial n_{app}} \Delta n_{app} + \frac{\partial c_{O2}}{\partial a} \Delta a + \frac{\partial c_{O2}}{\partial D_{O2}} \frac{\partial D_{O2}}{\partial D_w} \Delta D_w + \frac{\partial c_{O2}}{\partial D_{O2}} \frac{\partial D_{O2}}{\partial T} \Delta T \tag{9.6}$$

which yields the expression for maximal uncertainty in determination of c_{O2}

$$\Delta c = \left|\frac{\partial c}{\partial i_{\lim}}\right| \Delta c_{O2} + \left|\frac{\partial c}{\partial n_{app}}\right| \Delta n_{app} + \left|\frac{\partial c}{\partial a}\right| \Delta a + \left|\frac{\partial c}{\partial D_w}\right| \Delta D_w + \left|\frac{\partial c}{\partial T}\right| \Delta T \tag{9.7}$$

The total differential of (9.4) is the expression for the maximal error on c_{O2}:

$$\Delta c_{O2} = \frac{\exp\left(\frac{\Delta\alpha x_+ + \Delta\beta x_-}{RT}\right)}{4 n_{app} F a D_w \left(\frac{V}{V_w}\right)^{2/3}} \Delta i_{\lim} + \frac{i_{\lim} \exp\left(\frac{\Delta\alpha x_+ + \Delta\beta x_-}{RT}\right)}{4 n_{app}^2 F a D_w \left(\frac{V}{V_w}\right)^{2/3}} \Delta n_{app} + \frac{i_{\lim} \exp\left(\frac{\Delta\alpha x_+ + \Delta\beta x_-}{RT}\right)}{4 n_{app} F a^2 D_w \left(\frac{V}{V_w}\right)^{2/3}} \Delta a$$

$$+ \frac{i_{\lim} \exp\left(\frac{\Delta\alpha x_+ + \Delta\beta x_-}{RT}\right)}{4 n_{app} F a D_w^2 \left(\frac{V}{V_w}\right)^{2/3}} \Delta D_w + \frac{i_{\lim} \exp\left(\frac{\Delta\alpha x_+ + \Delta\beta x_-}{RT}\right)}{4 n_{app} F a D_w \left(\frac{V}{V_w}\right)^{2/3} T^2} \Delta T \tag{9.8}$$

The relative error on concentration can be calculated as follows

$$\frac{\Delta c_{O2}}{c_{O2}} = \frac{\text{eq}(9.8)}{c_{O2}} = \text{eq}(9.8) \times \frac{4 n_{app} F D_w \left(\frac{V}{V_w}\right)^{2/3} a}{i_{\lim} \exp\left(\frac{\Delta\alpha x_+ + \Delta\beta x_-}{RT}\right)} \tag{9.9}$$

which gives

$$\frac{\Delta c_{O2}}{c_{O2}} = \frac{\Delta i_{\lim}}{i_{\lim}} + \frac{\Delta n_{app}}{n_{app}} + \frac{\Delta a}{a} + \frac{\Delta D_w}{D_w} + \frac{\Delta T}{T^2} \tag{9.10}$$

After substituting all the Δx values for T=298 K (listed in section 4.2.1) and assuming that n_{app} and D_w are not a function of oxygen concentration (which is true in our case of linear relationship between $i_{\lim}$ and c_{O2}) the relative errors expressed in percentage are 15, 14 and 11 for a=5, 12.5, and 25 μm, respectively.

9.2.2 Error on c_{O2} with calibration curve available

The linear fit of the calibration points yields a function

$$i_{lim} = i_0 + B \times c_{O2} \tag{9.11}$$

After simple rearrangement we get the equation for c_{O2}

$$c_{O2} = \frac{i_{lim} - i_0}{B} \tag{9.12}$$

The total error on c_{O2} is defined as

$$\Delta c_{O2} = \left|\frac{\partial c_{O2}}{\partial i_{lim}}\right| \Delta i_{lim} + \left|\frac{\partial c_{O2}}{\partial i_0}\right| \Delta i_0 + \left|\frac{\partial c_{O2}}{\partial B}\right| \Delta B \tag{9.13}$$

The corresponding total differential allows calculation of the absolute error

$$\Delta c_{O2} = \frac{1}{B} \Delta i_{lim} + \frac{1}{B} \Delta i_0 + \frac{i_{lim} - i_0}{B^2} \Delta B \tag{9.14}$$

The relative error can be estimated as follows

$$\frac{\Delta c_{O2}}{c_{O2}} = \frac{1}{i_{lim} - i_0} \Delta i_{lim} + \frac{1}{i_{lim} - i_0} \Delta i_0 + \frac{1}{B} \Delta B \tag{9.15}$$

9.3 Calculations of error of $n_{app}=f(T)$

n_{app} was determined from the calibration curve:

$$i_{lim} = i_0 + 4n_{app}FD_{O2}c_{O2} \tag{9.16}$$

Thus

$$n_{app} = \frac{i_{lim} - i_0}{c_{O2}} \times \frac{1}{4FD_{O2}a} = \frac{B}{4FD_{O2}a} \tag{9.17}$$

where B is the slope of the calibration curve.

The error can then be calculated as the total differential of equation (9.17)

$$\Delta n_{app} = \left|\frac{\partial n_{app}}{\partial B}\right| \Delta B + \left|\frac{\partial n_{app}}{\partial D_{O2}}\right| \Delta D_{O2} + \left|\frac{\partial n_{app}}{\partial a}\right| \Delta a \tag{9.18}$$

Differentiation by all variables gives the expression for maximal uncertainty of n_{app}

$$\Delta n_{app} = \frac{1}{4FD_{O2}a} \times \left(\Delta B + \frac{B\Delta D_{O2}}{D_{O2}} + \frac{B\Delta a}{a} \right) \tag{9.19}$$

9.4 Oxygen reduction transients, variation of n_{app} depending on the timescale of experiment

An attempt was made to investigate the dependence of n_{app} on the timescale of experiment. It was shown (section 4.6) that n_{app} varies with the mass transfer coefficient, therefore this effect should also be observed at short times after the potential step, i.e. during the transition from semiinfinite linear diffusion to pseudohemispherical diffusion. The obtained data are incomplete and lack explanation. Nevertheless, for the completeness of the research record the methodology and some results are presented here in the appendix.

9.4.1 Transient response model

To establish principles for further analysis of oxygen reduction transients, it is necessary to identify a model current – time behaviour. Several models for the current response after a potential step at a microdisc are available in the literature and were briefly described in section 1.2.3.

In this work the emphasis is put on the first 50 ms of transient response, as this is the largest response time sought for the sensor. For smaller microelectrodes, in this time domain the dimensionless time τ falls into regimes described by both equations derived by Aoki and Osteryoung [17, 18] (see equations (1.3) (1.4) on page 5). Therefore it is convenient to use the function simulated by Shoup and Szabo [23], which combines both limiting cases into one equation valid for any values of τ:

$$i = 4nFDca\left(0.7854 + 0.8862\tau^{-1/2} + 0.2146\exp\left(-0.7823\tau^{-1/2}\right)\right) \tag{9.20}$$

To verify the applicability of this expression the simulated curves were compared to transients recorded for the reduction of $Ru(NH_3)_6^{3+}$. The results are shown in Figure 9.3, where the experimental response is plotted along with the theoretical transients according to Shoup and Szabo model. One can see a very good agreement between

the experiment and Shoup and Szabo model, thus it is chosen for the analysis of oxygen reduction transients in the following sections.

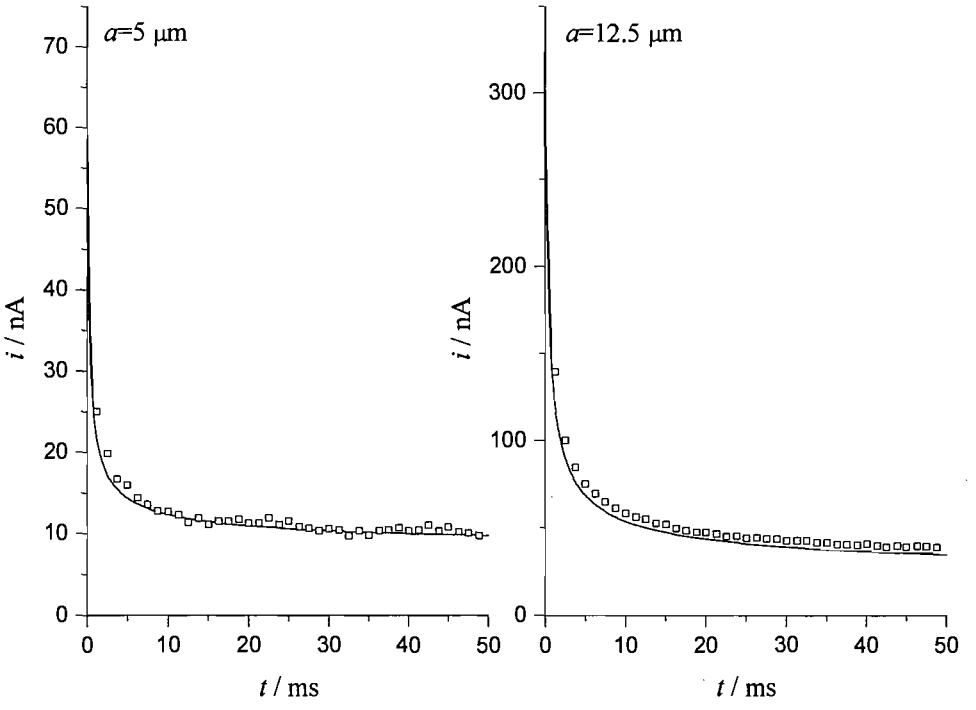

Figure 9.3 Comparison of $Ru(NH_3)_6^{3+}$ reduction transients (c=5 mM, in 250 mM KCl; squares) with theoretical curves according to Shoup & Szabo (solid line, equation (9.20)).

9.4.2 Oxygen reduction transients

The response to a potential step for oxygen reduction differs significantly from the one predicted by the Shoup and Szabo equation. An example of transient recorded at Pt microdisc (a=12.5 μm) in oxygen saturated 0.5 M NaCl solution is shown in Figure 9.4. It is compared to a transient simulated for the same experimental conditions (c_{O2}, D_{O2}, a) and using the value of n_{app} obtained from the steady state part of the transient (n_{app}=3.26).

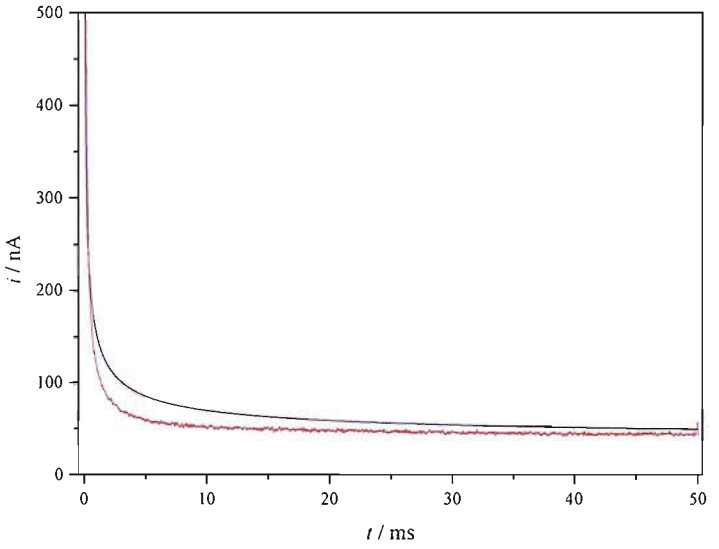

Figure 9.4 Oxygen reduction transient after the step from +0.2 to -1.05 V at Pt microdisc (a=12.5 μm) in oxygen saturated 0.5 M NaCl (red) and the curve simulated with Shoup an Szabo equation using experimental parameters and n_{app}=3.26 determined from the steady state current (black).

Clearly the experimental current is lower at short times and tends to the theoretical curve as time increases. Since all the other parameters are independent of time, this variation is ascribed to the changing value of n_{app}. Two approaches were used to estimate n_{app} as a function of time.

In the first approach the experimental current $i_{O2}(t)$ corrected for response in oxygen free solution $i_{Ar}(t)$ is compared to the model transient for n_{app}=1 (simulated using Shoup and Szabo equation (9.20), $i_{S\&S(n=1)}$). Thus the resulting function should correspond to the variation of n_{app} with time:

$$n_{app}(t) = \frac{i_{O2}(t) - i_{Ar}(t)}{i_{S\&S(n=1)}(t)} \tag{9.21}$$

The second approach utilises basically the same principle, but double potential step charges (corrected for blank measurements) are analysed instead of current transients. This form of analysis does not yield a function of n_{app} vs time but gives the average value of n_{app} over the potential step duration τ ($\bar{n}_{app}(\tau)$).

$$\bar{n}_{app}(\tau) = \frac{Q_{O2}(\tau) - Q_{Ar}(\tau)}{Q_{S\&S(n=1)}(\tau)} \tag{9.22}$$

where $Q_{O2}(\tau)$ and $Q_{Ar}(\tau)$ are the double potential step charges for step duration τ in oxygen and argon saturated solution, respectively, and $Q_{S\&S(n=1)}(\tau)$ is the theoretically predicted charge for n_{app}=1. The experiments were conducted for two values of resting potentials: 0.0 and 0.2 V vs SMSE, from which the potential was stepped to -1.05 V. The results for 5 and 12.5 μm microdisc radii are presented in Figure 9.5 and Figure 9.6, respectively.

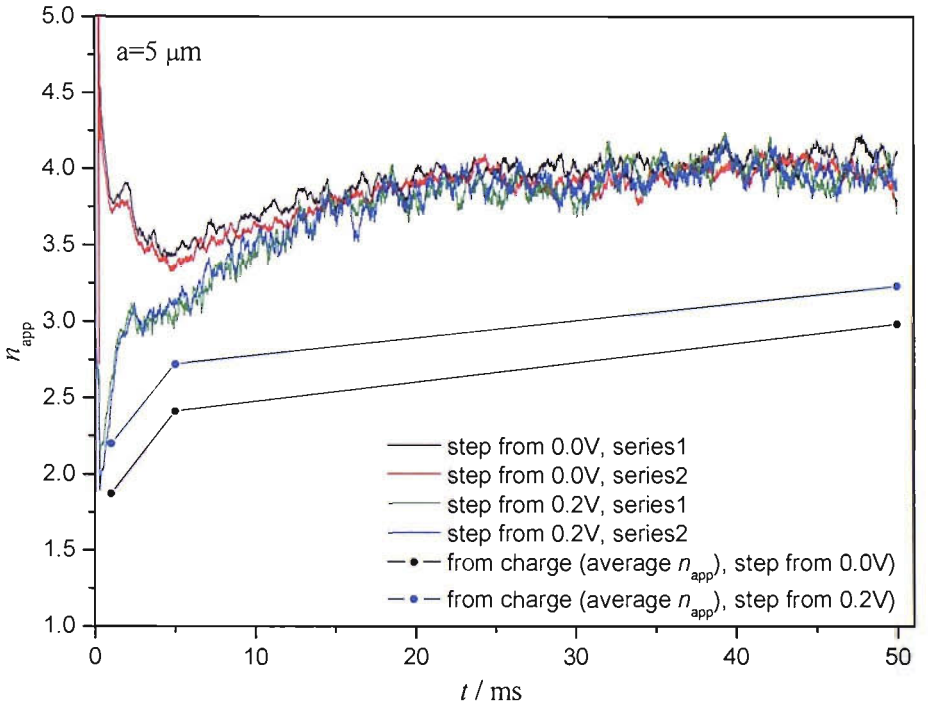

Figure 9.5 n_{app} as a function of time for oxygen reduction at Pt microdisc (a=5 μm) in oxygen saturated 0.5 M NaCl.

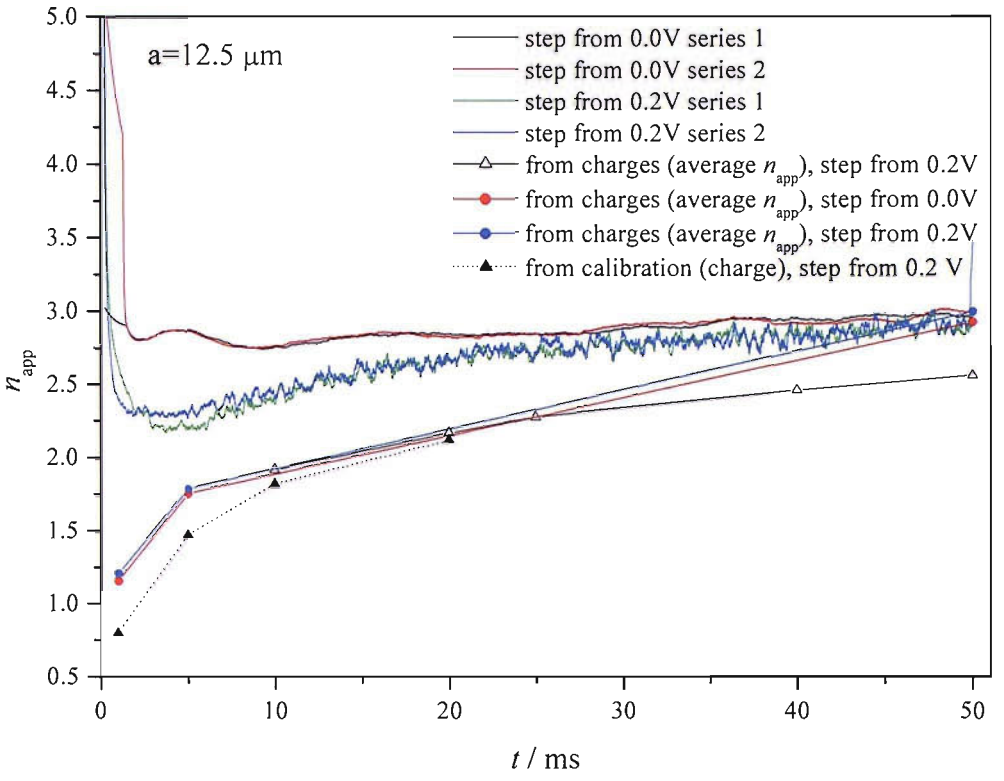

Figure 9.6 n_{app} as a function of time for oxygen reduction at Pt microdisc (a=12.5 μm) in oxygen saturated 0.5 M NaCl.

In all cases when the potential is stepped from +0.2 V an increase of n_{app} is observed. For 0.0 V resting potential the n_{app} is noticeably higher during first 20 ms. One could speculate that the platinum surface is free of oxide and therefore higher activity towards oxygen reduction is observed. However, this effect is not seen when the charges are analysed, where both trends are very similar. Another inconsistency is seen when the results for different sizes and absolute values of n_{app} are compared. While for a=12.5 μm the values tend to rise to n_{app} observed in the steady state (~3.3), for a=5 μm n_{app} quickly reaches 4, a value which is never seen for the microdisc of this size.

Overall, the above sets of data are inconclusive. Nevertheless, the values of n_{app} do appear to vary depending on the timescale of the potential step experiment. A possible application of DO measurements on millisecond timescales should thus be always preceded with a calibration of the microdisc.

10 References

[1] Mulkey, D. K.; Henderson, R. A.; Olson, J. E.; Putnam, R. W.; Dean, J. B., *J. Appl. Physiol.* **2001**, *90*, 1887.

[2] Pavia, L.; Myers, J.; Cesare, R., *Chest* **1999**, *116*, 808.

[3] Munger, M. A.; Stanek, E. J.; Nara, A. R.; Strohl, K. P.; Decker, M. J.; Nair, R. N., *American Journal of Cardiology* **1994**, *73*, 180.

[4] Vanderkooi, J. M.; Erecinska, M.; Silver, I. A., *American Journal of Physiology* **1991**, *260*, C1131.

[5] Vaupel, P.; Thews, O.; Kelleher, D. K.; Hoeckel, M. In *Oxygen Transport to Tissue Xx*, 1998; Vol. 454, pp 591.

[6] Greenhaff, P. L., *Journal of Physiology-London* **2003**, *551*, 397.

[7] Maisch, C.; Hofmann, V.; Benda, N.; Luft, D., *Angiology* **1998**, *49*, 203.

[8] Joos, F.; Plattner, G.-K.; Thomas, F. S.; Kortzinger, A.; Douglas, W. R. W., *EOS, Transactions, American Geophysical Union* **2003**, *84*, 197.

[9] Matear, R. J.; Hirst, A. C.; McNeil, B. I., *Geochem. Geophys. Geosyst.* **2000**, *1*, doi: 2000GC000086.

[10] Wightman, R. M., *Anal. Chem.* **1981**, *53*, 1125.

[11] Aoki, K., *Electroanalysis* **1993**, *5*, 627.

[12] Montenegro, M. I.; Queirós, M. A.; Daschbach, J. L., Eds. *Microelectrodes: Theory and Applications*; Kluwer Academic Publishers, 1991.

[13] Bard, A. J.; Faulkner, L. R., *Electrochemical Methods, Fundamentals and Applications*, 2nd ed.; John Wiley & Sons, Inc.: New York, 2001.

[14] Stulik, K.; Amatore, C.; Holub, K.; Marecek, V.; Kutner, W., *Pure Appl. Chem.* **2000**, *72*, 1483.

[15] Fleischmann, M.; Pons, S.; Rolison, D. R.; Schmidt, P. P., Eds. *Ultramicroelectrodes*; Datatech Systems Inc.: Morganton, NC, 1987.

[16] Cottrell, F. G., *Z. Phys. Chem.* **1903**, *42*, 385.

[17] Aoki, K.; Osteryoung, J., *J. Electroanal. Chem.* **1981**, *122*, 19.

[18] Aoki, K.; Osteryoung, J., *J. Electroanal. Chem.* **1984**, *160*, 335.

[19] Oldham, K. B., *J. Electroanal. Chem.* **1981**, *122*, 1.

[20] Kakihana, M.; Ikeuchi, H.; Sato, G. P.; Tokuda, K., *J. Electroanal. Chem.* **1981**, *117*, 201.

[21] Heinze, J., *J. Electroanal. Chem.* **1981**, *124*, 73.

[22] Aoki, K.; Osteryoung, J., *J. Electroanal. Chem.* **1981**, *125*, 315.

[23] Shoup, D.; Szabo, A., *J. Electroanal. Chem.* **1982**, *140*, 237.

[24] Mahon, P. J.; Oldham, K. B., *Electrochim. Acta* **2004**, *49*, 5041.

[25] Mahon, P. J.; Oldham, K. B., *Anal. Chem.* **2005**, *77*, 6100.

[26] Cope, D. K.; Tallman, D. E., *J. Electroanal. Chem.* **1990**, *285*, 79.

[27] Hitchman, M. L., *Measurement of Dissolved Oxygen*; John Wiley & Sons: New York, 1978.

[28] Winkler, L. W., *Berichte der Deutschen Chemischen Gesellschaft* **1888**, *21*, 2843.

[29] Hamlin, P. A.; Lambert, J. L., *Anal. Chem.* **1971**, *43*, 618.

[30] Demas, J. N.; DeGraff, B. A.; Coleman, P. B., *Anal. Chem.* **1999**, *71*, 793A.

[31] Stokes, M. D.; Somero, G. N., *Limnol. Oceanogr.* **1999**, *44*, 189.

[32] Kortzinger, A.; Schimanski, J.; Send, U., *J. Atmos. Ocean. Technol.* **2005**, *22*, 302.

[33] Glazer, B. T.; Marsh, A. G.; Stierhoff, K.; Luther, G. W., *Anal. Chim. Acta* **2004**, *518*, 93.

[34] Yim, H. S.; Meyerhoff, M. E., *Anal. Chem.* **1992**, *64*, 1777.

[35] Yim, H. S.; Kibbey, C. E.; Ma, S. C.; Kliza, D. M.; Liu, D.; Park, S. B.; Torre, C. E.; Meyerhoff, M. E., *Biosens. Bioelectron.* **1993**, *8*, 1.

[36] Meruva, R. K.; Meyerhoff, M. E., *Electroanalysis* **1995**, *7*, 1020.

[37] Meruva, R. K.; Meyerhoff, M. E., *Anal. Chim. Acta* **1997**, *341*, 187.

[38] Meruva, R. K.; Meyerhoff, M. E., *Biosens. Bioelectron.* **1998**, *13*, 201.

[39] Clark, L. C., Jr.; Wolf, R.; Granger, D.; Taylor, Z., *J. Appl. Physiol.* **1953**, *6*, 189.

[40] Linek, V.; Vacek, V.; Sinkule, J.; Benes, P., *Measurements of Oxygen by Membrane-Covered Probes*; John Wiley & Sons: New York, 1988.

[41] Gnaiger, E.; Forstner, H., Eds. *Polarographic Oxygen Sensors. Aquatic and Physiological Applications*; Springer-Verlag: Berlin, 1983.

[42] Revsbech, N. P., *Limnol. Oceanogr.* **1989**, *34*, 474.

[43] Mitsubayashi, K.; Wakabayashi, Y.; Murotomi, D.; Yamada, T.; Kawase, T.; Iwagaki, S.; Karube, I., *Sens. Actuators, B* **2003**, *95*, 373.

[44] http://unisense.net.dynamicweb.dk/Default.aspx?ID=466.

[45] Wittkampf, M.; Chemnitius, G. C.; Cammann, K.; Rospert, M.; Mokwa, W., *Sens. Actuators, B* **1997**, *43*, 40.

[46] McLaughlin, G. W.; Braden, K.; Franc, B.; Kovacs, G. T. A., *Sens. Actuators, B* **2002**, *83*, 138.

[47] Hinkers, H.; Hermes, T.; Sundermeier, C.; Borchardt, M.; Dumschat, C.; Bucher, S.; Buhner, M.; Cammann, K.; Knoll, M., *Sens. Actuators, B* **1995**, *24*, 300.

[48] Atkinson, M. J.; Thomas, F. I. M.; Larson, N., *J. Atmos. Ocean. Technol.* **1996**, *13*, 1267.

[49] Pletcher, D.; Sotiropoulos, S., *Anal. Chim. Acta* **1996**, *322*, 83.

[50] Preidel, W.; Rao, J. R.; Mund, K.; Schunck, O.; David, E., *Sens. Actuators, B* **1995**, *28*, 71.

[51] Brendel, P. J.; Luther, G. W., *Environ. Sci. Technol.* **1995**, *29*, 751.

[52] Rychen, P.; Gobet, J.; Santoli, R., Electrochemical Self-Cleaning & Self Calibrating Microdisk Array, *The 56th Annual Meeting of the International Society of Electrochemistry*, Busan, Korea 2005.

[53] Morita, K.; Shimizu, Y., *Anal. Chem.* **1989**, *61*, 159.

[54] Atkinson, M. J.; Thomas, F. I. M.; Larson, N.; Terrill, E.; Morita, K.; Liu, C. C., *Deep-Sea Res. Part I-Oceanogr. Res. Pap.* **1995**, *42*, 761.

[55] Braun, R. D.; Lanzen, J. L.; Snyder, S. A.; Dewhirst, M. W., *Am. J. Physiol.-Heart Circul. Physiol.* **2001**, *280*, H2533.

[56] Wainright, S. C.; Kremer, J. N.; Davanzo, C., *Water Res.* **1995**, *29*, 2035.

[57] Baumgärtl, H.; Lübbers, D. W. In *Oxygen supply*; Kessler, M., Ed.; Urban and Schwarzenberg: Munich, 1973, pp 130.

[58] Xu, K.; Dexter, S. C.; Luther, G. W., *Corrosion* **1998**, *54*, 814.

[59] Luther, G. W.; Rozan, T. F.; Taillefert, M.; Nuzzio, D. B.; Di Meo, C.; Shank, T. M.; Lutz, R. A.; Cary, S. C., *Nature* **2001**, *410*, 813.

[60] Luther, G. W.; Reimers, C. E.; Nuzzio, D. B.; Lovalvo, D., *Environ. Sci. Technol.* **1999**, *33*, 4352.

[61] Luther, G. W.; Brendel, P. J.; Lewis, B. L.; Sundby, B.; Lefrancois, L.; Silverberg, N.; Nuzzio, D. B., *Limnol. Oceanogr.* **1998**, *43*, 325.

[62] Atkinson, M. J., *Limnol. Oceanogr.* **1988**, *33*, 141.

[63] Thomas, F. I. M.; Atkinson, M. J., *J. Atmos. Ocean. Technol.* **1995**, *12*, 390.

[64] Thomas, F. I. M.; McCarthy, S. A.; Bower, J.; Krothapalli, S.; Atkinson, M. J.; Flament, P., *J. Atmos. Ocean. Technol.* **1995**, *12*, 687.

[65] Viollier, E.; Rabouille, C.; Apitz, S. E.; Breuer, E.; Chaillou, G.; Dedieu, K.; Furukawa, Y.; Grenz, C.; Hall, P.; Janssen, F.; Morford, J. L.; Poggiale, J. C.; Roberts, S.; Shimmield, T.; Taillefert, M.; Tengberg, A.; Wenzhofer, F.; Witte, U., *J. Exp. Mar. Biol. Ecol.* **2003**, *285*, 5.

[66] Taillefert, M.; Luther, G. W.; Nuzzio, D. B., *Electroanalysis* **2000**, *12*, 401.

[67] Daly, K. L.; Byrne, R. H.; Dickson, A. G.; Gallager, S. M.; Perry, M. J.; Tivey, M. K., *Mar. Technol. Soc. J.* **2004**, *38*, 121.

[68] Revsbech, N. P.; Jorgensen, B. B.; Blackburn, T. H., *Science* **1980**, *207*, 1355.

[69] Revsbech, N. P.; Sorensen, J.; Blackburn, T. H.; Lomholt, J. P., *Limnol. Oceanogr.* **1980**, *25*, 403.

[70] Revsbech, N. P.; Jorgensen, B. B.; Blackburn, T. H.; Cohen, Y., *Limnol. Oceanogr.* **1983**, *28*, 1062.

[71] Revsbech, N. P.; Ward, D. M., *Appl. Environ. Microbiol.* **1983**, *45*, 755.

[72] Jorgensen, B. B.; Revsbech, N. P., *Limnol. Oceanogr.* **1985**, *30*, 111.

[73] Revsbech, N. P.; Madsen, B.; Jorgensen, B. B., *Limnol. Oceanogr.* **1986**, *31*, 293.

[74] Archer, D.; Emerson, S.; Smith, C. R., *Nature* **1989**, *340*, 623.

[75] Gundersen, J. K.; Jorgensen, B. B., *Nature* **1990**, *345*, 604.

[76] Takeuchi, T.; Yokoyama, K.; Kobayashi, K.; Suzuki, M.; Tamiya, E.; Karube, I.; Utsunomiya, K.; Imai, O.; Masuda, Y., *Anal. Chim. Acta* **1993**, *276*, 65.

[77] Oldham, C., *Limnol. Oceanogr.* **1994**, *39*, 1959.

[78] Glud, R. N.; Gundersen, J. K.; Revsbech, N. P.; Jorgensen, B. B., *Limnol. Oceanogr.* **1994**, *39*, 462.

[79] McNeil, C. L.; Johnson, B. D.; Farmer, D. M., *Deep-Sea Res. Part I-Oceanogr. Res. Pap.* **1995**, *42*, 819.

[80] Dunne, J. P.; Devol, A. H.; Emerson, S., *J. Atmos. Ocean. Technol.* **2002**, *19*, 1709.

[81] Emerson, S.; Stump, C.; Johnson, B.; Karl, D. M., *Deep-Sea Res. Part I-Oceanogr. Res. Pap.* **2002**, *49*, 941.

[82] Chapman, C. S.; Van den Berg, C. M. G., *Environ. Sci. Technol.* **2005**, *39*, 2769.

[83] Kinoshita, K., *Electrochemical Oxygen Technology*; John Wiley & Sons, Inc: Chichester, 1992.

[84] Tarasevich, M. R.; Sadkowski, A.; Yeager, E. In *Comprehensive Treatise of Electrochemistry*; Conway, B. E., Bockris, J. O., Yeager, E., Khan, S. U. M., White, R. E., Eds.; Plenum Press: New York, 1983; Vol. 7, pp 301.

[85] Hoare, J. P., *The Electrochemistry of Oxygen*; Interscience: New York, 1968.

[86] Appleby, A. J., *J. Electroanal. Chem.* **1993**, *357*, 117.

[87] Yeager, E., *Electrochim. Acta* **1984**, *29*, 1527.

[88] Wroblowa, H. S.; Pan, Y.-C.; Razumney, G., *J. Electroanal. Chem.* **1976**, *69*, 195.

[89] Bagotskii, V. S.; Tarasevich, M. R.; Filinovskii, V. Y., *Elektrokhimiya* **1969**, *5*, 1218.

[90] Delahay, P., *J. Electrochem. Soc.* **1950**, *97*, 205.

[91] Zurilla, R. W.; Sen, R. K.; Yeager, E., *J. Electrochem. Soc.* **1978**, *125*, 1103.

[92] Hossain, M. S.; Tryk, D.; Yeager, E., *Electrochim. Acta* **1989**, *34*, 1733.

[93] Bagotzky, V. S.; Shumilova, N. A.; Khrushcheva, E. I., *Electrochim. Acta* **1976**, *21*, 919.

[94] Postlethwaite, T. A.; Hutchison, J. E.; Murray, R.; Fosset, B.; Amatore, C., *Anal. Chem.* **1996**, *68*, 2951.

[95] Huang, J.; Zhang, C.; Zhang, W.; Zhou, X., *J. Electroanal. Chem.* **1997**, *433*, 33.

[96] Anderson, A. B.; Albu, T. V., *J. Electrochem. Soc.* **2000**, *147*, 4229.

[97] Anderson, A. B.; Albu, T. V., *Electrochem. Commun.* **1999**, *1*, 203.

[98] Gnanamuthu, D. S.; Petrocelli, J. V., *J. Electrochem. Soc.* **1967**, *114*, 1036.

[99] Damjanovic, A.; Genshaw, M. A.; Bockris, J. O. M., *J. Electroanal. Chem.* **1967**, *15*, 173.

[100] Kolthoff, I. M.; Jordan, J., *J. Am. Chem. Soc.* **1952**, *74*, 4801.

[101] Kozawa, A.; Zilionis, V. E.; Brodd, R. J., *J. Electrochem. Soc.* **1970**, *117*, 1474.

[102] Pletcher, D.; Sotiropoulos, S., *J. Chem. Soc.-Faraday Trans.* **1995**, *91*, 457.

[103] Jiang, S. P.; Cui, C. Q.; Tseung, A. C. C., *J. Electrochem. Soc.* **1991**, *138*, 3599.

[104] Miyata, Y.; Asakura, S., *Corrosion Sci.* **2002**, *44*, 589.

[105] Jovancicevic, V.; Bockris, J. O., *J. Electrochem. Soc.* **1986**, *133*, 1797.

[106] King, F.; Quinn, M. J.; Litke, C. D., *J. Electroanal. Chem.* **1995**, *385*, 45.

[107] Kaska, S. M.; Sarangapani, S.; Giner, J., *J. Electrochem. Soc.* **1989**, *136*, 75.

[108] Pletcher, D.; Sotiropoulos, S., *J. Electroanal. Chem.* **1993**, *356*, 109.

[109] Brandt, E. S., *J. Electroanal. Chem.* **1983**, *150*, 97.

[110] Horanyi, G.; Solt, J.; Nagy, F., *J. Electroanal. Chem.* **1971**, *31*, 95.

[111] Horanyi, G.; Rizmayer, E. M., *J. Electroanal. Chem.* **1977**, *83*, 367.

[112] Kozawa, A., *J. Electroanal. Chem.* **1964**, *8*, 20.

[113] Griffith, J. S., *Proc. Roy. Soc. (London)* **1956**, *235A*, 23.

[114] Pauling, L., *Nature (London, United Kingdom)* **1964**, *203*, 182.

[115] Yeager, E., *J. Electrochem. Soc.* **1981**, *128*, C160.

[116] Adzic, R. R.; Wang, J. X., *J. Phys. Chem. B* **1998**, *102*, 8988.

[117] Fischer, P.; Heitbaum, J., *J. Electroanal. Chem.* **1980**, *112*, 231.

[118] Adzic, R. R.; Wang, J. X., *Electrochim. Acta* **2000**, *45*, 4203.

[119] Oldham, K. B., *J. Electroanal. Chem.* **1988**, *250*, 1.

[120] Chen, S. L.; Kucernak, A., *J. Phys. Chem. B* **2004**, *108*, 3262.

[121] Damjanovic, A.; Sepa, D. B.; Vracar, L. M.; Vojnovic, M. V., *Berichte der Bunsen-Gesellschaft* **1986**, *90*, 1231.

[122] Sepa, D. B.; Vojnovic, M. V.; Vracar, L. M.; Damjanovic, A., *Electrochim. Acta* **1986**, *31*, 91.

[123] Sepa, D. B.; Vojnovic, M. V.; Vracar, L. M.; Damjanovic, A., *Electrochim. Acta* **1986**, *31*, 97.

[124] Sepa, D. B.; Vracar, L. M.; Vojnovic, M. V.; Damjanovic, A., *Electrochim. Acta* **1986**, *31*, 1401.

[125] Zinola, C. F.; Castro Luna, A. M.; Arvia, A. J., *Electrochim. Acta* **1994**, *39*, 1951.

[126] Golas, J.; Drickamer, H. G.; Faulkner, L. R., *J. Phys. Chem.* **1991**, *95*, 10191.

[127] Sepa, D. B.; Vojnovic, M. V.; Vracar, L. M.; Damjanovic, A., *Electrochim. Acta* **1987**, *32*, 129.

[128] Himmelblau, D. M., *J. Phys. Chem.* **1959**, *63*, 1803.

[129] Battino, R.; Cleve, H. L., *Chem. Rev.* **1966**, *66*, 395.

[130] Carpenter, J. H., *Limnol. Oceanogr.* **1966**, *11*, 264.

[131] Miller, K. W.; Hildebrand, J. H., *J. Am. Chem. Soc.* **1968**, *90*, 3001.

[132] Benson, B. B.; Krause, D., Jr.; Peterson, M. A., *J. Solution Chem.* **1979**, *8*, 655.

[133] Bignell, N., *J. Phys. Chem.* **1984**, *88*, 5409.

[134] Tromans, D., *Hydrometallurgy* **1998**, *48*, 327.

[135] Rettich, T. R.; Battino, R.; Wilhelm, E., *J. Chem. Thermodyn.* **2000**, *32*, 1145.

[136] Rasmussen, H. N.; Rasmussen, U. F., *Analytical Biochemistry* **2003**, *319*, 105.

[137] Tromans, D., *Hydrometallurgy* **1998**, *50*, 279.

[138] Cramer, S. D., *Industrial & Engineering Chemistry Process Design and Development* **1980**, *19*, 300.

[139] Murray, C. N.; Riley, J. P., *Deep-Sea Research* **1969**, *16*, 311.

[140] Benson, B. B.; Krause, D., *Limnol. Oceanogr.* **1984**, *29*, 620.

[141] Garcia, H. E.; Gordon, L. I., *Limnol. Oceanogr.* **1992**, *37*, 1307.

[142] Han, P.; Bartels, D. M., *J. Phys. Chem.* **1996**, *100*, 5597.

[143] Vivian, J. E.; King, C. J., *AIChE Journal* **1964**, *10*, 221.

[144] Obrien, R. N.; Hyslop, W. F., *Can. J. Chem.-Rev. Can. Chim.* **1977**, *55*, 1415.

[145] Ferrel, R. T.; Himmelblau, D. M., *J. Chem. Eng. Data* **1967**, *12*, 111.

[146] Ho, C. S.; Ju, L. K.; Baddour, R. F.; Wang, D. I. C., *Chem. Eng. Sci.* **1988**, *43*, 3093.

[147] Hung, G. W.; Dinius, R. H., *J. Chem. Eng. Data* **1972**, *17*, 449.

[148] Tsushima, M.; Tokuda, K.; Ohsaka, T., *Anal. Chem.* **1994**, *66*, 4551.

[149] Morris, S. E., *Trac-Trends in Analytical Chemistry* **1988**, *7*, 227.

[150] Wise, D. L.; Houghton, G., *Chem. Eng. Sci.* **1966**, *21*, 999.

[151] Ikeuchi, H.; Hayafuji, M.; Aketagawa, Y.; Taki, J.; Sato, G. P., *J. Electroanal. Chem.* **1995**, *396*, 553.

[152] Jovancicevic, V.; Zelenay, P.; Scharifker, B. R., *Electrochim. Acta* **1987**, *32*, 1553.

[153] Vanstroe, A. J.; Janssen, L. J. J., *Anal. Chim. Acta* **1993**, *279*, 213.

[154] Akita, K., *Ind. Eng. Chem. Fund.* **1981**, *20*, 89.

[155] Glasstone, S.; Laidler, K., J.; Eyring, H., *The Thoery of Rate Processes*; McGraw-Hill Book Company, Inc.: New York, 1941.

[156] Craig, H.; Hayward, T., *Science* **1987**, *235*, 199.

[157] Bearman, G., Ed. *Seawater: its composition, properties and behaviour*, 3rd ed.; The Open University and Pergamon Press: Oxford, 1989.

[158] Sotiropoulos, S., Ph.D. Thesis, University of Southampton, Southampton, 1994.

[159] Bartlett, P. N. In *Biosensors: A Practical Approach*; Cass, A. E. G., Ed.; Oxford University Press: Oxford, 1990, pp 47.

[160] Denuault, G., *Chem. Ind.* **1996**, 678.

[161] Zoski, C. G., *Electroanalysis* **2002**, *14*, 1041.

[162] Hoare, J. P., *Electrochim. Acta* **1982**, *27*, 1751.

[163] Rand, D. A. J.; Woods, R., *J. Electroanal. Chem.* **1972**, *35*, 209.

[164] Pharr, C. M.; Griffiths, P. R., *Anal. Chem.* **1997**, *69*, 4665.

[165] Pharr, C. M.; Griffiths, P. R., *Anal. Chem.* **1997**, *69*, 4673.

[166] Pyo, M.; Bard, A. J., *Electrochim. Acta* **1997**, *42*, 3077.

[167] Banks, C. E.; Rees, N. V.; Compton, R. G., *J. Electroanal. Chem.* **2002**, *535*, 41.

[168] Banks, C. E.; Compton, R. G.; Fisher, A. C.; Henley, I. E., *Phys. Chem. Chem. Phys.* **2004**, *6*, 3147.

[169] Lovrecek, B.; Moslavac, K.; Matic, D., *Electrochim. Acta* **1981**, *26*, 1087.

[170] Capon, A.; Parsons, R., *J. Electroanal. Chem.* **1972**, *39*, 275.

[171] Gaur, J. N.; Schmid, G. M., *J. Electroanal. Chem.* **1970**, *24*, 279.

[172] Frankenthal, R. P.; Thompson, D. E., *J. Electrochem. Soc.* **1976**, *123*, 799.

[173] Ye, S.; Ishibashi, C.; Shimazu, K.; Uosaki, K., *J. Electrochem. Soc.* **1998**, *145*, 1614.

[174] Van Muylder, J.; Pourbaix, M. In *Atlas of Electrochemical Equilibria in Aqueous Solutions*; Pourbaix, M., Ed.; NACE International: New York, 1974.

[175] Kelsall, G. H.; Welham, N. J.; Diaz, M. A., *J. Electroanal. Chem.* **1993**, *361*, 13.

[176] Tunuli, M. S., *Talanta* **1992**, *39*, 85.

[177] Holland-Moritz, E.; Gordon, J.; Kanazawa, K.; Sonnenfeld, R., *Langmuir* **1991**, *7*, 1981.

[178] El-Deab, M. S.; Ohsaka, T., *Electrochem. Commun.* **2002**, *4*, 288.

[179] Strbac, S.; Adzic, R. R., *J. Electroanal. Chem.* **1996**, *403*, 169.

[180] Blizanac, B. B.; Lucas, C. A.; Gallagher, M. E.; Arenz, M.; Ross, P. N.; Markovic, N. M., *J. Phys. Chem. B* **2004**, *108*, 625.

[181] Yang, Y. F.; Denuault, G., *J. Electroanal. Chem.* **1996**, *418*, 99.

[182] Gilman, S., *J. Phys. Chem.* **1964**, *68*, 2098.

[183] Bagotzky, V. S.; Vassiyev, Y. B.; Weber, J.; Pirtskha.Jn, *J. Electroanal. Chem.* **1970**, *27*, 31.

[184] Molina, F. V.; Posadas, D., *Electrochim. Acta* **1988**, *33*, 661.

[185] Gilman, S., *J. Phys. Chem.* **1964**, *68*, 2112.

[186] Novak, D. M.; Conway, B. E., *J. Chem. Soc., Faraday Trans.* **1981**, *77*, 2341.

[187] Zolfaghari, A.; Conway, B. E.; Jerkiewicz, G., *Electrochim. Acta* **2002**, *47*, 1173.

[188] Wroblowa, H.; Rao, M. L. B.; Damjanovic, A.; Bockris, J. O. M., *J. Electroanal. Chem.* **1967**, *15*, 139.

[189] Bagotskii, V. S.; Tarasevich, M. R.; Filinovskii, V. Y., *Elektrokhimiya* **1972**, *8*, 84.

[190] Brummer, S. B., *J. Phys. Chem.* **1965**, *69*, 562.

[191] Birkin, P. R.; Elliott, J. M.; Watson, Y. E., *Chemical Communications (Cambridge)* **2000**, 1693.

[192] Elliott, J. M.; Birkin, P. R.; Bartlett, P. N.; Attard, G. S., *Langmuir* **1999**, *15*, 7411.

[193] Elliott, J. M.; Attard, G. S.; Bartlett, P. N.; Coleman, N. R. B.; Merckel, D. A. S.; Owen, J. R., *Chem. Mat.* **1999**, *11*, 3602.

[194] Attard, G. S.; Bartlett, P. N.; Coleman, N. R. B.; Elliott, J. M.; Owen, J. R., *Langmuir* **1998**, *14*, 7340.

[195] Jiang, J. J.; Kucernak, A., *Electrochem. Solid State Lett.* **2000**, *3*, 559.

[196] Markovic, N.; Gasteiger, H.; Ross, P. N., *J. Electrochem. Soc.* **1997**, *144*, 1591.

[197] Cook, D., 4th Year MChem Project, University of Southampton, Southampton, 2001.

[198] Keidel, F. A., *Journal of Industrial and Engineering Chemistry (Washington, D. C.)* **1960**, *52*, 490.

[199] Jeroschewski, P.; zurLinden, D., *Fresenius Journal of Analytical Chemistry* **1997**, *358*, 677.

[200] Wingo, W. J.; Emerson, G. M., *Analytical Chemistry* **1975**, *47*, 351.

[201] LeFevre, M. E., *Journal of applied physiology* **1969**, *26*, 844.

[202] Fatt, I.; Helen, R. S., *Journal of Applied Physiology* **1969**, *27*, 435.

[203] Carpenter, J. H., *Limnology and Oceanography* **1965**, *10*, 141.

[204] Austin, E., PhD Thesis, University of Southampton, Southampton, 2002.

[205] Austin, E., Evaluation of Optical Oxygen sensor for in-situ oceanographic measurements. 2nd experiment, **2005**

[206] Miller, J. C.; Miller, J. N., *Statistics for Analytical Chemistry*, 2nd ed.; Ellis Horwood: Chichester, 1988.

[207] Grasshoff, K.; Kremling, K.; Ehrhardt, M., Eds. *Methods of seawater analysis*, 3rd ed.; Wiley-VCH: Weinheim, Chichester, 1999.

[208] Evans, S. A. G.; Elliott, J. M.; Andrews, L. M.; Bartlett, P. N.; Doyle, P. J.; Denuault, G., *Anal. Chem.* **2002**, *74*, 1322.

[209] Evans, S. A. G., PhD Thesis, University of Southampton, Southampton, 2002.

[210] Andrieux, C. P.; Hapiot, P.; Saveant, J. M., *J. Phys. Chem.* **1988**, *92*, 5992.

[211] Floate, S.; Hahn, C. E. W., *Sens. Actuators, B* **2005**, *110*, 137.

[212] Zhou, Z. B.; Liu, W. J.; Liu, C. C., *Sens. Actuators, B* **1998**, *52*, 219.

[213] Lin, X. Q.; Guo, Z. Y., *Analytical Sciences* **2004**, *20*, 1645.

[214] Streeter, V. L., Ed. *Handbook of Fluid Dynamics*; McGraw-Hill Book Company, Inc.: New York, 1961.

[215] Toth, K.; Stulik, K.; Kutner, W.; Feher, Z.; Lindner, E., *Pure Appl. Chem.* **2004**, *76*, 1119.

[216] Booth, J.; Compton, R. G.; Cooper, J. A.; Dryfe, R. A. W.; Fisher, A. C.; Davies, C. L.; Walters, M. K., *J. Phys. Chem.* **1995**, *99*, 10942.

[217] Klymenko, O. V.; Evans, R. G.; Hardacre, C.; Svir, I. B.; Compton, R. G., *J. Electroanal. Chem.* **2004**, *571*, 211.

[218] Yu, J. S.; Zhang, Z. X., *J. Electroanal. Chem.* **1997**, *439*, 73.

[219] Fisher, A. C.; Gooch, K. A.; Henley, I. E.; Yunus, K., *Analytical Sciences* **2001**, *17*, i371.

[220] Amphlett, J. L.; Denuault, G., *J. Phys. Chem. B* **1998**, *102*, 9946.

[221] Fushimi, K.; Ammi, K.; Seo, M., *Electrochem. Commun.* **2004**, *6*, 959.

[222] http://www.sis-germany.com/doa.htm.

[223] http://www.seabird.com/products/spec_sheets/43data.htm.

[224] Kear, G.; Barker, B. D.; Walsh, F. C., *Corrosion Sci.* **2004**, *46*, 109.

[225] Tuthill, A. H., *Materials Performance* **1987**, *26*, 12.

[226] Li, Y. B.; Trush, M. A., *Carcinogenesis* **1993**, *14*, 1303.

[227] Bengough, G. D.; Jones, R. M.; Pirret, R., *Journal of the Institute of Metals* **1920**, *23*, 65.

[228] *UNESCO, Technical Papers in Marine Science* **1978**, *30*, 1.

[229] Fofonoff, N. P., *J. Geophys. Res.-Oceans* **1985**, *90*, 3332.

[230] Cunningham, S. A., RRS Discovery Cruise 279 (04 Apr - 10 May 2004): A Transatlantic Hydrography Section at 24.5°N, **2005**

[231] Bryden, H. L.; Longworth, H. R.; Cunningham, S. A., *Nature* **2005**, *438*, 655.

[232] Pascal, R. W. In *RRS Discovery Cruise 279 (04 Apr - 10 May 2004): A Transatlantic Hydrography Section at 24.5°N*; Cunningham, S. A., Ed.: Southampton, 2005, pp 193.